

# UC Berkeley

## UC Berkeley Electronic Theses and Dissertations

### Title

Interactions of Non-Thermal Air Plasmas with Aqueous Solutions

### Permalink

<https://escholarship.org/uc/item/6tv816wr>

### Author

Anderson, Carly Elizabeth

### Publication Date

2016

Peer reviewed|Thesis/dissertation

Interactions of Non-Thermal Air Plasmas with Aqueous Solutions

By

Carly Elizabeth Anderson

A dissertation submitted in partial satisfaction of the

requirements for the degree of

Doctor of Philosophy

in

Chemical Engineering

in the

Graduate Division

of the

University of California, Berkeley

Committee in charge:

Professor David B. Graves, Co-Chair

Professor Douglas S. Clark, Co-Chair

Professor Bryan D. McCloskey

Professor Evan R. Williams

Fall 2016

Interactions of Non-Thermal Air Plasmas with Aqueous Solutions

by  
Carly Elizabeth Anderson

© Copyright 2016  
All rights reserved

## Abstract

### Interactions of Non-Thermal Air Plasmas with Aqueous Solutions

by

Carly Elizabeth Anderson

Doctor of Philosophy in Chemical Engineering

University of California, Berkeley

Professors David B. Graves and Douglas S. Clark, Co-Chairs

Devices to produce non-thermal atmospheric-pressure plasma, or NTP, are gaining increasing attention for a wide range of applications. In addition to promising work in the field of plasma medicine, NTP has also been shown to effectively decontaminate food and surfaces, degrade organic pollutants, and open new routes for nanomaterials synthesis. In many of these applications, plasma-liquid interfaces play a key role in influencing reaction pathways and mediating the transport of reactive species to their intended targets in the liquid phase. Understanding the mechanisms by which reactive species are formed in the liquid phase will aid in the rational design of plasma devices for treating aqueous systems or tissues, and may enable the delivery of tailored ‘cocktails’ of reactive species.

In order to carry out this research, a device producing a pin-to-target plasma discharge in direct contact with a target solution was developed. NTP discharges in direct contact with an aqueous solution are known to produce reactive oxygen and nitrogen species in solution, including  $\text{OH}^\bullet$ ,  $\text{NO}_2^\bullet$  and  $\text{O}_2^\bullet$ . The type and geometry of the discharge employed, as well as the properties of the treated solution, affect the quantity and ratio of species produced. The resulting setup can be tuned for solution acidification, greater oxidative power, limited peak current flow or other attributes depending on the research priorities. The relationship between the voltage-current characteristics of the device, the properties of the solution (pH, conductivity), and the reactive species produced in solution was established.

Methods to measure reactive species produced by NTP in liquids were reviewed and developed where necessary. This allowed the evolution of reactive species (e.g.  $\text{H}_2\text{O}_2$ ,  $\text{NO}_2^-$ , and  $\text{OH}^\bullet$ ) produced in solution by NTP to be determined as a function of time and solution pH. Subsequent reactions of these species were considered, and a model of peroxyntrous acid ( $\text{O}=\text{NOOH}$ ) formation and degradation was developed and used to investigate the relevant reaction rates.

Evidence is provided that near-surface reactions generating hydroxyl radicals ( $\text{OH}^\bullet$ ) or other oxidizing species are the predominant source of active species in NTP-treated solution by tracking the degradation of indigo carmine, a common industrial dye. Selective use of buffers or other additives allows inactivation of certain reaction pathways, enabling contributions from either surface or bulk reactions to be identified. The observed rate of indigo oxidation in contact with the

discharge far exceeded predictions from modeling reaction networks based on concentrations of species measured in the bulk solution, indicating a high concentration of highly oxidizing species within a very short distance ( $< 1 \mu\text{M}$ ) of the plasma-liquid interface. The origin of the reactive species produced (gas phase, boundary layer, or bulk solution) and the relative importance of chemical kinetics versus transport were investigated during the oxidation of the target molecule in solution. Competition experiments and analysis of indigo carmine degradation products were used to identify active agents and properties of the NTP-treated solutions.

Furthermore, the effects of NTP on simple biomolecules was investigated. The effect of NTP on solutions of free amino acids, nucleic acids, and the anti-oxidant glutathione was assessed to determine the extent to which irreversible oxidation of these species is induced. This work provides initial evidence of key mechanisms for both *in vitro* and *in vivo* studies reported in the literature. These results have important implications for NTP device design and operation for future applications of NTP.

For my parents  
and grandparents

# TABLE OF CONTENTS

---

Abstract	1
1 Introduction	1
1.1 Background: Plasma-Liquid Interactions	1
1.2 Applications of Non-Thermal Plasmas in Contact with Liquids	1
1.3 Challenges in Understanding Plasma-Liquid Interactions	3
1.4 Aims of Project	4
2 Plasma Devices for the Direct Treatment of Liquids	6
2.1 Basics of Low-Temperature Plasmas	6
2.2 Positive-Polarity Corona Discharge (Transient Spark)	10
2.2.1 Mechanism of Operation	11
2.2.2 Discharge Modes and Key Characteristics	13
2.2.3 Equipment and Materials	15
2.2.4 Voltage and Current Characteristics	17
2.2.5 Influence of Ballast Resistor	24
2.2.6 Electrode Considerations	25
2.2.6.1 Anode	25
2.2.6.2 Cathode	28
2.2.7 Inter-electrode Gap	29
2.2.8 Other Design Considerations	30
2.3 Negative-Polarity Corona Discharge	31
2.3.1 Mechanisms of Operation	31
2.3.2 Discharge Characteristics	32
2.3.3 Use of Negative-Polarity Discharges in this Work	32
2.4 Dielectric Barrier Discharges	33
2.4.1 Overview	33
2.4.2 Design Considerations	34
2.4.3 Prototyping of Floating-Electrode DBD	35
2.5 Conclusions	39
3 Plasma-Generated Liquid Chemistry	41
3.1 Abstract	41
3.2 Species Generated by Plasma in Contact with Liquids	41
3.2.1 Gas-Phase Precursor Chemistry: Origin of Species in the Gas Phase	42

3.2.2	Mass Transfer at the Plasma-Liquid Interface and in the Bulk Solution	45
3.2.3	Evolution of Reactive Species in the Bulk Solution	51
3.2.4	Reactions at Submerged Electrode	56
3.3	Measurement of Reactive Oxygen and Nitrogen Species in Plasma-treated Solutions	57
3.3.1	Quantification of Aqueous H <sub>2</sub> O <sub>2</sub>	58
3.3.2	Quantification of Aqueous Nitrite and Nitrate	60
3.3.2.1	Direct Absorbance of Nitrite and Nitrate	60
3.3.2.2	Griess Method for Nitrite Measurement	61
3.3.2.3	Anion Chromatography	62
3.3.2.4	Ion-Specific Electrodes	63
3.3.3	Spin-Traps and Electron Paramagnetic Resonance (EPR)	63
3.3.4	Use of Indigo Carmine as a Non-Specific Indicator of General Oxidizing Agents	66
3.3.5	Positive Controls: Methods to Produce Oxidizing Species without Plasma	68
3.3.6	Competition Experiments with Radical Scavengers	68
3.4	Conclusions	76
4	The Role of Reactions at the Plasma-Liquid Interface in Direct Plasma Treatment	78
4.1	Motivation	78
4.2	Plasma Exposure Conditions	79
4.3	Generation of OH <sup>•</sup> through Reactions in the Bulk Liquid	79
4.4	Generation of OH <sup>•</sup> through Reactions at the Plasma-liquid Interface	84
4.5	Comparison of Surface and Bulk Liquid Contributions to Species Oxidation	86
4.6	Mass Transport at Plasma-Solution Interface	89
4.7	Analysis of Indigo Carmine Degradation Products	93
4.8	Discussion	96
4.9	Conclusions	98
5	Effects of Non-Thermal Plasma on Biological Targets	100
5.1	Abstract	100
5.2	Analytical Methods	100
5.2.1	NMR Spectroscopy	100
5.2.2	Mass Spectrometry	105
5.3	Effects of Non-Thermal Plasma on Nucleic Acids	106
5.3.1	Experimental Notes	106
5.3.2	Results	108



5.3.3	Discussion	110
5.4	Effects of Non-Thermal Plasma on Amino Acids	111
5.4.1	Experimental Notes	112
5.4.2	Results	112
5.4.3	Discussion	114
5.5	Further Study of Targets Containing Sulfhydryl Moieties	115
5.5.1	Cysteine	115
5.5.2	Glutathione	117
5.6	Conclusions	122
5.7	Supplementary Information: Mass spectra of nucleic and amino acids	123
6	Conclusions and Future Work	140
6.1	Non-thermal Plasma Device Development	140
6.2	Evolution of Reactive Species in the Bulk Solution	140
6.3	Sources of Oxidative Species in Liquids from Direct Plasma Exposure	141
6.4	Effects of Non-Thermal Plasma on Biological Targets	142
6.5	Suggestions for Future Work	142
7	References	144

## Acknowledgements

Coming to UC Berkeley for grad school was one of the best decisions I've made, but not for the reasons I expected. For the past five or so years, I have been surrounded by some of the most brilliant, insightful, dedicated, and caring people on the planet. Without these people, this thesis would not exist. My life would also be infinitely less rich.

I would first like to thank Dave Graves for his support and patience as we explored plasma-liquid interactions, and for the many, many hours of scientific discussion. More thanks to Doug Clark for allowing me to be part of the Clark Lab community, and for providing a sanity check and keeping us focused. I would also like to thank Jeff Reimer for supporting me through the first year of grad school (and first several projects), his yoda-like advice, and for his understanding when I wanted to take off on a different path.

This work would not have been possible without the expertise of my excellent labmates: particularly Brandon, who was there for the duration and always willing to answer questions on methods, hardware, software, and occasionally philosophy, depending on what was called for. Don for being engaged in everyone's research, for helpful discussions on modelling and system questions, and for keeping the lab stocked with coffee and baked goods. The talented undergraduates who leant their assistance: Nico, Jeremy, Michael, Richard, and Pritha. Postdocs and visiting scholars: particularly Prof. Zdenko Machala for helping me get started with corona discharges and for navigating Japan, and Alex Lindsay for modelling assistance and comradery.

There are many other people behind the scenes who made this work possible. A huge thank-you to Carlet Altamirano for keeping things on track, for organizing paella parties, and for keeping the department from dissolving into chaos. Jim Breen at the glass shop for making any crazy containers I needed, and providing life advice. Eric Granlund at the machine shop for turning my ill-conceived sketches into practical, functional devices. Phil Simon for the stories, the pug pictures, and the training (and many refreshers) in the student shop. Hasan Celik for NMR assistance, and Tony Iavarone for help with mass spectrometry. Gaelle Deshayes and Mike Kumpf for making the lab safety coordinator job not-terrible (except for that time she rooted for the Netherlands during the world cup). Last and perhaps most importantly, thanks to Ricardo at coffee lab for the caffeine, donuts and positive energy that kept me going on rough days.

Many lessons learned in grad school aren't captured explicitly in this thesis; for this, I am profoundly grateful to the greater community of Berkeley grad students for sharing the journey. The class of 2011 for always supporting each other and reinforcing that we are normal, properly socialized humans. The Isothermal PBRs for being themselves, in all incarnations. The Clark Lab ladies, particularly Kathryn, for academic writing and professional advice. The Berkeley Energy and Resource Collaborative folks, particularly Danny H., for connecting me to the greater energy and cleantech community and for all the free beer. All of those who shared trails

and crags, mountains and miles of asphalt. Allie and Stan for making backpacking trips happen (pace: grueling, rations: meager). OJ for hanging out in the back with me and telling riddles. Coach Teran for planning workouts and keeping me entertained on marathon training runs. The wine-bike-campers. Eddy, JPK and Maria for teaching me to climb, catching falls, and talking science on long car rides.

Finally, I want to thank my awesome housemates – Hilda, Lin, Jacob, Nico, Rachel and Melanie – for everything. For the time spent discussing projects, editing first drafts, and many rounds of practice talks. For helping me get access to equipment, and for sample code. For work-partying, thesis-partying, and encouraging me when we needed to buckle down, and actively facilitating fun plans at other times. For exploring California, sharing the driving, and ensuring that I always had a climbing/running/adventure buddy. For picking me up when I crashed my bike, living with clutter, and not being too mad when homebrew bottle-bombs explode all over the kitchen. For making coffee, keeping me fed (with the appropriate levels of sodium), and helping finish bottles of wine. For everything else.

I can't wait to see what comes next.

*Stay beautiful, and don't work too hard.*  
- Ricardo Perez

# 1 Introduction

## 1.1 Background: Plasma-Liquid Interactions

Perhaps the first reported experiments on plasma-liquid interactions were performed by Cavendish in 1785, who wrote about the generation of an electric spark in air, which produced nitric acid in adjacent water. [1] J. Gubkin is generally cited as the first to study plasmas formed at the surface of solutions. In 1887, he proposed that free electrons in a plasma could be used to reduce ions in solution. [2] This was followed by additional work on glow discharges and electrochemistry in the early 1900s by numerous authors. [3]–[5]

Such discharges were studied in the context of contact glow-discharge electrolysis (CGDE) as early as the 1950s. [6], [7] In conventional electrolysis, a voltage difference is applied to electrodes within an aqueous solution, resulting in water splitting and the creation of gaseous O<sub>2</sub> and H<sub>2</sub> at separate electrodes. In contact glow-discharge electrolysis, a dc glow (constant current) discharge is sustained between an electrode and the surface of the electrolyte, with the other electrode (generally the anode) submerged. Such devices are capable of improving the yields of chemical oxidation over those predicted from Faraday's Law. [8], [9] While CGDEs were initially studied in an electrochemical context, in the 1970s they became a target of research on the formation of amino acids at the plasma-liquid interface, related to the origin of life. [10], [11] Recent work has investigated the use of CGDEs for pollutant degradation and other environmental applications, given the efficiency at which OH• and O• are generated in these systems. [8], [12], [13]

Beginning in the late 1990s through the early 2000s, interest in plasma-liquid interactions expanded to include other types of discharges in contact with liquids. A good review of the classification of discharges in and in contact with liquids, the early work in this field and the challenges inherent in characterizing these plasmas was written by Bruggeman and Leys in 2009 [14]. New applications were also proposed; in addition to wastewater treatment and microbial killing [15], the first experiments with non-thermal plasma as a medical treatment were performed in the early 2000s. [16]–[18] Recently, research on plasma-liquid interactions has expanded to include even more applications, as discussed in the following section.

## 1.2 Applications of Non-Thermal Plasmas in Contact with Liquids

Non-thermal plasma discharges in contact with liquids generate strong electric fields, UV radiation, and active radicals (OH•, atomic oxygen, hydrogen peroxide, etc.), within the liquid phase. These phenomena and reactive species have the ability to break down organic molecules, or influence biological or electrochemical processes, depending on the strength of the plasma and the situation in which it is applied. Devices to produce “cold” (non-thermal) plasma at atmospheric-pressure are gaining increasing attention for an increasingly wide range of applications, including plasma medicine, microbial decontamination, wastewater and environmental remediation, analytical chemistry, plasma catalysis, and nanomaterials synthesis. These areas are briefly discussed below.

### *Plasma medicine*

The ability of CAPs to induce biological effects, primarily localized cell death, has sparked rapid growth in the field of “plasma medicine”— a relatively new branch of plasma science focusing on the application of non-thermal plasmas (NTPs) at atmospheric pressure for medical and public health applications. These

applications include surface, water and tissue disinfection, oral hygiene, wound healing, and even cancer treatment [19]–[22]. Unlike thermal plasmas, which have been used by surgeons since the 1970s for ablation and tissue cauterization [23], the gas temperature ( $T_g$ ) of these non-thermal or “cold” plasmas can remain near room temperature while electron temperatures ( $T_e$ ) exceed 10,000K (1 eV), and can thus contact tissues directly without thermal damage.

At this stage, two plasma devices for topical treatments have received approval from regulatory agencies in the European Union. Specifically, these devices have been used to reduce the bacterial load in chronic diabetic wounds and promote wound healing. [20], [24]–[26] Significant additional efforts are underway to develop non-thermal plasma treatments as an adjunctive cancer therapy. [27]–[30] Plasma treatment is also being investigated as a procedure for other medical treatments, including disinfection of eye tissue [17], dental surgery [31], [32] and for treating toe nail fungus [33].

### *Microbial inactivation*

Over the past decade, the body of work demonstrating the ability of low-temperature plasmas to inactivate bacteria and viruses has grown exponentially. [34], [35] The species shown to be inactivated by various plasma devices include feline calicivirus [36], staphylococcus aureus [17], candida albicans [17], [37], Pseudomonas aeruginosa [22], Bacillus atrophaeus [38], Staphylococcus epidermidis [39], and numerous E. coli studies, to name a few.

While the exact mechanisms of inactivation vary by organism and plasma device, some studies have begun to identify the responsible agents. For example, the inactivation of feline calicivirus in solution by a radio-frequency (RF) argon jet was attributed to the formation of  $^1O_2$  or O=NOOH, depending on whether  $O_2$  or air was added to the feed gas. [40] Pavlovich et al correlated E. coli death to the production of  $O_3$  by an indirect dielectric barrier discharge. [41]

### *Wastewater remediation*

Beginning with the early research in contact glow discharge electrolysis (CDGE), non-thermal plasmas have been recognized as a tool to generate highly oxidative species in liquids capable of mineralizing contaminants. Work continues on improving the energy and oxidation efficiencies of non-thermal plasma reactors. [8], [42] Brisset [43], Locke [44]–[46], and Thagard [47], [48] have done seminal work in this area.

### *Analytical Chemistry*

Plasma devices are often used in analytical chemistry applications in preparing solutions for analysis or as part of the sampling process. In essence, non-thermal plasmas can provide a controlled, relatively gentle means to produce ions from solutions in preparation for analysis. These techniques are typically based on glow discharges with liquid electrodes (e.g. for atomic spectroscopy [49], [50]), inductively coupled plasmas [51], and a variety of corona, dielectric barrier discharges and glow discharges as ionization sources for mass spectrometry [52], [53].

### *Plasma catalysis*

The unique electrical environments and radical species produced by plasma have attracted interest in applications to increase the efficiency of catalyzed reactions, including nitrogen fixation [54], hydrocarbon reformation [55]–[57], and general waste gas treatment [58]. The use of NTP can reduce the thermal requirements of reactions with certain catalysts. [58]

### *Synthesis of nanomaterials*

The flow of current through the aqueous solution (and production of electrons and ions by the plasma) drives electrochemical reactions including metal dissolution at a submerged anode and reduction of aqueous metal cations at the cathode / liquid interface. This approach has been used to produce of high-purity nanometer-sized metal particles directly from bulk metals or aqueous metal salts. [59]–[62] Microplasmas (plasma discharges in geometries where at least one dimension is sub-millimeter) are especially attractive for these applications due to their stability at atmospheric pressures, high electron densities, and other attributes; most of the reported synthesis techniques make use of this type of discharge.

## **1.3 Challenges in Understanding Plasma-Liquid Interactions**

In the applications just discussed, plasma-liquid interfaces are present and mediate the transport of reactive species generated by the plasma to their intended targets in the liquid phase. The physical and chemical processes occurring at the plasma-liquid interface represent a key challenge within this field. This challenge is particularly complex and multi-disciplinary due to the wide range of chemical species and physical effects which involve radical and reactive species, ions, electrons, (V)UV emission, electric fields, heat and neutral gas flows across the gas–liquid interface. On top of this, in plasmas with a liquid electrode, the electrode surface is deforming and usually evaporating. [13] While many of these individual processes are studied in distinct fields of research, there is a need to understand and connect the processes occurring in many different subfields.

Understanding the formation of reactive species and secondary chemical compounds by plasmas in liquids, including reactions rates, poses considerable challenges for diagnostic methods and in identifying the source of the observed plasma activity. The diagnostics for highly reactive (very short-lived) species generated by these plasmas in liquids are currently a great challenge because most available techniques are not selective or influence the plasma induced liquid phase chemistry. This dissertation investigates the role of species produced directly by plasma versus those generated through secondary reactions in the liquid phase. Part of this dissertation presents our results in measuring  $\text{OH}^{\bullet}$  with an indicator molecule, and discusses the controls and supporting analyses performed to assess the validity of this method.

In addition to and in light of the experimental challenges, advances are required in modeling of plasma interactions with the liquid–gas interface. In spite of the large number of factors and time scales that must be addressed to fully model plasma–liquid systems, significant progress has been made recently in addressing the coupled systems of atmospheric pressure plasmas and liquid phase reactivity. [63]–[67] Some of this progress came out of our group, as a visiting scholar was able to model the flow of neutral species in the corona discharge plasma system developed and described in this work. [66]

Introducing plasma-liquid interactions into biological systems introduces further challenges. The effects of individual reactive oxygen and nitrogen species (RONS) on specific biological targets have been well studied [30], [68]–[72]. However, less is known about the effects (and dominating active species) when the milieu of plasma-generated species is introduced, and the role of the plasma-liquid interface in mediating these effects [13]. The network of potential reactions and reaction partners becomes more complex, and the constraints become stricter.

Recently, the definition of a plasma “dose”, defining the therapeutic effects of plasma and species delivery in a medical context, has been seen as a major challenge in the quest to gain clinical acceptance. While measurements of reactive species in the gas phase can provide insights into the chemical processes and species to expect at the target, it is not straightforward to determine the flux reaching the target liquid from these measurements due to the complex transport processes encountered at the gas–liquid interphase and potentially complex make-up of the target solution. Several definitions of a plasma “dose” have been proposed, including H<sub>2</sub>O<sub>2</sub> fluence in the gas phase or concentration in the liquid phase (which are generally correlated), the total power delivered to the target, and the resulting oxidation potential of the liquid. [13]

#### 1.4 Aims of Project

As illustrated in this chapter, non-thermal plasmas are increasingly becoming a technology of interest. For many of the emerging high impact applications, understanding plasma behavior and chemical effects (complicated by the presence of the liquid and/or moist vapor layer) is necessary to gain regulatory approval or maximize the production of the desired active species chemicals.

In this dissertation, I directly address two challenges in understanding plasma-liquid interactions. First, the relative roles of reactive species produced directly by the plasma versus those generated through secondary reactions in the liquid phase are investigated, adding to our knowledge of the formation of reactive species and secondary chemical compounds by plasmas in liquids. Reaction rates and species fluxes are estimated, with consideration of the pH range and other conditions influencing the activity of these reaction pathways.

Secondly, the diagnostics for highly reactive (very short-lived) species generated by these plasmas in liquids are currently a challenge because most available techniques are not selective and may not influence the plasma induced liquid phase chemistry. In this work, the shortcomings of some diagnostic techniques are explored, and a simple method for monitoring the oxidative power of the solution through the oxidation of an indicator species is put forward (and its limitations discussed).

Throughout this research, following questions are asked:

1. *Why use plasma?* Plasma-liquid interface vs. bulk solution chemistry
2. *Which oxidizing species* produced by cold atmospheric plasma are active, and how can they be measured with confidence given the complex mixture of species present?
3. How does plasma-generated chemistry *influence subsequent reactions* in the liquid phase, or even biological pathways?

As a final comment on the motivation of this work: plasma-liquid interactions represent a region rich in interesting physics, chemistry and biology. Study of the fundamental processes involved in plasma-liquid

interactions leads to a greater under appreciation of the complexity of these systems, and of the importance of rigorous analysis in reaching meaningful scientific conclusions. Research in this area represents an exciting new opportunity to explore unknown scientific territory.



## 2 Plasma Devices for the Direct Treatment of Liquids

The first step in accomplishing this work was to construct a stable plasma device with the ability to operate reproducibly across a range of conditions. In the first section, some basic principles of atmospheric-pressure plasma discharges are discussed. This section is intended to provide background and highlight the major differences and similarities between the various types of plasmas used by the atmospheric pressure plasma community; more detailed resources are referenced where appropriate. The remaining sections describe all of the direct atmospheric-pressure plasma devices used in this work. The main device used, a direct current (DC) self-pulsed positive polarity discharge, is described in depth as the development, characterization and refinement of this device was a critical part of this effort. The subsequent sections describe other classes of plasma devices used peripherally in this work: negative-polarity DC self-pulsed discharges and dielectric barrier discharges.

### 2.1 Basics of Low-Temperature Plasmas

A key feature of low-temperature atmospheric pressure plasma is that the plasma is not at thermal equilibrium; the bulk gas molecules remain at or near atmospheric temperatures. In thermal or “hot” plasmas, all species (electrons, ions and neutrals) are in thermal equilibrium. Temperatures are typically 5000 to 50,000K. [73]. In contrast, non-thermal or “cold”<sup>1</sup> plasmas are characterized by a high electron temperature  $T_e$  but a low bulk gas temperature; the temperature of heavy particles (atoms, molecules, and ions) satisfies  $T_g \ll T_e$ . It is generally difficult to maintain such non-equilibrium states at high (atmospheric) pressures due to the high rate of collisions and short mean free paths of plasma species.

The deviation of a plasma from local thermodynamic equilibrium (LTE) can be expressed as:

$$\frac{T_e - T_g}{T_e} = \frac{m_g (\lambda_e e E)^2}{4m_e \left(\frac{3}{2}kT_e\right)^2} \quad (2.1)$$

Where  $\lambda_e$  is the mean free path of electrons,  $\lambda_e e E$  is the kinetic energy gained by an electron along one free path in the direction of the electric field  $E$ , and  $\frac{3}{2}kT_e$  is the average thermal energy. [73] Thus, large mean free paths (low pressure or density), high electric fields and low electron energies result in deviations from LTE. In our system, it is the application of *transient* locally high electric fields that enables the generation of non-thermal plasma.

To ignite ambient-pressure plasmas, a high potential difference is applied between two electrodes across a gap containing the working gas, which is may be air ( $N_2$  and  $O_2$ ), helium, argon, or a mixture of these, with or without humidity. Breakdown is initiated at the electrode with the highest radius of curvature (where the gradient in the local electric field is steepest). Free electrons are constantly present at a very low density (10-100 electrons /  $cm^3 \cdot s$ ) due to background radiation [73] (pg 29); in the presence of a strong electric field gradient, these electrons are accelerated towards the anode. If their energy is sufficient, collisions with neutral atoms or molecules will cause the ejection of another electron from the collision partner, producing

---

<sup>1</sup> Note that use of the term “cold” plasma generally refers to plasmas with low degrees of ionization (<1%); not necessarily low temperature or non-equilibrium plasmas.

a cascade of free electrons. This phenomenon, called a Townsend avalanche (after John S. Townsend, who first published this mechanism in 1901 [74]), is illustrated in Figure 2.1.

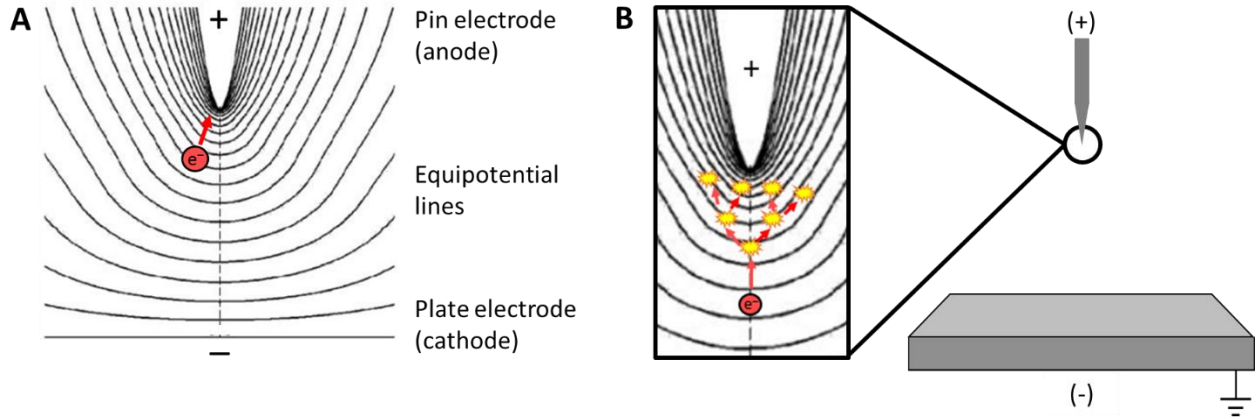


*Figure 2.1. A Equipotential lines around a pin with a high positive voltage applied (prior to discharge). A free electron (e.g. produced by cosmic rays) is accelerated down the electric field gradient, gaining kinetic energy. B At sufficient energies, collisions of free electrons with neutral gas molecules result in ionization events, creating additional free electrons in an electron “avalanche”.*

Important metrics characterizing this effect include the first and second Townsend coefficients. The first Townsend coefficient or ionization coefficient,  $\alpha$ , indicates the number of additional electrons produced from a single electron traveling 1 cm in the direction of the electric field,  $E$ . The second Townsend coefficient,  $\gamma$ , describes the number of secondary electrons produced at the cathode (per primary ion); it is dependent on both the cathode material and the working gas. For the discharge to be self-sustaining (in a homogenous electric field) the following general criterion (Townsend criterion) should be met:

$$\gamma(e^{\alpha d} - 1) = 1 \quad (2.2)$$

Where  $d$  is the distance between the electrodes. [73] Typical values for the second Townsend coefficient range from  $10^{-4} - 10^{-1}$  for various material/gas combinations, e.g. 0.1 for argon discharges with clean metal electrodes [75], [76]. Predictions of these coefficients for coronas and microdischarges have been made through modeling efforts; in general, values ranging from 0.001 – 0.1 on various discharge properties were evaluated and had little effect on the electron density or velocity of the ionization wave. [77], [78]

The second emission coefficient is generally derived from experimental data using the hypothesis that electron emission by ions is the only means of electron production from the cathode ([76], [79], [80]). While collisions with ions can be one of the major causes of electron emission, other causes may also play a significant role (e.g. photon-induced emission). [81] It is thus particularly hard to predict the electron emission when an aqueous or electrolyte cathode is used, such that the work function of the material is not well-defined and many other mechanisms for energy transfer (excitation, vibrational or rotational energy transfer, chemical reactions) are available.

Secondary electron emission from liquid cathodes remains an open area of study. However, the breakdown voltage for a radio-frequency discharge formed between a grounded metal electrode and a powered ionic liquid surface has been found to be lower than a similar discharge formed between two metal electrodes. [82] It was hypothesized that the ionic liquid can contribute to secondary electron emission and lower the threshold for breakdown by enhancing ionization processes in the plasma.

The voltage at which a self-sustained discharge occurs (breakdown voltage,  $V_{br}$ ) in a given gas, and with a given cathode material, is primarily function of the product of the pressure  $p$  and the electrode separation distance,  $d$ . This empirical relation, found by Paschen, is generally written as:

$$V_{br} = f(Nd) \quad (2.3)$$

Where  $N$  is the number density of the gas and  $d$  is again the interelectrode distance. (This removes the implicit temperature dependence.) The Paschen curve for air and other gases have been well documented; the value of  $V_{br}$  for dry air at 1 bar and 20°C is ~ 30kV/cm for a homogenous applied electric field. This relationship is not linear; however,  $V_{br}$  increases with increasing pressure-spacing product for  $d > 10\mu\text{m}$  at atmospheric pressure (e.g., 4.5 kV for  $d = 1\text{mm}$ , 8kV for 2mm, and 16 kV for 5mm). [83]

The breakdown voltage is also influenced by a number of other factors. The application of inhomogenous electric fields (e.g. use of highly curved electrodes) significantly reduces the minimum electric field required. Small amounts of humidity (up to ~1% water vapor) lower  $V_{br}$ ; beyond this point, increasing humidity increases  $V_{br}$ . [84] The frequency of the discharge and the cathode material also affect the breakdown voltage. The higher the number of secondary electrons produced at the cathode (per primary ion), the lower the required voltage; the frequency of the discharge can affect gas heating and other memory effects.

In practice, much work within the atmospheric-pressure community relies on direct experimental observation. Some classes of plasma devices commonly used by the atmospheric pressure plasma community to generate non-equilibrium discharges include:

- Corona Discharges are a class of DC discharges formed where steep gradients in electric fields are present. These may occur naturally at sharp points or areas of high curvature in high voltage lines; they are readily produced in air when a high voltage is applied to a suitable geometry. Many discharge modes are self-pulsed.
- A Dielectric Barrier Discharge (DBD) uses one or more dielectric layers between powered electrodes to limit current flow and prevent spark formation. The result is a capacitive discharge across a limited gap between the dielectric barrier and the electrode surface. These discharges generally offer a greater degree of control than corona discharges; the frequency and peak-to-peak voltage are set by the power supply.
- Noble Gas Plasma Jets ignite a discharge in a flow of rare gas (typically argon or helium), greatly reducing the necessary breakdown voltage and producing a more steady plasma. As the discharge is

generated in an open space and can extend for several centimeters beyond the device, plasma jets can be used to treat rather large objects; hence their appeal within the plasma medicine community.

These three classes of plasma devices are shown schematically in Figure 2.2. The first device shown is a form of corona discharge, the type of device used for the bulk of this work.<sup>2</sup> The main body of research on the interactions between plasma and cells has been done with the latter two types of discharges: dielectric barrier discharges (DBDs) and plasma jet-like devices (in the latter, helium or argon are generally used as the working gas). The latter two devices have been previously studied by members of Graves Lab.

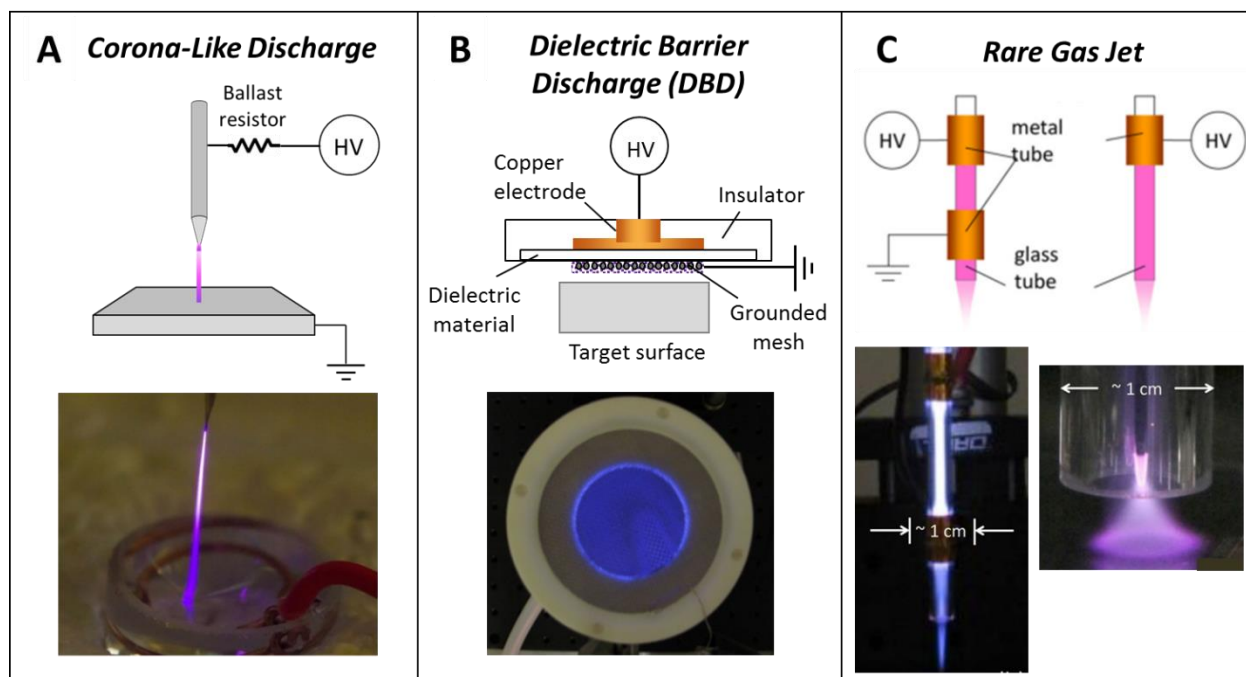


*Figure 2.2. Representative classes of plasma devices used in the non-equilibrium plasma community. A schematic and photograph of each class is included; photographs show devices used in Graves Lab. A Schematic for self-pulsed DC discharge (general); photo shows a positive-polarity transient spark (one mode of self-pulsed DC discharge). B A surface micro-discharge (SMD), an indirect DBD device. C Rare gas jets use flows of noble gases (He, Ar) to achieve steadier plasmas at lower breakdown potentials. Two configurations are shown; left photo: Discharge in argon, right photo: discharge with N<sub>2</sub> present.*

As direct plasma-liquid interactions were the subject of interest, a device capable of producing a discharge directly in contact with the treated solution (e.g., the solution acts as an electrode) was required. The main classes of atmospheric-pressure plasma sources that provide direct contact with a target include direct current (DC) devices with strongly asymmetrical electric fields (e.g. corona discharges, or interrupted spark), which can be produced with just a DC power supply and a means to limit current; and floating-electrode dielectric barrier discharges (FE-DBDs), which operate on the same principles as standard DBDs but with the target acting as the ground.

<sup>2</sup> The term “corona discharge” is often used to describe any plasma discharge that originates from a highly curved electrode; however in this report it will be used to refer to this specific device.

In this work, we chose to focus predominantly on corona-like discharges. These devices enable intense, direct contact between the plasma zone and a liquid – the situation we would like to investigate. This class of devices is highly tunable, allowing multiple discharge modes to be accessed. Even within a given discharge mode, the gas (and resulting liquid) chemistry can be varied considerably depending on the applied voltage and other parameters, creating a large phase space in which to work. Significant characterization of the electrical and gas-phase aspects of positive-polarity discharge modes had already been completed by collaborators at Comenius University, and additional work was in progress. [85]–[89] Lastly, the positive polarity discharges produce an “ion wind”, or net flow of gas against the target; this interesting phenomenon promotes convective mixing of the liquid phase, removing some transport limitations and simplifying liquid analyses.

## **2.2 Positive-Polarity Corona Discharge (Transient Spark)**

The term “corona discharge” is generally used to describe a low-current discharge caused by partial (or local) breakdown of a gas with a strongly inhomogeneous electric field applied. [73] These discharges can be formed simply by applying a sufficiently high voltage to an electrode with a high radius of curvature, such that local breakdown of the surrounding gas occurs near the electrode surface. This effect can cause frustrating electrical problems (power loss and insulator deterioration in high voltage transmission equipment, static noise), but also enables many useful technologies (electrostatic precipitation for particulate removal, ozone generation). [90]

Initial inroads into the nature of corona discharges were made by Loeb and Meek in the late 1930s and 1940s [91]–[93]. Several seminal texts on the physics and properties of corona-like discharges have been written ([90], [94]), and a discussion of these discharges is included in most plasma physics texts. Today, several groups within the atmospheric-pressure plasma community continue to study these discharges. Machala et al. have done significant work on the physics of point-to-plane DC discharges, determining the electron density [95], gas temperatures [96], circuit behavior [88], and on some potential applications [86], [97], [98]. Ono et. al. have studied the plasma chemistry in similar systems using both spectroscopic and modelling methods, determining the factors that promote the formation of various species in the plasma phase [99]–[103]. Other groups focus on negative-polarity corona-like discharges; these are discussed in Section 2.3.

For our purposes, a highly sharpened rod acts as the powered electrode (pin-to-plane geometry); however, other geometries such as multi-pin-to-plane, wire-to-plane, wire-to-pipe, coaxial wire-to-cylinder, etc. are possible. When operated in positive polarity, a positive voltage is applied to our pin electrode (anode); the grounded electrode is submerged in an aqueous solution, such that the solution surface acts as the cathode. A ballast resistance is added between the power source and the pin electrode to extinguish the discharge before the transition to spark is completed. The intermittency of the current limits heating of the gas, allowing the discharge to operate at a non-equilibrium thermal state.

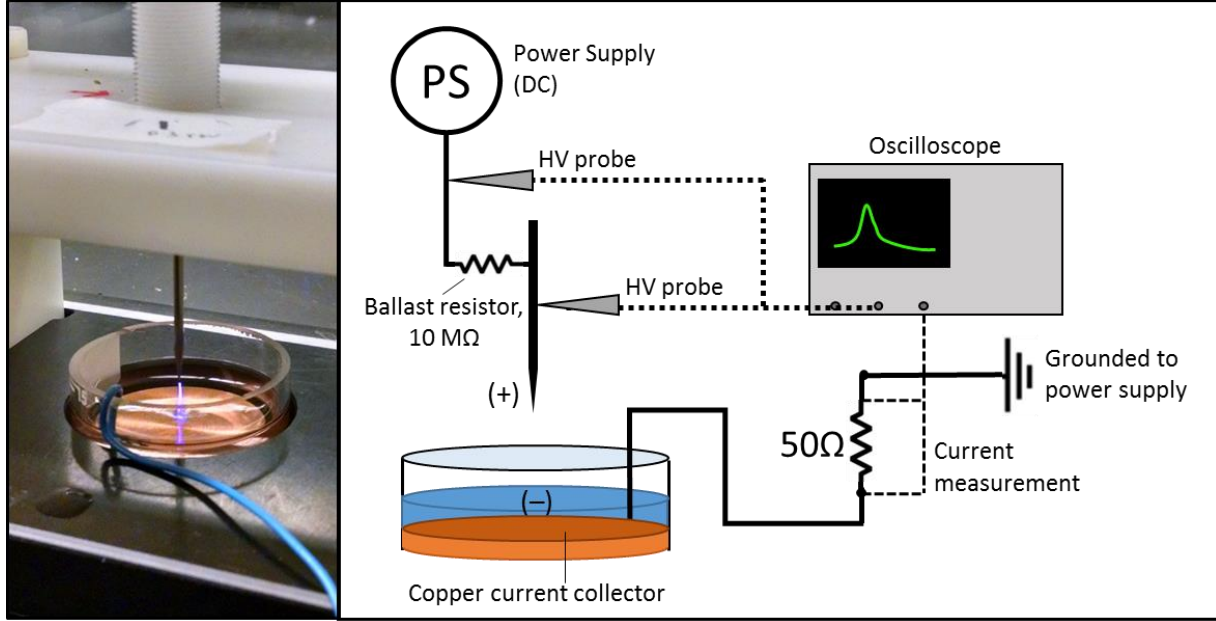


Figure 2.3. Schematic of device to generate self-pulsed DC discharges, operated in positive polarity with a  $10\text{M}\Omega$  ballast resistor to produce a stable, transient-spark discharge. The discharge as operated in air with  $d = 5\text{mm}$  is shown at left.

### 2.2.1 Mechanism of Operation

The breakdown mechanism for corona discharges differs from the description given in Section 2.1 depending on the polarity and homogeneity of the electric fields present. In negative-polarity discharges and in relatively homogenous electric fields, the breakdown mechanism proposed by Townsend—successive electron avalanches supported by secondary cathode emission—can reasonably explain the observed breakdown curves (see Figure 1). Under such conditions, where the space charge of a single electron avalanche does not significantly distort the electrical field applied to the gap, the electron density in the avalanche head remains below a critical value,  $e^{ad} \leq N_{cr}$ .

In positive-polarity corona-like discharges, the cathode is far from the initial ionization zone, limiting the role that secondary emission from the cathode can play in sustaining the discharge. Breakdown of the gas instead occurs through a mechanism known as “streamer breakdown”. This process occurs when the space-charge field created by positive ions behind the avalanche head becomes large enough to sustain its own ionization front, i.e. when is roughly equal to the applied electrical field. [104] Meek and Raether developed similar criteria to describe the requirement for the breakdown of gas in a non-uniform gap (with maximum field at the positive electrode); the generalized Meek’s formulation is shown in the equation below [94], [104]:

$$\int_0^x \left[ \alpha \left( \frac{E}{N} \right) - \beta \left( \frac{E}{N} \right) \right] dx = k \quad (2.4)$$

Here,  $\alpha$  is the first Townsend (ionization) coefficient at the avalanche head,  $\beta$  is the electron attachment coefficient,  $E/N$  is the reduced electric field, and  $x$  denotes the critical avalanche length, i.e., the length of the avalanche when it becomes unstable and streamers are formed. The constant  $k$  has a value of roughly 18-20 for air at atmospheric pressure. [105] Note that the critical distance,  $x$ , describes not only ionization, but the electron excitation zone; thus, it also corresponds to the zone of plasma luminosity (the visible size of the discharge). Significant treatment of the streamer mechanism can be found in [73], [90], [94]. For some geometries, it is possible to calculate the critical value of the electric field needed to ignite a corona using the Peek formula. [106]

These discharges are usually space-charge limited, since ions of mainly one polarity are produced and accumulate in the inter-electrode gap (electrons travel much more quickly). This results in a volt-ampere characteristic (VAC) that has a *positive* slope; an increase in the discharge current requires application of a higher voltage. [107] The streamer propagates primarily by photoionization across the inter-electrode space, with the positive ion head preceding a nearly neutral column. This process gives the positive streamer corona an active volume much greater than the other forms of DC discharges, which are confined by their generation mechanisms to the near-electrode regions. [107] The advance of a streamer across the interelectrode gap (preceded by the positive ion head) is shown schematically in Figure 2.4.

This dependence of positive corona-like discharges on photoionization for their propagation also means that the streamer head advances at a rate that is significantly faster than the motion of positive ions; according to one report, the positive streamer may advance at a speed of as much as one percent of the speed of light. [107]

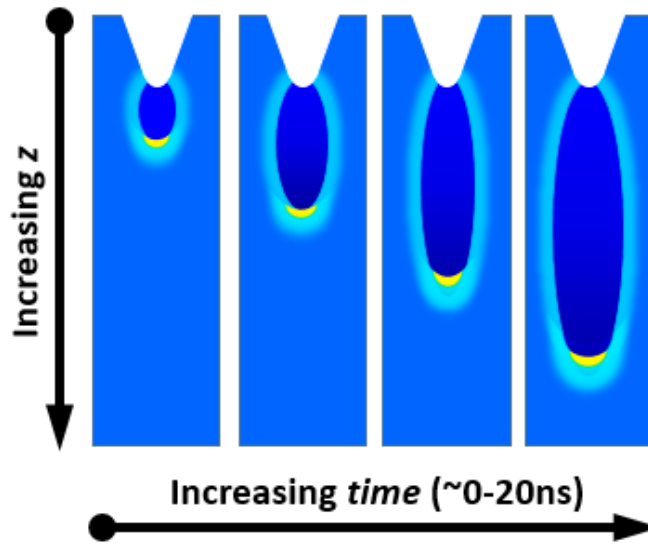


*Figure 2.4. Electric field created by a propagating positive streamer in a needle-plane geometry at advancing points in time. The light region at the front of the channel represents the streamer head, where steep gradients in space-charge exist (order 100-200 kV/cm) and advance as the ionization wave propagates. Visualization based on the model reported in [108].*



### 2.2.2 Discharge Modes and Key Characteristics

One notable feature of this DC discharge device is the ability to access multiple discharge modes by varying the electrical parameters (applied voltage, ballast resistance). For the system shown in Figure 2.3 (5 mm inter-electrode distance, 10 M $\Omega$  ballast resistor, standard reservoir with copper current collector) deflection of the water surface below the needle begins around 4.5 kV, although no visible discharge is observed. A weak but visible streamer discharge is first observed at an applied voltage of around 6 kV; the brightness of the discharge (and the discharge frequency) increase as the applied voltage is increased. At an applied voltage of roughly 8.5 kV, the discharge transitions from a streamer to an interrupted spark, or “transient spark discharge” (TS) [89]. In this mode, which has been well-characterized by Machala et. al. [87], [88], [109], [110], the capacitance of the circuit is completely discharged ( $V_{\text{electrode}}$  decreases to  $\sim 0$ ) with each pulse. At still higher voltages, the discharge transitions to a more classical spark with a dramatic rise in the discharge current; the discharge appears filamentary, and may wander across the solution/electrode surface. It should be noted that the discharge mode is also dependent on the strength of the ballast resistor used. If the ballast resistance is reduced to less than 5 M $\Omega$ , the voltage drop across the resistor during discharge is no longer sufficient to bring the electrode voltage below  $V_{\text{br}}$  and a constant-current glow discharge occurs at similar voltages.

These discharge modes (dark discharge, streamer, transient spark, spark, glow discharge) are quite distinct and are generally visually identifiable. Photographs of each discharge are shown in Figure 2.5 below.

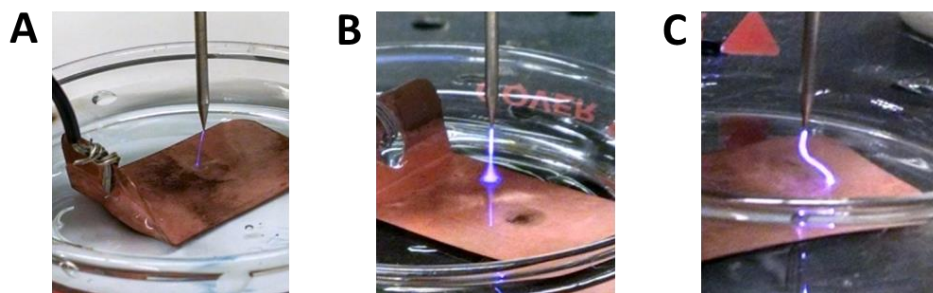


*Figure 2.5. Examples of various positive-polarity corona discharge modes: **A** the streamer discharge, a relatively weak (low current) discharge; **B** transient spark discharge, characterized by greater luminosity and the formation of a conductive channel that briefly bridges the entire inter-electrode gap; **C** a glow discharge, in which the luminous channel continuously bridges the inter-electrode gap (in the path taken by the initializing streamer pulse) and passes a small amount of current.*

A distinctive feature of positive corona discharges is the presence of a net flow of gas molecules to the surface, a so-called “ionic wind” [111]–[113]. This downward flow impinging on the treated surface is caused by the acceleration of positive ions towards the cathode / repulsion of these ions from the anode, which impart momentum to neutral molecules as well. When the discharge is in contact with a liquid, the impingement of the ionic wind on the surface induces convection currents in the liquid phase, as shown in a previous model [66]. The solution exposed to the discharge is thus effectively self-mixed up to depths of at least  $\sim 15$ mm based on visual observations. A demonstration of the self-mixing depth (and the effect of adding a “baffle”) in one of the solution geometries explored is shown in Figure 2.6.



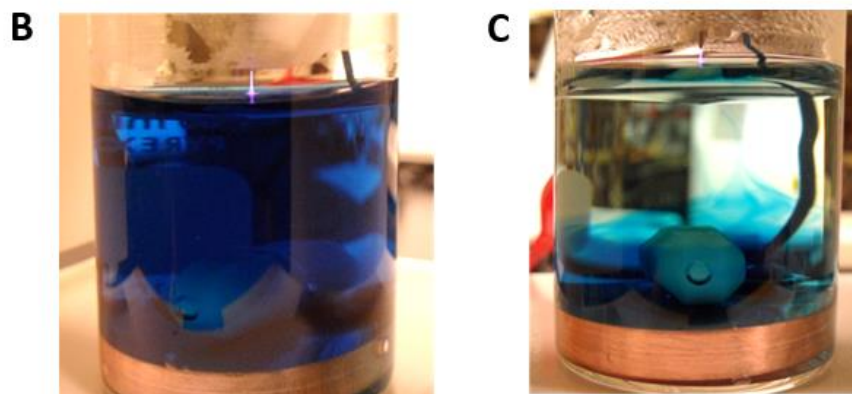
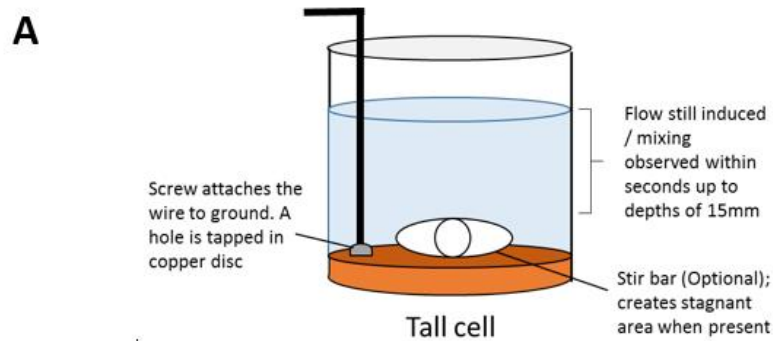


*Figure 2.6. Comparison of the effects of forced convection to the convection naturally induced by the ionic wind striking the surface and electrochemical gradients within the solution. A Schematic of the cell adapted for these experiments; B cell with 200 $\mu$ M indigo carmine at the start of transient spark treatment (plasma is visible in center of the liquid surface); C cell and contents after 10min of transient spark exposure. The dye remains in the stagnant areas (stir bar was stationary in this experiment), but is drawn up through a uniformly-oxidized layer (about 15mm deep) towards the plasma-liquid contact point.*

The transient spark discharge was generally used over other positive-polarity corona discharge modes in these studies based on:

- *Greater stability* above aqueous solutions (reduced variation between runs, smaller variation in rates of H<sub>2</sub>O<sub>2</sub> generation).
- *Greater H<sub>2</sub>O<sub>2</sub> production.* It is expected that the increased applied voltage results in higher electron impact-induced chemistry. This is expected to produce more reactive species and greater oxidative power.

Although the peak currents reached during a TS discharge pulse are relatively high (~50-400 mA, depending on inter-electrode distance and applied voltage), the pulses are sufficiently short (10-100 ns) to avoid thermalization of the plasma. Studies of this discharge mode report that a maximum electron

density,  $n_e$  of  $10^{16} - 10^{17} \text{ cm}^{-3}$  is reached at the onset of the spark<sup>3</sup>;  $n_e$  drops by an order of magnitude within 100 ns. [95]

### 2.2.3 Equipment and Materials

A Glassman MK 20P3.7 HV DC power supply was used to power the device. The power supply was operated in voltage control mode (such that power supply sought to maintain the voltage applied to the system at a set value); this value be set either locally or through a custom Matlab program. A metal-oxide ballast resistor with  $R = 1, 5, 10$  or  $20 \text{ M}\Omega$  (Vishay Dale ROX-3, rated to 10W) was placed in the circuit before the powered electrode. A stainless steel or tungsten welding rod with a diameter of  $1/16''$  (1.6 mm) was used as the powered electrode.<sup>4</sup> The powered electrode was mounted in a custom Delran screw and tapped stand. The threads on the screw (and mating to stand) were precisely machined with a pitch of 0.7938 mm per revolution. This allowed the inter-electrode distance (the distance from pin to target surface) to be adjusted with good accuracy (the stand is shown in Figure 2.7).

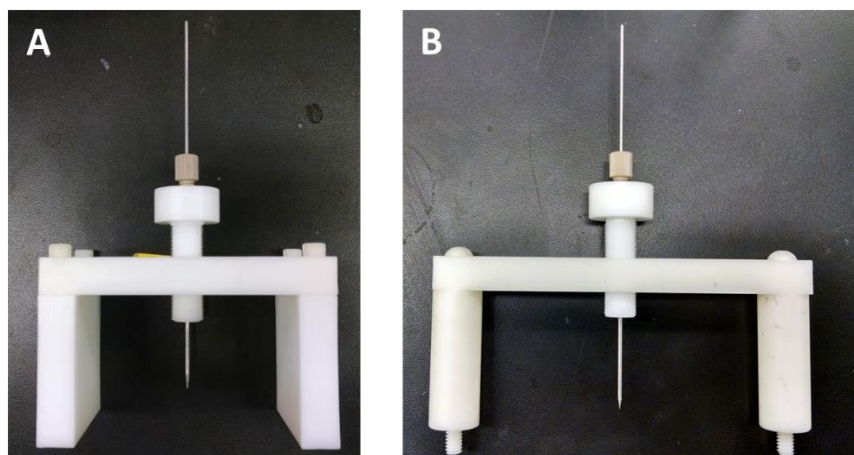


Figure 2.7. The inter-electrode distance could be adjusted by bringing the anode to the target (turning white dextran screw clockwise), then backing it out the desired distance based on the known thread pitch (one revolution = 0.79375 mm). Spacer **A** sits flat and fits into a standard solution holder for easy target centering; **B** can be mounted to a laser table, accommodates larger reservoirs, and blocks less light for imaging experiments.

One (1) or two (2) high voltage probes (Tektronix P6015A) were used to monitor the voltage at the outlet of the power supply (applied voltage,  $V_{app}$ ) and at the powered electrode ( $V_p$ ), as indicated in Figure 2.3. It

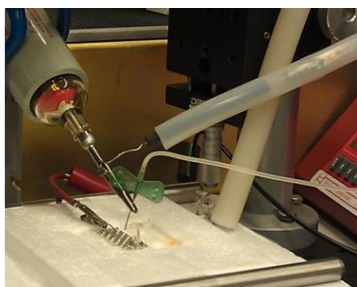
---

<sup>3</sup> The given estimates of electron density were estimated through kinetic modeling and Stark broadening. Increased pulse frequency correlated with *decreased* electron density:  $n_e = 10^{17} \text{ cm}^{-3}$  at  $\nu \approx 2 \text{ kHz}$ , and  $n_e = 10^{16} \text{ cm}^{-3}$  at  $\nu \approx 6 \text{ kHz}$ ; frequency was varied by adjusting the applied voltage. The inter-electrode distance was 5mm.

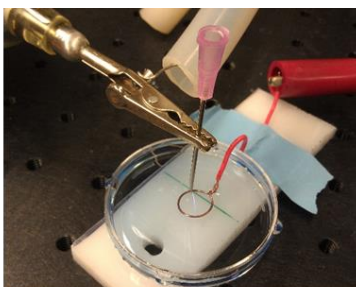
<sup>4</sup> See Section 2.2.6 for additional discussion of electrode considerations.

should be noted that these probes contribute to the overall impedance and capacitance of the system; these effects have been studied in detail by our collaborators [88], [104]. The high-voltage probes were connected to a digital oscilloscope (Tektronix TDS2024) with a sampling rate of up to  $2\text{GS s}^{-1}$ . The current to ground ( $I$ ) was calculated from the voltage drop across a  $50\ \Omega$  resistor, also measured with the oscilloscope. The frequency of the discharge was determined by the oscilloscope, triggered on a rise in current.

Several solution reservoir geometries and grounding paths were tested in the course of these studies. Figure 2.8 shows the evolution of cathode reservoir designs. The attributes of a subset of these configurations, with which significant data were collected, are summarized in Table 2.1.



**Electrospray system:** hypodermic needle as powered electrode, stainless steel (SS) mesh as current collector above 1 mL borosilicate reservoir



**Ring electrode:** empty hypodermic needle as powered electrode, copper wire “ring” as current collector, submerged in a plastic petri dish

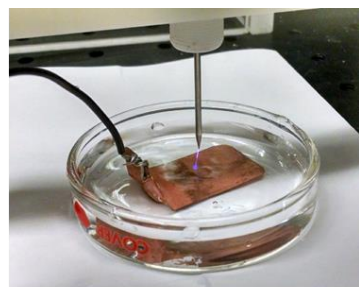
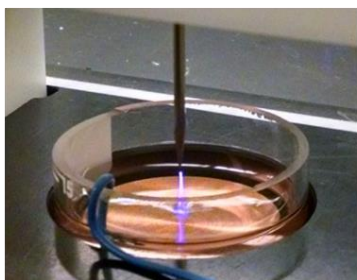
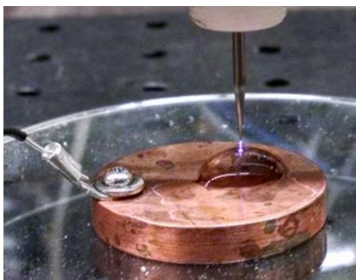


**Plate electrode:** thin copper “plate” electrode with hole punched to allow wire connection to ground, 10 mL pyrex petri dish



**Standard cell:** SS anode, 30 mL pyrex beaker (ID = 32 mm) cut to 22 mm tall with thick copper disc ( $d = 30\ \text{mm}$ ,  $h = 5\ \text{mm}$ )



**Bare electrode:** SS anode, 200 µL of solution pipetted onto thick copper disc ( $d = 3\ \text{cm}$ ,  $h = 5\ \text{mm}$ )



**Thimble cell:** SS anode, custom borosilicate vessel ( $OD = 15\ \text{mm}$ ,  $ID = 13\ \text{mm}$ ,  $h = 12\ \text{mm}$ ) with Pt lead

*Figure 2.8. Summary of anode and cathode combinations used in experiments. The standard cell (bottom left) was used in transient spark discharge experiments, unless otherwise noted. The bare electrode and thimble cell configurations were used to increase the relative concentration of modified to unmodified species in the experiments discussed in Section 5.5.*

Table 2.1. Attributes of solution reservoirs: dimensions and materials

Reservoir / Current collector	Volume of solution	Inter-electrode distance	Connection to ground (Material, Surface Area)
Standard cell	4-8 mL	1-5 mm	Cu, 7 cm <sup>2</sup>
Bare electrode	200-300 μL	0-1 mm	Cu, ~1.8 cm <sup>2</sup>
Thimble cell	500-800 μL	1-1.5 mm	Pt, 0.16 cm <sup>2</sup>

#### 2.2.4 Voltage and Current Characteristics

As previously mentioned, the voltage was measured at the outlet of the power supply (applied voltage,  $V_{app}$ ) and at the powered electrode ( $V_p$ ), with high voltage, high impedance probes. It should be noted that the use of such probes can contribute to the overall impedance and capacitance of the system, though such effects mainly become significant at high applied voltages when weaker ballast resistors ( $\leq 5 \text{ M}\Omega$ ) were used.<sup>5</sup> These effects have been studied in detail by other groups [88], [104]. In this work, discharges were characterized by applied voltage rather than applied field, for the reasons discussed in [114].

When the voltage at the pin ( $V_{anode}$ ) exceeds the breakdown value,  $V_{br}$ , a discharge event (pulse) occurs. A streamer bridges the inter-electrode gap, allowing *some* or *all* of the capacity of the circuit to drain to ground, depending on the discharge mode. When a discharge event occurs, the current across the inter-electrode space to ground increases according to equation 2.5,

$$I(t) \approx -C \frac{dV}{dt} \quad (2.5)$$

where  $V$  is the voltage at the powered electrode. The current grows to a peak value ( $I_{max}$ ) over a very short period, and the voltage measured on the anode drops to almost zero. An example of a typical voltage and current waveform for several discharge pulses in transient spark mode are shown in Figure 2.9. In this example, the breakdown voltage,  $V_{br} = 2.7 \text{ kV}$ , and the pulse frequency,  $\nu$ , was around 18 kHz.

---

<sup>5</sup> A secondary discharge of capacitance from the system, accompanied by an apparent drop in the voltage at the anode *below zero*, was observed when a relatively weak (5 MΩ) ballast resistor was used. This effect was not observed with 10 MΩ or 20 MΩ ballast resistors placed in the circuit.

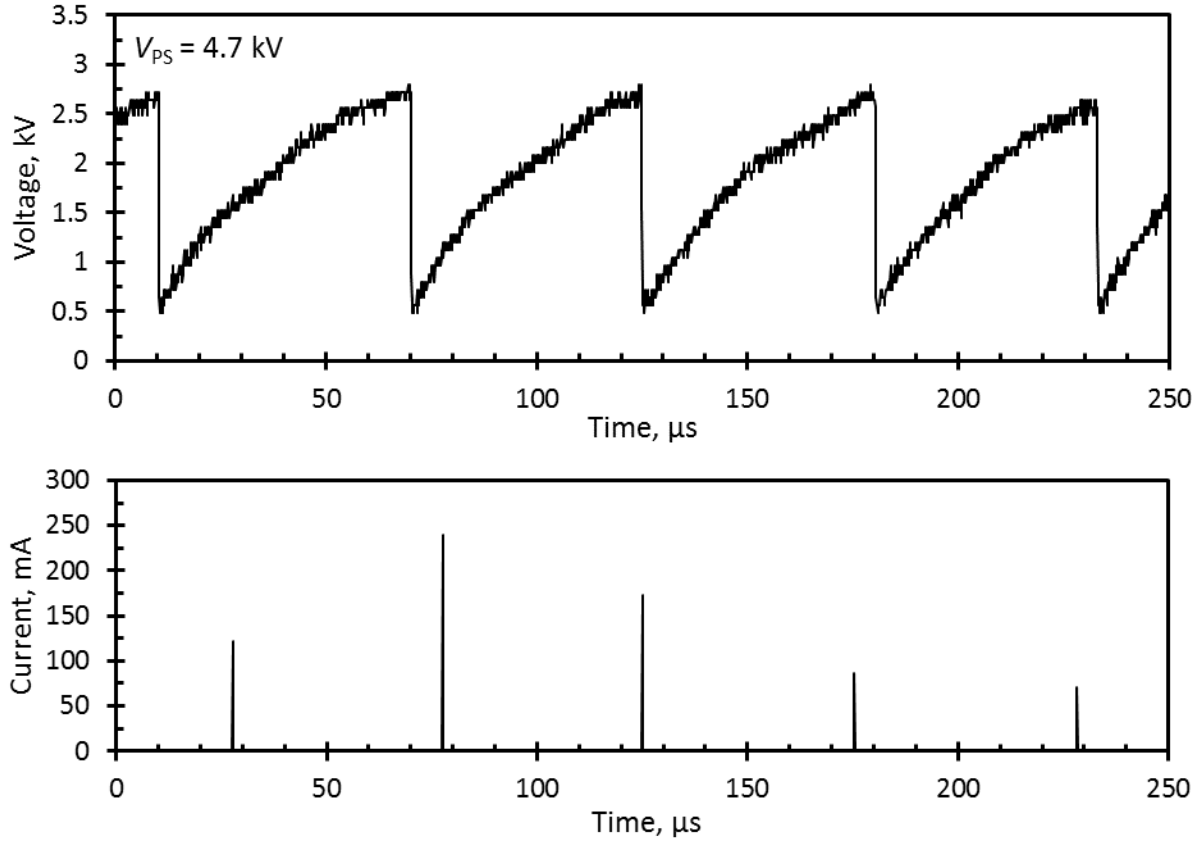


Figure 2.9. Typical voltage (above) and current (below) waveforms for a series of transient spark discharge pulses. Here the inter-electrode gap  $d = 2\text{mm}$ , the applied voltage  $V_{PS} = 4.7\text{kV}$ , the ballast resistance was  $10 \text{ M}\Omega$ , and the target solution was  $5 \text{ mL}$  of  $0.1 \text{ M}$  phosphate buffered solution in standard cell). For this treatment, discharge frequency  $\sim 18\text{kHz}$ ,  $V_{br} = 2.7\text{kV}$ , and the “peak current” ( $I_{max}$ ) =  $300\text{mA}$ . Note the wide variation in the maximum current reached between consecutive pulses.

The circuit capacitance,  $C$  can be estimated from the derivative of the voltage waveform and the measured current at the same point. It should be noted that this system (as shown in Figure 2.3) has several capacitive components: the plasma discharge and inter-electrode area,  $C_{int}$ , the HV probe(s)  $C_{probe}$ , and the high-voltage cable connecting the power supply to the ballast resistor,  $C_{cable}$ . The total system capacitance for such systems is on the order of  $10 \text{ pF}$ . [88] The capacity of each high voltage probe (Tektronix P6015A) is  $3 \text{ pF}$ ; the capacity of the HV cable is on the order of  $5\text{-}35\text{pF}$  (depending on length); and the internal capacitance of the discharge region is unknown. The optimization and tuning of elements of this circuit have been described by Janda et. al. [88]

Following the streamer event, the capacitance within the system is recharged and  $V_{anode}$  increases with time until the breakdown voltage,  $V_{br}$ , associated with the inter-electrode gap is again attained:

$$V_{anode}(t) = V_{PS} \left[ 1 - \exp\left(\frac{-t}{RC}\right) \right] \quad (2.6)$$

Here  $V_{PS}$  is the voltage applied by the power source,<sup>6</sup>  $R$  is the resistance from just past the ballast resistor to ground, and  $C$  is the total capacitance of the system. This process can be related to the frequency of current pulses observed,  $\nu$ , per equation 2.7.

$$\nu = \frac{1}{T} = \frac{1}{RC \ln \left[ \frac{V_{PS}}{V_{PS} - V_{TS}} \right]} \quad (2.7)$$

However, it should be noted that the expected frequency cannot be easily calculated from the circuit parameters ( $V_{PS}$ ,  $R$  and  $C$ ) through equation 2.7. The breakdown voltage  $V_{TS}$  decreases as the frequency is increased, an effect that can be explained by an increase in gas temperature at higher frequencies. As  $T_g$  increases, the gas density decreases, and a lower  $V_{TS}$  is required to achieve the same E/N. [104]

From these values, the RC time constant is estimated to be 65  $\mu$ s. The system capacitance ( $C_{int} + C_{probe} + C_{cable}$ ).

The discharge power was calculated by integrating  $I \cdot V_p$  over individual pulses and multiplying by the frequency of the discharge pulse, using an average over several seconds.

$$P = \sum_{\substack{\text{one pulse,} \\ \sim 1 \mu\text{s}}} i \cdot V_{anode} \cdot \Delta t \quad (2.8)$$

Where  $i$  is the current passing from the cathode to ground,  $V_{anode}$  is the voltage measured by a high-voltage probe at the pin electrode (anode), and  $\Delta t$  is equal to 1 / frequency of oscilloscope sampling (1 ns). This is a conservatively large value, as the maximum current measured by the oscilloscope was used as input but peak current reached during discharge varied significantly from pulse to pulse. The general shape of the current pulse for a streamer and transient spark discharge are shown in Figure 2.10. Despite the variation in the height of individual current pulses (as evidenced in Figure 2.9), the maximum or “peak” current reached over the oscilloscope sampling interval is relatively steady when this current is maintained below ~100mA.

---

<sup>6</sup> Note that under some conditions, the charging rate is limited by the maximum current that the power supply can output (~3.4 mA).

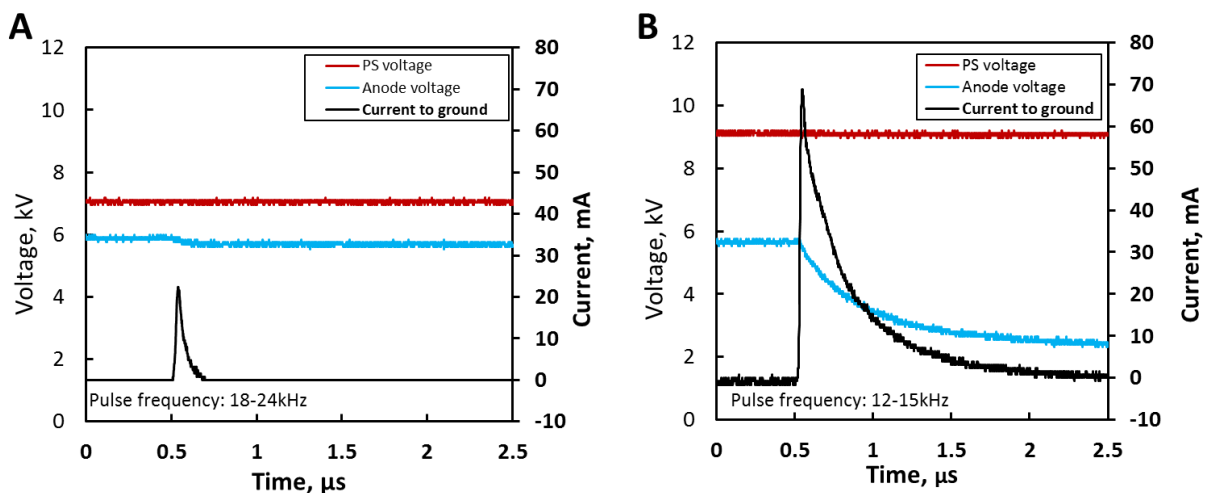


Figure 2.10. Typical waveforms from (A) streamer plasma discharge and (B) transient spark discharge. The ballast resistor in both cases is  $10\text{ M}\Omega$  and the inter-electrode distance is 5mm. The power supply voltage (PS) is in red (top trace), and fixed at 7 or 9 kV; this dictates the discharge mode under these conditions. The anode voltage, in blue, is lower due to the potential drop across the ballast resistor. The corresponding current is shown on the right axis, in black. In the case of the transient spark discharge (B), a conductive channel (nearly) bridges the inter-gap during the current pulse, resulting in a significant drop in the anode voltage. In contrast, the streamer type discharge causes only a small perturbation in the anode voltage below the initial value (the threshold voltage), and the corresponding magnitude and duration of the current pulse is significantly lower. The visible appearance of these discharges is shown in Figure 2.5.

The increase in power dissipated by the discharge as a function of applied voltage (for a fixed inter-electrode distance and ballast resistance) is shown in Figure 2.11. As expected, the power dissipated by the plasma increases with applied voltage, and the solution pH does not affect the dissipated power. Interestingly, the amount of power dissipated in the plasma appears to decrease with increasing solution conductivity for the same applied voltage. It is possible that less current is lost in transporting charges from the gas phase to liquid phase (less resistance is present) when the solution conductivity is increased. Greater “spreading” of the discharge across the liquid surface has been observed when the discharge is in contact with a weak electrolyte versus a stronger one in negative polarity systems [115]. It is also possible that the effective work function of the surface is reduced with greater concentrations of ions present in solution, or that decreased surface tension (due to the presence of additional salts) allows for easier electron removal. The discontinuity between the power dissipated in the streamer versus transient spark mode was also greatest for the low conductivity solution, suggesting that the mechanism for the transient spark discharge may be somehow affected.



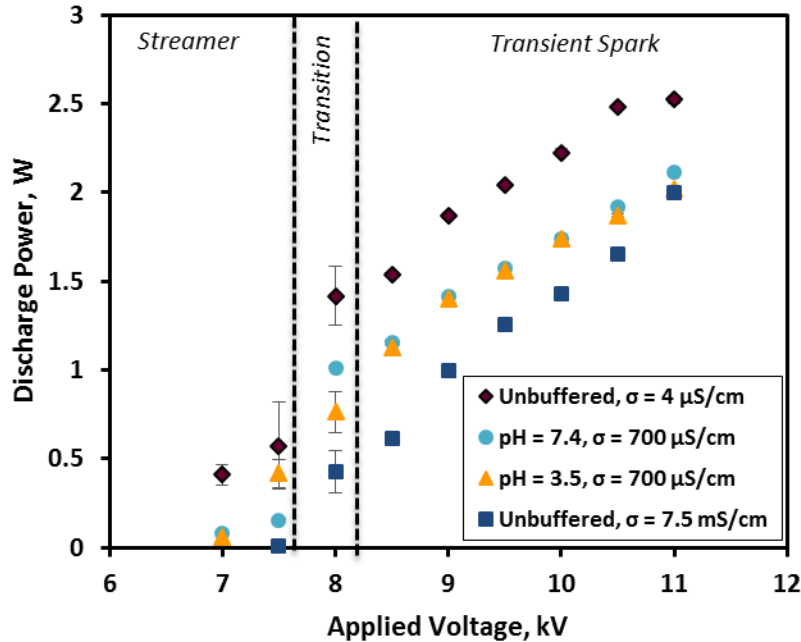


Figure 2.11. Power discharged by the positive-polarity self-pulsed DC discharge as a function of the voltage applied ( $d = 5\text{ mm}$ ). In the transition region, the discharge oscillates between low and high power modes, leading to large variations in power consumption. The solution pH did not affect the power dissipated at a given voltage; however, a negative correlation between solution conductivity and power consumption is observed.

The evolution of the current pulse shape observed with increasing applied voltage (at one ballast resistance) within the transient spark mode shown in Figure 2.12 (for discharges above phosphate and citrate-buffered solutions).



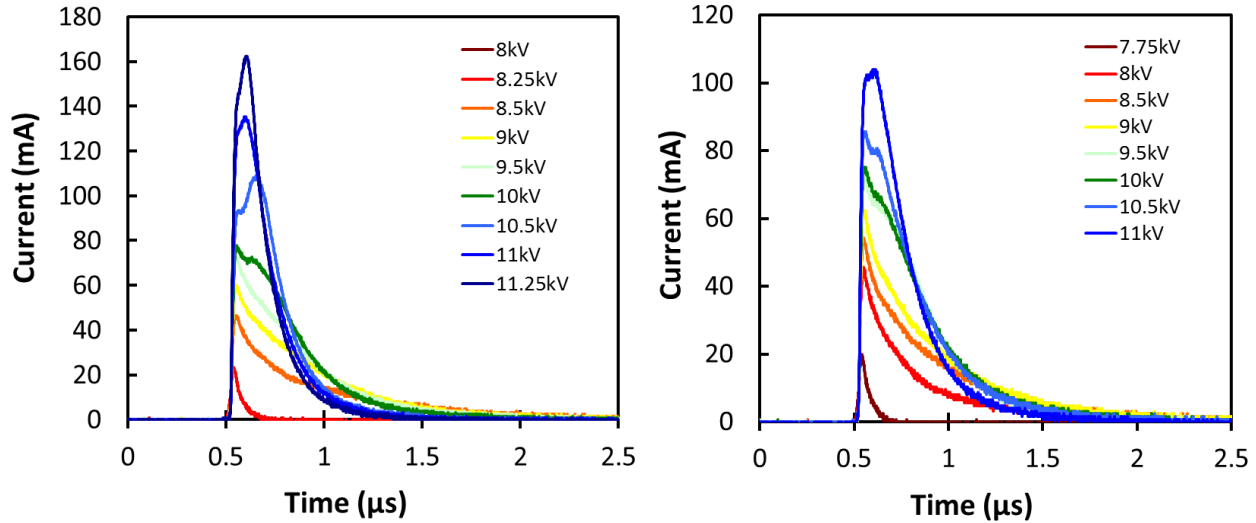


Figure 2.12. Evolution of current waveform with increasing applied voltage for the transient spark discharge mode. Examples are shown for two different target solutions, 10mM phosphate buffer (left) and 10mM citrate buffer (right). The solutions have conductivities of 1.8 mS/cm (phosphate buffer, pH 7.4) and 0.7 mS/cm (citrate buffer, pH 3.5) respectively. At applied voltages of 7.5-8.5kV (within the transition region indicated in Figure 2.11) the shape of the current waveform oscillates between streamer and transient spark forms. At left, the trace at 8.25kV shows the low peak current pulse duration characteristic of the streamer discharge, whereas the 8kV trace at right shows a peak current of ~50mA and long pulse duration characteristic of the transient spark (refer to Figure 2.10 for characteristic current waveforms). An interesting feature of the series of current shapes with increasing voltage is that the duration (or width) of the current pulse initially increases, but then shrinks at higher applied voltages and greater currents. This behavior is captured in a parameter based on the width of the current pulse at half of its maximum height, the “full-width half max” (FWHM) shown in Table 2.2 and Table 2.3. This behavior suggests faster transport of current and a change or increase in the dominant charge carriers in the region limiting current flow (which may be the partially ionized channel between anode and liquid, the plasma-liquid interface, the bulk solution, or the release of electrons into solution from the submerged electrode).

Table 2.2. Effect of increasing the applied voltage on measured electrical characteristics of the plasma discharge in transient spark mode, over a 10mM citrate-buffered solution ( $\sigma = 700 \mu\text{S}/\text{cm}$ ,  $\text{pH} = 3.5$ ). The ballast resistance was 10 M $\Omega$  and the inter-electrode distance was set to 5mm in all cases; applied voltages above 8kV, a transient spark discharge was produced. The frequency of the discharge events (discharge event = single current pulse, as shown in Figure 2.9 and Figure 2.12) was 13-16 kHz for these discharges, with the frequency increasing slightly at higher applied voltages. The peak (maximum) current reached, the energy transmitted per discharge event, and the power dissipated by the plasma increase with increasing voltage. At 7.75 and 8kV, the discharge oscillated between streamer and transient spark discharge modes; streamer pulses occurred with greater frequency and dissipated less power on a per-pulse and integrated basis. (TS = transient spark discharge)

Applied Voltage (kV)	Peak Current (mA)	Full-Width Half Max, FWHM ( $\mu\text{s}$ )	Energy Per Pulse ( $\mu\text{J}$ )	Frequency Range (kHz)	Power Dissipated (W)
11	120	226	127	15-17	2.0
10.5	96	275	134	13-15	1.9
10	79	295	112	14-15	1.6
9.5	73	358	123	11-12.5	1.4
9	59	332	105	12-13	1.3
8.5	53	265	86	12-14	1.1
8	32	103	25	14-15 (TS) 18-21 (Streamer)	0.37
7.75	21	71	4.0	15-16 (TS) 21-23 (Streamer)	0.06

Table 2.3. Effect of increasing the applied voltage on measured electrical characteristics of the plasma discharge in transient spark mode, over a 10mM phosphate-buffered solution ( $\sigma = 1800 \mu\text{S/cm}$ ,  $\text{pH} = 7.4$ ). Similar trends are observed in electrical characteristics, including the onset of the transient spark discharge mode. (nm = no measurement available; TS = transient spark discharge)

Applied Voltage (kV)	Peak Current (mA)	Full-Width Half Max, FWHM ( $\mu\text{s}$ )	Energy Per Pulse ( $\mu\text{J}$ )	Frequency Range (kHz)	Power Dissipated (W)
11.25	143	0.19	136	nm	nm
11	125	0.22	140	15-15.5	2.1
10.5	105	0.24	129	14-15	1.9
9.5	73	0.34	114	13-14	1.5
9	55	0.37	98	13-14	1.3
8.5	45	0.32	84	nm	nm
8.25	48	0.25	80	13.5-14	1.1
8	20	0.06	2	14-16 (TS) 22-23 (Streamer)	0.03

### 2.2.5 Influence of Ballast Resistor

The ballast resistor is responsible for preventing the transition to spark. As the current flowing through the system increases (i.e. during a discharge pulse), the voltage drop across the ballast resistor increases. This decreases the voltage at the anode; when the anode voltage drops below the threshold breakdown voltage, the discharge can no longer be sustained. Thus, the greater the ballast resistance, the lower the current required to extinguish the discharge. This can be seen when comparing the max current achieved in experiments with a  $10\text{M}\Omega$  and  $20\text{M}\Omega$  ballast resistor (Figure 2.13); using a  $20\text{M}\Omega$  ballast resistor reduced the peak current by a factor of 2 or more, compared to the  $10\text{M}\Omega$  case.

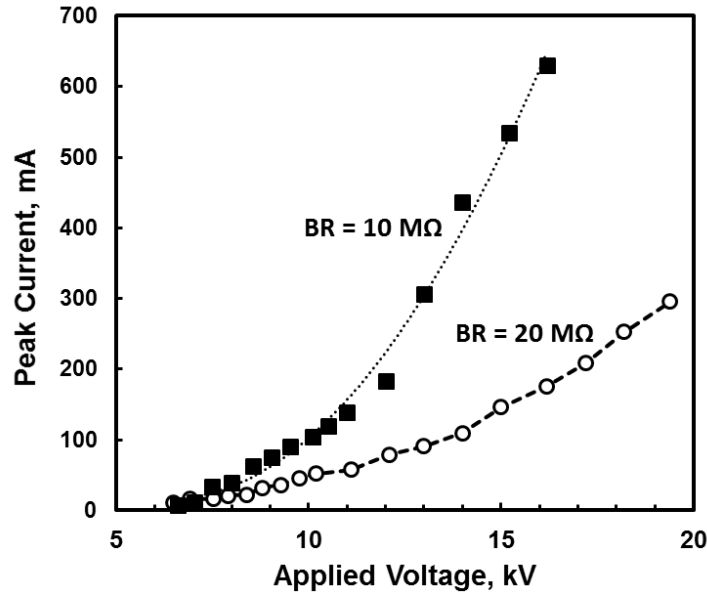


Figure 2.13. Maximum (peak) current achieved as a function of voltage applied to the device. Using a large ballast resistance ( $20\text{M}\Omega$ ), the current is limited to  $<0.3\text{ A}$  even with  $19\text{ kV}$  applied (the maximum output from the power supply).

The ballast resistor experiments further highlight the tunability of this class of discharges. Increasing the ballast resistance is an effective strategy to employ when building a device for applications in which the peak current must be limited; e.g. direct treatment of tissue. This strategy was exploited to good effect in the work of Pei, et. al. [116], in which an array of corona discharges was used in conjunction with large ( $50\text{M}\Omega$ ) ballast resistors to create a handheld “plasma flashlight”, which could contact skin without damage.

## 2.2.6 Electrode Considerations

### 2.2.6.1 Anode

The characteristics of the discharge are highly determined by the high degree of curvature of the powered electrode, the anode (in this polarity). One of the major challenges in obtaining a reproducible discharge was obtaining and maintaining an electrode in the same state. A sharpened stainless steel welding rod of  $d = 1/16''$  (1.6mm) with a radius of curvature of  $\sim 100\mu\text{m}$  was found to yield the more reproducible results (in terms of consistent discharge VAC, less visible oxidation/nitride formation on rod) than lanthanated tungsten (1.5% La). Other groups using point-to-plane discharges above an electrolyte have reported the use of stainless steel [115] or titanium [117] rods as anodes.

Optical microscopy images of the electrodes (as received from the machine shop) are shown in Figure 2.14A to highlight the initial variation in the critical radius of curvature (a photograph of the rod-electrode is shown in Figure 2.14B for scale). It was critically important to prepare the anode before each set of experiments to ensure consistent voltage-current characteristics from experiment to experiment. Electrode preparation consisted of gently sanding the pointed surface (moving from thick to thin end of sharpened point) to remove spurs or pre-existing oxides (see Figure 2.14D). The discharge was then run over a solution

for 10 minutes to condition the electrode and to establish a consistent oxidation state. The radius of curvature of the stainless steel electrodes generally converged to  $\sim 100\mu\text{m}$  with use (see Figure 2.14C); electrodes were imaged with simple light microscopy to ensure that the radius of curvature remained consistent. The same electrode was used for all experiments within a given study to prevent slight differences in anode curvature from influencing the results.

The use of anodes with smaller radii of curvature decreases the breakdown voltage required. However, electrodes that were sharpened to a finer point tended to oxidize in a non-uniform manner (see Figure 2.14E). Use of anodes with a radius of curvature of  $\sim 100\mu\text{m}$  resulted in a good compromise between the voltage needed for discharge and the complexities associated with constantly preparing/monitoring anodes, and produced relatively consistent discharges.

An example of how changes in the anode shape and extent of oxidation upon initial use affect the current waveform are shown in Figure 2.15. In the experiments shown in Figure 2.15, solutions of differing conductivity were used as the cathode. Nitric acid was used to change the conductivity, as it is one of the main species formed from air plasmas in contact with water. The order in which the solutions were tested was varied to determine if changes in current pulse shape were primarily due to a) evolution of the anode or b) ionic strength.

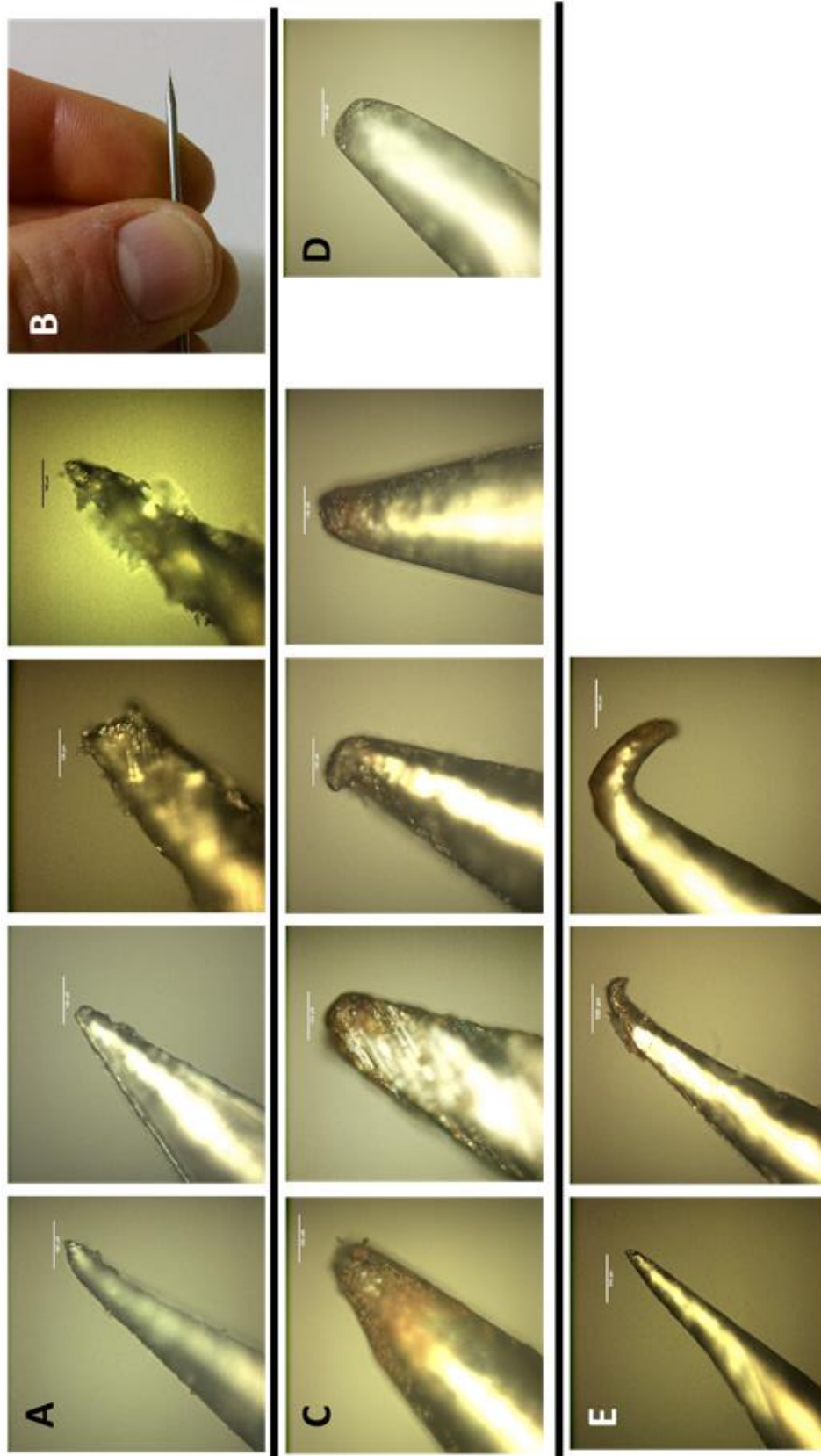


Figure 2.14. Variations in the radius of curvature of the anode tip can have a major effect on the uniformity of the discharge and the threshold voltage at which breakdown occurs. **A** Optical microscope (20X) images of sharpened stainless steel anodes before use. The scale bar represents 100 $\mu$ m. These images show that the initial curvature of the point varies significantly. **B** The size of the anode tip relative to the human hand for context. **C** Examples of used anodes showing that the radius of curvature converges to  $\sim$ 100 $\mu$ m with use. **D** Fine grit sandpaper removes the oxides from the previous runs, leaving shape intact. **E** Sequential images taken of a “too sharp” anode before use, after one day of experiments, and after multiple days. While increasing the radius of curvature reduces the voltage necessary for breakdown, this leads to a less robust device. The “bending” shown above can significantly alter the electrical and convective forces within the system.

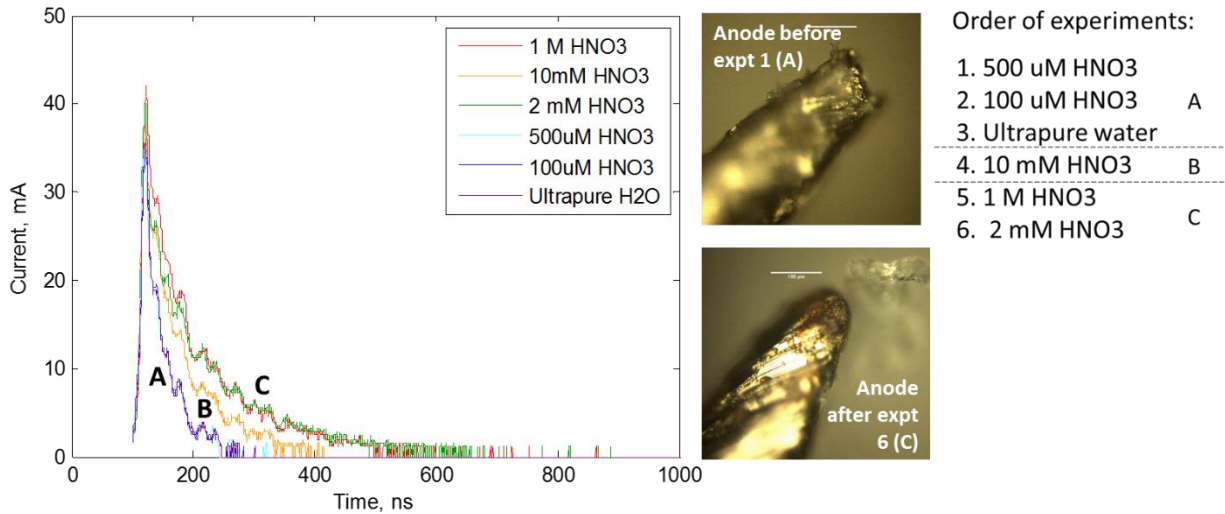


Figure 2.15. Effect of changes in anode shape on current waveform. Experiments with waveform A were performed first, followed by B and C. The duration of the current pulse increased as the anode was smoothed and oxidized (as shown in the before and after photographs). The waveform did not appear responsive to changes in the ionic strength of the solution; no correlation between ionic strength and waveform was observed in these experiments.

### 2.2.6.2 Cathode

For positive polarity discharges to metal cathodes, the cathode material does not significantly affect the electrical properties of the discharge. For instance, it has been shown that argon discharges to metal cathodes (Ni, Cu, Au, brass, stainless steel) display similar threshold breakdown voltage. [76] When the cathode is an electrolyte, the discharge behavior was also similarly unaffected (compared to a bare copper cathode at the same inter-electrode distance), provided that:

- A sufficiently strong electrolyte solution was used (e.g. 0.1 M buffer) such that the discharge did not spread across the solution surface.
- The ionic wind did not significantly disturb the surface, varying the inter-electrode distance. The velocity of the ion wind increases with inter-electrode distance; thus, this effect is less relevant at small separation lengths.

To push the limit of small-volume plasma treatment, experiments were performed with a drop of solution placed directly on the metal surface, as shown in Figure 2.16. However, the following considerations had to be taken into account:

- Evaporation of the solution necessitated brief ( $\leq 3$  min) treatment times. Evaporation rates of water in contact with a discharge were roughly 7 mg/min (total mass loss for a 3min treatment was 16-30 mg, or 8-15%). (The variation in evaporation rate was related to the power deposited.)

- The surface tension of the solution ceased to effectively maintain the droplet shape with the addition of mM levels of target molecules (e.g. cysteine and glutathione). The droplets spread along the surface as shown in Figure 2.16, preventing meaningful comparison to controls.

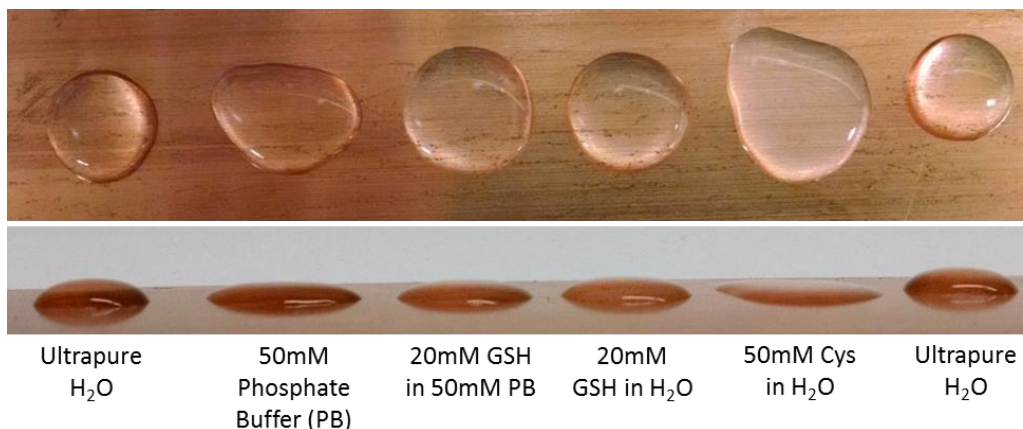


*Figure 2.16. Variation in droplet shapes due to decreasing surface tension. Droplets at each edge are ultrapure water; these could be applied to a surface and treated with plasma reproducibly. Direct plasma treatment of small volumes of analytes is not recommended due to spreading of the droplet prior to treatment, which can lead to drying (as well as greater transport limitations to droplet edges.)*

The convection patterns within the liquid are strongly affected by not only the overall shape of the vessel holding the solution, but the location of the current collector within the solution. Significantly greater mixing was (visually) observed directly in the path between the point-of-contact between the plasma and solution, and the current collector. This was not intuitive; initially, it was assumed that the driving force from convection came entirely from shear of the ion wind (neutral species and ions) impinging on the liquid. The observation of this phenomenon underscores the complexity of this system, and the challenges associated with modeling it. Transport phenomenon, including convection, are discussed in Section 3.2.2.

### 2.2.7 Inter-electrode Gap

The spacing between the electrodes affects the breakdown voltage, the amount of current passed (and energy delivered) per discharge pulse, and the intensity of the ion wind. From the Paschen relation, we know that larger inter-electrode gaps require a higher threshold voltage to achieve a self-sustaining discharge. This means that a greater voltage must be applied to the system to access the same discharge mode, and  $V_{br}$  (the voltage measured at the anode upon discharge) increases.

At greater inter-electrode distances, the ion wind imparts greater force on the solution surface. (Higher breakdown voltages are required to achieve discharge and produce greater repulsive pulses at the anode, which in turn impart greater kinetic energy to the ions and neutral species). This leads to a slight increase



in the variation in  $V_{br}$  and other parameters due to the deflection of the solution surface, which changes the inter-electrode distance.

As the inter-electrode gap distance decreases (and  $V_{br}$  decreases), the average peak current reached during each discharge pulse tended to *increase* (for a constant voltage applied to the system). This may result from a combination of factors:

- Additional collision events occur when the ions must travel farther to the cathode, resulting in lower but prolonged current pulses.
- The DC power supply attempts to deliver more power as the system voltage moves farther from the set-point; at lower  $V_{br}$ , the circuit sits at a lower voltage on average. The power supply may therefore spend more time trying to deliver the maximum current (3.4 mA for this device).

The effect of increasing inter-electrode distance on the energy passed per current pulse, and the change in the shape of the current waveform, are shown in Figure 2.17.

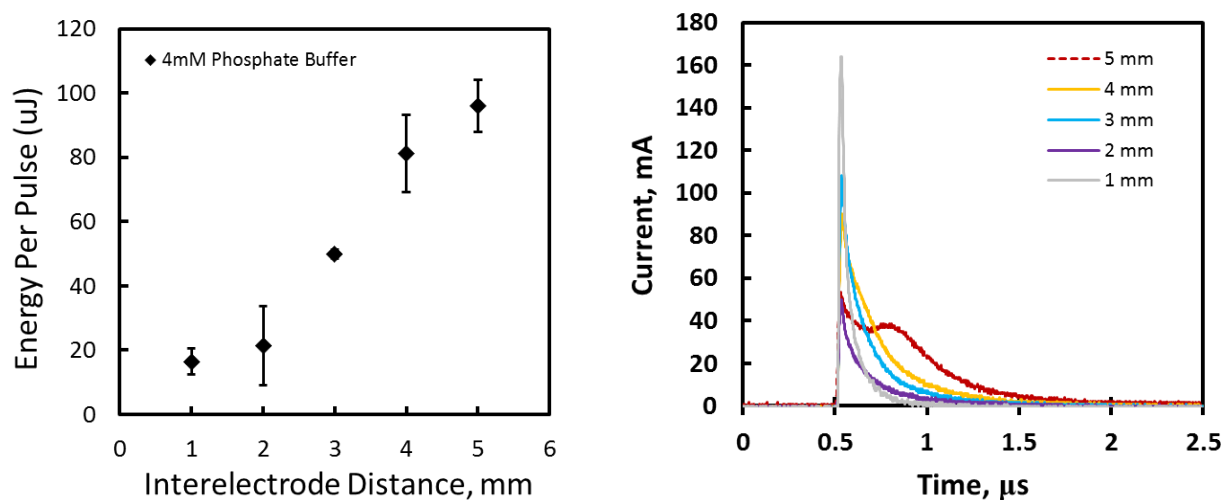


Figure 2.17. Effect of the inter-electrode distance on the energy transmitted per pulse and the shape of the current pulse. Applied voltage: 9kV, 10 MΩ ballast resistor, over 4mM phosphate-buffered solution. A similar trend was observed when operated at 7 or 8kV.

### 2.2.8 Other Design Considerations

A few more notes:

- Consider the air flow in the working space. A set-up that works fine on an open bench may not work if it is relocated to a fume hood (where minimum flow velocities are 100L/min!). Fans from an adjacent power supply have been observed to weaken the discharge when they turn on. Isolating the air space is one option; however, if the gas volume is constrained, the increase in humidity (and other gaseous plasma-generated species) will affect the discharge.

- This device produces significant electrical noise which can interfere with adjacent experiments of others.

### 2.3 Negative-Polarity Corona Discharge

When the corona discharge device is run in the opposite (negative) polarity, the powered electrode becomes the cathode, and the plate (or gas-solution interface) serves as the anode of the discharge. Like positive-polarity corona-like discharges, regular negative-polarity discharge pulses can be observed in air at atmospheric pressure. The presence of regular relaxation pulses was first reported by Trichel in 1938 [118].

The sparking potential is much higher than for the positive polarity mode; for this reason, electrostatic precipitators make use of negative polarity corona discharges. [73] Recently, negative polarity discharges above a water/electrolyte solution have received considerable attention from the academic community as a tool to produce and study solvated electrons. [64], [115], [119]

#### 2.3.1 Mechanisms of Operation

The negative corona generally propagates by electron impact ionization of the gas molecules. [107] In this case, Townsend's criterion (see equation 2.2) can be used to describe the conditions of onset. Once a plasma is established, the inter-electrode gap can be divided into two parts: a charged particle generation region in the vicinity of the cathode, and a drift region, which occupies most of the gap (see Figure 2.18). Ionization processes occur close to the cathode, where the electrical field gradients are high. The drift region is filled with a cloud of negative volume charge (in the case of air mainly consisting of negative ions) that drifts towards the anode. In accordance with the electrical field distribution, the light emission in this mode comes from the ionization region only. The inter-electrode gap is essentially dark.

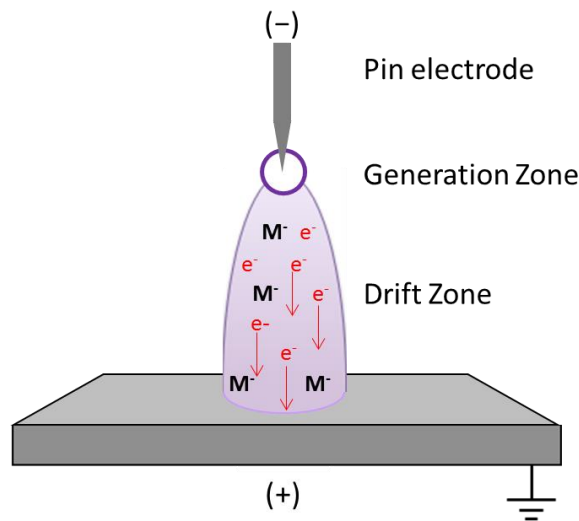


Figure 2.18. Schematic of a negative polarity corona-like discharge. Charged particle generation occurs primarily in the generation zone very close to the cathode, where secondary electrons are emitted upon

*the impact of cations. The rest of the gap is filled with a negative volume charge (assuming that air is the working gas).*

The effect of different electrode geometries on the voltage-current characteristics (VAC) for negative corona discharges, capturing various mode transitions, has been previously reported. [120]

### 2.3.2 Discharge Characteristics

In the pin-to-plate configuration, the initial form of the discharge is a non-steady “Trichel” pulse corona, which is characterized by brief, regular pulses, a visible glow around the tip of the pin (the ionization zone) and the dark inter-electrode gap. [73] (pg 43) In static air, the frequency of these pulses is reported to increase from 1-100kHz with increasing current (up to 120 – 140  $\mu$ A). As the applied voltage is further increased, the discharge transitions to a negative glow corona (for clean electrodes), or the noisy “tuft” form before transitioning to spark. [107] This discharge mode is compared to a positive polarity streamer (in air, above a liquid anode) in Figure 2.19.

Transient spark discharge  
(Positive polarity, higher applied voltage)



Streamer discharge  
(Positive polarity, lower applied voltage)



Trichel pulse discharge  
(Negative polarity, moderate applied voltage)



*Figure 2.19. Visual differences between transient spark, streamer and trichel pulse (negative polarity) discharges in air. Note that the area of luminosity for the trichel pulse (right) is restricted to an area very close to the cathode, where the bulk of ionization events occur.*

### 2.3.3 Use of Negative-Polarity Discharges in this Work

Negative polarity discharges were used early in this work, in investigating the effects of corona discharges on free nucleic acids and nucleic acids in solution. These experiments are discussed in Sections 5.3 and 5.4. In these experiments, the applied voltage was 10kV, the ballast resistance was 20 M $\Omega$ , and the inter-electrode (pin-to-solution) distance was 5mm. This resulted in a trichel pulse discharge with a frequency of 3-5 MHz and peak currents of 0.3-0.4 mA.

## 2.4 Dielectric Barrier Discharges

Dielectric barrier discharges are a class of plasma discharges in which at least one dielectric barrier is present, necessitating the use of alternating current. The dielectric constant of the material, the dielectric thickness and geometry, and the rate at which the applied voltage changes determine the displacement current through the material. When the electric field at the gas-dielectric interface exceeds the breakdown potential of the gas, discharge occurs. [121] After noble gas jets, these are the most commonly used plasma devices for medical applications, particularly in dermatology. [25], [122] One of these (the PlasmaDerm device, CINOGY GmbH) has already obtained regulatory approval for medical use in the European Union. [20], [24]

### 2.4.1 Overview

This class of plasma discharges includes the floating electrode dielectric barrier discharge (FE-DBD) and the surface micro-discharge (SMD), both of which are widely used by the plasma medicine community. The FE-DBD is a direct discharge- the target surface or tissue serves as the ground, and plasma filaments form between the dielectric material and the target. A surface micro-discharge is created by placing a grounded mesh against the dielectric, opposite the powered electrode. This results in the formation of tiny discharge filaments between the dielectric and points on the grounded mesh. Reactive neutral species produced by the SMD reach the target surface or tissue through diffusion. Schematics of an FE-DBD (B) and SMD (C) are shown in Figure 2.20.

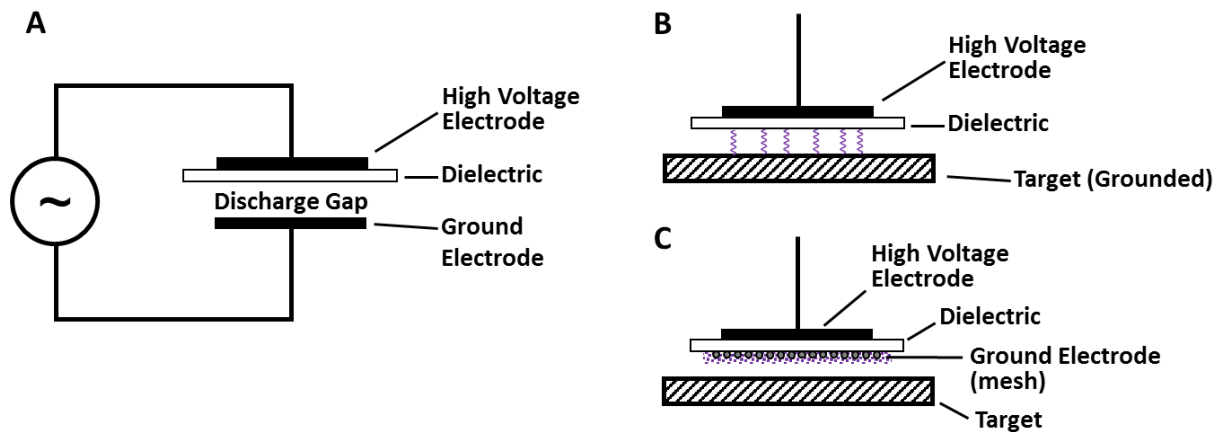


Figure 2.20. Schematics of various DBDs. **A** A general dielectric barrier discharge (DBD) configuration. One or more dielectric layers separate the two electrodes. **B** A floating-electrode DBD (FE-DBD), in which the target surface provides the path to ground. **C** a surface microdischarge (SMD); here, discharges occur across a very small gap between the dielectric and the grounded mesh. Reactive species must diffuse through a gas layer to reach the target surface.

### 2.4.2 Design Considerations

It would be informative to compare the effects of the corona discharge plasma device used in the bulk of this work to the effects of a floating-electrode DBD, another form of direct discharge, given the body of work on DBDs that has been generated by the field. In addition to the extensive work surrounding the development of devices for clinical use, studies with other FE-DBDs have examined oxidative DNA damage [123], sterilization [124], and cellular responses [28].

Examples of DBD devices that have been used by the non-thermal plasma community are shown in Table 2.4, which indicates some of the operating parameters (peak-to-peak voltage, frequency) and materials of construction. In general, surface microdischarges (SMDs) are more widely used; they require lower applied voltages (2-6 kV) relative to floating-electrode (FE-)DBDs (10-30 kV), and can be operated over a larger range of frequencies. The FE-DBD devices reported in literature were operated in a lower frequency range (1 Hz – 2 kHz), with very small inter-electrode distances and relatively large planar electrode surface areas.

*Table 2.4. Dielectric Barrier Discharge (DBD) designs used by the non-thermal plasma community (partial list). The discharge devices are generally either indirect or use a floating-electrode (FE) configuration, in which the surface or solution to be treated serves as one of the electrodes. Key materials of construction and electrical operating parameters are also indicated. (SMD = surface microdischarge;  $V_{pp}$  = peak-to-peak voltage)*

<b>Group</b>	<b>Type</b>	<b>Design / Electrode Materials</b>	<b>Solution / Target</b>	<b>Power / electrical</b>	<b>Reference</b>
Graves, UCB	Indirect DBD	Parallel plates: Cu (5 cm), glass, SS mesh (SMD)	Cells in petri dish, ~4 cm below SMD	2-6 kV, 10 kHz	[41], [125], [126]
Oehrlein, UMD	Indirect DBD	Parallel plates: Cu (5 cm), glass, SS mesh (SMD)	Polymers, lipopolysaccharide	6 kV <sub>pp</sub> , 41 kHz	[127], [128]
Von Woedtke, Greifswald	Indirect DBD	Patterned epoxy-glass fiber with etched Cu (powered), and flat Cu plate	Unbuffered physiological saline, PBS	0.25 W/cm <sup>2</sup> ; 10 kV <sub>pp</sub> ; 20 kHz	[129],[130]
Choi, Seoul	Indirect DBD	Parallel plates: Ag, 1.8mm glass, SS mesh (SMD)	Cell media	5.7 W (neon sign transformer; 60 Hz)	[131]–[133]
Vandamme; Alin de Pape; Orlean	FE-DBD	Parallel plates; HV electrode in 8mm Ba-titanate ceramic layer w/ thin polyimide film. 2mm gap	Mouse skin or U87MG and HCT-116 cells in media	17-23 kV; 1 Hz – 2 kHz; 0.67 W/cm <sup>2</sup>	[28]
Fridman, Drexel	FE-DBD	Parallel plates; Cu electrode	Melanoma cells in cell media	10-30 kV; 0.13-0.8 W/cm <sup>2</sup> , 1.5 kHz	[134], [135]
Jie, China	DBD (cyl.)	Cylindrical; grounded mesh	Water with indigo carmine	10-29 kV; 1-200 Hz	[136]

### 2.4.3 Prototyping of Floating-Electrode DBD

This section describes our preliminary efforts to construct a dielectric barrier discharge device in direct contact with a liquid solution, with the goal of being able to draw some conclusions about the mechanism of activity in FE-DBDs compared to the corona discharge device. While this work did not produce significant experimental results, it may be informative to those interested in developing such a device.

Initially, it seemed wise to hold as many aspects of the device constant as possible between the corona discharge and a direct DBD setup. Thus, an FE-DBD attachment was built that could be screwed onto the Delran corona discharge stand in place of the sharpened anode. This attachment consisted of a Delran holder with threaded sleeve, a small copper disc ( $d = 6\text{mm}$ ) brazed to the end of a stainless-steel rod (identical to the ones sharpened to make anodes for the corona discharge, i.e. same diameter), and a 10mm dielectric

disc (material and thickness variable) sitting between the copper disc electrode and the Delran holder. This attachment is shown in Figure 2.21. The hypothesis was that this small direct DBD device would yield a greater plasma-liquid contact area and be more “controllable” than the corona discharge, since the frequency of the applied alternating current (AC) voltage could be set in addition to the amplitude.

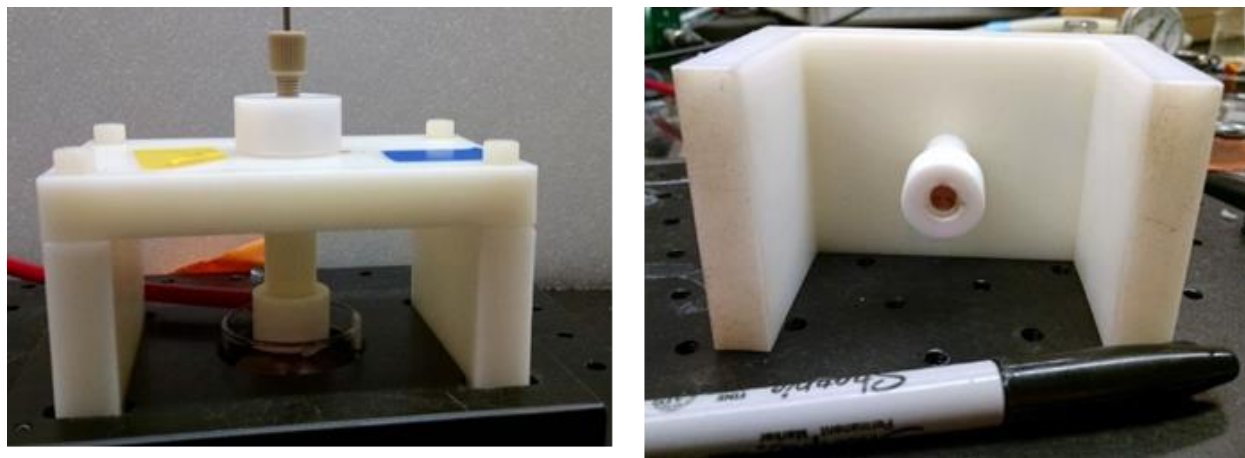


*Figure 2.21. Floating-electrode (FE-DBD) attachment to corona discharge device. A 6mm copper disc is brazed to the end of a stainless steel rod (an unsharpened corona discharge electrode), which is inserted through the spacer as usual. A 10mm dielectric (borosilicate, quartz or “Gorilla glass”) fits over the copper electrode and is held against it by the white Delran holder (which screws onto the threaded spacer.)*

Several power supplies were tested with this system, including a neon sign transformer (CPI Advanced Inc., 10kV 60Hz 35mA), a high-voltage power amplifier (Trek, 10/40A, 10kV) with function generator (Protek, Model 9301), and a custom power supply built by Brandon Curtis. Because the powered electrode no longer has a high radius of curvature, it was necessary to both apply higher voltages and reduce the inter-electrode gap distance in order to initiate a plasma. Neither of the 10kV power supplies were sufficient to ignite a discharge; however, a discharge was successfully ignited with the custom power supply at an applied voltage of 12 kV, a frequency of 37 kHz and a current of 30mA. A glass slide over a bare copper electrode was used as the target.

When a solution was used as the target (the “standard cell” solution reservoir in Figure 2.8), the system failed dramatically within a few minutes of operation. Specifically, arcing from the relatively sharp edges of the copper disc resulted in failure of the dielectric material. When the borosilicate failed, a 0.3mm hole was melted through the glass where the glass met the edge of the copper disc. When quartz was tested, the material cracked. Still images of the device during failure, and the failed dielectric materials are shown in Figure 2.22.



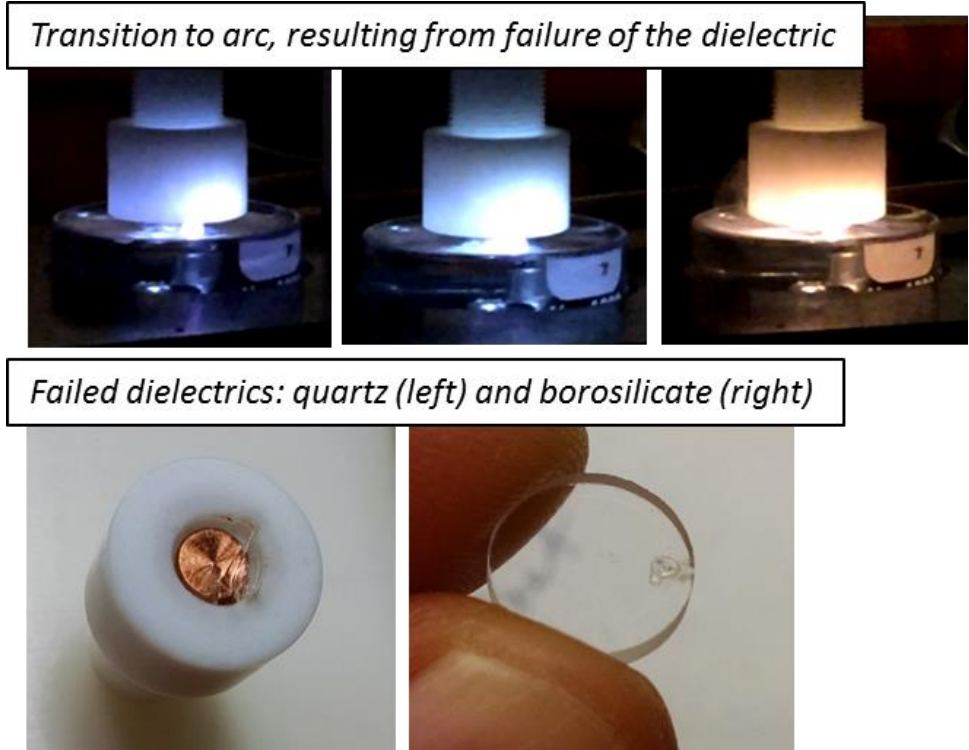


*Figure 2.22. Failure of dielectric during operation of FE-DBD over liquid solution at an applied voltage of ~12 kV. Top: FE-DBD attachment during normal operation (left), increasing in temperature (center) and arcing (right). This transition happened after 1 minute of uneventful operation, over a period of ~3 seconds. Bottom left: quartz dielectric after failure; the quartz over the copper is cracked. Bottom right: the channel formed in the borosilicate dielectric after failure/arcing.*

This failure illustrated the importance of understanding the electric fields produced by the electrode geometry. As a second attempt, an FE-DBD electrode arrangement with a larger planar area and with a dielectric that extended much further beyond the edge of the powered electrode was created. The edges of the copper discs used as the powered electrode were sanded down to help reduce strong electric field gradients at the edges. Copper discs (1", 1.5" and 2" in diameter) were centered on large quartz discs (2", 3", and 3" in diameter) and fixed to the quartz by applying epoxy around the edge of the copper. The copper discs were soldered to a copper rod (1/8" diameter), to which the high-voltage line from the power supply could be attached. The resulting electrodes (and spacing stand) are shown in Figure 2.23A and B.

The device was powered by a DC power supply (Jameco 301955) with custom flyback transformer (built by Brandon Curtis) to convert the DC power supplied to AC with a frequency of ~20 kHz. The device was tested first over a bare copper electrode (Figure 2.23C). Many individual filaments were formed between the quartz dielectric. The device was also operated over a large electrolyte reservoir (containing 0.5 M phosphate buffer, pH 7.4), as shown in Figure 2.23D. When operated over liquid, the oscillating electric fields significantly disturbed the liquid surface even when the discharge did not ignite, effectively “pulling” the liquid surface up towards the powered electrode. An inter-electrode distance of at least 2mm had to be maintained to prevent the liquid from meeting the powered electrode. When a discharge was ignited, the plasma was filamentary in nature, with distinct individual filaments forming and wandering over the liquid



surface. The liquid surface was significantly perturbed by the presence of these streamers, resulting in relatively large changes in the inter-electrode distance over short time periods (< 1s).

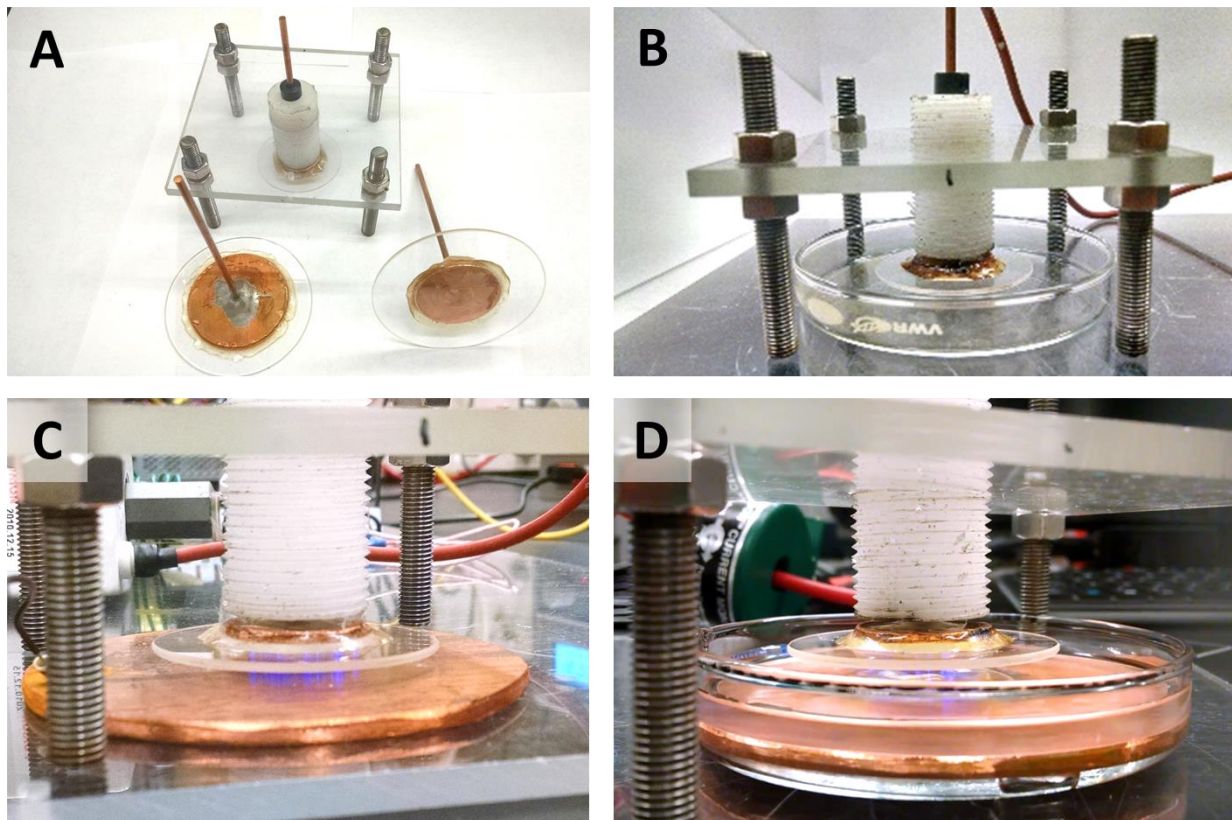


*Figure 2.23. Prototype of large planar FE-DBD device. (A) Three electrodes of different areas and dielectric-to-electrode diameter ratios. (B) Electrode spacer and stand, with 10mm petri dish solution reservoir. (C) FE-DBD operation over bare copper electrode. (D) FE-DBD operation over electrolyte solution (0.5 M phosphate buffer, pH 7.4) with large submerged electrode. In (C) and (D), the discharge formed transient, filamentary streamers that wandered across the electrode (or electrolyte) surface.*

These prototyping experiments illustrated some of the challenges inherent in designing a dielectric barrier discharge to operate over liquids. The relatively high voltages required (compared to corona discharge or SMD operation) and currents produced require more advanced power systems than anticipated. The oscillations induced in the liquid surface by AC current were unanticipated; while they are extremely interesting, they are not conducive to stable device operation. At present this device is a more complex and energetic system that is currently less well-behaved and adjustable than the corona discharge. Future work in this area should consider using a power source capable of operating at lower frequencies – this may help mitigate fluid-surface oscillations and allow smaller inter-electrode distances, and hence lower voltages, to be used. It may also be interesting to explore hydrogels or other materials that could provide an aqueous target with fixed surface.

## 2.5 Conclusions

This chapter described the development and characterization of non-thermal plasma devices in contact with liquids, with a focus on positive-polarity corona discharges. The device developed for this project to study plasma-liquid interactions, which produces a pin-to-plane corona-like plasma discharge in direct contact with the liquid surface, was studied in detail. The dominant plasma discharge mode formed as a function of the applied voltage, inter-electrode distance, and ballast resistance was established for positive polarity operation of this device. It was also shown that  $\text{H}_2\text{O}_2$  and other reactive species produced in solution can be controlled by adjusting the electrical and circuit parameters and the properties of the target solution (pH, conductivity). The resulting device can be tuned for solution acidification, greater oxidative power, limited peak current flow or other attributes depending on the user's priorities.

Corona-like discharges have several advantages over other plasma devices. These plasmas can be generated with a relatively simple and inexpensive direct-current (DC) power supply, and do not require function generators, matching networks, or tuning of the circuit. While the absence of these components does restrict the control one has over certain electrical parameters (e.g. discharge pulse frequency and duty cycle), these parameters can still be adjusted to some degree by changing the controllable properties of the setup: the applied voltage, the ballast resistance, and the inter-electrode distance. The presence of a highly curved allows us to produce a discharge in air (as opposed to a noble gas like helium or argon) at a voltage significantly below what would otherwise be required. With other types of discharges, specifically plasma jets, the use of a noble gas with a lower breakdown threshold (lower first ionization energy) allows a more uniform discharge to be formed at lower applied voltages; however, this increases costs and requires a gas delivery system.

The characteristics of positive-polarity corona discharges offer other advantages. The convective mixing induced in the liquid phase by the ionic wind improves the uptake of some reactive species from the gas phase. Such devices allow access to a range of discharge modes with a single device, and can produce a plasma discharge in direct contact with the liquid. The investigator can vary the relative abundances of the reactive species produced, for instance by decreasing power to increase the ratio of reactive oxygen species relative to nitrogen oxides. While the power can also be used to adjust the active species in surface-microdischarge (SMD) plasma devices, these are indirect plasma devices (cannot be operated with a liquid electrode). While it is possible to engineer dielectric barrier devices (DBDs) in direct contact with a liquid electrode (i.e. a floating-electrode DBD, or FE-DBD), engineering such devices is considerably more complex. Specifically, maintaining a sufficiently small yet uniform inter-electrode gap becomes challenging.

The use of a corona discharge device does impose some limitations. As previously stated, the operator has little control over the frequency within a given discharge mode. The plasma- contact area in the system developed is very small (area  $\sim 0.8 \text{ mm}^2$  or less). This could be increased by creating an array of points in series (similar the approach taken by Pei et al. [116]), or by changing the electrode geometry (e.g. to a wire-to-plane). There are other challenges to achieving stable, reproducible operation. This device is very sensitive to small changes in the anode curvature, as these greatly affect the electric field gradients responsible for inducing breakdown. Likewise strong air flows and changes in humidity may influence the discharge. Maintaining highly consistent experimental conditions is crucial to achieving reproducible

results. Despite these limitations, the corona discharge provides an excellent model system to study the fundamental interactions between non-thermal plasmas and an aqueous phase.

## **3 Plasma-Generated Liquid Chemistry**

### **3.1 Abstract**

Plasma-liquid interactions represent a critical area of research to advance many non-thermal plasma applications. While electrochemical experiments on plasmas interacting with liquids date back to over a hundred years ago [2], relatively little is known about how reactive species are transported to or formed in an adjacent aqueous phase by non-thermal plasma. The use of more complex and higher frequency plasma discharges, as well as advances in analytical tools have further stoked interest in this area. Understanding the mechanisms by which reactive species are formed in the liquid phase will aid in the rational design of plasma devices for treating aqueous systems or tissues, and may enable the delivery of ‘cocktails’ of reactive species tailored for the intended application.

Despite the increased interest in plasma-liquid interactions, many research challenges remain. For example, the importance of convection and diffusion in establishing specie penetration depth, and the role of charged species at the interface are poorly understood. Plasma-liquid chemistry is inherently complex, involving the transport of highly energetic and often unstable species across multiple phases, and through high concentration and electrical field gradients. The chemical precursors formed above the liquid depend on the energy of electrons, ions, metastables, and photons produced by the plasma, which vary spatially and temporally and require many different, often complicated measurements to form even a partial picture of the species present.

Because every lab’s plasma device is different, establishing the operating characteristics of the device described in Chapter 2 was a necessary first step for the results to be meaningful to the plasma community. In this chapter, we extend our analysis of the experimental system developed to examine the species generated in the liquid phase. The species formed by the plasma above the liquid are first discussed, along with transport processes affecting the rate at which they are taken up by the liquid. The observed changes in the concentrations of plasma-generated species in solutions exposed to a transient spark discharge are presented. The final section discusses the methods and characterization techniques used to detect and quantify species formed in solution as a result of plasma exposure.

### **3.2 Species Generated by Plasma in Contact with Liquids**

The influence of cold atmospheric plasma on liquids can be considered a several-step process. First, excited and ionized species are generated within the discharge; some of these travel towards the cathode, and are present in significant concentrations at the plasma-liquid or vapor-liquid interface. Some of these species may cross the interface and enter the liquid phase, depending on the properties of the species and the relevant transport limitations. Within the liquid-phase boundary layer at the solution surface, concentrations of some species may accumulate and new targets may be encountered, causing additional reaction pathways to become available. The species transported from the gas phase, and products of additional chemical pathways in the boundary layer, eventually propagate into the bulk solution and may undergo additional reactions. In these highly complex systems, other factors and processes exist and may play a role; for instance, evaporation, sputtering of the liquid surface, or electrolysis (Figure 3.1).

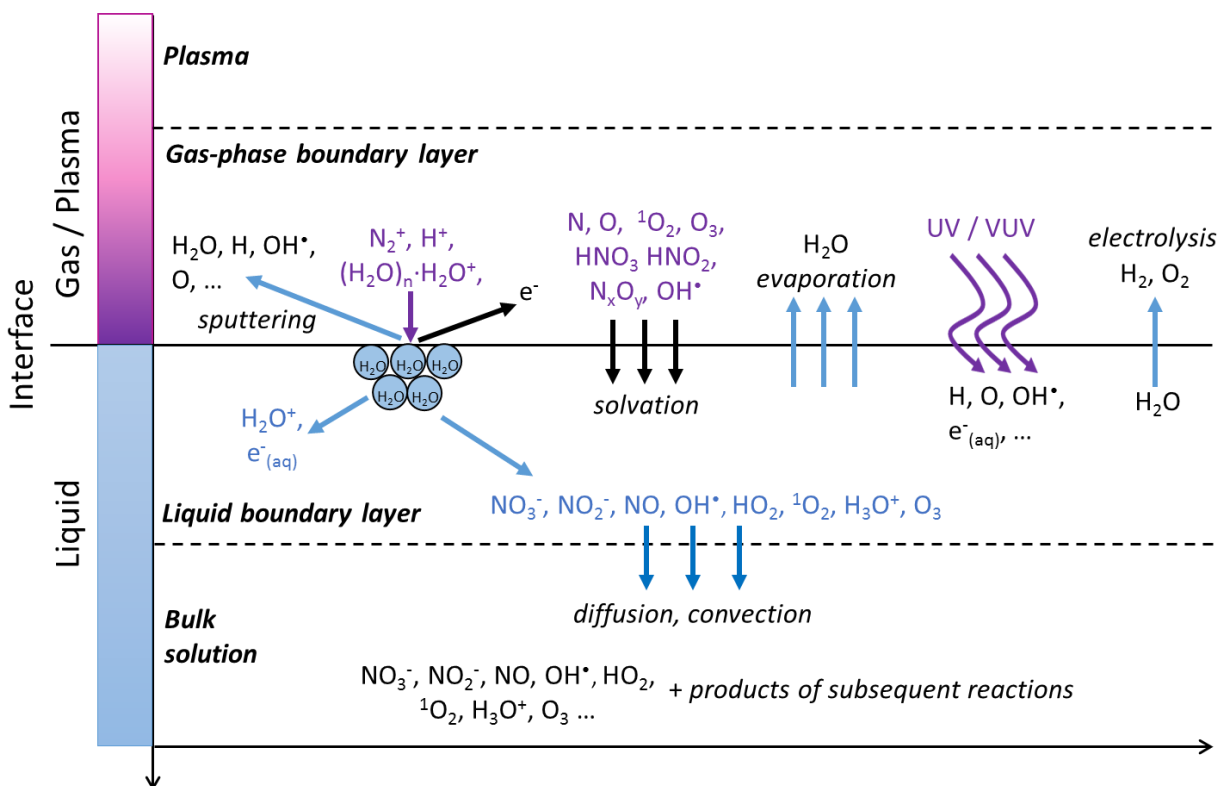


Figure 3.1. Schematic illustrating the complexity of plasma-liquid systems; some of the species flow and transfer processes at the plasma-liquid interface and associated boundary layers are shown. [137]

These processes are discussed in the sections that follow, from the formation of gaseous reactive oxygen and nitrogen species in air by the discharge, transport across the gas and liquid boundary layers and interface, to their continued evolution in the bulk liquid. [138]

### 3.2.1 Gas-Phase Precursor Chemistry: Origin of Species in the Gas Phase

Plasma discharges in air produce a complex mix of charged and excited species, dissociated molecules, and stable neutral species. This mixture varies both spatially and temporally, creating significant challenges for gas-phase characterization. Some progress has been made on both the experimental and computational fronts.

The ignition of the discharge, and therefore the beginnings of gaseous chemistry, are dependent on collisions of electrons with neutral species. As previously discussed, the breakdown of dry air in inhomogeneous electrical fields produces electrons with a mean energy on the order of 1-3 eV. [73] (pg 27) In this electron energy range, oxygen dissociation is the most efficient reaction; thus, the dominant new species produced (beyond N<sub>2</sub>, O<sub>2</sub> and other elements of air) are other oxygen species (ozone, excited molecular oxygen) and nitrogen oxides.

Emission spectroscopy can be used to measure molecular (OH<sup>\*</sup>, NO<sup>\*</sup>, CN<sup>\*</sup>) and atomic (O, H, N) radicals, as well as the rotational, vibrational and electronic temperatures. In air plasmas, the emission of N<sub>2</sub> species

is generally dominant. Emission spectroscopy studies of streamer, transient spark and glow discharges in air in the UV and visible-near-IR regions have been published by Machala et al. [96] They indicate the formation of excited metastable  $N_2$  species (e.g.  $A^3\Sigma_u^+$ , energy  $\sim 6\text{eV}$  above ground state). It is known that these can have relatively short lifetimes due to quenching by  $O_2$ . In transient spark plasmas, the emission of  $N_2^+$  (first negative system) and N, O, and H lines were observed. Atomic N, O, and H radicals are known to initiate further plasma chemical reactions, such as formation of ozone ( $O_3$ ), peroxy radicals ( $HO_2$ ), and other reactive species.

The gas-phase temperatures for the streamer and transient spark discharge (rotational/bulk gas and vibrational modes) are shown in (3.1) and (3.2):

$$\text{Streamer (26kHz): } T_g \approx T_{rot} = 350 \pm 100 \text{ K}, T_{vib} = 2000 \pm 500 \text{ K} \quad (3.1)$$

$$\text{Transient Spark (1 kHz): } T_g \approx T_{rot} = 550 \pm 100 \text{ K}, T_{vib} = 3000 \pm 500 \text{ K} \quad (3.2)$$

When no water was present in the surrounding environment, the same discharges at approximately the same parameters gave slightly higher temperatures (about 50K more in SC and TS, and 100K in GD). [96] It should also be noted that the transient spark temperatures above were measured for a discharge with significantly lower frequency (1 kHz vs 12-18 kHz typical of our system, see Table 2.2 and Table 2.3) and higher current (max 1.5A, vs max 0.1-0.5A in our system). A recent 0-D model by Bobkova et al. gives further predications of the plasma-generated species for a DC air discharge with water cathode. [139]

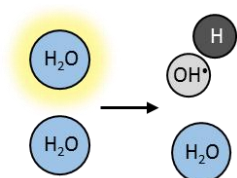
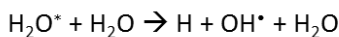
Concentrations of  $OH^*$  [66],  $NO^*$  [140], and atomic oxygen [141] can be measured through laser-induced fluorescence (LIF). This measurement technique uses lasers to excite  $OH^*$  radicals (or other species of interest) such that they fluoresce upon relaxation. The cross-section irradiated by the laser is generally 1 to 3mm square (this corresponds to the size of the area sampled). Several methods for extrapolating the  $OH^*$  concentration from this data have been applied. [142] For corona-like discharges in humid air, the  $OH^*$  density was found to be approximately proportional to the energy dissipated in the discharge, and increased with increasing relative humidity. [102], [143], [144] In addition to average densities, two-dimensional images of spatial profiles can be obtained by changing the mechanism of fluorescence detection from a photomultiplier tube (PMT) to an intensified charge coupled device (ICCD) camera; these studies indicated that the  $OH^*$  is formed preferentially in streamer channels. [102], [144] Literature values for the density of  $OH^*$  in non-thermal plasma systems are shown in Table 3.1. The measurements for positive corona discharges in air are used in “sanity-checking” some of our measurements and assumptions in Section 4.6.

Table 3.1. Literature values for gas-phase OH\* density in various plasma systems

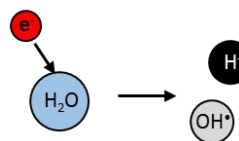
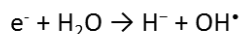
Plasma Source	Gas-Phase OH* Density	Measurement Technique	Ref.
Positive corona discharge in humid air	$3 \times 10^{14} - 1 \times 10^{15} \text{ cm}^{-3}$	LIF	[99], [102], [144]
DBD over water	$10^{12} - 10^{13} \text{ cm}^{-3}$	Model	[145]
Ar-H <sub>2</sub> O plasma jet in air (kINPen)	$10^{14} - 10^{15} \text{ cm}^{-3}$	LIF	[142]
He jet operated in air over cell media	$6 \times 10^{13} - 5 \times 10^{14} \text{ cm}^{-3}$	LIF	[146]

The concentrations of OH\* described in Table 3.1 can arise from several plasma-mediated processes. Some of the processes to form OH\* (including both gas-phase mechanisms and reactions at the plasma-liquid interface) are shown in Figure 3.2.

**Vibrational excitation reactions (< 2eV)**

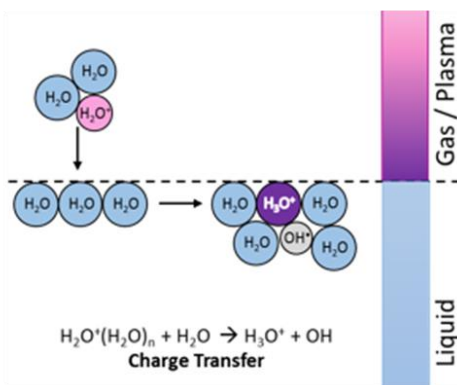


**Dissociative electron attachment (2-5eV)**



**Charge transfer**

from positive ions impacting surface



**UV/VUV photolysis of H<sub>2</sub>O**

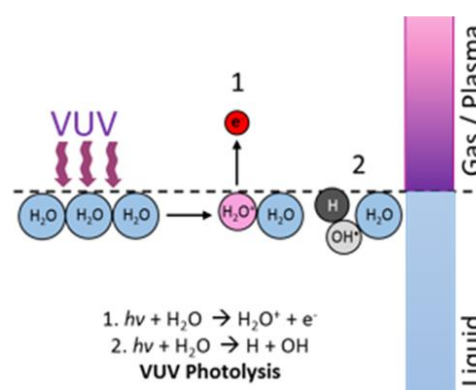
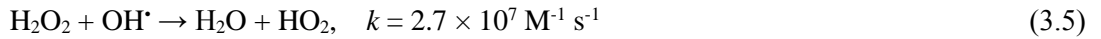


Figure 3.2. Mechanisms through which OH\* is formed in non-thermal plasmas in contact with water. The average electron energy reported for similar systems is 2-3eV; thus, the distribution of electron energies is sufficient for both vibrational excitation and dissociative electron attachment reactions to occur. These mechanisms are described in greater detail by Tian and Kushner. [63]

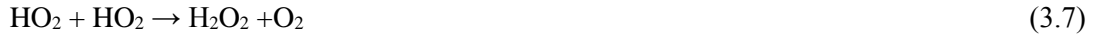
The formation of  $\text{H}_2\text{O}_2$  through the three-body mediated combination of two hydroxyl radicals in the plasma channel (equation 3.3) has been shown to be the dominant source of the  $\text{H}_2\text{O}_2$  eventually measured in the aqueous phase; however,  $\text{H}_2\text{O}_2$  may also be formed in the aqueous phase through the reaction of two aqueous hydroxyl radicals (3.4) at sufficiently high local concentrations [46], [63], [147], [148]:



where M is a collision partner (e.g.  $\text{N}_2$ ,  $\text{H}_2\text{O}$ ). The rate of  $\text{H}_2\text{O}_2$  generation is thus sometimes used as a relative indicator of hydroxyl radical ( $\text{OH}^{\bullet}$ ) generation [149]. Hydrogen peroxide and  $\text{OH}^{\bullet}$  can also react to form the hydroperoxyl radical, further complicating the chemistry where high concentrations of both species exist near the plasma-liquid interface. [46]



In non-thermal plasmas in the absence of humidity, where oxygen concentration is high and the local  $\text{OH}^{\bullet}$  radical concentration is low, hydrogen peroxide is primarily formed by hydroperoxyl radical ( $\text{HO}_2^{\bullet}$ ) recombination (reaction (3.6)), where the  $\text{HO}_2^{\bullet}$  precursor is formed by reaction (3.7).



The concentrations of ozone and nitrogen oxides formed by a dielectric barrier discharge (DBD) in air was studied by previous lab members using FTIR. [126], [150] Although this analysis has not been extended to corona-like discharges, the general principles established in this work apply to corona-like discharges as well as DBDs. As the discharge power is increased, the amount of  $\text{NO}_x$  species generated ( $\text{NO}_2$ ,  $\text{N}_2\text{O}_2$ ,  $\text{HNO}_2$ ,  $\text{HNO}_3$ ) increases, while the gas phase concentrations of  $\text{O}_3$  and  $\text{NO}^{\bullet}$  decrease precipitously. The development of significant concentrations of  $\text{NO}_2^-$  and  $\text{NO}_3^-$  in solutions treated with the transient spark discharge suggest that  $\text{NO}_x$  species dominate the gas-phase chemistry. This is consistent with the lack of  $\text{O}_3$  observed in solution-phase. Other researchers have noted that significant amounts of singlet oxygen ( $^1\text{O}_2$ ) were generated only by  $\text{O}_2$  and  $\text{CO}_2$  rare gas plasma jets [151]. This suggests that the presence of dissociated or ionized nitrogen species are likely to quench  $^1\text{O}_2$  as well, and we should not expect to see high concentrations of singlet oxygen produced by this relatively high-energy air plasma.

### 3.2.2 Mass Transfer at the Plasma-Liquid Interface and in the Bulk Solution



In the case of positive-polarity corona-like discharges in contact with liquids, the impinging flow of gas (positive particles and neutral species) against the liquid surface induces currents in the liquid phase and significantly affects mass transfer. This phenomenon can be observed by adding a drop of dye or small particles to the reservoir during plasma treatment – swirling of the dye or movement of the particles occurs according to the currents in the liquid, such that the solution is well-mixed within seconds.

A 2-dimensional COMSOL model of the non-electrical forces in this system (heat, mass and momentum transport) was developed by our collaborator Alex Lindsay (NC State). The flow patterns induced in the gas and liquid phases, as predicted by the model, are shown in Figure 3.3. Note that the plasma is modeled as a gas jet, with an exit velocity of 7.75 m/s (based on the calculations of Zhao et al. [112]). As discussed at length in transport texts [152], momentum transport in such systems is described by the continuity equation (equation 3.8) and the Navier-Stokes equation for incompressible flow (equation 3.9):

$$\nabla \cdot \vec{u} = 0 \quad (3.8)$$

$$\rho \left( \frac{\partial \vec{u}}{\partial t} + \vec{u} \cdot \nabla \vec{u} \right) = -\nabla p + \mu \nabla^2 \vec{u} \quad (3.9)$$

Where  $\vec{u}$  represents the fluid velocity,  $\rho$  is the overall mass density,  $p$  is the static pressure, and  $\mu$  is the viscosity. In the model shown in Figure 3.3, the transient equations 3.8 and 3.9 are solved until the velocity components and pressure reach steady state. The steady-state velocity field is then used as inputs into the convection terms, equations 3.10 and 3.11, describing heat and mass flow:

$$\rho C_p \vec{u} \cdot \nabla T = \nabla \cdot (k \nabla T) \quad (3.10)$$

$$\nabla \cdot (-D_i \nabla C_i) + \vec{u} \cdot \nabla C_i = R_i \quad (3.11)$$

Where  $C_p$  is the constant pressure heat capacity,  $T$  is the temperature,  $k$  is the thermal conductivity,  $D$  is the species diffusivity (diffusion constant),  $C_i$  is the concentration of species  $i$ , and  $R_i$  is the net rate of production of species  $i$  through chemical reactions. These are solved for physical times on the order of 10-15 minutes, consistent with the typical length of plasma exposure experiments.

A circulating liquid current (in the  $z$ -axis) is induced in the liquid phase by the flowing adjacent gas. Fluid initially moves outwards from the plasma contact point towards the reservoir edge as the impinging air spreads out across the surface. The magnitude of the fluid velocity is necessarily considerably lower than the gas velocity, but also falls significantly beyond a radius of 15mm. At the bottom of the reservoir, liquid is drawn back towards the center and eventually up to the surface beneath the plasma-liquid contact point. The magnitude of the liquid velocity is highest directly below the plasma-liquid contact point, consistent with our experimentally observed flow patterns.

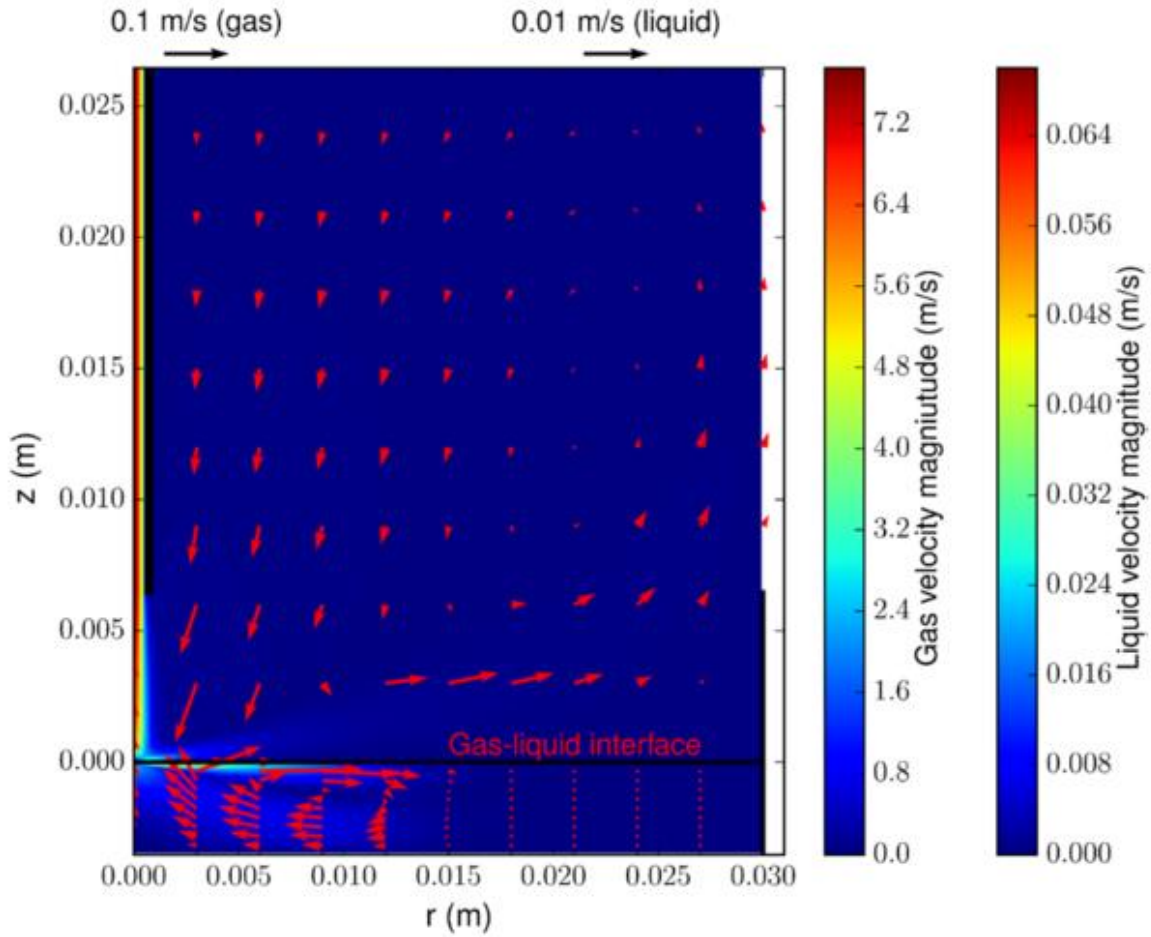


Figure 3.3. Simulated fluid velocity (magnitude and direction) in gas and liquid phases, shown as red arrows. Gas-Liquid interface is at  $z=0$ ; axis of symmetry is at  $r = 0$ . Red color represents higher velocity; blue color represents lower velocity. Velocity vectors in liquid phase are scaled 12.5 times larger in liquid phase.

In the model above, the interface is considered a flat plane. In reality, the impinging flow in positive-polarity discharges creates a “dimple” or depression in the liquid surface where the discharge contacts the liquid. In negative-polarity systems (i.e. where the electrolyte serves as the anode), this effect is significantly reduced.

At either side of the interface, a concentration gradient develops as species are depleted from the gas near the interface. The rate at which each species from the gas phase cross the gas-liquid interface is determined by its Henry’s law constant, which specifies the ratio between gas and liquid concentrations:

$$H_i \equiv C_{i, \text{aq}} / p_{i, \text{gas}}, [=] \text{ M / atm, etc.} \quad \text{or} \quad H_i \equiv C_{i, \text{aq}} / C_{i, \text{gas}} \quad [\text{unitless}] \quad (3.12)$$

Where  $C_{i, \text{gas}}$  and  $C_{i, \text{aq}}$  are the concentrations of species  $i$  in the gas and aqueous phases, respectively,  $p_{i, \text{gas}}$  is the partial pressure of species  $i$  in the gas phase, and  $H_i$  is the proportionality constant (Henry’s constant).

The Henry's constants at  $T = 25^\circ\text{C}$  for a subset of plasma-generated species that may enter the liquid phase are shown in Table 3.2.

*Table 3.2. Henry's Law Constants at Standard Conditions for Molecules Produced by Non-Thermal Plasmas in Air*

Species	Henry's Constant, $H_i$ (unitless)	Reference
OH	$6.92 \cdot 10^2$	[63]
H <sub>2</sub> O <sub>2</sub>	$1.92 \cdot 10^6$	[63]
NO	$4.4 \cdot 10^{-2}$	[63]
NO <sub>2</sub>	$2.8 \cdot 10^{-1}$	[63]
N <sub>2</sub> O <sub>4</sub>	$3.69 \cdot 10^1$	[63]
HNO <sub>2</sub>	$1.15 \cdot 10^3$	[63]
HNO <sub>3</sub>	$4.8 \cdot 10^6$	[63]
O <sub>3</sub>	$2.7 \cdot 10^{-1}$	[153]
CO <sub>2</sub>	$8.3 \cdot 10^{-1}$	[154]

It should be noted that the Henry's constants for the molecules in Table 3.2 may depend on solution pH and ionic strength as well as temperature. For example, the solubility (and corresponding Henry's constant) of O<sub>3</sub> decreases as the ionic strength of the solution is increased, e.g. with additional phosphate buffer. [155]

The visible plasma-liquid contact area is relatively small, on the order of 0.1-1 mm in diameter depending on the discharge mode, power, and solution conductivity. The net flow of gas to and along the surface may increase the effective plasma-liquid contact area by carrying plasma-generated species outward across the surface. Thus, to properly predict the flux of species across the interface would require knowledge of the radial variation in gas-phase species concentrations at the gas/plasma/liquid interface, which is difficult to estimate. In constructing a model for this system [66], the concentrations of species generated by plasma in the gas phase were taken from the work of Tian and Kushner et al. [63] as a reasonable first approximation. Tian and Kushner's work, which simulated the chemical species produced by a DBD in air over a tissue surface, describes both gas and liquid-phase reactions of the major reactive species produced by the plasma and reviews the importance of each. As it describes a DBD system, the geometry, duty cycle (duration of active plasma) and the absence of convective flow undoubtedly result in different distributions of species, but it remains a good resource.

The distribution of species within the liquid phase strongly depends on the diffusive and convective forces present. In the absence of convection (as in the case of surface-microdischarges, or other indirect plasma discharges where there is no gas flow at the surface), the rates of species transport throughout the bulk are determined solely by diffusion (and possibly temperature gradients). The diffusion coefficients for major plasma-generated species are shown in Table 3.3.

Table 3.3. Diffusion Coefficients for Species in the Gas and Aqueous Phases. (Temperature,  $T = 298K$  unless otherwise noted)

Species	Diffusion Constant $D$ , $m^2 s^{-1}$	Reference
OH(g)	$4 \cdot 10^{-5}$	[156]
H <sub>2</sub> O <sub>2</sub> (g)	$2 \cdot 10^{-5}$	[156]
NO(g)	$2 \cdot 10^{-5}$	[156]
NO <sub>2</sub> (g)	$1.7 \cdot 10^{-5}$	[156]
N <sub>2</sub> O <sub>4</sub> (g)	$1 \cdot 10^{-5}$	[156]
HNO <sub>2</sub> (g)	$2.1 \cdot 10^{-5}$	[156]
HNO <sub>3</sub> (g)	$2.1 \cdot 10^{-5}$	[156]
H <sub>2</sub> O(g)	$2.3 \cdot 10^{-5}$	[156]
OH(aq)	$2.8 \cdot 10^{-9}$ (T = 310K)	[157]
H <sub>2</sub> O <sub>2</sub> (aq)	$1.7 \cdot 10^{-9}$	[158]
NO(aq)	$2.2 \cdot 10^{-9}$	[159]
NO <sub>2</sub> (aq)	$1.85 \cdot 10^{-9}$ (T = 296K)	[160]
N <sub>2</sub> O <sub>4</sub> (aq)	$1.5 \cdot 10^{-9}$	Estimate
HNO <sub>2</sub> (aq)	$2.5 \cdot 10^{-9}$	By analogy with HNO <sub>3</sub>
HNO <sub>3</sub> (aq)	$2.5 \cdot 10^{-9}$	[161]
O=NOOH(aq)	$2.5 \cdot 10^{-9}$	By analogy with HNO <sub>3</sub>
NO <sub>2</sub> <sup>-</sup> (aq)	$1.7 \cdot 10^{-9}$	[162]
NO <sub>3</sub> <sup>-</sup> (aq)	$1.7 \cdot 10^{-9}$	[162]
H <sub>3</sub> O <sup>+</sup> (aq)	$7 \cdot 10^{-9}$	[163]
OH <sup>-</sup> (aq)	$5.29 \cdot 10^{-9}$	[164]

The effects of convective forces on the distribution of species adsorbed from the gas phase within the bulk solution is shown in Figure 3.4. In the left image, the distribution of HNO<sub>3</sub> in solution is predicted from the model inputs described above, while in the right image, convective forces are “turned off”, a condition not accessible experimentally. Comparing the right and left images, we see that convection predicted from the impinging gas flow is very effective in dispersing species generated at the surface (HNO<sub>3</sub> in this example). It is important to note that for hydrophilic (high  $H$ ) species like HNO<sub>3</sub>, the total uptake of HNO<sub>3</sub> does not change between the convection-dominated and diffusion dominated cases. Conversely, for less soluble species like NO<sup>•</sup>, the presence of convection increases the volume-averaged uptake significantly by maintaining a stronger concentration gradient across the interface (stronger driving force).

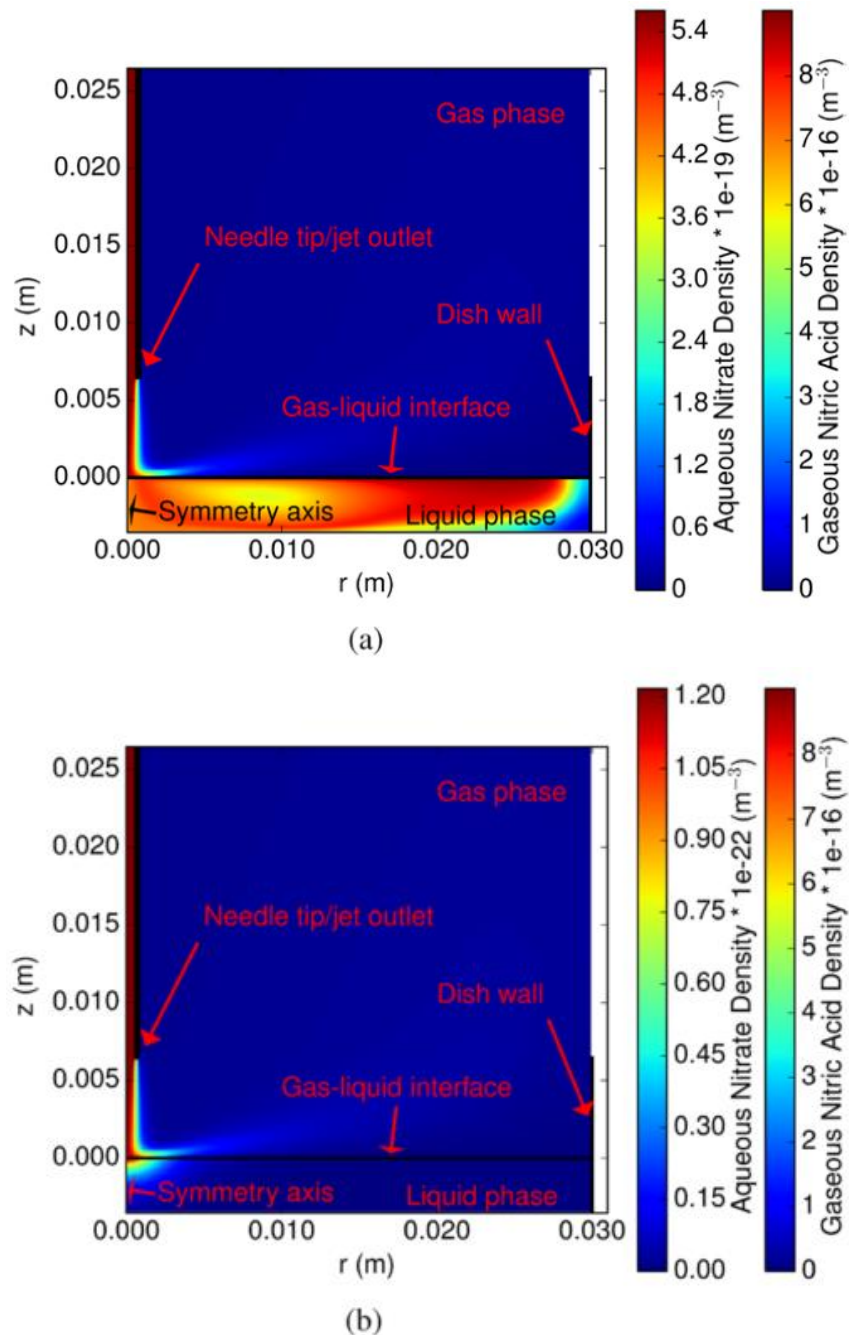


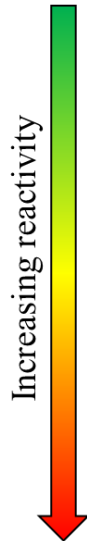
Figure 3.4. Simulated distribution of  $\text{HNO}_3$  in the bulk liquid solution (a) with or (b) without convective forces imposed by impinging flow on the solution surface. As expected, induced convective flow in the liquid significantly changes the distribution of species relative to a diffusion-only scenario.

In the above example, reactions within the liquid phase had been “turned off”. For very highly reactive species (e.g. most radicals), their distribution within the liquid phase is limited by the distance they can diffuse before meeting a potential reaction partner; these considerations are discussed in Section 4.6. Other transport phenomenon relevant to plasma-liquid interactions have been reviewed in [47], [165].

### 3.2.3 Evolution of Reactive Species in the Bulk Solution

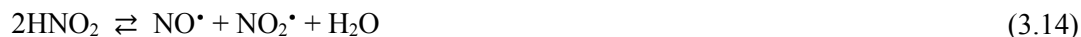
The extent to which species entering the aqueous phase from the gas phase accumulate in the bulk solution is determined by the rate at which they react with other species and are consumed, and in some cases, the rate at which they are formed through other reactions in the liquid phase. The presence of convective mixing prevents concentration gradients in the bulk solution, and thus reduces the influence that diffusivity plays in limiting the rates at which species are able to react. In general, highly reactive species (e.g. radicals) are present in the bulk at very low concentrations, while species that are less reactive (e.g. H<sub>2</sub>O<sub>2</sub>, NO<sub>2</sub><sup>-</sup>) may accumulate to millimolar levels and persist for hours or days. The approximate lifetimes for a number of plasma-generated species in physiological environments (pH = 7.4, with 1M linoleic acid) are shown in Table 3.4.

Table 3.4. Typical lifetimes of species that may be generated in aqueous solutions by non-equilibrium atmospheric pressure plasma, NEAPP. Based on a model of half-lives in a 1M linoleic acid solution at pH 7.4. [166]

	Active Species	Lifetime (T <sub>1/2</sub> , s)
	H <sub>2</sub> O <sub>2</sub> , HOCl	stable
	NO <sub>3</sub> <sup>-</sup> , NO <sub>2</sub> <sup>-</sup>	
	RO <sub>2</sub> <sup>•</sup>	5–20
	<sup>1</sup> O <sub>2</sub>	10
	NO <sup>•</sup>	1–10
	ONOO <sup>•-</sup>	10 <sup>-2</sup>
	NO <sub>2</sub> <sup>•</sup>	~10 <sup>-6</sup>
	CO <sub>3</sub> <sup>•-</sup>	~10 <sup>-6</sup>
	RO <sup>•</sup>	~10 <sup>-6</sup>
	O <sub>2</sub> <sup>•-</sup>	< 10 <sup>-6</sup>
OH <sup>•</sup>	< 10 <sup>-9</sup>	

Ultrapure water without the addition of buffers or other species becomes acidified when treated with NEAPP. [130], [167], [168] This arises primarily from the uptake of nitric acid, HNO<sub>3</sub> generated by the plasma, and from HNO<sub>3</sub> generated in the liquid phase through the decomposition of nitrous acid, HNO<sub>2</sub> (a significantly weaker acid). The one reported pathway for the decomposition of HNO<sub>2</sub> in aqueous solutions is shown in equations 3.13 through 3.15 [169], [170]; however, this is not a simple reaction and the mechanism(s) are not completely established. [15]



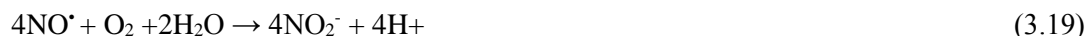


The evolution of solution pH and nitric acid concentration with increasing NEAPP treatment time (for solutions initially containing only ultrapure water) is shown in Figure 3.5. The accumulation of H<sub>2</sub>O<sub>2</sub> and nitrite, NO<sub>2</sub><sup>-</sup> in solution is also shown. The concentrations of H<sub>2</sub>O<sub>2</sub> and NO<sub>2</sub><sup>-</sup> initially increase, then level off and begin to decline as the rate at which they are consumed through subsequent reactions increases. H<sub>2</sub>O<sub>2</sub> and NO<sub>2</sub><sup>-</sup> react together under acidic conditions to form peroxyntrous acid O=NOOH, which then decomposes through one of two pathways as shown in equations 3.15-3.17. Above the pK<sub>a</sub> of O=NOOH, 6.8 ([171], [172]), peroxyntrite decomposition occurs through other mechanisms.

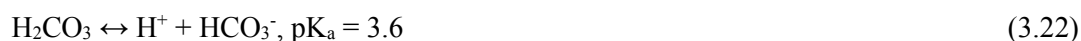
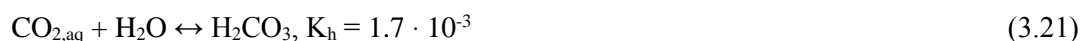


Once the solution pH approaches the pK<sub>a</sub> of nitrous acid (HNO<sub>2</sub>) (pH < 3.5), decomposition of HNO<sub>2</sub> to nitric oxide (NO<sup>•</sup>) and nitrogen dioxide (NO<sub>2</sub><sup>•</sup>) acts to further reduce the NO<sub>2</sub><sup>-</sup> concentration through the pathway shown in equations 3.13 to 3.15. [169], [170] The evolution of NO<sub>2</sub><sup>-</sup> (as shown in Figure 3.5) diverges from the concentration of H<sub>2</sub>O<sub>2</sub> around pH 3.4, consistent with the above reactions.

If dissolved oxygen is present, aqueous NO<sub>2</sub><sup>•</sup> and NO<sup>•</sup> radicals can react according to equations 3.21 and 3.22, further acidifying the solution. [172] The expected level of dissolved oxygen in water in equilibrium with room-temperature air is 8-9 mg/L (500-560 μM) so these reactions may play a role in the near-surface region when plasma discharges producing NO<sup>•</sup> and NO<sub>2</sub><sup>•</sup> are used.



In all solutions performed in air, it can be expected that dissolution of CO<sub>2</sub> from the gas phase will naturally lead to carbonic acid and bicarbonate in solution (H<sub>2</sub>CO<sub>3</sub> and HCO<sub>3</sub><sup>-</sup>, respectively). Aqueous CO<sub>2</sub> in neutral water is reversibly hydrated to carbonic acid per equation 3.21, with a hydration equilibrium constant K<sub>h</sub> of 1.7 · 10<sup>-3</sup> [173]. Carbonic acid is a weak acid and is only partially dissociates to bicarbonate in water; hence both are present (pK<sub>a1</sub> = 3.6 at 25°C [174]):



Given that the typical concentration of  $\text{CO}_2$  in air is 400ppm and its Henry's law constant is 0.034 M/atm, the concentration of  $\text{CO}_2$  in solution is  $\sim 14 \mu\text{M}$ , leading to a pH of 5.6–5.7. The ultrapure water solution thus begins with an initial pH of  $\sim 5.7$ , and a dissolved oxygen concentration of  $\sim 550 \mu\text{M}$ . These are expected to be the only species initially present in solution at  $t = 0$  in Figure 3.5.

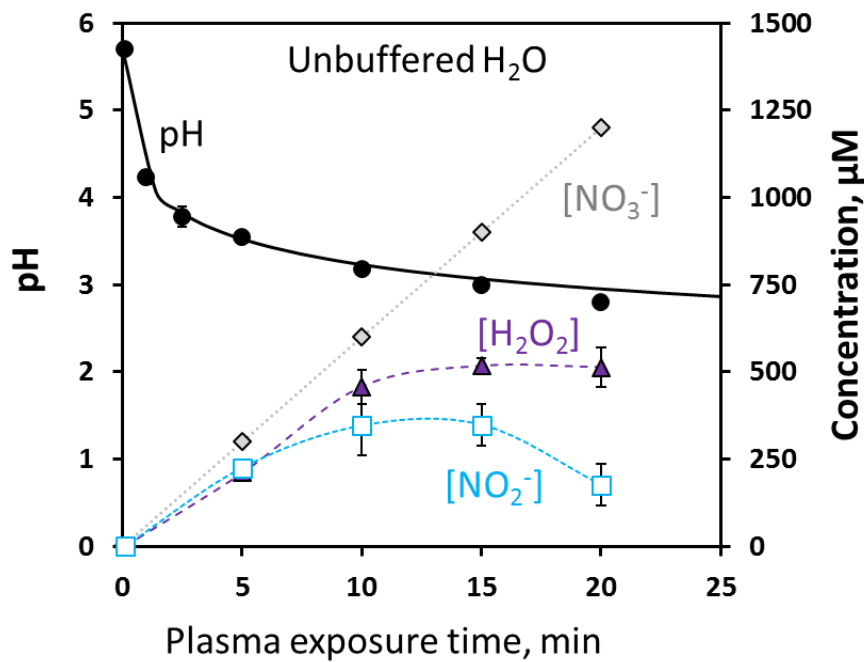


Figure 3.5. Evolution of  $\text{NO}_3^-$ ,  $\text{NO}_2^-$  and  $\text{H}_2\text{O}_2$  concentrations in unbuffered, ultrapure water treated with NEAPP with time. Concentrations of  $\text{H}_2\text{O}_2$  and  $\text{NO}_2^-$  and solution pH markers ( $\blacktriangle$ ,  $\square$ ,  $\bullet$ ) represent measured values (see Section 3.3.1 and 3.3.2 for analytical methods). Experiments were stopped at the indicated time point for sample analysis (e.g. for a 15-minute time point, the solution was treated continuously for 15 minutes and then analyzed without further NEAPP treatment). Error bars represent one standard deviation from the mean value;  $N \geq 4$ . The concentration of  $\text{NO}_3^-$  was predicted from the change in pH, based on calibration and verification with using ion-specific electrode (ISE) measurements (see Section 3.3.2.4).

Since the target solution is ultrapure water, the rate of  $\text{HNO}_3$  uptake by the liquid is directly correlated to the pH or the increase in solution conductivity. The relationship between these three properties (pH, solution conductivity and  $[\text{HNO}_3]$ ) is shown in Figure 3.6.



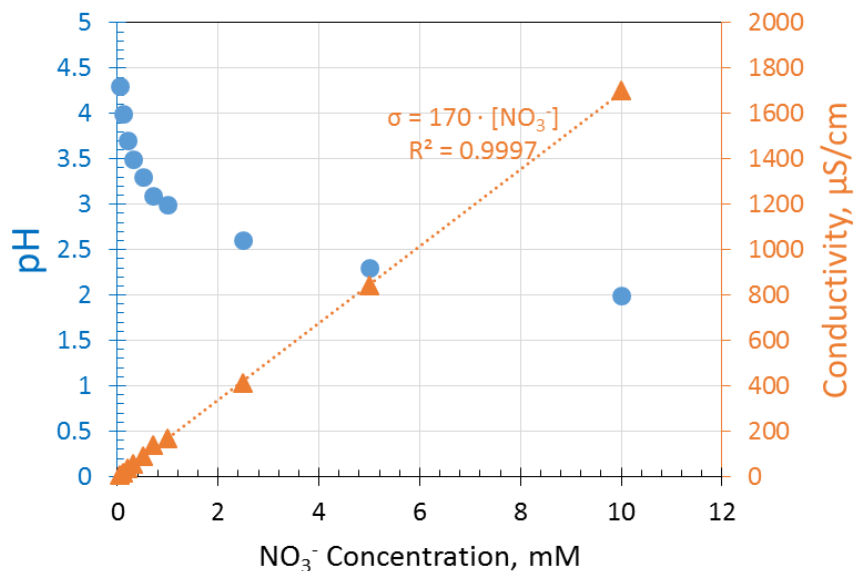


Figure 3.6. Relationship between  $[\text{NO}_3^-]$ , pH and solution conductivity in the absence of buffers.

For many proposed applications, particularly in biomedicine, the pH and conductivity of the solution is expected to fixed (e.g. at pH 7.2 – 7.4 for applications in physiological solutions or cell culture). Thus the evolution of these species with time during NEAPP treatment was also determined at fixed pH. Phosphate buffer was used for studies at a pH of 7.4. To avoid the complexity introduced by nitrite decomposition below pH 3.5 (and lack of verified kinetic data), a pH of 3.5 was chosen to study the effects of NEAPP in acidic environments, at least initially. Citrate buffer was used to maintain a constant pH in these experiments. The accumulation of  $\text{H}_2\text{O}_2$  and  $\text{NO}_2^-$  with time at fixed pH (pH = 3.5 or 7.4) are compared to the accumulation of these species in the absence of buffer in Figure 3.7A and Figure 3.7B respectively.

The initial rates of  $\text{H}_2\text{O}_2$  and  $\text{NO}_2^-$  production are similar regardless of solution pH. This supports our assertion that the pH of the solution does not affect the discharge; if this were not the case, we would expect to see differences in species generation even before they had accumulated to significant concentrations in the liquid phase. At neutral pH (pH = 7.4), the rate of  $\text{H}_2\text{O}_2$  and  $\text{NO}_2^-$  accumulation in solution is roughly constant. This rate of accumulation can be used to predict the concentration in the bulk solution at any given time and is used in the models discussed in Section 4.3.

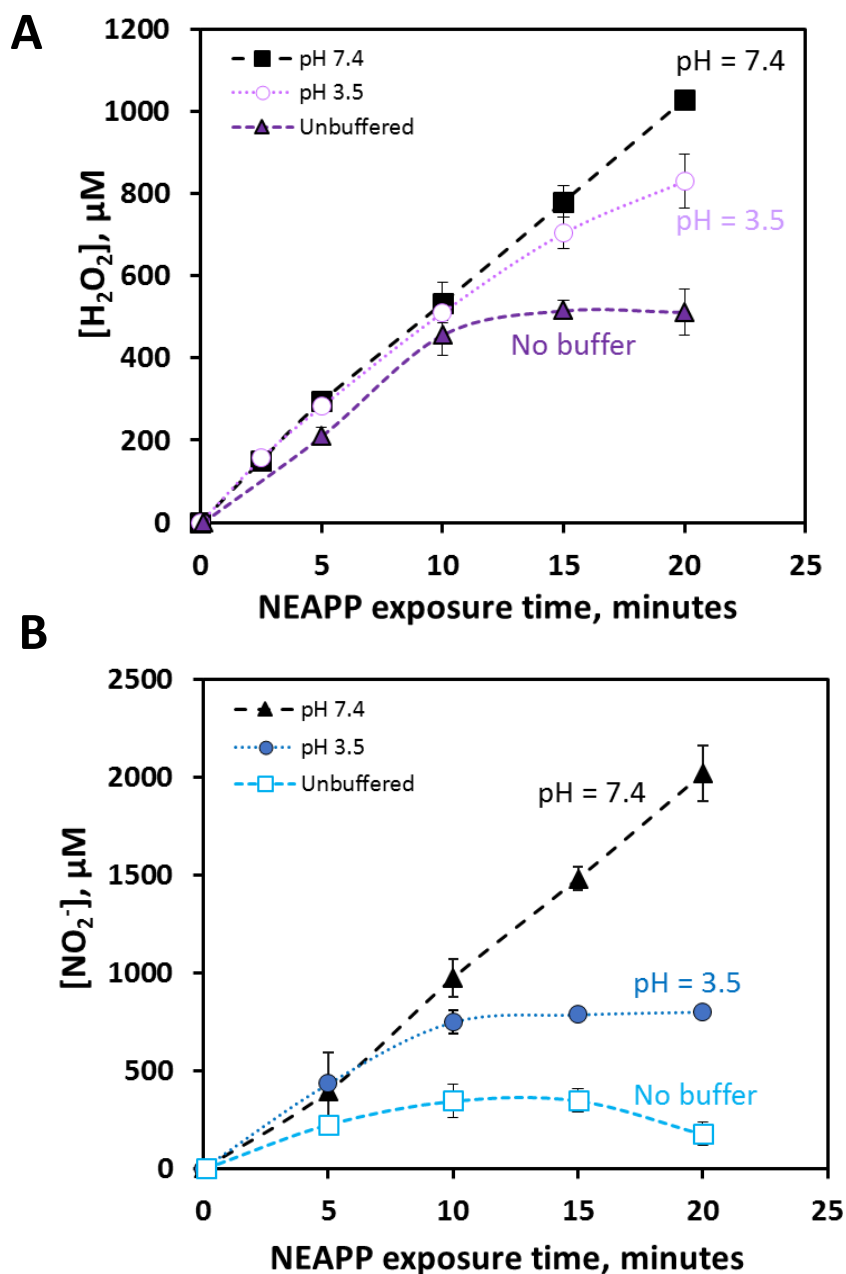


Figure 3.7. The increase in (A)  $H_2O_2$  and (B)  $NO_2^-$  concentrations in buffered and unbuffered solutions as a function of plasma (NEAPP) exposure time. The concentrations of both  $H_2O_2$  and  $NO_2^-$  begin to level off or decrease in acidic solutions due to their reaction to form  $O=NOOH$  (equations 3.16 – 3.18). At neutral pH, the production of  $H_2O_2$  and  $NO_2^-$  through plasma-liquid contact can be approximated as a constant (the slope of the line):  $dH_2O_2/dt = 8.7 \times 10^{-7} M/s$  ( $dn_{H_2O_2} = 4.4 \times 10^{-10} mol/s$ ) and  $dNO_2^-/dt = 1.7 \times 10^{-6} M/s$  ( $n_{NO_2^-} = 8.3 \times 10^{-9} mol/s$ )

The concentrations of  $H_2O_2$ ,  $NO_2^-$ , and  $NO_3^-$  formed by the transient spark discharge (as shown in Figure 3.7) are on the same order of magnitude as those measured in solutions electro-sprayed through a similar

positive-polarity corona-like discharge used by Machala et al. [98], while Lukes et al reported slightly lower accumulation of these species in larger-volume solutions (900mL) treated by a DC plasma (frequency = 50 Hz,  $V_{\text{applied}} = 27\text{kV}$ ). [172] Typical concentrations of  $\text{H}_2\text{O}_2$  generated in liquids by various non-thermal plasmas and their relative energy efficiencies are reviewed by Locke and Shih in [46].

Despite the limited number of reactions used to describe the major trends shown in Figure 3.7, a large number of other reactions between reactive oxygen and nitrogen species are possible and undoubtedly occur. Section 3.3 discusses methods of detecting these reactive species in the liquid phase. As we are particularly concerned with the generation and consumption of hydroxyl radical,  $\text{OH}^\bullet$ , reactions of  $\text{OH}^\bullet$  with other plasma-generated species in aqueous solutions are shown in Table 3.5.

*Table 3.5. Rate constants for the reaction of  $\text{OH}^\bullet$  with various species that may be present in plasma-treated solutions, from the work of [175] and Tian and Kushner [63].*

Reaction	Rate constant, k (T = 293K)	Reference
$\text{OH}^\bullet + \text{NO}_2^- \rightarrow \text{NO}_2^\bullet + \text{OH}^-$	$1.1 \times 10^{10} \text{ M}^{-1} \text{ s}^{-1}$	[175]
$\text{OH}^\bullet + \text{CO}_3^{2-} \rightarrow \text{OH}^- + \text{CO}_3^\bullet$	$3.9 \times 10^6 \text{ M}^{-1} \text{ s}^{-1}$	[175]
$\text{OH}^\bullet + \text{H}_2\text{O}_2 \rightarrow \text{HO}_2 + \text{H}_2\text{O}$	$2.7 \times 10^7 \text{ M}^{-1} \text{ s}^{-1}$	[175]
$\text{OH}^\bullet + \text{HO}_2^- \rightarrow \text{O}_2^\bullet + \text{H}_2\text{O}$	$7.5 \times 10^7 \text{ M}^{-1} \text{ s}^{-1}$	[175]
$\text{OH}^\bullet_{\text{aq}} + \text{OH}^\bullet_{\text{aq}} \rightarrow \text{H}_2\text{O}_{2,\text{aq}}$	$5.5 \times 10^9 \text{ M}^{-1} \text{ s}^{-1}$	[63]
$\text{OH}^\bullet_{\text{aq}} + \text{OH}^-_{\text{aq}} \rightarrow \text{O}^-_{\text{aq}} + \text{H}_2\text{O}$	$1.3 \times 10^{10} \text{ M}^{-1} \text{ s}^{-1}$	[63]
$\text{OH}^\bullet_{\text{aq}} + \text{HO}_{2,\text{aq}} \rightarrow \text{O}_{2,\text{aq}} + \text{H}_2\text{O}$	$6 \times 10^9 \text{ M}^{-1} \text{ s}^{-1}$	[63]
$\text{OH}^\bullet_{\text{aq}} + \text{O}_2^-_{\text{aq}} \rightarrow {}^1\text{O}_{2,\text{aq}} + \text{OH}^-$	$8 \times 10^9 \text{ M}^{-1} \text{ s}^{-1}$	[63]

### 3.2.4 Reactions at Submerged Electrode

There has been little work to date by the non-thermal plasma community on the mechanism of current transfer from the liquid electrolyte to the submerged electrode and vice versa. Even questions as naïve as the potential drop across the liquid are difficult to answer with certainty, thus complicating electrochemical analyses. The potential drop across the aqueous solution should be limited by the electrochemical stability window of water, 1.23 V. Early models have predicted large potential gradients over small distances at the plasma-liquid interface. [119] Some potentially important reactions are shown with their standard electrochemical potential in Table 3.6.

Table 3.6 Standard Potential of Relevant Electrochemical Reactions (vs Standard Hydrogen Electrode), from [176]

Standard Potential (V)	Reduction Half-Reaction
-0.83	$\text{H}_2\text{O} + \text{e}^- \rightarrow \frac{1}{2} \text{H}_2 + \text{OH}^-$
0	$2\text{H}^+ + 2\text{e}^- \rightarrow \text{H}_2$
0.401	$\text{O}_2 + \text{H}_2\text{O} + 4\text{e}^- \rightarrow 4\text{OH}^-$
0.337	$\text{Cu}^{2+} + 2\text{e}^- \rightarrow \text{Cu}$
1.229	$\text{O}_2 + 4\text{H}^+ + 4\text{e}^- \rightarrow \text{H}_2\text{O}_2$

The lack of information about the potential at the submerged electrode makes it difficult to predict which reactions are taking place. Some evidence that reactions do in fact occur at this interface was provided by ICP measurements, which indicated increased copper dissolution from the submerged electrode in plasma-treated solutions vs solutions exposed to nitric acid alone. The concentration of copper in solution after 5 minutes of transient spark treatment was 2 ppm, vs 0.2 ppm in solutions exposed to the copper electrode with a similar concentration of nitric acid for 5 minutes. Additional observations of oxide removal from the surface of the submerged copper electrode during plasma treatment also suggest that reduction of existing oxides occurs. Figure 3.8 shows one example of this effect: after 10 min streamer treatment of ultrapure water, the surface was visibly less fouled (Figure 1b). For these tests, a 20M $\Omega$  ballast resistor was used so the maximum current passed was relatively low (~50mA).

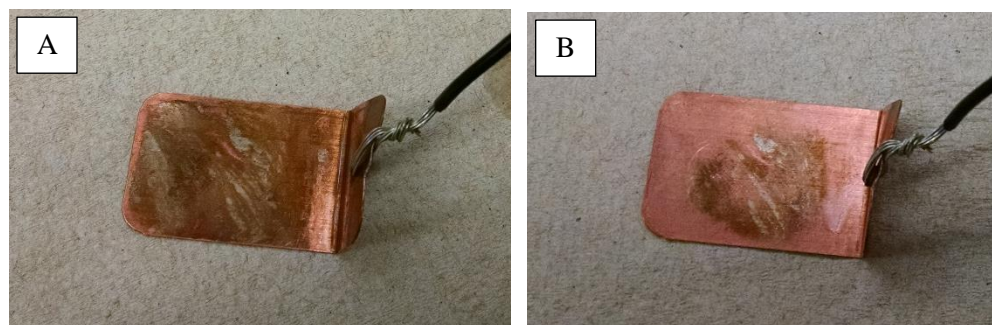


Figure 3.8. Removal of oxidation on copper electrode due to plasma treatment of water solution. Photographs taken (A) before and (B) after 10 minutes of exposure to a streamer discharge over water.

### 3.3 Measurement of Reactive Oxygen and Nitrogen Species in Plasma-treated Solutions

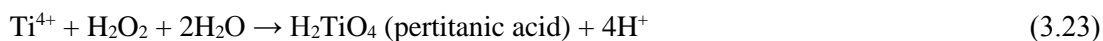
The measurement of relatively stable species formed in aqueous solutions by non-thermal air plasmas, hydrogen peroxide and nitrogen species ( $\text{NO}_2^-$  and  $\text{NO}_3^-$ ), is discussed in Section 3.3.1 and Section 3.3.2 respectively. These sections describe both the spectrophotometric methods (UV-visible absorption) that were ultimately used and alternate procedures that were evaluated.

Sections 3.3.3 through 3.3.6 describe methods and approaches to measure highly reactive oxygen species, such as OH<sup>•</sup>, with lifetimes in solution on the order of seconds or less. Section 3.3.3 discusses the direct measurement of radicals through EPR. The remaining sections describe the use of indigo carmine as an indicator of reactive species, and the use of positive controls and scavenger experiments to help identify the active species.

### 3.3.1 Quantification of Aqueous H<sub>2</sub>O<sub>2</sub>

Standard colorimetric techniques were used to quantify the H<sub>2</sub>O<sub>2</sub> and NO<sub>2</sub><sup>-</sup> generated in solution. Such techniques make use of Beer's Law (Absorbance =  $\epsilon \cdot l \cdot c$ ) to determine the concentration of a compound (typically formed from reaction with the species of interest) from the measured absorbance at a specified wavelength. The extinction coefficient,  $\epsilon$  is determined by making a calibration curve with a standard solution and/or taken from the literature.

The concentration of H<sub>2</sub>O<sub>2</sub> produced in solution was quantified using the TiSO<sub>4</sub> procedure developed by Eisenberg in 1943 [177]. In this procedure, the aqueous H<sub>2</sub>O<sub>2</sub> is allowed to react with a titanium ion (from a dissociated titanium sulfonate reagent) to produce pertitanic acid, which is yellow in color, as shown in equation 3.23.



The reaction is effectively instantaneous and the yellow-colored complexes are stable for at least 6 hours [178]. The pertitanic acid has a maximum absorbance at roughly 407nm and an extinction coefficient of ~480 M<sup>-1</sup> cm<sup>-1</sup>. The titanium sulfate reagent can either be purchased (e.g. Aldrich, 15 wt% titanium oxysulfate solution, 495379) or can be made by dissolving solid TiSO<sub>4</sub> in concentrated H<sub>2</sub>SO<sub>4</sub> per the procedure related by Satterfield et. al. [179]. H<sub>2</sub>O<sub>2</sub> concentrations could be determined with  $\pm$  5% accuracy down to 30  $\mu$ M. The range of H<sub>2</sub>O<sub>2</sub> concentrations over which this technique was validated is shown in Figure 3.9.

The reaction requires an acidic environment; if the reagent is added to a solution that is not sufficiently acidic, TiO<sub>2</sub> precipitates out of solution (turning solution a milky white color before eventually settling out). This problem can be avoided by diluting the sample (such that the H<sub>2</sub>SO<sub>4</sub> in the reagent is sufficient to keep the pH acidic) and/or adding sufficient additional H<sub>2</sub>SO<sub>4</sub> to acidify the solution prior to reagent addition.

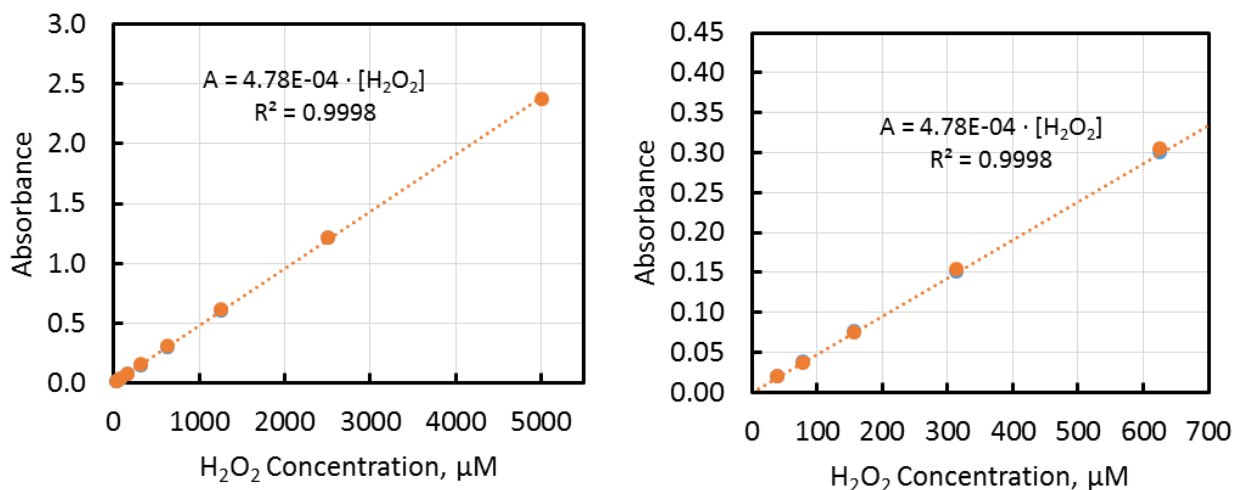
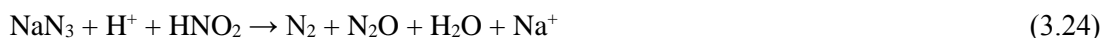


Figure 3.9. Relationship between H<sub>2</sub>O<sub>2</sub> concentration and solution absorbance at 407nm for high and low concentration ranges. The path length was 1 cm. The extinction coefficient for the dye is 478M<sup>-1</sup> cm<sup>-1</sup> based on these data.

Reaction 3.23 is pH dependent [180] and should be formed in acidic solutions (below the pK<sub>a</sub> of HNO<sub>2</sub>/NO<sub>2</sub><sup>-</sup>, 3.3). For plasma-treated solutions in which NO<sub>2</sub><sup>-</sup> was also present in solution, NaN<sub>3</sub> was added to a concentration of 10 – 60 mM to reduce the NO<sub>2</sub><sup>-</sup> to N<sub>2</sub> (through reaction 3.24). This will prevent it from reacting with H<sub>2</sub>O<sub>2</sub> (per Machala et al. and Lukes et al. [98], [172] ). The rate constant for reaction 3.24 is relatively low ( $k_{24} = 6.21 \times 10^{-1} \text{ M}^{-1} \text{ s}^{-1}$ ); an excess of NaN<sub>3</sub> is recommended, and even then bubble formation was observed for several minutes in solutions with high nitrite concentrations.



It should be noted that NaN<sub>3</sub> is highly toxic and must be disposed of as hazardous waste; the addition of NaN<sub>3</sub> to strong acids (such as solutions containing the titanium sulfate reagent) can produce hydrazoic acid (HN<sub>3</sub>). Solid NaN<sub>3</sub> is explosive. The presence of some organic compounds in the solution, specifically formaldehyde, may also produce interferences by reaction with the H<sub>2</sub>O<sub>2</sub> in solution. Acetaldehyde and methanol did not interfere. [179]

An alternative method to quantifying H<sub>2</sub>O<sub>2</sub> in solution is through iodometric titration. While not based on absorbance, this method also involves a color change in solution. In the first step, H<sub>2</sub>O<sub>2</sub> in solution oxidizes iodide (I<sup>-</sup>) to iodine (I<sub>2</sub>) in the presence of acid and molybdate catalyst (reaction 3.25). The iodine-containing solution is then titrated with a thiosulfate solution to reduce the iodine (reaction 3.26). Near the endpoint of the titration, a starch indicator is added – when the endpoint is reached, the solution goes from a deep blue color to straw yellow, as the iodine-starch complex is reduced to iodide. The amount of H<sub>2</sub>O<sub>2</sub> originally in solution can be determined from the quantity of sodium thiosulfate required to reduce the iodine.



This procedure is not appropriate for solutions in which nitrite is present. Nitrous acid reacts with iodide according to the following stoichiometry [181], [182]:



Furthermore, in the presence of oxygen, the nitric oxide (NO) generated through reaction 3.27 is oxidized to nitrogen dioxide which partly reacts with water, forming nitrous and nitric acid. Thus, the presence of nitrite creates a cycle which produces large quantities of iodide, which can no longer be attributed to H<sub>2</sub>O<sub>2</sub>.

Because nitrite was expected to be present in almost all solutions studied in this work, the titanium sulfate method was used exclusively. If future work requires a) greater resolution, b) detection of concentrations < 30 μM and/or c) high concentrations of neutral or basic buffers, (and N<sub>2</sub> is excluded from the system) iodometric titration is a good alternative for H<sub>2</sub>O<sub>2</sub> quantification. Another possible method for H<sub>2</sub>O<sub>2</sub> detection include electrochemical detection with “biochemistry analyzers” (as used by Traylor et al [183]) which monitor the current produced by its oxidation on platinum.

### 3.3.2 Quantification of Aqueous Nitrite and Nitrate

Several strategies for measuring nitrite and nitrate ions in aqueous solutions were explored:

1. Direct absorbance measurements of the ions in solution (UV-vis spectroscopy)
2. Griess method for the direct measurement of nitrite. Nitrate may be reduced to nitrite and quantified through this method.
3. Anion chromatography
4. Use of an ion-specific electrode (nitrate)

Direct quantification of nitrate produced in solution due to plasma treatment is more difficult than measurement of nitrite, for which the Griess method (a simple and sensitive colorimetric method) is available. Each of the above methods is discussed in the sections that follow.

#### 3.3.2.1 Direct Absorbance of Nitrite and Nitrate

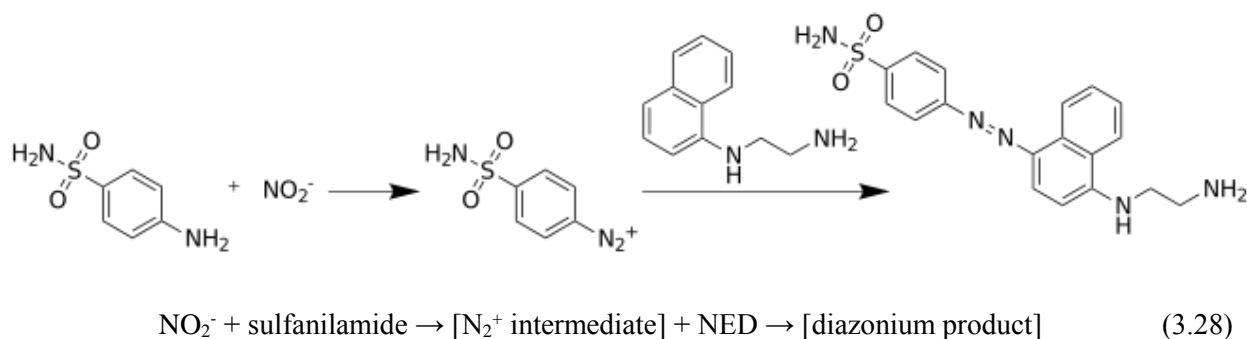
The absorption spectra of NO<sub>2</sub><sup>-</sup> and NO<sub>3</sub><sup>-</sup> are characterized by intense π → π\* bands at 205nm (ε = 5500 M<sup>-1</sup> cm<sup>-1</sup>) and 200nm (ε = 9900 M<sup>-1</sup> cm<sup>-1</sup>) respectively, and by weaker n → π\* bands at 360nm (ε = 22.5 M<sup>-1</sup> cm<sup>-1</sup>) and 310nm (ε = 7.4 M<sup>-1</sup> cm<sup>-1</sup>). [184] Hydrogen peroxide does not have significant absorption bands above 200 nm and thus does not interfere.

Depending on the type of spectrometer and cuvette used, the upper or lower bands may be used for quantification. The lower bands (~200nm) are challenging to deconvolute due to their proximity, and also require the use of quartz cuvettes and spectrophotometers with a deuterium or xenon arc lamp (rather than a tungsten filament) to supply monochromatic wavelengths below 300nm. However, if restricted to the weak bands in the 300-400nm range, absorbance measurements were only accurate to within ± 10% at

concentrations of ~800  $\mu\text{M}$  and above. Signal overlap of the  $\text{NO}_2^-$  and  $\text{NO}_3^-$  peaks was deconvoluted by standard fitting and error minimization techniques.

### 3.3.2.2 Griess Method for Nitrite Measurement

Aqueous nitrite was quantified using the Griess method. Griess reagents (e.g. Sigma-Aldrich, 03553) generally contain a strong acid and two active components, sulfanilamide, and N-(1-naphthyl)-ethylenediamine (NED) (or similar azo dye). A typical Griess reagent contains 0.2% naphthylethylenediamine dihydrochloride (NEDD), and 2% sulfanilamide in 5% phosphoric acid. The  $\text{NO}_2^-$  in solution first reacts with sulfanilamide to form an intermediate, which then reacts with NED or NEDD to form a chromophore with a high absorbance at 548nm, as shown in reaction 3.28 [185], [186]:



Blank, standard and test solutions were allowed to develop in the dark for 30 minutes after reagent addition to allow the above reactions to near completion. The effective extinction coefficient was re-determined or confirmed at the beginning and end of each reagent bottle. A typical calibration curve illustrating the range over which this assay was valid (solution absorbance at 548nm for a 1cm path length) is shown in Figure 3.10.



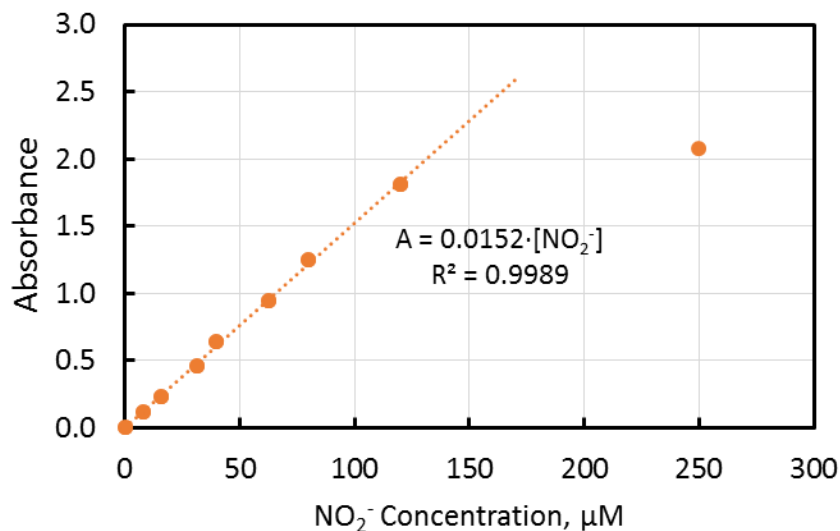


Figure 3.10. Relationship between  $\text{NO}_2^-$  concentration and solution absorbance at 548nm for solutions consisting of 1:1 vol/vol Griess reagent and sample. After the Griess reagent was added to the sample, the solution was developed in the dark for 30 minutes prior to measuring the absorbance.

The commercial Griess reagent used in this work (containing 2-Naphthylamine as the azo dye) is classified as a carcinogen, a known reproductive toxin, and as “Acutely Toxic” (GHS07). Care should be taken when working with this reagent, and all wastes should be disposed of as hazardous, carcinogenic waste.

Quantification of  $\text{NO}_3^-$  by reduction to  $\text{NO}_2^-$  with  $\text{VCl}_3$  under acidic-HCl conditions and subsequent Griess analysis was attempted per the procedure reported by Miranda et al. [187] However, the disadvantages of this method (rapid oxidation of the reagent solution, requiring daily preparation; and high toxicity of vanadium(III) ) were such that other analytical methods were pursued. A detailed review of Griess-based assays for nitrite and nitrate has been written by Tsikas. [188]

### 3.3.2.3 Anion Chromatography

Anion chromatography for the quantification of  $\text{NO}_2^-$  and  $\text{NO}_3^-$  was performed on a Thermo LC-5000+ HPLC system with a conductivity detector. A Dionex AS11 column (4 x 250mm) was used to separate the anions. The column, packed with small (13µM) plastic particles functionalized with alkonal quaternary ammonium groups, retains anions to different extents.

A gradient method with sodium hydroxide eluent (1.0mL/min, increasing from 5mM to 38mM hydroxide over 10 minutes followed by 5 minute flush) was used to separate anions along the column. Gradient methods, in which the concentration of hydroxide is increased with time during elution, typically provide greater resolution over isocratic methods, in which the concentration of eluent is kept constant. This was necessary due to the proximity of the  $\text{Cl}^-$  and  $\text{NO}_2^-$  peaks. A typical calibration run showing the elution time of various ions ( $\text{F}^-$ ,  $\text{Cl}^-$ ,  $\text{NO}_2^-$ ,  $\text{Br}^-$ ,  $\text{NO}_3^-$ ,  $\text{PO}_4^-$ , and  $\text{SO}_4^-$ ) with time is shown in Figure 3.11. The quantity of each analyte is determined by integrating to find the area under each peak, and comparing the value to a calibration curve generated with standard solutions.

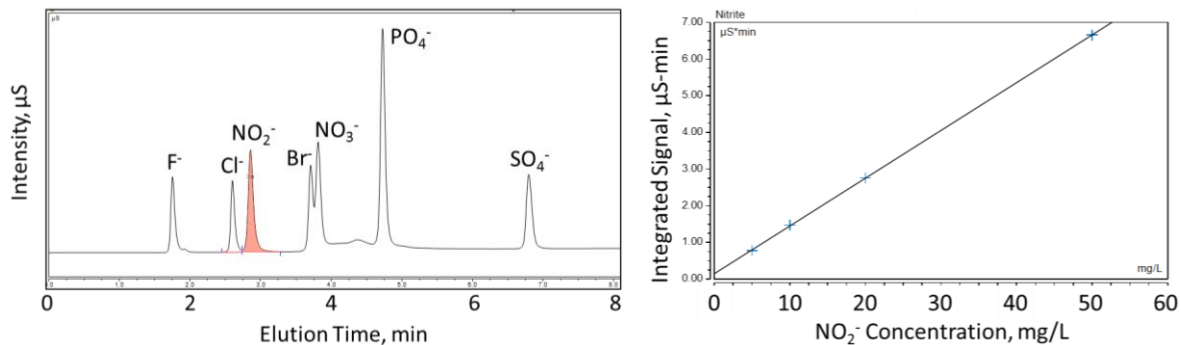


Figure 3.11. Example of anion separation (left) and integration of the resulting peaks for nitrite (shown on right) or nitrate measurement on HPLC system with conductivity detector. The method shown utilized an eluent gradient and suppression.

### 3.3.2.4 Ion-Specific Electrodes

A ThermoFisher Orion nitrate combination ISE (9707BNWP) in conjunction with an Orion pH/conductivity/ISE meter was used for the ISE measurements in this work. The sensing and reference electrodes are combined in a single probe; this was desirable due to the low volumes of plasma-treated solutions ( $< 5\text{mL}$ ). A glass container roughly 8mm larger than the radius of the probe was used for measurements to decrease the volume of solution required, and samples were often diluted 2-5x. Linearity of the signal over the concentration range of the actual and diluted solutions was confirmed using standards when dilution was required. A 10mM  $\text{NO}_3^-$  solution is equivalent to 620 ppm  $\text{NO}_3^-$  or 140 ppm as N. Nitrate concentrations of 100  $\mu\text{M}$  or below require a low-concentration calibration procedure due to deviation from linearity in this region.

Ion-specific electrodes (ISEs) use the activity of specific ions in solution to generate an electric potential (as described by the Nerst Equation). Thus, measurements are highly temperature dependent. Nitrate ionic strength adjustment solution (ISA) should be included (1:50 ratio) to provide a constant background ionic strength for samples and standards. If other ions are present (i.e. interferences), an interference suppressor solution should be used.

### 3.3.3 Spin-Traps and Electron Paramagnetic Resonance (EPR)

One way to directly measure radical species is through electron paramagnetic resonance (EPR). In this technique, a sample is placed in a tunable magnetic field ( $B_0$ ) and excited with a microwave source at a frequency near that necessary to produce a spin-spin excitation. The most commonly used EPR instruments are X-band systems, with a microwave frequency of  $\nu = 9.75\text{ GHz}$ . The magnetic field is scanned over a specified range during the experiment; when the microwave frequency matches the energy separation between the up-down spin states for a population of electrons within the sample at the current value of  $B_0$ , the energy is absorbed. This change in microwave absorbance is detected by the instrument, and is usually shown as a plot of the first derivative of the energy as a function of  $B_0$ .

Due to the short lifetimes of radical species in solution, EPR experiments typically make use of “spin-traps”, or molecules capable of accepting a free electron from a target radical and stabilizing it for an extended period of time. Common examples include DMPO, BMPO, TEMP, PBN, POBN, MNP and DEPMPO; their splitting patterns and other information are well-documented. [189]–[191]

The plasma community is beginning to employ this technique to identify radical species produced by specific plasma devices, mainly noble gas jets. Wu et al. [192] detected  $\text{OH}^\bullet$  and  $^1\text{O}_2$  produced by a He/O<sub>2</sub> jet using DMPO and TEMP respectively. Tresp et al [193] attempted to quantify production of  $\text{OH}^\bullet$  and  $\text{O}_2^{\bullet-}$  in solutions treated with an argon jet (kinpen) using DMPO and BMPO respectively. Superoxide ( $\text{O}_2^{\bullet-}$ ) was reported to be the dominant radical formed in pH 7.4 buffered solution when oxygen shield gas was used; when identical experiments were performed with cell media or more complex mixtures at pH 7.4, indications of  $\text{O}_2^{\bullet-}$  were absent, indicating that this compound either didn't form or else quickly reacted with other species in solution. The authors noted that the time delay before measurement, the source of the spin-trap, and the presence of other species in solution (amino acids, vitamins or other possible antioxidants or scavengers) all strongly influenced the results. Work by Takamatsu, et al. on radicals produced with different feedgases (He, Ar, N<sub>2</sub>, O<sub>2</sub>, N<sub>2</sub>/O<sub>2</sub>, CO<sub>2</sub>) showed that the “mock air” plasma jet was the only gas-mixture combination that did not produce observable DMPO signal [151], which the authors inferred to mean that  $\text{OH}^\bullet$  was not produced. Additionally, significant amounts of  $^1\text{O}_2$  were generated only by O<sub>2</sub> and CO<sub>2</sub> plasmas. [151] The production of  $\text{OH}^\bullet$  and  $\text{H}^\bullet$  atoms in solution treated with an argon jet, with and without other biological species, was also investigated by Uchiyama et al. in 2015 [194]. Recently, Gorbanev used a combination of spin traps (including DEPMPO) to show that  $\text{H}^\bullet$  radicals are created close to the plasma liquid interface, and that  $\text{O}_2^{\bullet-}$  and  $\text{OH}^\bullet$  production was dependent on feed-gas humidity (with greater humidity producing more  $\text{O}_2^{\bullet-}$ ). [148]

The spin traps that have been used in studies of argon and helium jets in contact with/above liquids are shown in Table 3.7. There is currently a lack of EPR studies of other types of plasmas in contact with liquids.

Table 3.7. Spin traps used in EPR studies of rare gas plasma jets above aqueous solutions, with the reaction partner for formation of an EPR-active adduct shown.

Spin Trap	Chemical Name	Donor Radicals / Species	Reference
DMPO	5,5-dimethyl-1-pyrroline N-oxide	$\text{OH}^\bullet$ , $\text{O}_2^{\bullet-}$ , $\text{CH}_3^\bullet$ , $\text{CN}^\bullet$	[147], [148], [151], [192]– [194]
BMPO	5-tert-Butoxycarbonyl-5-methyl-1-pyrroline-N-oxide	$\text{OH}^\bullet$ , $\text{O}_2^{\bullet-}$	[147], [193]
TEMP	2,2,6,6 tetramethylpiperidin	$^1\text{O}_2$ , $\text{O}_3$	[148], [192]
PBN	N-tert-butyl-a-phenylnitron	$\text{H}^\bullet$ , $\text{O}_2^{\bullet-}$	[148], [194]
DEPMPO	5-(diethoxyphosphoryl)-5-methyl-1-pyrroline N-oxide	$\text{O}_2^{\bullet-}$ , $\text{H}^\bullet$ , $\text{OH}^\bullet$	[148]
TPC	2,2,5,5-tetramethyl-3-pyrroline-3-carboxamide	$^1\text{O}_2$	[151]
MGD-Fe	N-methyl-D-glucamine dithiocarbamate iron	$\text{NO}^\bullet$	[151]

The EPR system available to us is a “bench-top” Active Spectrum instrument. The signal of 2,2,6,6-tetramethyl-piperidinyloxy (TEMPO), a stable nitroxide radical commonly used as an EPR standard, in water during microwave power calibration experiments is shown in Figure 3.12. Because aqueous samples are “lossy” and absorb microwaves well, the sample volume is restricted to a 1.7mm capillary tube (centered inside a borosilicate or quartz 5mm EPR/NMR tube with an o-ring). With larger volumes of polar solvents, the system will be unable to lock.

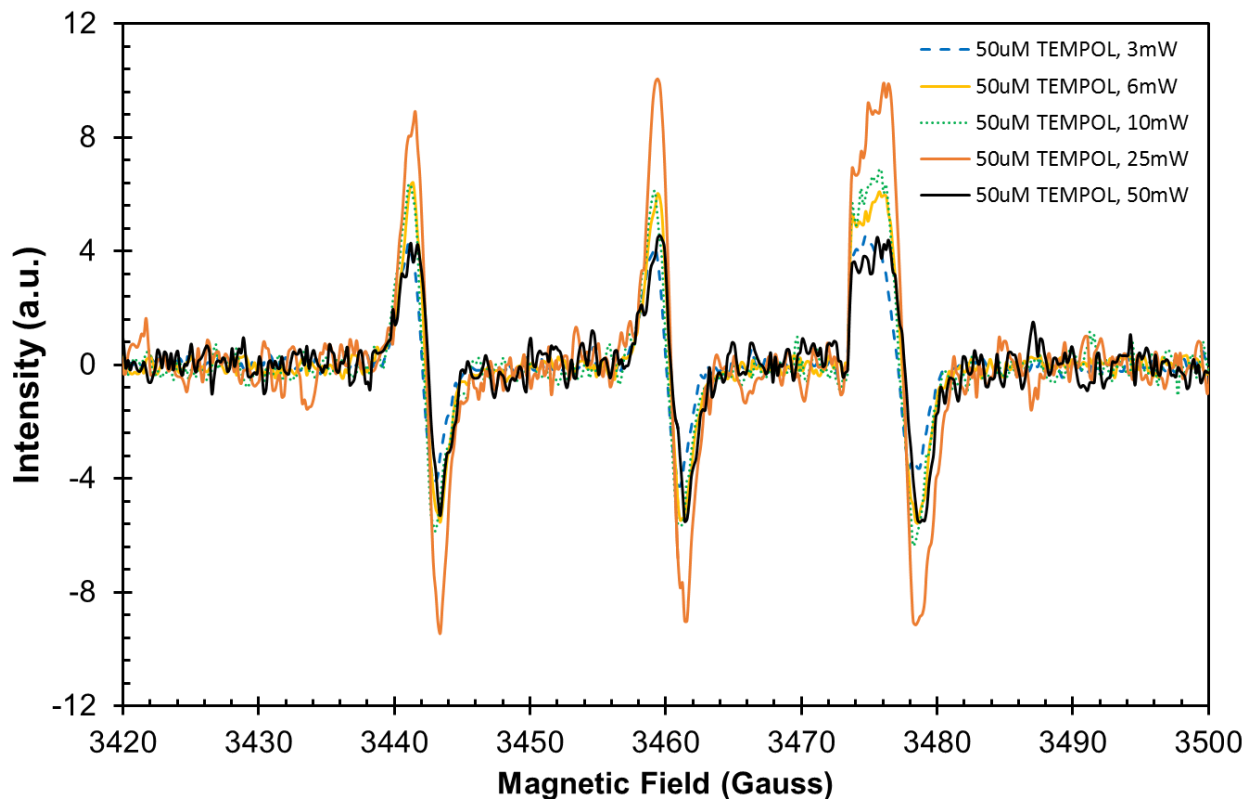


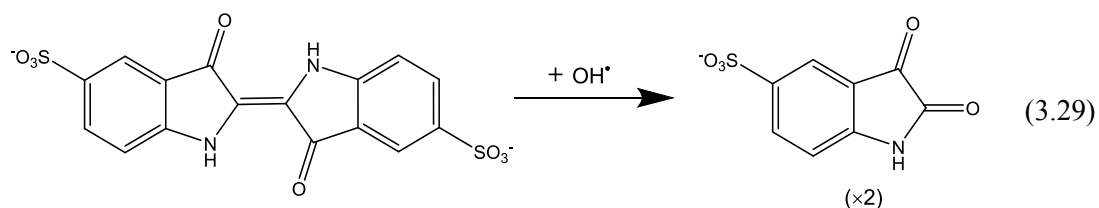
Figure 3.12. EPR spectra of 50 $\mu$ M TEMPOL in H<sub>2</sub>O at increasing microwave powers; series of single scans. These experiments are run to determine the optimal microwave power for experiments.

EPR studies of plasma systems in our lab were carried out in collaboration with Yi-Wei Yang. No EPR signal was observed from solutions of DMPO treated with the transient spark for 5-20 minutes, or from solutions with H<sub>2</sub>O<sub>2</sub> and NO<sub>2</sub><sup>-</sup> mixed to produce OH<sup>\*</sup> through O=NOOH decomposition. In the former case, concerns were initially that the transient spark treatment was “too rough” for the DMPO spin trap, causing it to undergo ring-opening reactions and prematurely degrade. However, given that DMPO-OH was observed when Fenton reagents (H<sub>2</sub>O<sub>2</sub> and FeSO<sub>4</sub>) were used to produce OH<sup>\*</sup>, the lack of DMPO-OH signal observed in acidic H<sub>2</sub>O<sub>2</sub> and NO<sub>2</sub><sup>-</sup> solutions suggests that O=NOOH interacts with DMPO to form other species. While the mechanisms through which O=NOOH and the anion, O=NOO<sup>-</sup> oxidize targets in biological systems are still poorly understood, there is evidence that these species interact with DMPO to form other adducts [195], [196]. It is reported that DMPO-OH decomposes by direct reactions with NO<sub>2</sub><sup>\*</sup> (and O=NOO<sup>-</sup>). [197] EPR work has shifted to the analysis of solutions treated with an Ar/O<sub>2</sub> plasma jet (in a controlled head space) using TEMP as the spin trap.

### 3.3.4 Use of Indigo Carmine as a Non-Specific Indicator of General Oxidizing Agents

An alternative strategy to quantify highly reactive species, including hydroxyl radical, is to use an indirect reactive probe that responds to the presence of OH<sup>\*</sup> in a manner that is easily observable. Indigo carmine, a common industrial dye (also called acid blue 74), is suitable for this purpose. Its strong absorbance peak

around 600nm is lost upon oxidation of its highly susceptible central C=C bond by OH<sup>•</sup>. The reaction of indigo carmine with OH<sup>•</sup> to produce isatin sulfonic acid (ISA) is shown in reaction scheme (3.29) [198], [199].



The loss of indigo absorbance at 608nm (through UV-vis absorption measurements) can thus be used as an upper bound for the cumulative production of OH<sup>•</sup> or other oxidizing species. Due to the high extinction coefficient of indigo carmine,  $\sim 20,000 \text{ M}^{-1} \text{ cm}^{-1}$ , the linear absorbance regime extends only up to  $\sim 100 \mu\text{M}$ , as shown in Figure 3.13.

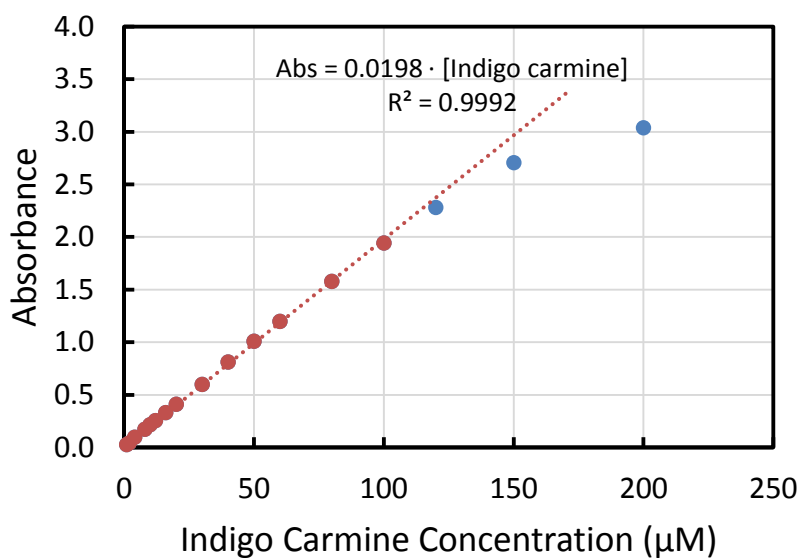


Figure 3.13. Absorbance of indigo carmine dye in aqueous solution at a wavelength of 608nm over the concentration range from 2-200  $\mu\text{M}$ . The path length was 1 cm. The extinction coefficient for the dye is  $19,800 \text{ M}^{-1} \text{ cm}^{-1}$  based on these data. Indigo carmine solutions were diluted to 100  $\mu\text{M}$  or less in order to remain within the linear regime.

Reaction 3.29 occurs rapidly and irreversibly, with a rate constant  $k_{29}$  of  $1.8 \times 10^{10} \text{ M}^{-1} \text{ s}^{-1}$  [200], similar to reported rate constants for the reaction between OH<sup>•</sup> and tyrosine or glutathione [201]. Indigo carmine also reacts on a similarly rapid time scale with O<sub>3</sub>, O<sub>2</sub><sup>•-</sup>, OCl<sup>-</sup>, and other strong oxidizers [198],[202]. With this caveat in mind, we provide various observations and calculations in Section 4 that suggest that OH<sup>•</sup> is the dominant oxidizing reaction partner under certain conditions.

The use of non-thermal plasma to decolorize organic dyes has been investigated in the context of reducing color pollution [203]–[205] and wastewater abatement [206], [207]. However, previous studies have focused on the rate of de-colorization of the dye rather than its implications for measuring oxidizing species. In this work, decomposition of aqueous indigo carmine is used as an indicator of OH<sup>•</sup> generation and oxidative strength.

### 3.3.5 Positive Controls: Methods to Produce Oxidizing Species without Plasma

Two methods were explored to produce OH<sup>•</sup> without exposure to plasma. The first, the reaction of H<sub>2</sub>O<sub>2</sub> and NO<sub>2</sub><sup>-</sup> under acidic conditions to form O=NOOH and its subsequent decomposition, is discussed in Section 3.2.3. As an alternate method, OH<sup>•</sup> was produced through Fenton chemistry, a class of reactions involving the reduction of H<sub>2</sub>O<sub>2</sub> by metal ions (generally Fe<sup>2+</sup> or Cu<sup>+</sup>). [208] Due to their importance in native biological systems [209], [210] and as an advanced oxidative process for wastewater remediation [211], there has been much discussion of this mechanism in those communities. Two general reactions are involved. In the first, H<sub>2</sub>O<sub>2</sub> is reduced to OH<sup>•</sup> and OH<sup>-</sup>. In the second, Fe<sup>3+</sup> (or Cu<sup>2+</sup>) is reduced back to Fe<sup>2+</sup>: [212]



There is some debate in the literature over whether OH<sup>•</sup> is primarily responsible for the oxidation observed in solutions of Fenton reagents, or whether a combination of OH<sup>•</sup>, O<sub>2</sub><sup>-•</sup> and chelated iron species are responsible. [210], [212], [213] Both OH<sup>•</sup> and O<sub>2</sub><sup>-•</sup> have been implicated at neutral pH (7.2). Under acidic conditions, there are reports of ferryl ion (FeO<sup>2+</sup>) as the primary oxidant. [214] The active oxidant may also be related to the metal-binding affinity of the target; OH<sup>•</sup> damage generated by Fenton chemistry in biological systems is ‘site-specific’, in that it is localized at or near metal-binding sites of macromolecules. [208], [215] It is thus interesting that histidine (which has a strong affinity for metal ions [216]) appeared to increase oxidative damage to indigo carmine when it was included as a OH<sup>•</sup> scavenger in Fenton chemistry experiments (see Figure 3.18). Other species may also participate in Fenton chemistry, including the spin trap DMPO. [213]

For the purpose of these studies, H<sub>2</sub>O<sub>2</sub> and FeSO<sub>4</sub> were combined at a ratio between 5:1 and 10:1. The optimum pH for maximum OH<sup>•</sup> production through equations 3.30 and 3.31 was reported to be 2.8-3.0 [211]; thus, phosphate buffers were used to maintain the pH at 3 during these experiments.

### 3.3.6 Competition Experiments with Radical Scavengers

Another way to elucidate the active species from a set of possible oxidants is through the use of “scavenger” or competitor molecules to scavenge particular species of interest, or otherwise alter the reaction kinetics in an observable way. This strategy was also pursued for further evidence of the species responsible for indigo carmine oxidation (and the modification of other targets) in plasma-treated solutions. Several species

used as scavengers in the literature (particularly with biochemical relevance) were selected: ascorbic acid, histidine, mannitol, and  $\text{NaN}_3$ . In addition to being a potent antioxidant, ascorbate is present in cellular systems at relatively high concentrations [217]. The chemical structures of these species are shown in Figure 3.14. The rates of reaction for both target molecules and selected scavenger species with plasma-generated RONS are shown in Table 3.8.

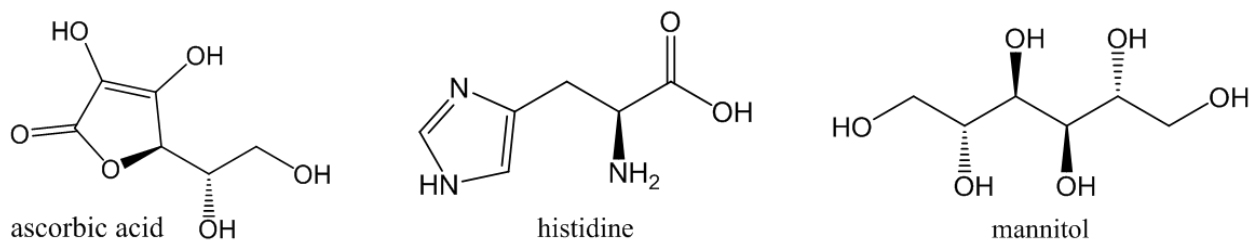


*Figure 3.14. Chemical structures of “scavengers” of oxidizing species used in competition experiments: ascorbic acid, mannitol and histidine.*



Table 3.8. Rate constants for the reactions of target species (indigo carmine, cysteine and glutathione) and common hydroxyl radical ( $\text{OH}^\cdot$ ) scavengers (mannitol, histidine, ascorbic acid, and sodium azide) with  $\text{OH}^\cdot$  and other oxidizing species. It is important to note that  $\text{OH}^\cdot$  reacts rapidly with both targets and scavengers, such that experiments with both present are essentially competition experiments. The pH at which the rate constant was determined is noted when available. The reaction of indigo carmine with  $\text{H}_2\text{O}_2$  is reported to be negligible based on our own control experiments.

Target Species or Scavenger	Rate constant ( $\text{M}^{-1} \text{s}^{-1}$ ) for reaction with:						
	$\text{OH}^\cdot$	$\text{O}=\text{NOOH}$	$\text{O}=\text{NOO}^\cdot$	$\text{O}_3$	$^1\Delta\text{O}_2$	$\text{O}_2^\cdot$	$\text{H}_2\text{O}_2$
Indigo carmine	$1.8 \cdot 10^{10}$			$> 10^7$ [198]			negligible
Cysteine (Cys)	$1.8 \cdot 10^{10}$ [218]		5900 [219]	$1.6 \times 10^9$ [220]	$8.9 \times 10^6$ (pH 7) [221]		2.9 [222]
Glutathione (GSH)	$\sim 10^{10}$ [222]	$1.35 \times 10^3$ [223]	700 [222]	$7 \times 10^8$ [220]	$2.9 \times 10^6$ (pH 7) [221]	$10^{-2} - 10^{-3}$ [224]	15 [225]
D-Mannitol	$1.8\text{-}2.7 \cdot 10^9$ (pH 7) [40], [226]				$< 10^3$ [40]		
L-Histidine	$5 \cdot 10^9$ (pH 6-7) [40]			$1.9 \times 10^5$ [220]; $3.9 \times 10^3$ (pH 7) [40]		$3.2 \times 10^7$ [40]	
Ascorbic acid	$1.1 \cdot 10^{10}$ (pH 1.5) [40]	$1 \times 10^6$ (pH 5.8) [40]; $\sim 10^2$ (pH 7.4) [223]		$6 \times 10^7$ [220]	$8.3 \times 10^6$ [227]	$2.7 \times 10^5$ [228]	
Sodium azide ( $\text{NaN}_3$ )	$1.1 \times 10^{10}$ (pH 9) [40]				$2.2 \times 10^8 - 10^9$ [40], [228]		

As a first study, the rate of indigo carmine oxidation by O=NOOH (produced from the reaction of H<sub>2</sub>O<sub>2</sub> and NO<sub>2</sub><sup>-</sup> at low pH, as described in Section 3.2.3) was determined in the presence or absence of the OH<sup>•</sup> scavengers ascorbic acid, histidine, and mannitol. Scavengers were added at a concentration of 5 mM, 50 times greater than the initial concentration of indigo carmine (90 μM). At time = 0, H<sub>2</sub>O<sub>2</sub> and NaNO<sub>2</sub> were added to a pre-loaded cuvette to initial concentrations of 1mM each, sufficient to almost completely oxidize 100 μM indigo carmine in 15 minutes at pH 3 in the absence of scavengers. The oxidation of indigo carmine was monitored spectrophotometrically at 1 minute intervals, based on the reduction in absorbance at 608nm. The resulting decrease in the concentration of indigo carmine with time is shown in Figure 3.15.

As shown in Figure 3.15, indigo carmine (initially present at 90 μM) was almost completely oxidized within 15 minutes of H<sub>2</sub>O<sub>2</sub> and NO<sub>2</sub><sup>-</sup> addition at pH 3. The presence of ascorbic acid in excess completely eliminated indigo carmine oxidation under these conditions. In tests where histidine was used as a scavenger, the rate of indigo carmine oxidation was slowed significantly (~50% degraded in 15 minutes). This trend is consistent with the higher rate constant for the reaction of ascorbic acid with OH<sup>•</sup> relative to histidine (see Table 3.8). However, tests with mannitol consistently resulted in *more rapid* oxidation of indigo carmine. Work by Alvarez et al. discusses possible stabilization of peroxyxynitrite and peroxyxynitrous acid by hydrogen bonding to mannitol or ethanol [229]; one possible explanation for our result is that, in stabilizing peroxyxynitrous acid, mannitol promotes the rearrangement of O=NOOH to OH<sup>•</sup> and NO<sub>2</sub><sup>•</sup> (rather than H<sup>+</sup> and NO<sub>3</sub><sup>-</sup>). Oxygen consumption was observed during reaction with peroxyxynitrite, suggesting an alternate explanation in that mannitol may be partially oxidized by O=NOO<sup>•</sup>/O=NOOH to form a radical species which could participate in subsequent reactions with indigo carmine. Studies of the effects of peroxyxynitrite on DNA strand breaks also reported that mannitol failed to prevent DNA oxidation, and two more efficient OH<sup>•</sup> scavengers (DMSO and benzoate) increased oxidation; only Trolox was effective, which also scavenges a reactive form of O=NOOH. [230] Thus, the results of the experiments with mannitol suggest that indigo oxidation resulting from H<sub>2</sub>O<sub>2</sub> and NO<sub>2</sub><sup>-</sup> in solution may occur through reaction with a reactive form or intermediate of O=NOOH, rather than solely OH<sup>•</sup> produced through O=NOOH decomposition.

Indeed, there is a significant body of literature related to the question of whether peroxyxynitrite-mediated oxidation is due to OH<sup>•</sup> or reactive intermediates. Radi et al. report that histidine does not react directly with peroxyxynitrite (although the amino acids cysteine, methionine and tryptophan do). [223] Elsewhere, free L-histidine exposed to peroxyxynitrite was reported to produce radicals similar to those observed from the incubation of histidine with Fenton reagent assigned, based on <sup>13</sup>C labeling, to the histidinyl radical [231], suggesting scavenging of OH<sup>•</sup>. The effects of ascorbic acid are also consistent with oxidation due to OH<sup>•</sup> since ascorbic acid reacts with OH<sup>•</sup> at a significantly faster rate than with O=NOOH (Table 3.8) and resulted in the greatest protection of indigo carmine.

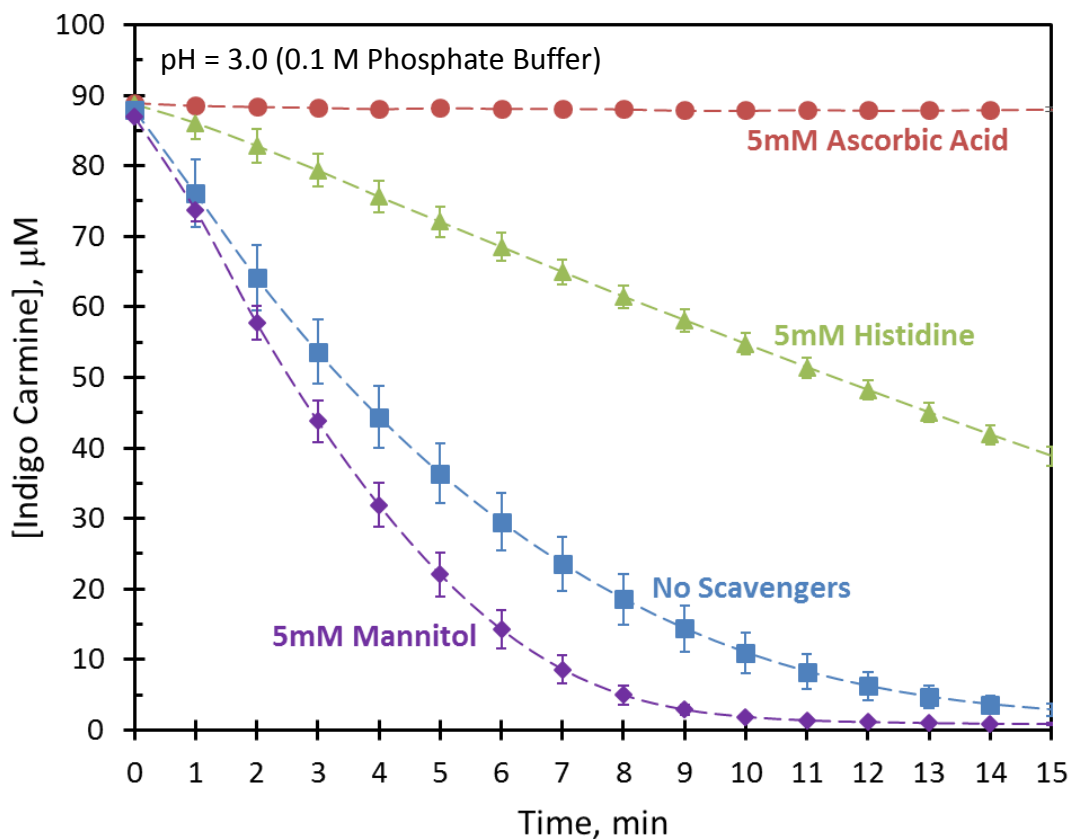


Figure 3.15. Oxidation of indigo carmine in acidic solution with  $O=NOOH$  precursors, with and without  $OH^\bullet$  scavengers. Solutions consisted of 0.1M phosphate buffer (pH 3.0), 100 $\mu$ M indigo carmine, 5mM scavenger (mannitol, histidine, or ascorbic acid) if present, 1mM  $NaNO_2$ , and 1mM  $H_2O_2$  combined in that order.  $H_2O_2$  and  $NaNO_2$  were added simultaneously at time = 0. Ascorbic acid ( $\bullet$ ) completely protected indigo carmine from oxidation, while histidine ( $\blacktriangle$ ) slowed the rate of oxidation. The oxidation of indigo carmine in the absence of scavengers is shown by the blue squares ( $\blacksquare$ ). Unexpectedly, the presence of 5mM mannitol ( $\blacklozenge$ ) appeared to accelerate indigo carmine oxidation. The reason for this is currently unknown, but may be the result of interactions between mannitol and  $O=NOOH$  which promote decomposition through the mechanism producing  $OH^\bullet$ .

At higher initial concentrations of indigo carmine (5mM indigo carmine vs 0.1mM), equivalent to the concentration of scavenger added, similar trends were observed as shown in Figure 3.16. Under these conditions, ascorbic acid and histidine both prevented any significant (observable) levels of indigo carmine oxidation. This indicates that similar quantities of indigo carmine ( $< 0.1\text{mM}$ ) were oxidized in the presence of histidine regardless of significant differences in the concentration of indigo carmine; a loss of  $50\ \mu\text{M}$  (as observed in Figure 3.15) would not have been detectable in the study shown in Figure 3.16.

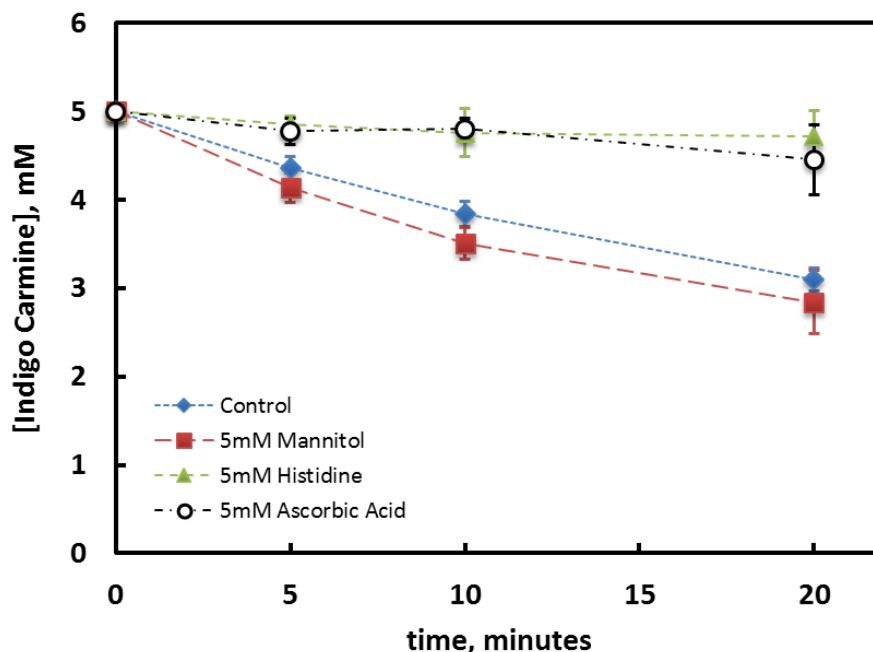


Figure 3.16. Oxidation of indigo carmine by  $O=\text{NOOH}$  chemistry in the presence of scavengers at equivalent initial concentrations (5mM). Both histidine and ascorbic acid prevented significant oxidation of indigo carmine, whereas the presence of mannitol resulted in slightly increased degradation.

Control studies of the rate of indigo carmine loss in the presence of only  $\text{H}_2\text{O}_2$ , and  $\text{NO}_2^-$  show only minimal loss of indigo carmine in the presence of these plasma-generated species, with the presence of  $\text{NO}_2^-$  having the greatest effect (likely due to the production of radical species through its conversion to  $\text{NO}_3^-$  at pH 3). Control experiments with mannitol were also performed to rule out reactions of this species directly with indigo carmine, or with  $\text{H}_2\text{O}_2$  or  $\text{NO}_2^-$  to produce oxidizing by-products. The results of these experiments are shown in Figure 3.17.

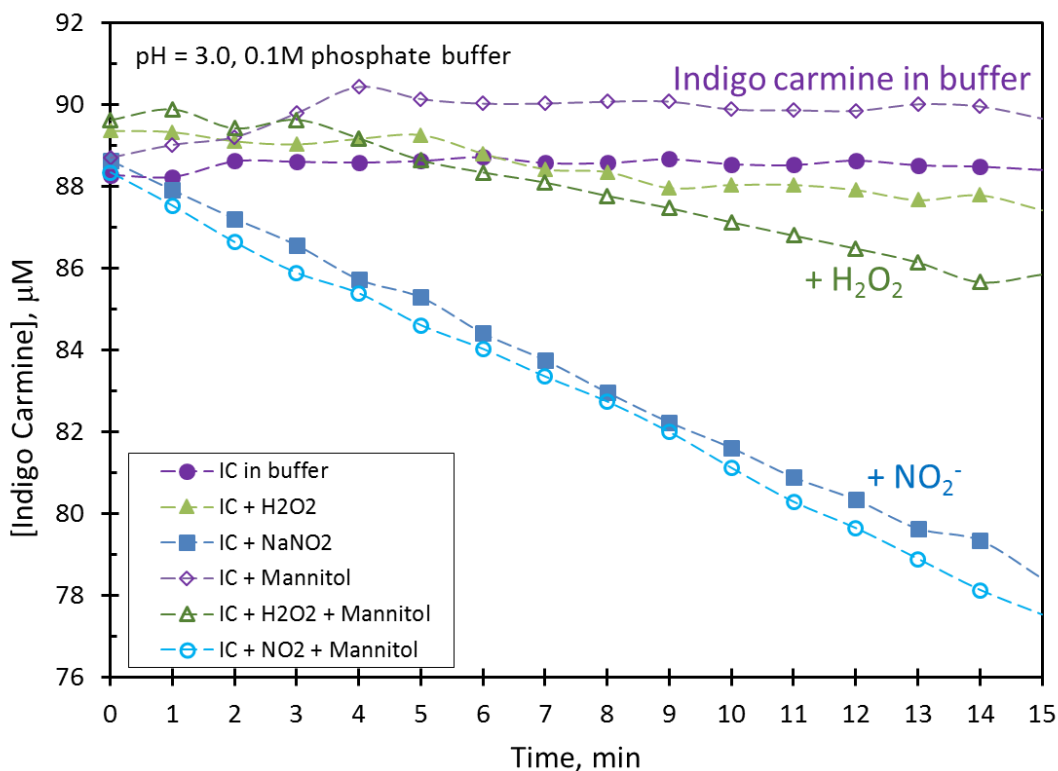


Figure 3.17. Effects of H<sub>2</sub>O<sub>2</sub>, NO<sub>2</sub><sup>-</sup> and mannitol on the degradation of indigo carmine in aqueous solution at pH 3 (control studies). Closed markers indicate no mannitol; open markers indicate that 5mM mannitol was present in solution; mannitol did not have a significant effect on indigo carmine loss. H<sub>2</sub>O<sub>2</sub> alone (1 mM) produced only slight oxidation of indigo carmine over the 15 minute observation period.

The results of positive control experiments in which OH<sup>•</sup> produced through Fenton chemistry (i.e. the reaction of H<sub>2</sub>O<sub>2</sub> and FeSO<sub>4</sub>), was used to oxidize indigo carmine in the presence and absence of scavengers (sodium azide NaN<sub>3</sub>, ascorbic acid, mannitol and histidine) are shown in Figure 3.18. Both NaN<sub>3</sub> and ascorbic acid were highly effective in scavenging the oxidizing species produced. Mannitol again resulted in an increase in the rate and total degradation of indigo carmine observed relative to the control (Fenton chemistry without scavenger) experiments. However, the presence of histidine resulted in an even more dramatic increase in indigo carmine oxidation, leading to effectively complete degradation of the dye. This may be related to histidine's affinity for metals.

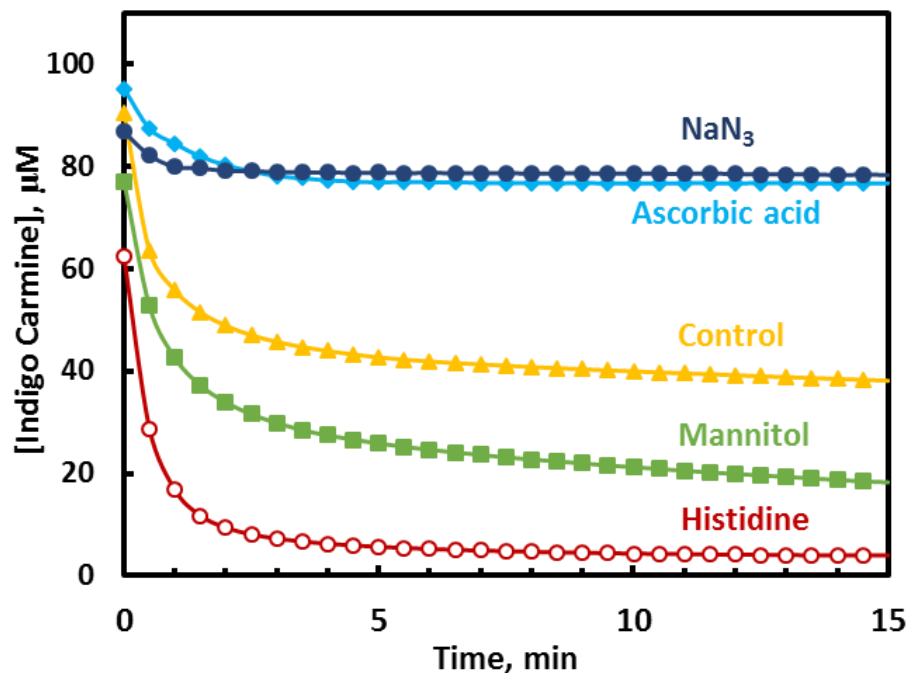


Figure 3.18. Oxidation of indigo carmine by Fenton reagents ( $1\text{mM H}_2\text{O}_2 + 0.2\text{mM FeSO}_4$ ) as a function of time. Solutions initially contained  $0.1\text{ mM}$  indigo carmine,  $100\text{mM}$  phosphate buffer ( $\text{pH } 3$ ), and  $5\text{mM}$  scavenger if present, either sodium azide,  $\text{NaN}_3$  ( $\bullet$ ), ascorbic acid ( $\blacklozenge$ ), mannitol ( $\blacksquare$ ), or histidine ( $\circ$ ). The control sample ( $\blacktriangle$ ) contained only indigo carmine and Fenton reagents.

The effects of the presence of each scavenger on indigo carmine decomposition during plasma treatment are shown in Figure 3.19. Solutions were exposed to a transient spark discharge for 5 minutes, at which point the loss of indigo carmine was determined. In these experiments, the concentration of scavenger was only 5x the initial concentration of indigo carmine ( $1\text{ mM}$ ). Mannitol and histidine did not increase indigo carmine oxidation, as was observed in the positive control experiment with Fenton chemistry; however, they were not effective in preventing oxidizing species from reacting with indigo carmine. It should be noted that the rate constants of these species with  $\text{OH}^\bullet$  are slightly lower than that of indigo carmine with  $\text{OH}^\bullet$  ( $\sim 10^9$  vs  $\sim 10^{10}\text{ M}^{-1}\text{ s}^{-1}$ ), but all are potentially diffusion limited; if both indigo carmine and scavenger are present at similar concentrations,  $\text{OH}^\bullet$  will react with whichever it encounters first. Thus it is not surprising that oxidation of indigo carmine occurs under these conditions. Ascorbic acid was the most effective in protecting indigo carmine, although it was only effective in preventing  $\sim 60\%$  of the loss of indigo carmine. The ability of  $\text{NaN}_3$  to scavenge  $\text{OH}^\bullet$  and other species may have been reduced due to its reaction with  $\text{NO}_2^-$  as it was taken up by the solution.

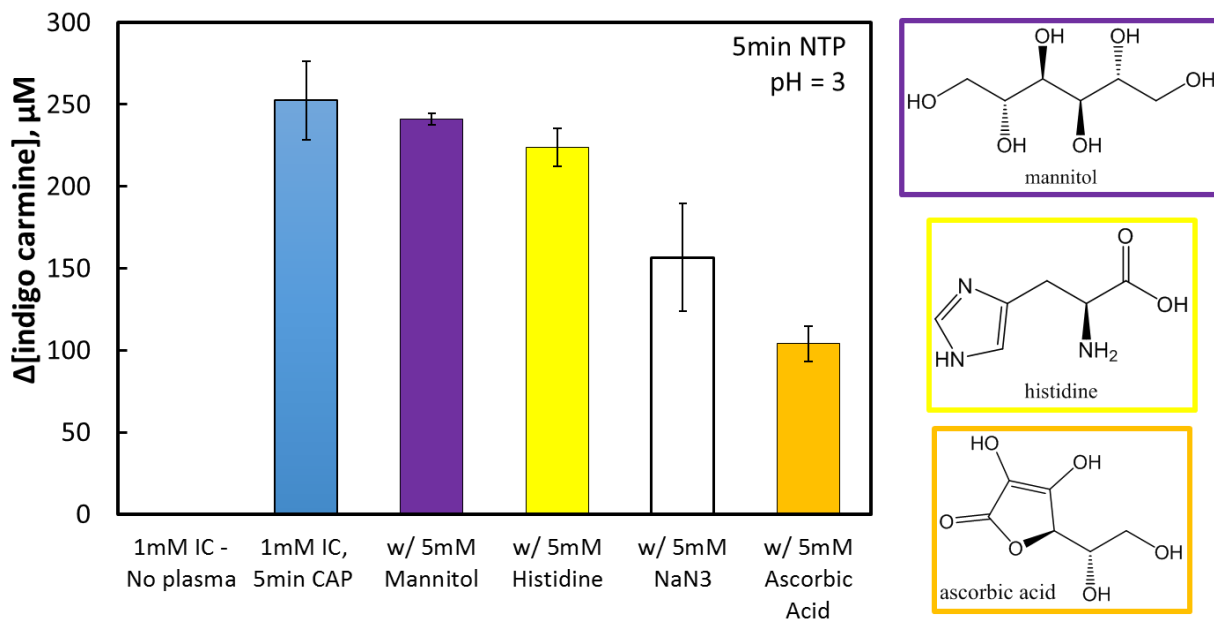


Figure 3.19. Effect of  $\text{OH}^\bullet$  scavengers on indigo decomposition due to non-thermal plasma exposure. Solutions initially containing 1mM indigo carmine and 5 mM of the indicated scavenger in pH 3 buffer (0.1 M phosphate buffer) were exposed to a transient spark discharge for 5 minutes, at which point the loss of indigo carmine was determined. Ascorbic acid was the most effective in protecting indigo carmine, whereas mannitol and histidine had relatively little effect. The ability of  $\text{NaN}_3$  to scavenge  $\text{OH}^\bullet$  and other species may have been compromised by its reaction with  $\text{NO}_2^-$  formed in solution.

These scavenger and positive control experiments demonstrate the complexity of interactions in even simple mixtures of reactive oxygen species and organics. Care should be taken when interpreting experiments using these scavengers, as clearly additional reactions occur beyond the simple reactions with  $\text{OH}^\bullet$  shown in Table 3.8.

### 3.4 Conclusions

The 'cocktail' of species formed in the plasma by the transient spark discharge and other non-thermal air plasmas is highly complex, although some progress has been made in determining the relative concentrations of certain species through laser induced fluorescence (LIF), infrared spectroscopy (FTIR) and optical emission spectroscopy (OES). For example, the density of hydroxyl radicals near the liquid cathode is typically measured to be on the order of  $10^{14} - 10^{15} \text{ cm}^{-3}$ .

A 2-dimensional model of the flow of neutral species through this system demonstrates that liquid convection induced by the plasma jet impacting the liquid (water) surface is important in facilitating the uptake of hydrophobic species by the liquid. The rate at which hydrophilic species are solvated is relatively insensitive to changes in convection, though the spatial distribution of these species in the liquid phase changes considerably in the presence of convection.

Unbuffered solutions exposed to a transient spark discharge (and other air plasmas) are quickly acidified due to the uptake and generation of  $\text{HNO}_3$  in solution, which is also responsible for the observed changes in solution conductivity. While the flux of  $\text{H}_2\text{O}_2$  and  $\text{NO}_2^-$  into the liquid is roughly constant (a zero-order process), acid-catalyzed reactions result in significant consumption of these species at low pH ( $< 3.4$ ). Buffering the target solution at neutral pH (e.g. 7.4) eliminates most of these reactions, and  $\text{H}_2\text{O}_2$  and  $\text{NO}_2^-$  concentrations increase linearly with plasma-treatment time. The measurement of these species is easily accomplished with colorimetric techniques, provided that the possibility for competing reactions is considered and eliminated.

Indigo carmine was used as an indicator to follow the evolution of highly reactive species in solution, such as the hydroxyl radical. This method was preferable to EPR in this system due to interference from  $\text{O}=\text{NOOH}$  and other complications arising from the use of spin-traps. Non-plasma methods to produce  $\text{OH}^\bullet$ , specifically Fenton chemistry and the formation of  $\text{OH}^\bullet$  through the  $\text{O}=\text{NOOH}$  pathway, were investigated as positive controls; however, results of scavenger experiments with these chemistries illustrated some of the pitfalls of this approach. For example, both histidine and mannitol *increased* indigo carmine degradation in solutions with Fenton reagents. Also, mannitol increased indigo carmine degradation in acidic solutions containing  $\text{H}_2\text{O}_2$  and nitrite ( $\text{O}=\text{NOOH}$  chemistry). These results are counter-intuitive. Understanding the complex interplay between the species generated in plasma-treated solutions, particularly when small organic molecules are added, clearly requires a rigorous analysis of many possible reaction networks.



## 4 The Role of Reactions at the Plasma-Liquid Interface in Direct Plasma Treatment

In this chapter, we investigate the sources of highly oxidative species in solutions exposed to a self-pulsed corona discharge in air. Indigo carmine, a common organic dye, is used as an indicator of oxidative strength and in particular, hydroxyl radical ( $\text{OH}^\bullet$ ) production. It is shown that the observed rate of indigo oxidation in direct contact with the discharge far exceeds that predicted to result from reactions occurring in the bulk solution. This is consistent with a high concentration of highly oxidizing species such as  $\text{OH}^\bullet$  at the plasma-liquid interface, as suggested by the generation of  $\text{H}_2\text{O}_2$ . These results indicate that reactions at the air plasma-liquid interface play a dominant role in species oxidation during direct non-equilibrium atmospheric pressure plasma (NEAPP) treatment.

### 4.1 Motivation

The reactive species responsible for the effects of plasma treatment may be either produced directly by the plasma discharge, or may form from secondary reactions within the bulk liquid phase. Many previous studies of 'plasma-activated medium' have demonstrated the importance of secondary chemical reactions in producing active species with important phenomenological affects [69], [183], [232], [233]. However, one of the key features of direct discharges is the ability to produce highly reactive species at point-of-use that cannot be stored or applied later. Here, we consider the relative importance of these two sources in producing one potentially desirable oxidative species: the highly reactive hydroxyl radical  $\text{OH}^\bullet$ , which is known to form in plasmas with vapor or liquid water present, and in the bulk liquid phase solution through the reaction of plasma-generated species to  $\text{O}=\text{NOOH}$  and subsequently  $\text{OH}^\bullet$ . These two sources of  $\text{OH}^\bullet$  are highlighted in Figure 4.1, which shows the flow of the major species through the plasma-liquid system.

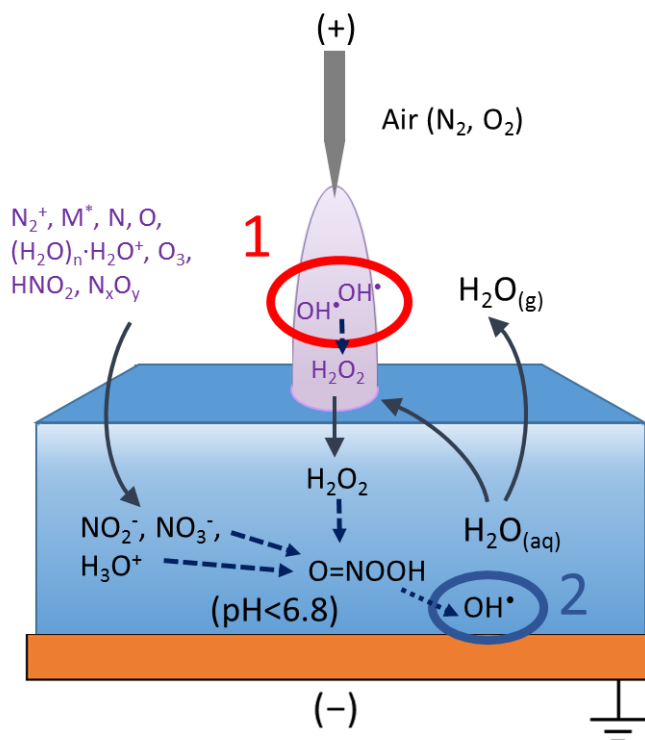


Figure 4.1. Schematic of two sources of  $\text{OH}^\bullet$  in plasma-treated solutions: 1)  $\text{OH}^\bullet$  produced through near-surface reactions, active only in a thin boundary layer near the plasma-liquid interface; 2)  $\text{OH}^\bullet$  produced through reactions in the bulk liquid; here, the pathway by which  $\text{H}_2\text{O}_2$  and  $\text{NO}_2^-$  react under acidic conditions to form  $\text{O}=\text{NOOH}$ , which produces  $\text{OH}^\bullet$  as one of its degradation products is shown.

In the sections that follow, we examine the production of hydroxyl radicals and the oxidation of a model organic species, indigo carmine, first in the bulk liquid phase, and then from near-surface reactions between plasma-generated species and the liquid phase.

## 4.2 Plasma Exposure Conditions

We are specifically interested in the direct effects of the plasma in contact with a liquid phase; thus a set of operating conditions were chosen such that high production of  $\text{OH}^\bullet$  was expected. Hydrogen peroxide production in the solution is expected to be related to the relative  $\text{OH}^\bullet$  density near the plasma-liquid interface as discussed in Section 3.2.1 [149]; thus, this metric was used as a rough indicator of oxidizing strength. The plasma exposure experiments reported in this section used a transient spark discharge; the voltage applied to the system was 9kV, the inter-electrode distance ( $d_i$ ) was 5mm, and the ballast resistance was 10M $\Omega$ . In all experiments, a pH buffer was added at sufficient concentration to maintain a constant pH in solution over the entire treatment period.

## 4.3 Generation of $\text{OH}^\bullet$ through Reactions in the Bulk Liquid

The main pathway reported for the formation of highly reactive species in plasma-activated water (PAW) solutions under acidic conditions is the reaction of  $\text{H}_2\text{O}_2$  and  $\text{NO}_2^-$  to form peroxyntrous acid,  $\text{O}=\text{NOOH}$ . [172] The decomposition of  $\text{O}=\text{NOOH}$  below its  $\text{pK}_a$  (6.8) is known to produce  $\text{OH}^\bullet$  and  $\text{NO}_2^\bullet$ , with roughly 30% of  $\text{O}=\text{NOOH}$  decomposing through this pathway.

The contribution of  $\text{OH}^\bullet$  from the bulk solution chemistry can be predicted if the concentrations of precursor species,  $\text{H}_2\text{O}_2$  and  $\text{NO}_2^-$ , the pH, and the kinetic rate constants and ratios for these reactions are known. The rates of  $\text{H}_2\text{O}_2$ ,  $\text{NO}_2^-$  and  $\text{NO}_3^-$  generation and concentrations of these species with plasma treatment were reported in Chapter 3. The kinetic rate constants for these species have been reported in the literature and are shown in Table 4.1.

Table 4.1. Rate constants for the formation of  $\text{OH}^\bullet$  through the peroxyntrous acid pathway

	Reaction	Rate constant, $k$ ( $T = 293\text{K}$ )	Reference
R1	$\text{NO}_2^- + \text{H}_2\text{O}_2 + \text{H}^+ \rightarrow \text{O}=\text{NOOH} + \text{H}_2\text{O}$	$1.1 \times 10^3 \text{ M}^{-2} \text{ s}^{-1}$	[172]
R2	$\text{O}=\text{NOOH} \rightarrow [\text{ONO}\cdot\text{OH}]$	$0.13 + 0.87 \cdot [\text{H}^+] \text{ s}^{-1}$	[234]
	(a) $[\text{ONO}\cdot\text{OH}] \rightarrow \text{NO}_2^\bullet + \text{OH}^\bullet$ ,	$b$	[234]
	(b) $[\text{ONO}\cdot\text{OH}] \rightarrow \text{NO}_3^- + \text{H}^+$	$(1 - b)$	[234]
R3	$\text{OH}^\bullet + \text{indigo carmine} \rightarrow \text{products}$	$1.8 \times 10^{10} \text{ M}^{-1} \text{ s}^{-1}$	[200]

Thus, the generation of  $\text{OH}^\bullet$  species at a constant pH (e.g. pH 3.5) can be modeled by solving the following ODEs:

$$d[\text{H}_2\text{O}_2]/dt = -r_1 = -k_1[\text{H}_2\text{O}_2][\text{NO}_2^-][\text{H}^+] \quad (4.1)$$

$$d[\text{NO}_2^-]/dt = -r_1 = -k_1[\text{H}_2\text{O}_2][\text{NO}_2^-][\text{H}^+] \quad (4.2)$$

$$d[\text{O}=\text{NOOH}]/dt = r_1 - r_2 = k_1[\text{H}_2\text{O}_2][\text{NO}_2^-][\text{H}^+] - (0.13 + 0.87[\text{H}^+]) \cdot [\text{O}=\text{NOOH}] \quad (4.3)$$

$$d[\text{OH}^\bullet]/dt = r_2 = (0.13 + 0.87[\text{H}^+]) \cdot [\text{O}=\text{NOOH}] \cdot b \quad (4.4)$$

The changes in concentration of these species ( $\text{H}_2\text{O}_2$ ,  $\text{NO}_2^-$ ,  $\text{O}=\text{NOOH}$ ,  $\text{OH}^\bullet$ ) predicted by this model are shown in Figure 4.2A (for a solution initially containing 1mM of  $\text{H}_2\text{O}_2$  and  $\text{NO}_2^-$  at pH 3.5). It should be noted that the quantity of  $\text{OH}^\bullet$  generated is highly dependent on the ratio of the two competing  $\text{O}=\text{NOOH}$  decomposition pathways,  $b$ . The cumulative generation of  $\text{OH}^\bullet$  from the same initial conditions at varying values of  $b$  (within the range reported in the literature) is shown in Figure 4.2B.

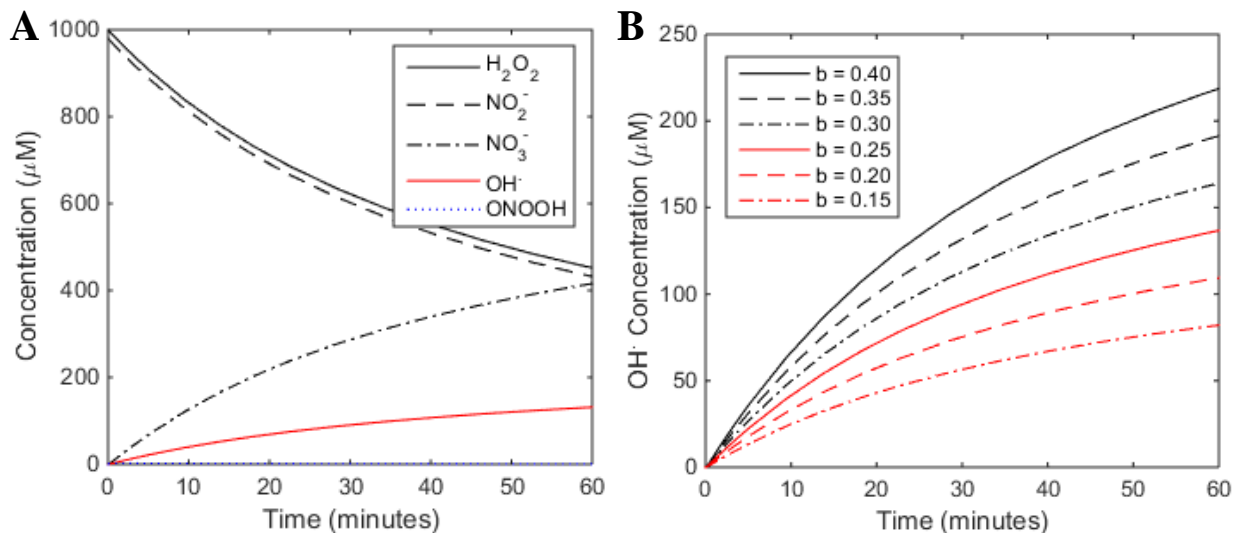


Figure 4.2. **A** Evolution of the species involved in the production of  $\text{OH}^\bullet$  through the  $\text{O}=\text{NOOH}$  pathway with time at  $\text{pH} = 3.5$ . The concentration of  $\text{OH}^\bullet$  represents the cumulative production of this radical, as subsequent reactions are not included. **B** Cumulative production of  $\text{OH}^\bullet$  in solution at different values of the branching ratio,  $b$ . Clearly twice as much  $\text{OH}^\bullet$  is predicted when  $b$  is increased from 0.2 to 0.4; both of which are reasonable values based on the literature.

The percentage of  $\text{O}=\text{NOOH}$  decomposing to  $\text{OH}^\bullet$  through reaction (2a) was determined experimentally by combining  $\text{H}_2\text{O}_2$ ,  $\text{NO}_2^-$  and nitric acid at known concentrations. We refer to these solutions as ‘artificial PAW.’ More specifically,  $\text{NO}_2^-$  and  $\text{NO}_3^-$  are added into buffered water at the final concentrations reported for a 20min plasma exposure at  $\text{pH} 3.5$ : 0.8 mM  $\text{NaNO}_2$  and 1.2 mM  $\text{HNO}_3$ . At time  $t = 0$ ,  $\text{H}_2\text{O}_2$  and indigo carmine are added and vigorously mixed in the volume, where the oxidation of indigo carmine is followed spectrophotometrically. Because no plasma is involved – and therefore no species beyond  $\text{H}_2\text{O}_2$ ,  $\text{NaNO}_2$  and  $\text{HNO}_3$  –  $\text{OH}^\bullet$  produced through  $\text{O}=\text{NOOH}$  degradation is the only oxidizing species present. Modeling the artificial PAW experiments as before confirmed the kinetics of this system and enabled the relation between  $\text{O}=\text{NOOH}$  production and indigo loss to be determined. In brief, this model of the decline in indigo carmine concentration assumed that:

- The solution is well mixed.
- $\text{H}_2\text{O}_2$  and  $\text{NO}_2^-$  react to produce  $\text{O}=\text{NOOH}$  per reaction (R1).
- $\text{O}=\text{NOOH}$  decomposes through a pathway described by reactions (R2) with some fraction,  $b$ , of the  $\text{O}=\text{NOOH}$  producing  $\text{OH}^\bullet$  through reaction (R2a). This parameter ( $b$ ) is determined by fitting the model to the experimental artificial PAW data.
- Each  $\text{OH}^\bullet$  that is produced reacts with a single molecule of indigo carmine.
- All indigo carmine degradation occurs due to reaction with  $\text{OH}^\bullet$ , per the kinetics shown in reaction R3, such that the following relation is valid:

$$d[\text{IC}]/dt = -d[\text{OH}]/dt = -r_2 = - (0.13 + 0.87[\text{H}^+]) \cdot [\text{O}=\text{NOOH}] \cdot b \quad (4.5)$$

At a controlled  $\text{pH}$  of 3.5, the degradation of indigo carmine in artificial PAW was in good agreement with our predictions based on the kinetic rate data reported in [172] with a rate constant for reaction (R1),  $k_1$ ,

equal to  $1.1 \times 10^3 \text{ M}^{-2} \text{ s}^{-1}$ . Minimizing the error between these data and the model predictions per the method of least squares returned a value of 0.24 for  $b$ , in good agreement with the range of branching coefficients reported in the literature for O=NOOH decomposition (~30%) [171]. Note that here,  $b$  represents not just the fraction of O=NOOH decomposing to OH $\cdot$ , but the fraction decomposing through reaction 2a then reacting with indigo carmine.

We next observed the degradation of indigo carmine upon addition to *actual* plasma-activated water (PAW) solution (buffered to pH 3.5). In these experiments, indigo carmine is added to the plasma-activated solution immediately after NEAPP treatment, and its degradation is again monitored spectroscopically. The observed oxidation of indigo carmine in the ‘artificial PAW’ experiments was compared to that predicted by our model. The resulting decay curve of indigo carmine added to pH 3.5-buffered PAW solutions (treated for 20 min) is similar to the artificial PAW experiments, as shown in Figure 4.3A.

This same set of experiments was performed in solutions buffered to neutral pH (pH = 7.4). Under these conditions, no OH $\cdot$  should be produced through the O=NOOH pathway and therefore no degradation of indigo carmine should be observed. Artificial PAW with concentrations of H<sub>2</sub>O<sub>2</sub>, NO<sub>2</sub><sup>-</sup> and nitric acid identical to those measured following 20min of NEAPP treatment at pH 7.4 produced no significant oxidation of indigo carmine, consistent with the predictions of our model of OH $\cdot$  formation through the O=NOOH pathway at this pH. This confirmed that the O=NOOH pathway to form OH $\cdot$  is not active at a pH of 7.4. When indigo carmine was added to PAW buffered to pH 7.4 immediately after NEAPP treatment, the observed rate of indigo carmine oxidation was similarly low. These data and the model prediction at pH 7.4 are shown in Figure 4.3B.

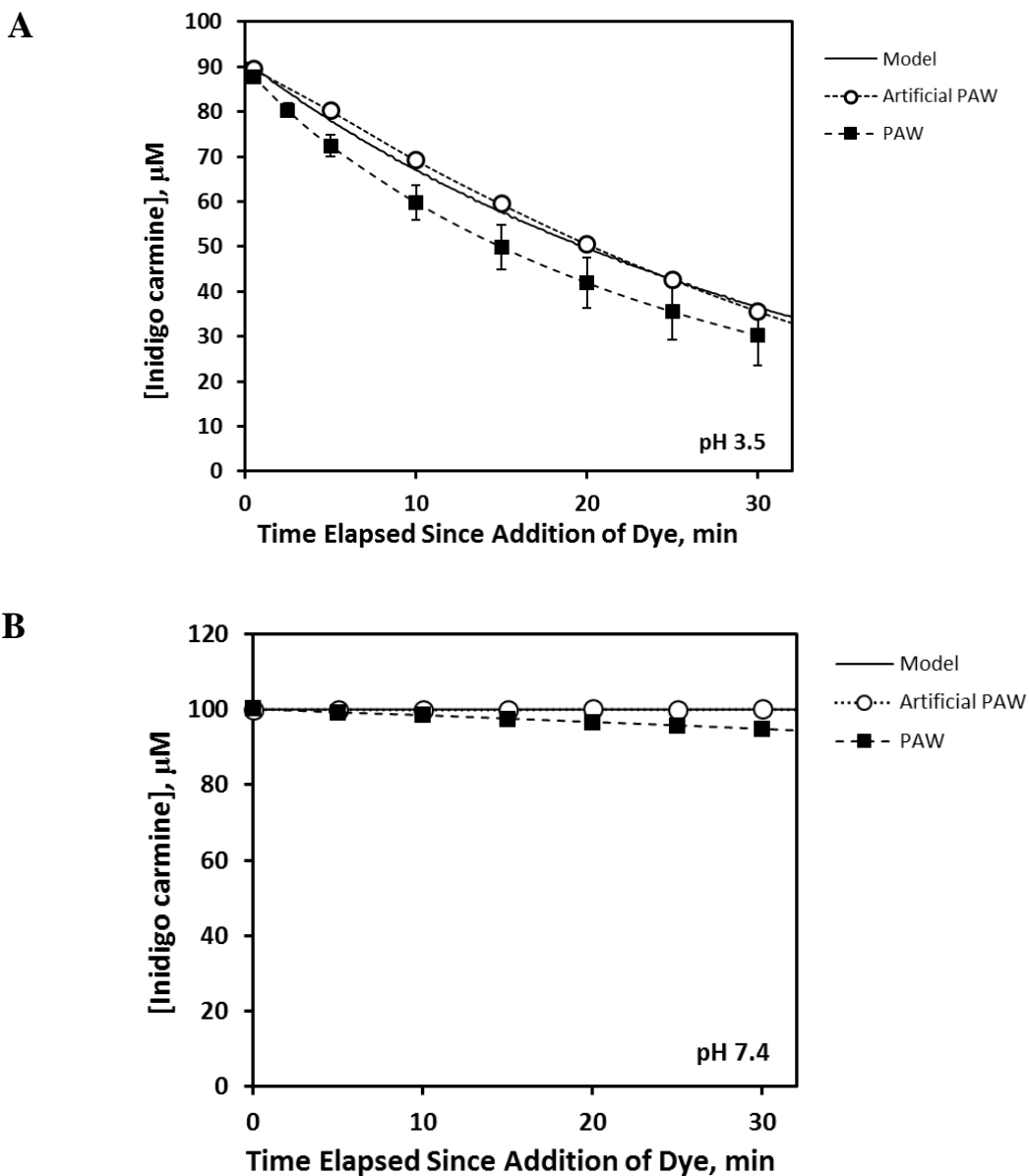


Figure 4.3. Degradation of indigo carmine in plasma-activated water, PAW (■), artificial PAW (○), or predicted by the model (—) described in Online Resource 1 at **A** pH3.5 and **B** pH 7.4. Solutions shown in **A** initially contained 800  $\mu\text{M}$   $\text{H}_2\text{O}_2$  and 800  $\mu\text{M}$   $\text{NO}_2^-$ ; solutions in **B** contained 1mM  $\text{H}_2\text{O}_2$  and 2mM  $\text{NO}_2^-$ , as measured in samples treated with NEAPP for 20min.

The results of the PAW and artificial PAW experiments at pH 3.5 and pH 7.4 demonstrate that the subsequent reaction of plasma-generated  $\text{H}_2\text{O}_2$  and  $\text{NO}_2^-$  to form  $\text{O}=\text{NOOH}$ , and its subsequent decomposition are sufficient to explain the activity of acidic PAW. This set of results also implies that  $\text{OH}^\bullet$  produced through  $\text{O}=\text{NOOH}$  decomposition is in fact the primary oxidizing agent in these plasma-activated water solutions in the absence of active plasma. If significant concentrations of dissolved  $\text{O}_3$  were present at the end of NEAPP treatment, for example, the  $\text{O}_3$  or  $\text{O}_2^{\bullet-}$  would react with indigo carmine almost instantly ( $k_{\text{O}_3} > 10^7 \text{ M}^{-1} \text{ s}^{-1}$ , [198], [202]), rather than over the course of several minutes as shown in Figure 4.3. The

pH dependence of the observed oxidation is also consistent with the O=NOOH pathway to produce OH<sup>•</sup>. Although some loss of indigo carmine was observed over time when indigo carmine was immediately added to pH 7.4 PAW solutions, the limited extent of indigo carmine oxidation (< 6 μM over 30 minutes) indicates that PAW solutions do not contain significant concentrations of other long-lived, non-acid catalyzed oxidizing species. Finally, these results show that the model developed for artificial PAW can be applied to assess the contribution from bulk solution chemistry in plasma-treated solutions.

#### 4.4 Generation of OH<sup>•</sup> through Reactions at the Plasma-liquid Interface

The contribution of plasma-generated OH<sup>•</sup> near the surface to the overall oxidation was estimated from experimental data. At a pH of 7.4, the O=NOOH pathway and any other reactions arising from stable RONS in the bulk solution (specifically H<sub>2</sub>O<sub>2</sub>, NO<sub>2</sub><sup>-</sup>, and NO<sub>3</sub><sup>-</sup>) do not significantly oxidize indigo carmine, as was shown in Section 4.3. Thus, the degradation of indigo carmine during NEAPP treatment at neutral pH is attributed to reaction with OH<sup>•</sup> or other highly reactive species at or near the plasma-liquid interface. These species are not expected to diffuse beyond several microns; these effects are therefore described as “near surface” reactions.

As discussed in Chapter 3, gas-phase plasma chemistry above liquids is highly complex, involving multitudes of potential species and reactions. [165] The OH<sup>•</sup> responsible for reacting to form H<sub>2</sub>O<sub>2</sub> and oxidize targets in solution may be generated from a combination of mechanisms; some of the mechanisms by which OH<sup>•</sup> is produced in the gas-phase and at the liquid surface were summarized in Figure 3.2. As the average electron energy for corona discharges is on the order of 2–3 eV, both vibrational excitation (reaction 4.6, < 1eV) and dissociative attachment (4.7, 1.5 – 4eV) reactions likely contribute to the formation of OH<sup>•</sup> in the gas phase. [46]



The rate of indigo carmine oxidation that is attributed to reaction with OH<sup>•</sup> or other oxidizing species arriving or formed at the plasma-liquid interface (“near surface”) was determined from the observed rate of indigo carmine oxidation from the initial loss during NEAPP treatment at pH = 7.4. The first time point at 2.5 minutes was used as an initial estimate since the concentration of indigo carmine in the bulk solution is not significantly depleted at this point. The initial rate of indigo loss during NEAPP treatment is thus estimated to be approximately 6.2 μM/min (1.0 × 10<sup>-7</sup> M/s), in an initial volume of 5 mL.

$$d[\text{IC}]_{\text{initial}}/dt = -6.2 \mu\text{M}/\text{min} = 1.0 \times 10^{-7} \text{ M/s} \approx -k_3[\text{OH}^{\bullet}]_{\text{surf}}[\text{IC}]_{\text{initial}} \quad (4.8)$$

In equation 4.8, indigo carmine is abbreviated as “IC” and [OH<sup>•</sup>]<sub>surf</sub> describes the average concentration of OH over the volume in which it reacts with the dye. Over the timescale of these experiments, the rate of

hydroxyl radical consumption is expected to be roughly equal to its rate of generation, such that the system is at pseudo-steady state and the concentration of OH<sup>•</sup> near the surface is roughly constant:

$$d[\text{OH}^{\bullet}]_{\text{surf}}/dt \approx 0 \rightarrow [\text{OH}^{\bullet}]_{\text{surf}} \approx \text{constant} \quad (4.9)$$

The concentration of OH<sup>•</sup> can thus be lumped into the rate constant to estimate an effective rate constant,  $k_{\text{eff}}$ , with units of s<sup>-1</sup>. Knowing the initial concentration of indigo carmine, 100 μM (10<sup>-4</sup> M), we solve equation 4.10 to estimate  $k_{\text{eff}}$ .

$$\begin{aligned} d[\text{IC}]_{\text{initial}}/dt = -6.2 \mu\text{M}/\text{min} (1.0 \times 10^{-7} \text{ M/s}) &\approx -k_3[\text{OH}^{\bullet}]_{\text{surf}}[\text{IC}]_{\text{initial}} \\ &\approx -k_{\text{eff}}[\text{IC}]_{\text{initial}} \rightarrow k_{\text{eff}} \approx 1.0 \times 10^{-3} \text{ s}^{-1} \end{aligned} \quad (4.10)$$

Because this rate is calculated from the time point at 2.5 min and is not measured instantaneously, it does not take into account the dependence on indigo carmine concentration. Fitting this expression to the loss of indigo carmine during NEAPP treatment, we find  $k_{\text{eff}} = 1.2 \times 10^{-3} \text{ s}^{-1}$ . The plasma-induced degradation of indigo carmine due to surface reactions only (pH = 7.4) is thus written as:

$$d[\text{IC}]/dt = -k_{\text{eff}}[\text{IC}] \quad \text{where } k_{\text{eff}} = 1.2 \times 10^{-3} \text{ s}^{-1} \quad (4.11)$$

The oxidation of indigo carmine occurring due to plasma treatment at pH 7.4, and the model generated from this data (the result of solving equation 4.11) are shown in Figure 4.4. The amount of indigo carmine degraded under these conditions is significant, despite the demonstrated inactivity of the O=NOOH pathway under these conditions.



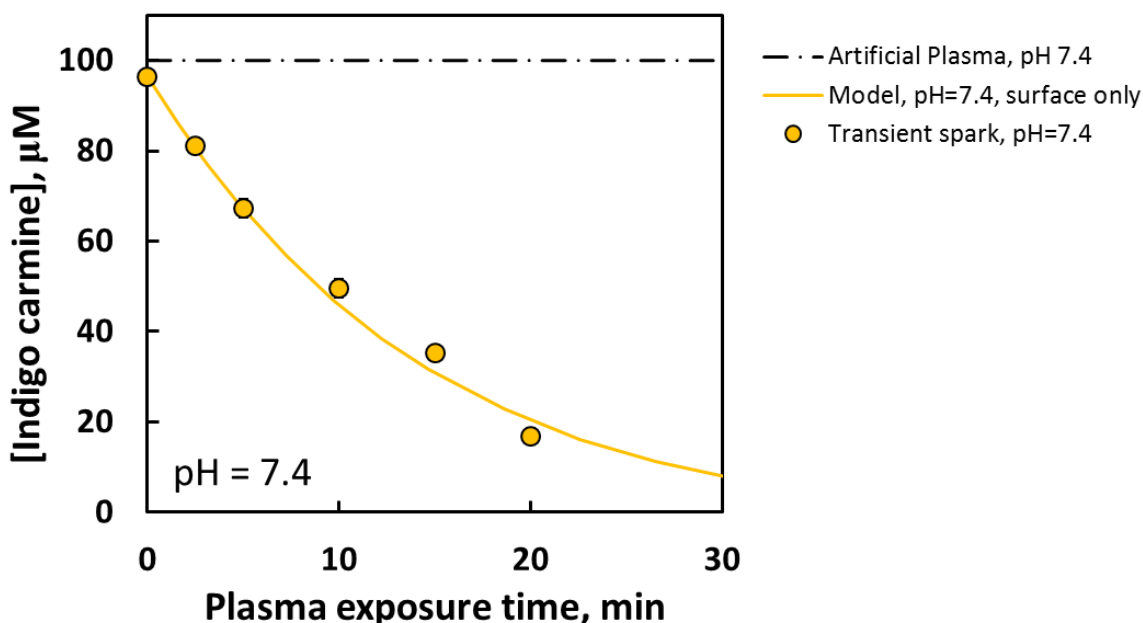


Figure 4.4. Degradation of indigo carmine due to exposure to transient spark discharge at pH 7.4: experimental results (●) and model fit (—). The observed loss of indigo carmine in solution with  $H_2O_2$  and  $NO_2^-$  is shown for reference (- · -). Note that the concentrations of  $H_2O_2$  and  $NO_2^-$  in the plasma system (“Transient spark”) and model increase with time, whereas the artificial plasma experiments begin from a set concentration.

#### 4.5 Comparison of Surface and Bulk Liquid Contributions to Species Oxidation

When pH = 3.5, indigo carmine is degraded by both direct interaction with plasma and through the O=NOOH pathway in the bulk solution. Unlike the rate of indigo decomposition due to bulk solution chemistry in PAW or artificial PAW, the rate of degradation in the bulk liquid during plasma treatment will change with time as the influx of  $H_2O_2$  and  $NO_2^-$  at the plasma-liquid surface must be considered. A model describing this condition therefore developed. The rates of plasma-mediated generation of  $H_2O_2$  and  $NO_2^-$  in solution were determined from the measured concentrations of these species at up to 5 minutes of plasma treatment as shown in Figure 3.7, and represent the net increase in bulk liquid concentration of these species in the absence of consumption reactions. At later time points, the rate of generation is convoluted by significant loss of these species through their reaction to form O=NOOH (Reaction R1).

$$r_{H_2O_2} = 1.0 \cdot 10^{-6} \text{ M/s} \quad (4.12)$$

$$r_{NO_2^-} = 1.6 \cdot 10^{-6} \text{ M/s} \quad (4.13)$$

The model of the evolution of  $H_2O_2$ ,  $NO_2^-$ , and O=NOOH in the bulk solution during plasma treatment was then modified to include these rates of generation. Similar to the artificial PAW analysis, the rate of indigo

carmine loss through the O=NOOH pathway occurring in the bulk solution is related to the rate of O=NOOH formation. Expression 4.17 is written for early time points, prior to significant indigo depletion.

$$d[\text{H}_2\text{O}_2]/dt = r_{\text{H}_2\text{O}_2} - k_1[\text{H}_2\text{O}_2][\text{NO}_2^-][\text{H}^+] \quad (4.14)$$

$$d[\text{NO}_2^-]/dt = r_{\text{NO}_2^-} - k_1[\text{H}_2\text{O}_2][\text{NO}_2^-][\text{H}^+] \quad (4.15)$$

$$d[\text{O}=\text{NOOH}]/dt = k_1[\text{H}_2\text{O}_2][\text{NO}_2^-][\text{H}^+] - (0.13 + 0.87[\text{H}^+]) \cdot [\text{O}=\text{NOOH}] \quad (4.16)$$

$$(d[\text{IC}]/dt)_{\text{bulk, initial}} = -k_3[\text{IC}]_{\text{initial}}[\text{OH}^*]_{\text{bulk}} = b \cdot (0.13 + 0.87[\text{H}^+]) \cdot [\text{O}=\text{NOOH}] \quad (4.17)$$

Because the initial concentration of indigo carmine is again known, this expression can be rearranged to write an expression for  $-k_3[\text{OH}^*]_{\text{bulk}}$  which follows from the concentration of O=NOOH assuming that all OH\* produced reacts according to Reaction R3.

$$-k_3[\text{OH}^*]_{\text{bulk}} = b \cdot (0.13 + 0.87[\text{H}^+]) \cdot [\text{O}=\text{NOOH}] / [\text{IC}]_{\text{initial}} \quad (4.18)$$

$$(d[\text{IC}]/dt)_{\text{bulk}} = -k_3[\text{IC}][\text{OH}^*] = b \cdot (0.13 + 0.87[\text{H}^+]) \cdot [\text{O}=\text{NOOH}] \cdot [\text{IC}]/[\text{IC}]_{\text{initial}} \quad (4.19)$$

Thus, the total loss of indigo carmine at pH = 3.5 from both surface and bulk liquid oxidation of indigo carmine is modeled as:

$$d[\text{IC}]/dt = -k_{\text{eff}}[\text{IC}] - b \cdot (0.13 + 0.87[\text{H}^+]) \cdot [\text{O}=\text{NOOH}] \cdot [\text{IC}]/[\text{IC}]_{\text{initial}} \quad (4.20)$$

The model of both near-surface and bulk solution degradation of indigo carmine at pH = 3.5, are compared to the loss of indigo carmine observed experimentally during transient spark treatment at pH 3.5 in Figure 4.5. The experimental and model results at pH 7.4 are also included for comparison.

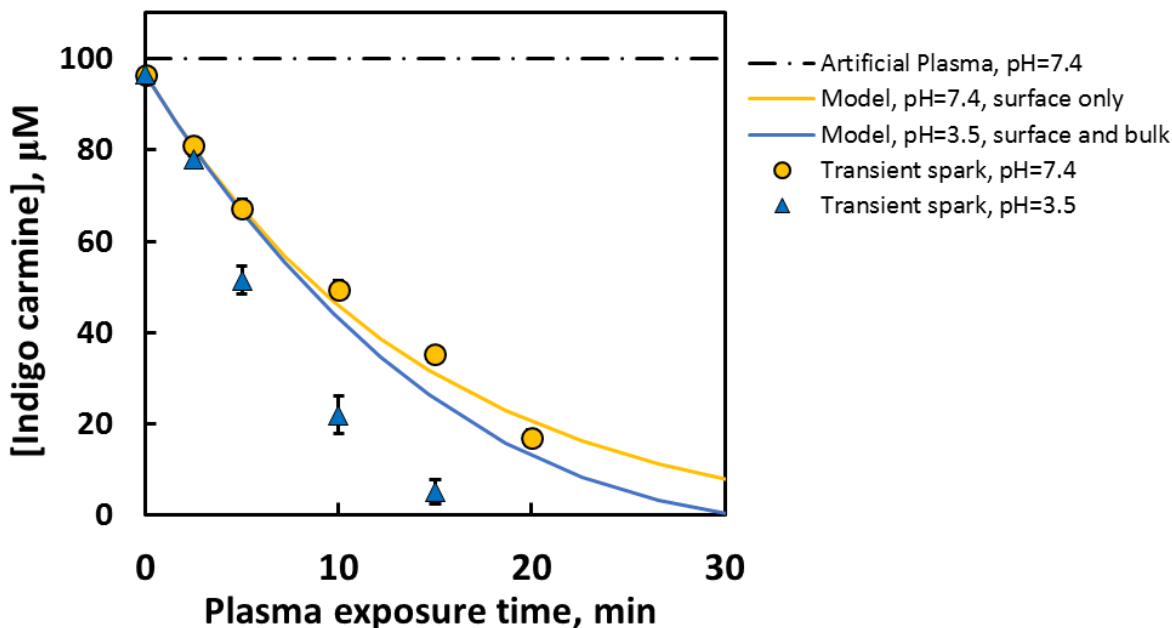
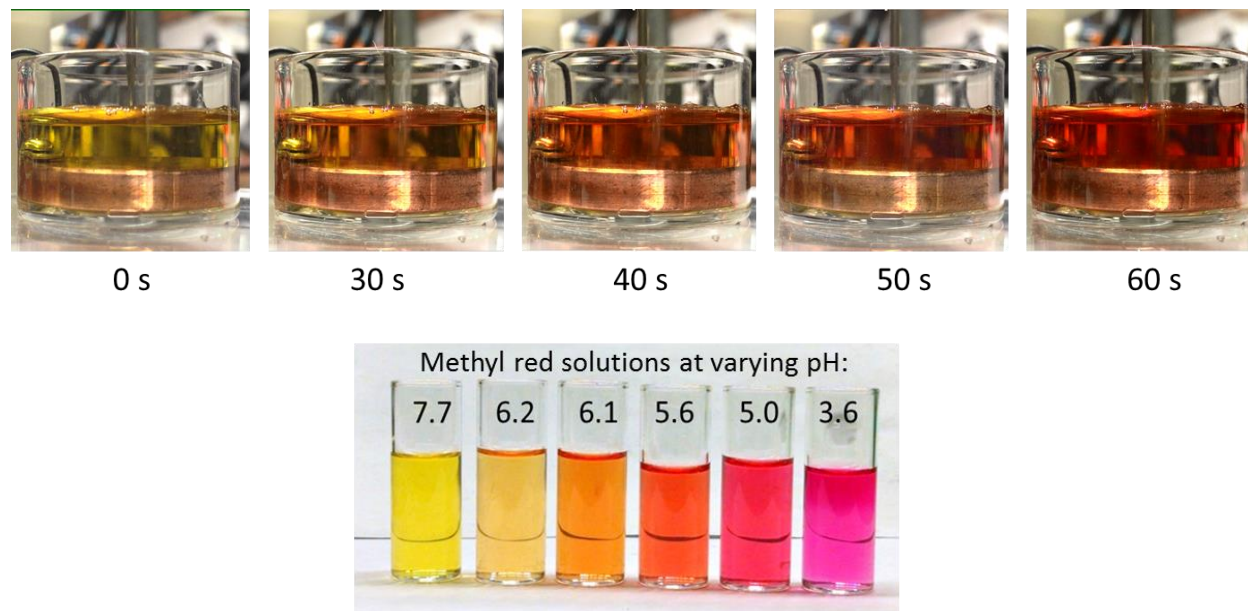


Figure 4.5. Modelled (—, —) and experimentally observed (●, ▲) degradation of indigo carmine at pH = 3.5 and 7.4. The pH 7.4 model was fit to the experimental data. The model at pH 3.5 includes both the pH 7.4 component capturing near-surface degradation and the predicted loss due to generation of  $H_2O_2$  and  $NO_2^-$  in the bulk solution. Clearly, additional indigo carmine is oxidized at pH 3.5 than can be accounted for through  $O=NOOH/OH^*$  produced in the bulk solution.

It is evident that the loss of indigo carmine exposed to plasma at a pH of 3.5 is significantly greater than that predicted by the model that includes both surface and bulk solution effects. This suggests an increase in the rate of reaction of indigo carmine at the surface when the solution is buffered to pH = 3.5 (with a buffer concentration of 10mM citrate/citric acid). The solution pH does not affect the properties of the transient spark discharge, as was discussed in Section 2.2.4. This effect must therefore arise from conditions in the liquid phase, such as increased concentrations of certain reactive oxygen and nitrogen species (RONS) and/or decreased pH (the buffer is locally overcome) very near the plasma-liquid interface, such that the rate of indigo carmine decomposition due to acid-catalyzed reactions in this region is increased beyond that observed when the pH near the surface is held at 7.4. Both series of data suggests that interactions at the plasma-liquid interface (rather than reactions in the bulk liquid) play a dominant role in plasma-liquid chemistry.

In an effort to test this first hypothesis, that the buffer is locally overcome near the plasma liquid interface, a pH sensitive dye (methyl red) was used to visualize pH gradients within the solution. Methyl red is an azo dye that transitions from yellow to red between pH 6.2 and pH 4.4. A solution initially buffered to pH 7.4 (with 0.1mM phosphate buffer) with methyl red was subjected to plasma treatment at  $t = 0$ . The resulting color change (shown in Figure 4.6) occurred relatively uniformly over the entire solution; no early color change to red was observed at the liquid surface or at the plasma-liquid contact point. These results are consistent with the observations of Shimizu et. al. [235], who likewise showed that convective forces induced in the bulk liquid prevented a drop in pH of visible dimensions at the plasma-liquid interface. Slight

gradients in color (deeper red, e.g. more acidic) were observed in the path between the plasma-liquid contact point and the wire to ground, suggesting possible electrochemical effects.



*Figure 4.6. **Above:** Change in color of methyl red solution with 0.5 mM phosphate buffer (initial pH = 7.4) exposed to transient spark discharge; photographs taken at 0, 30, 40, 50 and 60 seconds of plasma exposure. The color of the solution remained uniform, i.e. gradients in color (indicating gradients in pH) were not observed at the plasma-liquid interface. **Below:** Color exhibited by methyl red solutions at pHs varying from 7.7 to 3.6, shown for reference.*

#### 4.6 Mass Transport at Plasma-Solution Interface

The distance that  $\text{OH}^\bullet$  and other highly reactive species penetrate into an adjacent phase (defining the surface reaction zone) is difficult to determine precisely due to the fast reaction kinetics of these species and hence strong dependence on the concentrations of a suite of possible reaction partners. However, most published models of plasma-liquid interactions show that the concentration of  $\text{OH}^\bullet$  entering from the gas phase drops by orders of magnitude over a few microns or tens of microns from the surface. For example, calculations by Lindsay et al. suggest a 9-order of magnitude decrease in  $\text{OH}^\bullet$  concentration within  $50\mu\text{m}$  of the surface in unbuffered water [66]. A model of DBD-treated tissue by Tian and Kushner [63] indicates that the liquid-phase  $\text{OH}^\bullet$  concentration becomes negligible after a similar distance. Biological reviews report  $\text{OH}^\bullet$  diffusion distances that are even smaller: on the order of “a small protein” [236], perhaps 10-100nm. Experimental studies of X-ray irradiation of mammalian cells suggest an average intracellular diffusion distance for  $\text{OH}^\bullet$  of 10nm [237]. Thus, the near-surface region in which indigo carmine and  $\text{OH}^\bullet$  react is expected to extend between  $\sim 100\text{nm}$  to possibly several tens of micrometers into the liquid phase.

Within the near-surface region, several processes may limit the rate of indigo carmine oxidation:

1.  $\text{OH}^\bullet$  must either:
  - a. Arrive at the plasma-liquid interface and be solvated to enter the solution.
  - b. Be formed within the liquid-phase boundary layer through reactions of other species.
2.  $\text{OH}^\bullet$  and indigo carmine must meet and react.
3. Indigo carmine must diffuse from the bulk solution into the liquid boundary layer to replace the oxidized species.

These processes are illustrated in Figure 4.7. Steps 1 and 3 describe transport limitations, while step 2 represents a possible kinetic limitation.

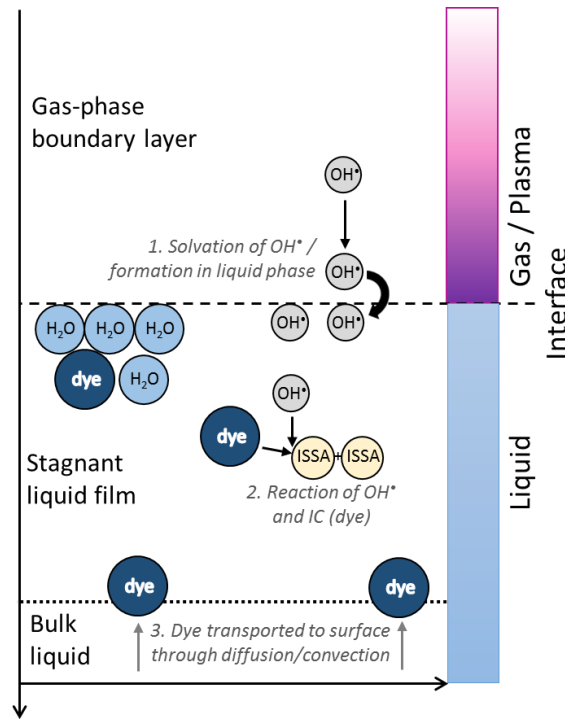


Figure 4.7. Illustration of possible processes limiting the rate of indigo carmine oxidation by  $\text{OH}^\bullet$  in the region near the plasma-liquid interface.

Well-known metrics for comparing the time scales of reaction to diffusion (or other transport properties) are the Damkohler numbers [152]. The second Damkohler number relates the reaction rate of  $\text{OH}^\bullet$  with indigo carmine to its diffusive mass transfer rate:

$$\text{Da}_{\text{II}} = \frac{\text{reaction rate}}{\text{diffusive mass transfer}} = \frac{k' L^2}{D_{\text{OH}}} \quad (4.21)$$

Where  $k'$  = effective rate constant,  $k'[\text{indigo carmine}] = 10^6 \text{ s}^{-1}$   
 $L$  = boundary layer thickness  
 $D_{\text{OH}}$  = diffusion coefficient,  $2.8 \times 10^{-9} \text{ m}^2 \text{ s}^{-1}$  [157]

The rate constant,  $k$  for the reaction of  $\text{OH}^\bullet$  with indigo carmine is on the order of  $10^{10} \text{ M}^{-1} \text{ s}^{-1}$  [200], [238]. Given the initial indigo carmine concentration used in these studies,  $100 \text{ } \mu\text{M}$ , the effective rate constant ( $k \cdot [\text{indigo carmine}]$ ) is  $10^6 \text{ s}^{-1}$ . For an assumed boundary layer thickness of  $10 \text{ } \mu\text{m}$ ,  $\text{Da}_{\text{II}} = 10^4$ , indicating that reaction occurs on a significantly faster time scale, i.e. diffusion/arrival of  $\text{OH}^\bullet$  to the solution limits the degradation of indigo carmine at this length scale. Given these parameters, for reaction and diffusion occur on similar time scales ( $\text{Da}_{\text{II}} \sim 1$ ),  $L$  must be roughly  $100\text{nm}$ .

This analysis indicates that the boundary layer over in which  $\text{OH}^\bullet$  reacts with indigo carmine extends on the order of a few hundred nanometers from the plasma-liquid interface, the low end of our previous estimate based on the literature. Thus, for liquid depths greater than  $100\text{nm}$ , diffusive transport of a) indigo carmine from the bulk solution to the surface, or b)  $\text{OH}^\bullet$  produced at or near the surface limits the rate of reaction. Just as the concentrations of  $\text{OH}^\bullet$  and other plasma-generated RONS may differ significantly from their bulk values near the plasma-liquid interface, indigo carmine and the buffers used to control pH may be depleted in this region. It is almost certainly the case that thin boundary layers with relatively high concentrations of oxidizing species at the surface create areas of depletion of such species. In this case, diffusive or convective transport of the dye to this region from the bulk may be limiting, although this is expected to occur on time scales of milliseconds or less. However, given the presence of significant convective forces in this system (induced by the ionic wind at the surface), the arrival of  $\text{OH}^\bullet$  at the plasma-liquid interface was suspected to limit the oxidation of indigo carmine.

To demonstrate whether the concentration of indigo carmine at the interface was limiting, we considered the effect of decreasing the initial concentration of indigo carmine on the quantity of indigo carmine degraded over a fixed period. Decreasing the initial concentration of indigo carmine from  $1\text{mM}$  to  $0.5\text{mM}$  did not affect the number of moles of indigo carmine lost, as shown in Figure 4.8. This provides strong evidence that the oxidation of indigo carmine is limited by arrival/generation of  $\text{OH}^\bullet$  or other oxidizing species rather than diffusion of the dye to the reaction zone.

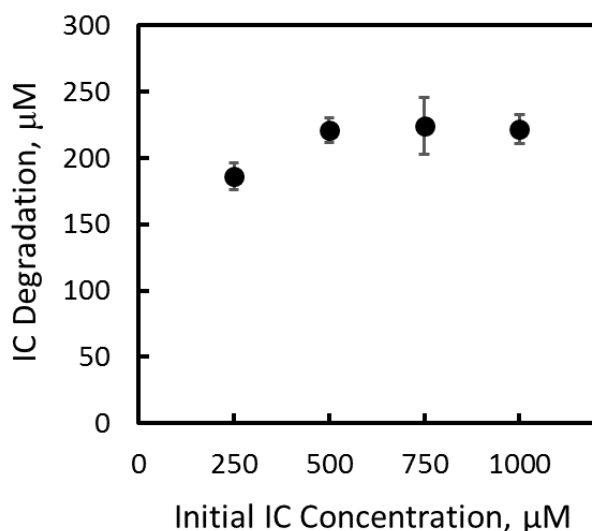


Figure 4.8. Reducing the initial concentration of indigo carmine (IC) does not affect the amount of IC degraded by direct treatment with a transient spark discharge (as indicated by the reduction in indigo carmine (IC) concentration from a  $0.8 \text{ mL}$  volume).

At this point, we have inferred that the limiting factor in the oxidation of indigo carmine is the concentration of oxidizing species at the surface. It is therefore germane to ask whether the arrival of OH<sup>•</sup> from the gas phase can realistically account for the oxidation observed, or whether an alternative explanation (production of OH<sup>•</sup> through high concentrations of H<sub>2</sub>O<sub>2</sub> / NO<sub>2</sub><sup>-</sup> near the interface, or the action of a different oxidizing species) is necessary.

To this end, we compare the estimated influx of OH<sup>•</sup> required to oxidize indigo carmine (as observed experimentally) to the expected concentration of OH<sup>•</sup> reaching the solution from the gas phase. From the loss of indigo carmine at pH 7.4 in Figure 4.4, we can calculate that 5 × 10<sup>-10</sup> mol/s of indigo carmine in solution are degraded due to transient spark exposure at neutral pH (based on the change in concentration in a 5mL solution volume). Assuming that this degradation is due to reaction with OH<sup>•</sup>, NEAPP exposure must produce at least 5 × 10<sup>-10</sup> moles/s of OH<sup>•</sup>. The influx of OH<sup>•</sup> from the gas phase must at least equal this rate to cause the loss of indigo observed.

As OH<sup>•</sup> radicals are uncharged, their rate of collision with the liquid surface can be described by gas kinetic theory [152]:

$$\begin{array}{l} \# \text{ OH}^\bullet \text{ collisions} \\ \text{with surface} \end{array} = \frac{1}{4}n\bar{v} = \frac{n}{4}\sqrt{\frac{8k_B T}{\pi m}} \quad (4.22)$$

where  $n_{\text{OH}} = \text{OH}^\bullet/\text{cm}^3$  (to be estimated)  
 $T = 300\text{K}$   
 $m = \text{molecular mass, } 17 \text{ g/mol} \rightarrow 2.82 \times 10^{-26} \text{ kg (per molecule)}$

The probability that an impinging OH<sup>•</sup> will “stick” and be taken up by the liquid,  $\alpha$ , was assumed to be 0.1 [239], [240]. The diameter of the visible transient spark is on the order of 1 mm, suggesting a plasma-liquid contact area,  $A$ , of  $7.8 \cdot 10^{-3} \text{ cm}^2$ . If the rate of OH<sup>•</sup> arrival at the surface is equated to the minimum influx of OH necessary to produce the indigo carmine oxidation observed, we arrive at:

$$\frac{n}{4}\sqrt{\frac{8k_B T}{\pi m}} \times \alpha \times A = 5 \times 10^{-10} \text{ mol/s OH}^\bullet \text{ entering solution} \quad (4.23)$$

Rearranging and solving for  $n$ , we find that a gas-phase OH<sup>•</sup> density of  $2.5 \times 10^{13} \text{ cm}^{-3}$  near the liquid surface is required to account for the indigo oxidation observed. The gas phase OH<sup>•</sup> density near the plasma-liquid interface for a transient spark discharge is expected to lie between  $10^{12}$  and  $10^{15} \text{ cm}^{-3}$  based on literature values [99], [103], [142], [144]–[146]. These literature values are summarized in Table 3.1 below. Note that the plasma device and setup used in references [18], [20], and [22] most closely parallels the transient spark discharge used in this work. Comparing these results, the direct reaction of OH<sup>•</sup> with indigo carmine near the surface could thus reasonably explain the degradation of indigo carmine observed.

Table 4.2. Literature values for gas-phase OH<sup>•</sup> density found in air plasmas

Plasma Source	Gas phase OH <sup>•</sup> density	Measurement technique	Ref.
Positive corona discharge in humid air	$3 \times 10^{14} - 1 \times 10^{15} \text{ cm}^{-3}$	LIF	[99], [102], [144]
DBD over water	$10^{12} - 10^{13} \text{ cm}^{-3}$	Model	[145]
Ar-H <sub>2</sub> O RF plasma jet in air	$10^{14} - 10^{15} \text{ cm}^{-3}$	LIF	[142]
He jet operated in air over cell media	$6 \times 10^{13} - 5 \times 10^{14} \text{ cm}^{-3}$	LIF	[146]

We conclude that the observed rates of indigo carmine oxidation in pH 7.4 solution are not inconsistent with arrival of OH<sup>•</sup> from the gas phase (assuming concentrations produced by a positive DC discharge in humid air, and given reasonable assumptions about the rates of mass transfer of OH<sup>•</sup> from the gas phase to the liquid).

#### 4.7 Analysis of Indigo Carmine Degradation Products

The decomposition products of indigo carmine were analyzed to a) confirm that the expected degradation product, isatin sulfonic acid (ISA) is present, and b) assess the extent to which OH<sup>•</sup> subsequently reacts with these species. Plasma-treated indigo carmine solutions are analyzed with mass spectrometry and <sup>1</sup>H NMR spectroscopy. Electrospray ionization mass spectrometry of NEAPP-treated solutions containing indigo carmine yield a dominant signal at m/z = 226 in negative ion mode, consistent with isatin sulfonic acid (ISA) as the main decomposition product. Additional small signals were observed at m/z = 244 (ISA + O) and 147 (ISA-SO<sub>3</sub>+H) in negative ion mode, and at m/z = 143 and 190 (unassigned) in positive ion mode. No evidence of nitrated species was observed.

NEAPP-treated indigo carmine solutions are also analyzed with <sup>1</sup>H NMR to support our assignment of the peak observed at m/z = 226 to ISA. Indigo carmine standards produce <sup>1</sup>H NMR peaks at δ = 8.04(s), 7.74(d) and 6.86(d) ppm. NEAPP-treated indigo carmine solutions showed <sup>1</sup>H signals consistent with indigo carmine, and also at δ = 7.14(t) and 7.94(m). The latter correspond to the <sup>1</sup>H NMR spectra from ISA standards, providing further evidence that ISA is the primary decomposition product of indigo carmine under these conditions. No peaks corresponding to other possible decomposition products, such as sulfoanthranilic acid, malic acid, or tartaric acid [207], [241] are observed. Representative <sup>1</sup>H NMR spectra are shown in Figure 4.9 and Figure 4.10. Significantly more indigo carmine is degraded at pH 3.5 relative to pH 7.4, as is seen from comparing Figure 4.9 (NEAPP-treated pH 3.5 solution) to Figure 4.10 (NEAPP-treated pH 7.4 solution). Due to the relatively high initial concentration of indigo carmine used in the <sup>1</sup>H NMR studies (2 mM vs. 100 μM), all samples contained high concentrations of unreacted indigo carmine, even after 30 minutes of NEAPP treatment.

If all indigo carmine lost is oxidized by NEAPP to ISA with no subsequent reaction, loss of 1 mM indigo carmine should be accompanied by a 2 mM increase in the ISA concentration. Integration of the peaks assigned to indigo carmine (6.86 ppm) and ISA (7.14 ppm) in Figure 4.9 indicates that ISA concentrations



are roughly 60% of the expected levels. This suggests that further degradation of indigo carmine does in fact occur (perhaps all the way to  $\text{CO}_2$ , given the lack of other products observed. Thus, competition for  $\text{OH}^\bullet$  or other oxidizing species from ISA and other degradation products should be considered in analyzing such systems.

Despite the above caveat, both analyses show clear evidence of isatin sulfonate as the main decomposition product and no other products were observed in significant concentrations. The production of ISA is consistent with  $\text{OH}^\bullet$  as the primary near-surface oxidizing agent, but is not definitive proof that this is the sole active agent.

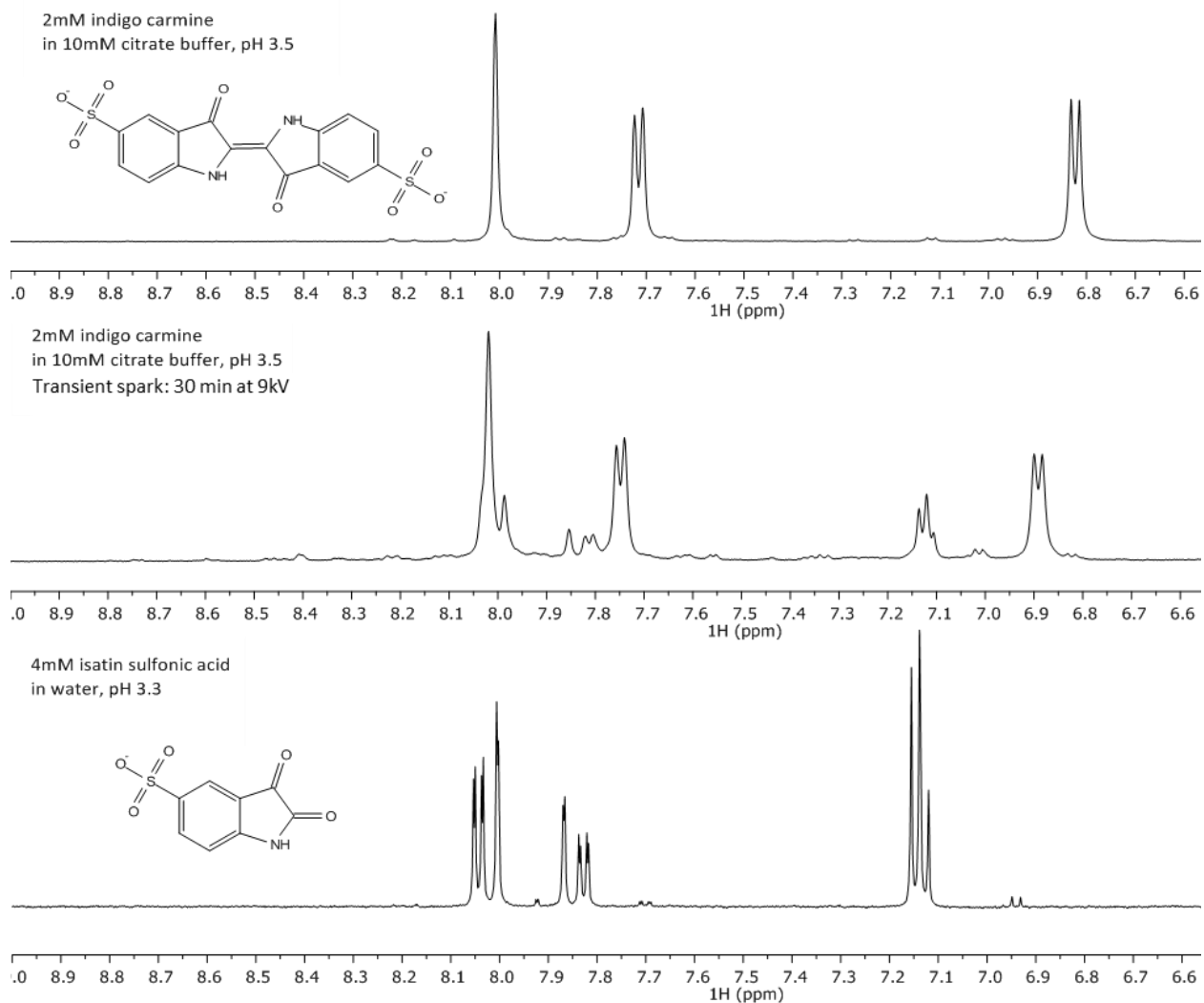


Figure 4.9.  $^1\text{H}$  NMR spectra of indigo carmine solutions buffered to pH 3.5 (top to bottom): 2mM indigo carmine in pH 3.5 citrate buffer, no plasma exposure; 2mM indigo carmine in pH 3.5 citrate buffer, exposed to transient spark for 30 minutes (applied voltage = 9kV, inter-electrode distance = 5mm); 4mM isatin sulfonic acid (ISA) in water, pH = 3.3. The plasma-exposed sample shows signals at chemical shifts of 7.14, 7.85, and around 8ppm, indicating the presence of ISA.

Table 4.3. Expected vs. measured concentration of ISA in NEAPP-treated solutions of indigo carmine at a pH of 3.5. The amount of ISA observed (quantified by integration of  $^1\text{H}$  peak at 7.14ppm) is roughly 60% of that expected, indicating that subsequent degradation of ISA occurs.

	Concentration, $\mu\text{M}$		
	Indigo carmine	ISA, from NMR	ISA, expected
Initial	1.8	0	0
20 min NEAPP	1.3	0.6	1
30 min NEAPP	1.00	1	1.6

$$[\text{ISA}]_{\text{expected}} = 2 \times (\text{Initial} [\text{IC}] - \text{Final} [\text{IC}])$$

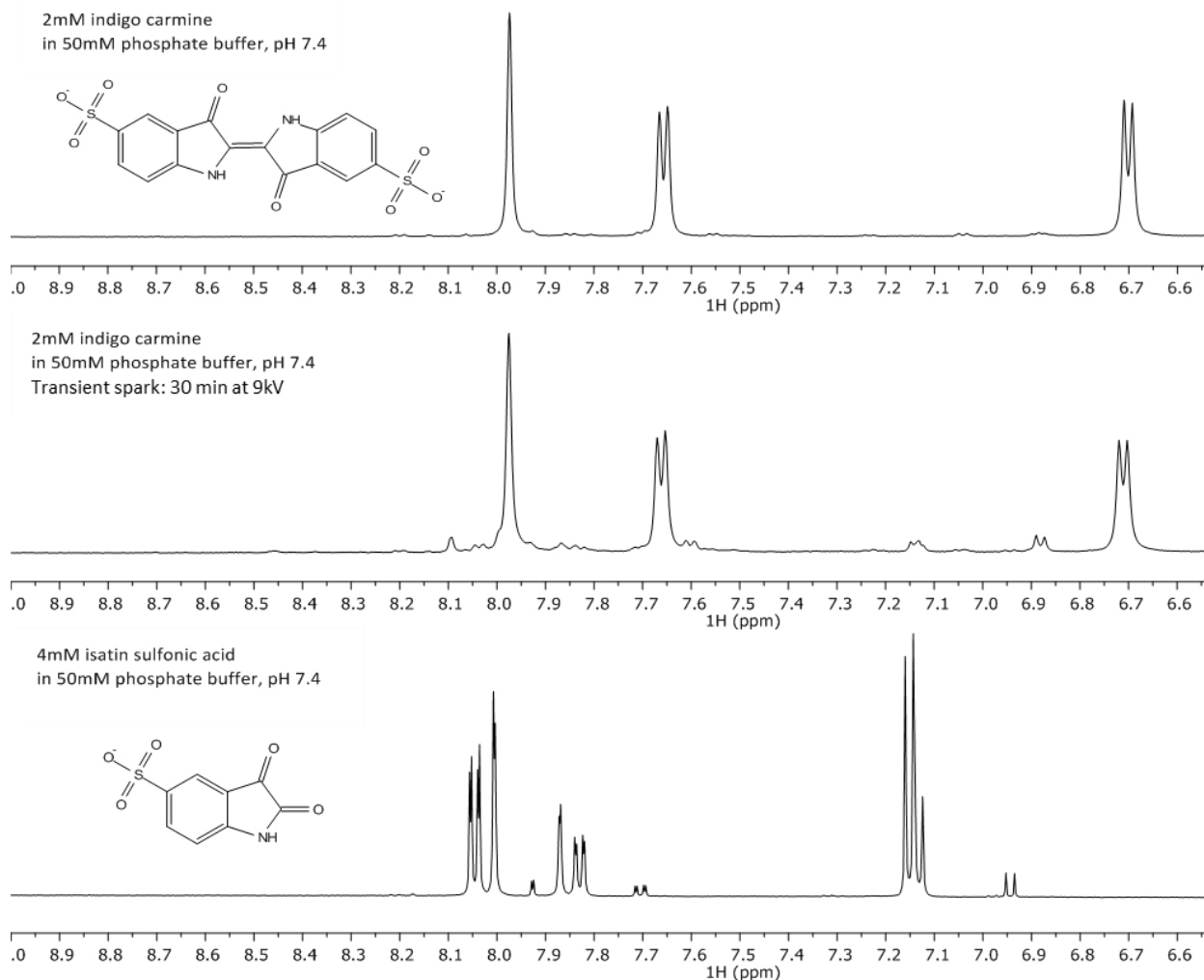


Figure 4.10.  $^1\text{H}$  NMR spectra of indigo carmine solutions buffered to pH 7.4 (top to bottom): 2mM indigo carmine in pH 7.4 phosphate buffer, no plasma exposure; 2mM indigo carmine in pH 7.4 phosphate buffer, exposed to transient spark for 30 minutes (applied voltage = 9kV, inter-electrode distance = 5mm); 4mM isatin sulfonic acid (ISA) in pH 7.4 phosphate buffer. Less degradation of indigo carmine is observed compared in the plasma-exposed sample relative to the identical treatment in pH 3.5 solution (see Figure 4.9); however, small signals at chemical shifts corresponding to ISA are observed.

## 4.8 Discussion

It is apparent that loss of indigo carmine at pH 7.4 greatly exceeds that expected from reactions in the bulk solution (namely the  $\text{O}=\text{NOOH}$  pathway). At a pH of 7.4, the  $\text{O}=\text{NOOH}$  pathway (reactions 7-9) should be inactive, although the local pH very close to the plasma-liquid interface may differ significantly from the

bulk.<sup>7</sup> Clearly, an additional source of OH<sup>•</sup> (beyond the O=NOOH pathway in the bulk solution) is required to explain the oxidation observed during NEAPP treatment. The following effects may be responsible: a) OH<sup>•</sup> or other highly oxidizing species generated directly by the plasma react with indigo carmine at or very near the plasma-liquid interface; b) the interaction of NEAPP and NEAPP-generated species with the liquid creates a thin surface region with elevated concentrations of H<sub>2</sub>O<sub>2</sub> and NO<sub>2</sub><sup>-</sup>, and/or where the buffer is overcome and pH is significantly reduced, leading to an accelerated rate of OH<sup>•</sup> formation through the O=NOOH pathway; c) indigo carmine at/near the surface is degraded by UV or other energetic plasma species. Note that in two of these cases, OH<sup>•</sup> is the primary oxidizing species responsible for modifying the target (indigo carmine).

Other possible oxidizing species include ozone (O<sub>3</sub>), the superoxide anion (O<sub>2</sub><sup>-</sup>), and singlet oxygen (<sup>1</sup>O<sub>2</sub>). Ozone is known to be produced in the gas phase by positive polarity DC discharges, but its reaction with indigo carmine is too rapid to account for the observed bulk decomposition when indigo is added to PAW after plasma treatment. If O<sub>3</sub> were present in solution following NEAPP exposure, it would react with the indigo carmine immediately upon addition of the dye, rather than over the course of several minutes. Furthermore, the elevated gas temperatures of the transient spark discharge (~550K) are expected to produce less ozone than low-power discharge modes, as more NO<sub>x</sub> species are produced [126] and ozone is decomposed at a higher rate [103].

The superoxide radical has been shown to be generated by plasma jets and negative polarity dc discharges [147], [192], [242]. However, O<sub>2</sub><sup>-</sup> formation in the gas-phase may be less likely in positive polarity dc discharges such as the one used in this study, in which water-vapor cluster positive ions (i.e. H<sub>3</sub>O<sup>+</sup>[H<sub>2</sub>O]<sub>n</sub>) are the dominant charge carriers [243], [244]. Furthermore, the formation of significant quantities of O<sub>2</sub><sup>-</sup> at the plasma-liquid surface is unlikely given that the water acts as the cathode. Nevertheless, we cannot exclude the possibility that O<sub>2</sub><sup>-</sup> is playing a significant role near the interface without additional studies. At pH values significantly above the pK<sub>a</sub> of O=NOOH (6.8) the production of superoxide radicals from the decomposition of O=NOOH is expected to play a more significant role.

Singlet oxygen (<sup>1</sup>O<sub>2</sub>) is also a possible oxidant that has recently received a great deal of attention in the plasma community due to recent evidence that it can be an important active species in cell treatment studies [40], [123], [192]. However, previous studies suggest that indigo carmine does not react with singlet oxygen to a significant extent [245], [246].<sup>8</sup> Considering that the rate of indigo carmine oxidation by singlet oxygen is likely orders of magnitude below the reported rate of physical quenching ( $3.2 \times 10^8 \text{ M}^{-1} \text{ s}^{-1}$ ) and comparing this to the rate of indigo carmine oxidation by hydroxyl radical,  $1.8 \times 10^{10} \text{ M}^{-1} \text{ s}^{-1}$ , significantly more <sup>1</sup>O<sub>2</sub>

---

<sup>7</sup> In simple experiments in which methyl red solutions (buffered to pH 7.4) were treated with NEAPP, no color change (indicating a gradient in pH) was observed near the surface or anywhere in solution. Solutions were treated with NEAPP until the buffer was overcome, at which point the color uniformly changed from yellow to red. This is in contrast to experiments performed by Witzke et al [266] (in the absence of convection), in which spatial gradients in pH were observed at the plasma-liquid interface. This suggests that any gradients in pH that exist are restricted to very near the surface.

<sup>8</sup> The rate at which <sup>1</sup>O<sub>2</sub> is quenched (reduced to the triplet state) by indigo carmine is  $3.2 \times 10^8 \text{ M}^{-1} \text{ s}^{-1}$  per the results of Gandra et. al. [246]. Moreover, the quenching of <sup>1</sup>O<sub>2</sub> observed in these experiments was stated to occur through “physical quenching”, or processes that convert <sup>1</sup>O<sub>2</sub> to <sup>3</sup>O<sub>2</sub> by reducing the energy state of indigo carmine rather than changing its structure (“chemical quenching”). Oxidation products of indigo carmine were only observed after extended irradiation periods (several hours of <sup>1</sup>O<sub>2</sub> production).

must be present (perhaps 3-4 orders of magnitude or more) near the plasma-liquid surface to produce the same rate of indigo carmine loss than if the oxidizing species were OH<sup>•</sup>.

In this system, the evaporation and ionization of water at the plasma-liquid interface is expected to produce significant levels of OH<sup>•</sup>, based on the concentrations produced by a similar device as determined by LIF [99], [102], [144] and the observed concentrations of H<sub>2</sub>O<sub>2</sub> generated in solution. Given our present knowledge of the system, OH<sup>•</sup> is likely to be the dominant oxidizer of indigo carmine. However we reiterate that this has not been proven. In this work, we investigate the origin of the observed oxidation of a model compound (indigo carmine), and highlight the importance of the plasma-liquid interface in specie modification. The next logical step is to assess the identity of ROS present (OH<sup>•</sup> vs <sup>1</sup>O<sub>2</sub> or O<sub>2</sub><sup>•-</sup>) through direct measurements with EPR and with competitive kinetic experiments. For a more detailed understanding of the near-surface plasma-water chemistry must await future work in which known scavengers or selected reaction partners can be added to react selectively with various possible oxidizing agents [40].

#### 4.9 Conclusions

Studies of the effects of H<sub>2</sub>O<sub>2</sub> and NO<sub>2</sub><sup>-</sup> on indigo carmine are consistent with the established kinetics of OH<sup>•</sup> production through the O=NOOH pathway, with 24% of O=NOOH going to OH<sup>•</sup> generation and the oxidation of indigo carmine. When indigo carmine is added to plasma-activated solutions, the observed decay rate follows that observed when H<sub>2</sub>O<sub>2</sub> and NO<sub>2</sub><sup>-</sup> are added to solution without plasma exposure at the same pH. This set of results also implies that OH<sup>•</sup> produced through O=NOOH decomposition is in fact the primary oxidizing agent in these plasma-activated water solutions in the absence of active plasma. It supports the conclusion that NEAPP treatment does not generate significant concentrations of other, long-lived reactive species in the buffered solutions investigated. Lastly, these results show that the model developed for artificial PAW can be applied to assess the contribution from bulk solution chemistry in plasma-treated solutions this system.

Experiments using indigo carmine as an indicator of oxidative strength during NEAPP exposure demonstrate that the activity of OH<sup>•</sup> (or other highly oxidizing species) near the plasma-liquid interface dominates the effects of NEAPP treatment. This result is striking given the small area of contact between the discharge and liquid (<1 mm<sup>2</sup>), and highlights the importance of gas-liquid transport phenomena in these systems. The observed effects could be due to either a) direct reaction with plasma-generated species, most likely OH<sup>•</sup>, at the interface, b) locally elevated concentrations of H<sub>2</sub>O<sub>2</sub>, NO<sub>2</sub><sup>-</sup>, and/or local reduction in the pH at the surface, leading to acceleration of the O=NOOH pathway in this region; c) the effect of plasma-generated species such as UV and/or ions directly on indigo carmine, or d) complicating effects of citrate in solution. Although these hypotheses await confirmation, our initial results are consistent with OH<sup>•</sup> being the primary oxidizing agent.

Analysis of the degradation products of indigo carmine found that isatin sulfonic acid (ISA) was the major decomposition product, consistent with indigo carmine degradation by other advanced oxidative processes [247]. Quantification of ISA formed in solutions treated with NEAPP at a pH of 3.5 suggest that further oxidation of ISA takes place, and that future models should incorporate these reactions.

While we have estimated that the oxidation of indigo carmine observed could reasonably be attributed to OH<sup>•</sup> produced in the gas phase (based on LIF measurements of the gas-phase OH<sup>•</sup> density reported in the

literature), the previously mentioned results suggest that the situation is more complicated, and that conditions in the liquid phase may strongly affect near-surface reactions.

A simple estimate of diffusive and kinetic resistances for indigo oxidation, combined with the presence of convective forces in the liquid phase, strongly suggest that the arrival of reactants limits the oxidation process. Comparison of dye oxidation at varied initial concentrations of indigo carmine indicates that diffusion of indigo carmine to the surface is not limiting. Thus, oxidation is limited by the generation or arrival of  $\text{OH}^\bullet$  or other oxidative species in the liquid phase. This suggests that, for applications in which greater oxidizing power is desired, the focus should be on increasing the plasma-mediated generation of oxidative species rather than on transport limitations.

## 5 Effects of Non-Thermal Plasma on Biological Targets

### 5.1 Abstract

As discussed in the introduction to this work, there is a growing body of research from the plasma medicine community demonstrating the effects of plasma treatment on eukaryotic cells *in vitro* and increasingly *in vivo*. These studies have focused on the ability of plasma jets or indirect DBD devices to induce apoptosis, or reduce cell viability by monitoring specific damage markers. In other cases, cells are incubated with “plasma-activated” cell media rather than being exposed to plasma directly, demonstrating that the activity of relatively long-lived reactive species rather than transiently excited species or photons is also an important facet of non-thermal plasma therapies.

In beginning to address how reactive species generated by the plasma interact with biomolecules and aqueous environments, it is necessary to understand the changes occurring at the molecular (as well as metabolic) level in investigating the effects of non-thermal plasma on these systems. Insights into this process will permit determination of which reactive species are desired, and how to create and deliver those species more effectively. Techniques for assessing the effects of redox active species on small molecules via mass spectrometry and other methods are well established [166], but remain under-utilized in the context of plasma medicine, although this is beginning to change.

It is therefore of interest to probe how these plasma-generated species interact with biomolecules (such as would be present in cell media, a layer of moisture on tissue, or in the intracellular space). In this very preliminary work, we began by assessing the effects of our plasma device on relatively simple targets – single amino and nucleic acids. We employed a combination of analytical techniques (specifically mass spectrometry and nuclear magnetic resonance (NMR)) to assess the effects of the non-thermal plasma sources used in our group on these species.

### 5.2 Analytical Methods

Plasma-induced modifications to the target species investigated in this work were probed through nuclear magnetic resonance (NMR) and mass spectrometry (MS). The latter techniques and instruments used are described in brief in the corresponding sections below.

#### 5.2.1 NMR Spectroscopy

NMR provides a powerful way to observe changes to the structure of chemical species, particularly proton-rich targets. From  $^1\text{H}$  NMR spectra, we get information from the chemical shift, which tells us about the chemical environment of each proton. We can also get information on the total number of each protons within each population by integrating over each peak, since every proton is NMR active (assuming that a sufficient time delay,  $T_1$ , is used). The scalar coupling ( $J$ ), or distance between peaks in the same multiplet, provides information on through-bond coupling (i.e. conformational information).

$^1\text{H}$  NMR was used to identify the degradation products of indigo carmine and other targets exposed to plasma discharge or other oxidative chemistries. Samples were run on an Avance Bruker 400MHz or an Avance 500MHz instrument. At least 10%  $\text{D}_2\text{O}$  was added to enable locking, and 1mM (trimethylsilyl)propionic acid, TMSP ( $\delta = 0$  ppm) generally used as an internal standard. Figure 5.1 shows a typical  $^1\text{H}$  spectrum from one of the molecules studied, glutathione, in  $\text{D}_2\text{O}$ . The areas under each peak indicate the number of protons at that location; an area of  $\sim 1.0$  indicates two protons, e.g. sites (b) and (f), while  $\sim 0.5$  indicates a single proton, e.g. (a) and (d). The splitting patterns reflect how many protons are coupled (bound to nearby atoms): the two isolated protons at site (f) appear as a singlet, whereas the protons at site (b) are split by the 3 adjacent protons at (a) and (c), yielding a quartet pattern. The proton at site (d) is split by the 2 protons at (e) with slightly different coupling constants; this produces a doublet of doublets.

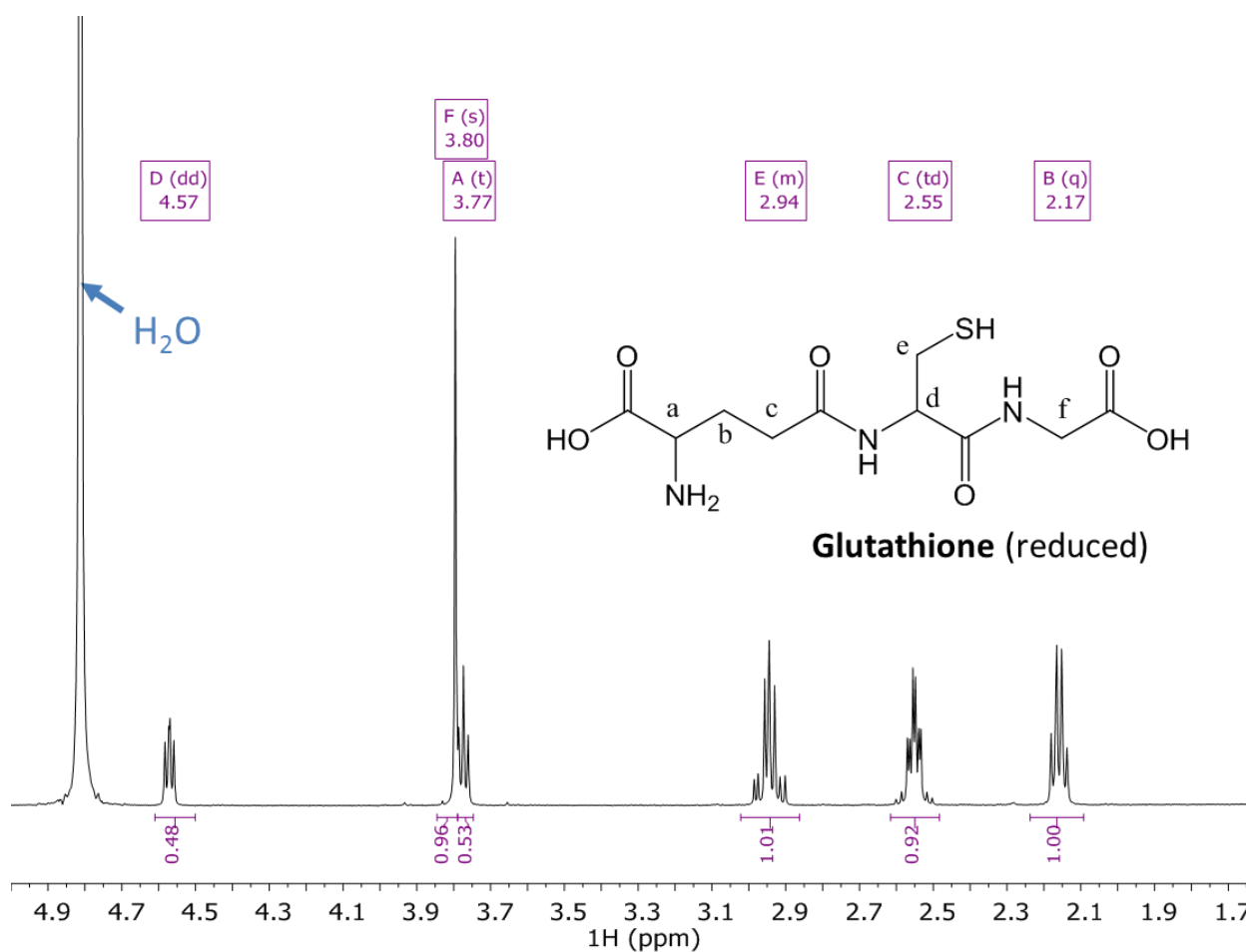


Figure 5.1.  $^1\text{H}$  NMR spectrum of glutathione in  $\text{D}_2\text{O}$ . The spectrum is referenced to the chemical shift of TMSP at 0 ppm. There is a solvent impurity ( $\text{H}_2\text{O}$ ) at 4.81 ppm. The splitting patterns indicate how many protons are bound to nearby carbon atoms: the two isolated protons at site (f) appear as a singlet, whereas the protons at site (b) are split by the 3 adjacent protons at (a) and (c), yielding a quartet pattern. The areas arising from each signal (shown beneath each peak) correspond to the number of protons present. In this spectrum, the area corresponding to the 2 protons at site (b) is set to 1.00; the other sites with 2 protons also have integrated areas of  $\sim 1.0$ , and sites with 1 proton have  $\frac{1}{2}$  the area, or areas of  $\sim 0.5$ .



One of two solvent-suppression sequences was used to saturate the peak corresponding to water for  $^1\text{H}$  scans of samples not composed entirely of  $\text{D}_2\text{O}$ . Initially, the ZGPR pulse sequence was used. However, an excitation sculpting water suppression pulse sequence (ESGP) recommended by the facility director Hasan Celik gave much better targeted signal reduction. It is slightly more complicated to set up, requiring the power level and the width of the frequency window to be saturated to be set, in addition to the proton 90-time and frequency to be suppressed.

The concentrations used in experiments to date (up to 15mM of small molecules such as glutathione or indigo carmine) are too dilute for a  $^{13}\text{C}$  signal to be acquired within a short time ( $< 2$  hrs). Specifically, a solution of 10mM glutathione, 2.5 mM histidine, 1mM TMSP, and 0.5 mM indigo carmine in  $\text{D}_2\text{O}$  was analyzed with the standard Bruker TopSpin  $^{13}\text{C}$  pulse sequence on the 700MHz magnet (with cryoprobe) for 1500 scans without the appearance of a strong signal. It is recommended to use either higher concentrations or to run such samples overnight on a high field instrument (600 or 700 MHz).

Several well-established 2-dimensional NMR experiments (plotted with two frequency axes, or dimensions) have become standard for the identification and analysis of small organic molecules. These are described briefly below to aid in the planning of future experiments.

**Correlational Spectroscopy (COSY)** is a homonuclear experiment in which through-bond coupling between  $^1\text{H}$  nuclei is observed. It allows protons located on nearby carbons to be identified (separated by up to a few bonds) by looking for *cross peaks* in the spectra (signals lying off the diagonal). It is one of the fastest to run, as it does not require observation of  $^{13}\text{C}$  (and sufficient polarization of these nuclei).

**Nuclear Overhauser Effect Spectroscopy (NOESY)** provides similar information to COSY, but polarization is transferred through space rather than through covalent bonds. Thus, correlated protons are physically near each other rather than on adjacent carbons. This technique is particularly important in protein structural analyses.

**Heteronuclear single-quantum correlation spectroscopy (HSQC)** provides information about correlations between nuclei of two different types (usually  $^1\text{H}$  and  $^{13}\text{C}$  or  $^{15}\text{N}$ ) which are separated by one bond (in other words, lie near a specific coupling constant).

**Heteronuclear multiple-bond correlation spectroscopy (HMBC)** provides information about connections over longer ranges (2–4 bonds) but with decreased sensitivity compared to HSQC. The absence of one of the delay times (that enables couplings over a wider range to be detected, e.g. up to multiple bonds) also may introduce phase distortions into the resulting signal.

Correlational spectroscopy (COSY) experiments were performed to assist in identifying degradation products of target biomolecules; these results are discussed in Section 5.5. An example of how the data from these experiments are interpreted is shown in Figure 5.2, which shows the spectrum from a  $^1\text{H}$ - $^1\text{H}$  gCOSY experiment on 10mM glutathione in  $\text{D}_2\text{O}$  with TMSP added as an internal reference (the “g” indicates that the COSY pulse sequence included a gradient pulse). The location of the cross-peaks gives information about proton connectivity; in this example, the presence of a cross-peak indicates that the two protons are bound to adjacent carbon atoms. This technique can be used to confirm proton assignments made from a simple 1-D experiment.

A sample HSQC experiment on a 10mM glutathione control was performed; the results are shown in Figure 5.3. While the number of scans performed was insufficient to give good resolution on the  $^{13}\text{C}$  channel at the sample concentration, the chemical shifts of the  $^{13}\text{C}$  nuclei can still be read from this spectrum; this is the power of correlational experiments. It should be noted that this experiment was made possible by the availability of a 700MHz instrument with cryoprobe (which greatly improves the signal-to-noise ratio); the spectrum shown took 7.5 minutes to collect, whereas it would have taken hours on the 400 and 500MHz instruments in the facility. This data is included to give future researchers a data point for setting up follow-up experiments.



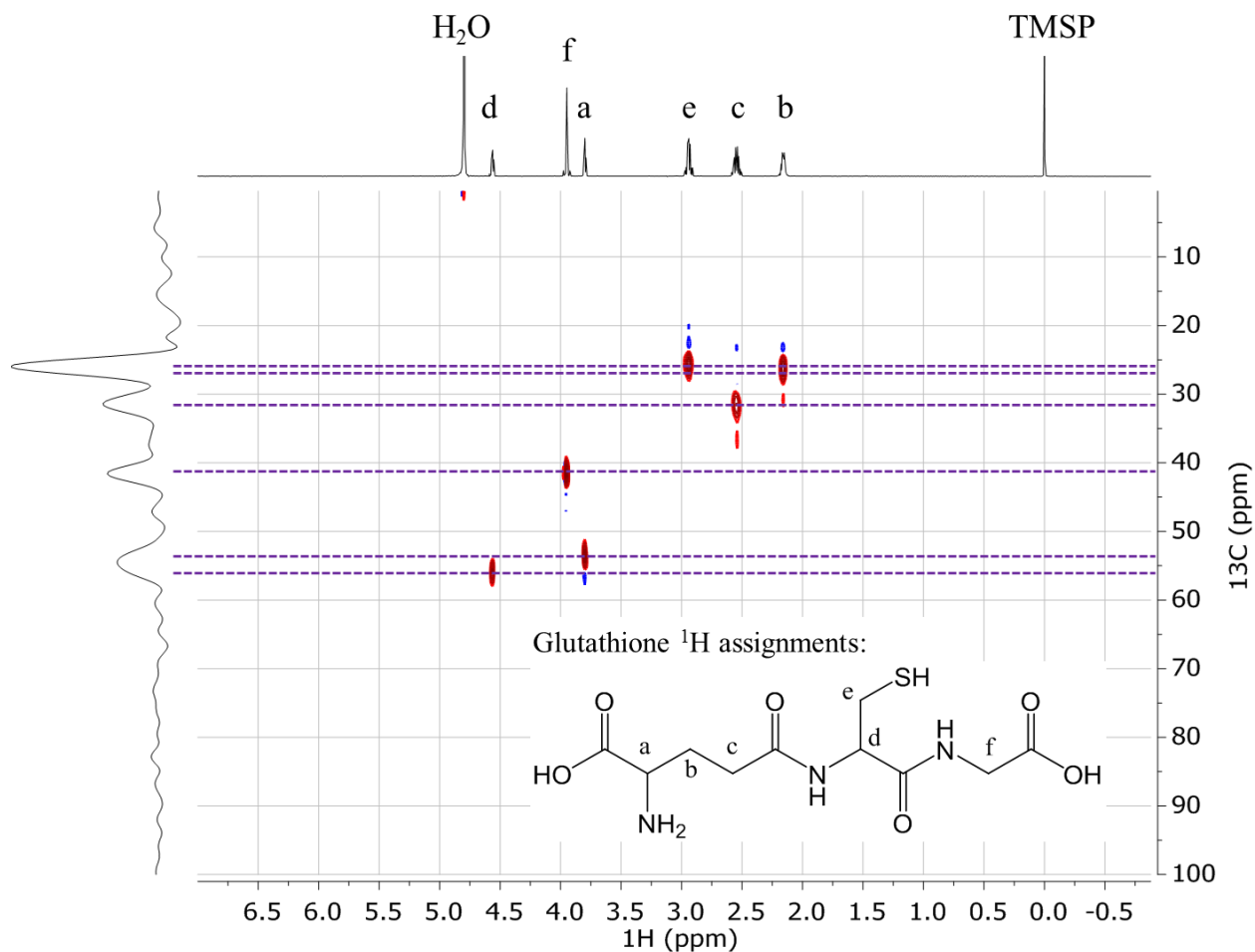


Figure 5.3. 700MHz ( $^1\text{H}$ - $^{13}\text{C}$ ) HSQC spectrum of 10mM glutathione in  $\text{D}_2\text{O}$ . The sample is referenced to 1mM (trimethyl-silyl)propionic acid, TMSP, as an internal standard; some water contamination is also visible. The structural assignments of the proton peaks is shown in the inset. The horizontal trace shows the  $^1\text{H}$  proton spectrum from this sample; the vertical trace shows the unreferenced projection of the 2D data as a  $^{13}\text{C}$  spectrum was not obtained. However, the approximate chemical shifts of the carbon nuclei in this environment can be identified and read from this spectrum based on their correlation with bonded protons. HSQC experiments give correlations over a single bond length; for example, the chemical shift of the carbon with proton (b) is  $\sim 27$  ppm, consistent with the expected range for a  $\text{R}_2\text{CH}_2$  carbon.

### 5.2.2 Mass Spectrometry

Mass spectrometry was used to assist in identifying the effects of plasma exposure on target organic molecules, specifically oxygen adducts. For the small molecules used in this work, electrospray ionization (ESI), a relatively soft method of ionization, was used to ionize the sample and introduce it into the mass spectrometer. The method of ion separation and detection depended on the instrument used. Data are reported in terms of signal (or counts) as a function of the mass-to-charge ratio ( $m/z$ ). Because different

molecules are ionized at different efficiencies, the ratio of intensities between two peaks is not quantitative, and simply gives a rough indication of relative abundance.

The work on free nucleic acids and many of the amino acids studied was performed on an Orbitrap LC/MS using electrospray ionization (ESI) in collaboration with Dr. Anthony Iavarone. Later experiments on the plasma-induced oxidation of tryptophan, and the identification of indigo carmine decomposition products were performed on an Agilent QTOF mass spectrometer. Samples were directly injected into the instrument in both negative and positive ion mode, based on the presence of sulfate and amine groups in the parent molecule. In some cases, a C18 reverse-phase HPLC column was used to eliminate buffers in the sample (by sending them directly to waste) and increase separation of products.

### **5.3 Effects of Non-Thermal Plasma on Nucleic Acids**

#### *5.3.1 Experimental Notes*

Solutions of free nucleic acids were treated with either a surface microdischarge (SMD) plasma device or a corona discharge. The SMD device was identical to that used by Pavlovich et al. in prior work within our group. [126], [248] This is an indirect plasma device, meaning that reactive species are generated by the plasma with the electrodes separated from the liquid (in this case by 4 cm of air); reactive species reach the solution by diffusing through this volume to the solution. The SMD can be operated in low-power (LP) mode, generating more O<sub>3</sub> and oxygen species in the gas phase, or high-power (HP) mode, which produces more NO<sub>x</sub>. Treatments consisted of running the SMD in an enclosed air space above the target solutions for 5 minutes. This was followed by immediately opening the SMD chamber, capping the containers holding the target solution, and vortexing vigorously for 15 seconds.

The corona discharge used in these experiments was an early version of the device described in Section 2.2. In this version, the solution to be treated was electro-sprayed through a hypodermic needle (22 gauge) to which a positive or negative voltage was applied. The solution to be treated was loaded into a plastic syringe, and a syringe pump was used to drive the fluid through the system at a low flow rate (usually 0.15 mL/min, though the range from 0.1 – 0.4 mL/min was explored). The solution was collected in a 1 mL glass cup over several minutes. A stainless steel mesh above the cup was connected to ground and served as the target for the electrospray. This setup is pictured in Figure 5.4 (the glass cup used to capture samples is recessed below stainless steel mesh).

Solutions of all five nucleic acids (adenine, cytosine, guanine, thymine, and uracil) in unbuffered water were studied. The structure of these compounds is shown in Figure 5.5.

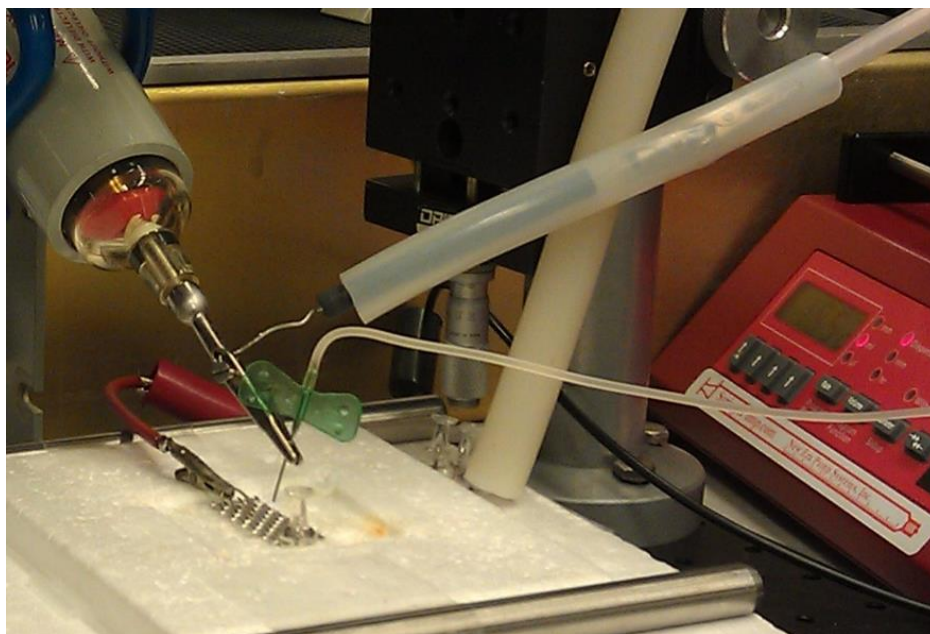
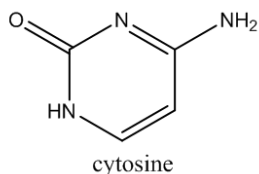
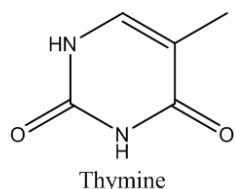


*Figure 5.4. Orientation of electrodes in electro-spray corona discharge setup. A syringe pump (right) controls the flow of solution through the hollow needle, which is suspended above the stainless steel mesh by a high voltage probe. The stainless steel mesh is grounded and serves as a counter-electrode. The current arrangement is for a positive-polarity corona discharge. For a negative polarity discharge, the ballast resistor (black cylinder) and high voltage line (coming from top right in this photo) are attached to the mesh, and the electro-spray needle is grounded. The mesh allows the electro-sprayed solution to pass through to the collection cup; however, large droplets can form on the mesh, resulting in additional exposure of this liquid to the plasma. This mesh/cup system would later be replaced by a submerged electrode and static liquid.*

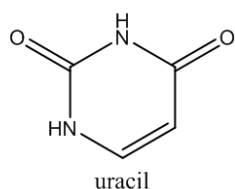
Chemical Formula:  $C_4H_5N_3O$   
Exact Mass: 111.04  
m/z: 111.04 (100.0%), 112.05 (4.3%), 112.04 (1.1%)



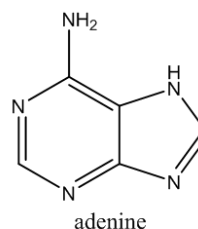
Chemical Formula:  $C_5H_6N_2O_2$   
Exact Mass: 126.0429  
m/z: 126.0429 (100.0%), 127.0463 (5.4%)



Chemical Formula:  $C_4H_4N_2O_2$   
Exact Mass: 112.03  
m/z: 112.03 (100.0%), 113.03 (4.3%)



Chemical Formula:  $C_5H_5N_5$   
Exact Mass: 135.0545  
m/z: 135.0545 (100.0%), 136.0579 (5.4%), 136.0515 (1.8%)



Chemical Formula:  $C_5H_5N_5O$   
Exact Mass: 151.05  
m/z: 151.05 (100.0%), 152.05 (5.4%), 152.05 (1.8%)

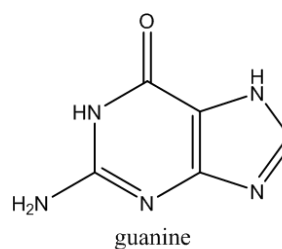


Figure 5.5. Structures, exact masses and m/z predictions (pre-ionization) for nucleic acids.

### 5.3.2 Results

Of the nucleic acids investigated (adenine, cytosine, guanine, thymine and uracil), plasma treatment of guanine and thymine resulted in the greatest degree of oxidation. A five-minute exposure to SMD followed by vortexing generally resulted in greater oxidation of nucleic acids than electrospray corona treatment.

The results of experiments in which adenine, cytosine, guanine, thymine, and uracil were either electrosprayed through positive or negative corona discharge (CD+ / CD-), or treated with a surface microdischarge (SMD) at low power (LP) or high power (HP) are summarized below. The SMD and CD+ experiments were repeated on two different days; the results of SMD LP treatment of guanine were considerably different, for reasons not fully understood. Mass spectra of these samples are included as supplementary material at the end of this chapter as indicated.

*Adenine.* Little to no modification to this molecule was observed following any of the plasma exposures. Evidence of an oxygen adduct (adenine + O) was observed in CD+, CD- and SMD HP samples. This includes the CD+ samples from both dates (1.7% parent molecule intensity in 8/23 spectra; 0.9% in 7/03). Because adenine and guanine have the same chemical formulas, contamination is a concern; thus, adenine solutions were run before guanine to ensure no carryover. (See Figure 5.12 and Figure 5.13.)

*Cytosine.* A large signal corresponding to the two-oxygen adduct, cytosine + 2O, at  $m/z = 144.04$  was observed after exposure to the SMD at low power. Very small signals corresponding to this adduct were also observed following electrospray through either a positive and negative corona discharge (CD+ and CD-). (See Figure 5.14.)

*Guanine.* In initial experiments, the intensity of the guanine-oxygen adduct (guanine + O,  $m/z = 168.05$ ) did not exceed that of the parent compound (at  $m/z = 152.06$ ) in any experiment. The largest adduct signals (arising from guanine + 2O and guanine + 2H + 2O) were observed in the solution exposed to the surface microdischarge at low power (SMD LP). Signals corresponding to guanine + O and guanine - NH + 2O were also observed in this sample. Follow-up experiments resulted in significantly greater oxidation of guanine solutions exposed to SMD LP; the signal arising from guanine + O was stronger than the parent compound, and adducts at  $m/z = 186.06$  and  $208.04$  corresponding to guanine + 2O + 2H were also observed. These adducts were not present in the corona discharge-treated solutions. (See Figure 5.15.)

*Thymine.* The thymine solution exposed to the SMD at low power appeared almost entirely oxidized to thymine - C + 2O in all experiments with this plasma treatment. Little modification of oxidation or modification to thymine was observed in solutions exposed to other plasma treatments. (See Figure 5.16.)

*Uracil.* No significant modifications or oxidation products of uracil were observed following any of the plasma treatments applied. (See Figure 5.17.)

In solutions electrosprayed through the corona discharge, a large peak at  $192.16$  ( $C_9H_{21}NO_3$ ) was often present in the mass spectrum. As this peak did not appear in experiments where identical solutions were treated with SMD, our hypothesis is that it arose from leaching of the plastic syringe or tubing between the syringe and electrospray needle. Iron appeared in some solutions treated with the SMD at high power; while this may have been an impurity introduced after treatment, it is possible that sputtering from the stainless steel mesh used as the solution-side electrode occurred.

A summary of the major adducts observed in the second round of experiments and their intensities relative to the unmodified amino acid signal (parent molecule) are shown in Table 5.1.



*Table 5.1. Major adducts of adenine, guanine, cytosine and thymine observed with LC-MS following either 5 minute exposure to a surface microdischarge in low power mode (SMD LP) or electrosprayed through a positive-polarity corona discharge (CD+). In general, electrospraying through corona discharge did not lead to significant modification of amino acids; the contact time between the discharge and liquid in these experiments was relatively short (once the liquid exited the plasma channel, exposure to further oxidizing species was limited). Guanine and thymine were significantly oxidized by SMD LP exposure.*

Molecule	Plasma Device	MS products	Abundance Rel. to Parent Molecule
Adenine	CD+, mesh	Adenine+O	1.7%, 0.9%
	SMD LP	Adenine+O	<0.5%
Guanine	SMD LP	<b>Guanine+O</b>	<b>125%, 13%</b>
	SMD LP	Guanine+2O+2H	28%, 31%
	SMD LP	Guanine+2O	16%, 22%
Cytosine	SMD LP	<b>Cytosine+2O</b>	<b>~85%</b>
Thymine	SMD LP	<b>Thymine-C+2O</b>	<b>&gt;&gt;100%</b>

SMD LP = Surface microdischarge, low power

### 5.3.3 Discussion

In this preliminary study, we confirmed that guanine is the most readily oxidized nucleobase, a fact well known in the biological literature. [249], [250] Adenine and cytosine are not reported to have a high oxidation/nitration/nitrosation efficiency in the literature; thus, it is not surprising that only low levels of oxidation were observed. This may be related to the higher degree of protonation at neutral and slightly acidic pH. [251]

Previous work by Cui et al. showed that singlet oxygen ( $^1\text{O}_2$ ), peroxyxynitrite, and  $\gamma$ -irradiation (which produces  $\text{OH}^\bullet$  and hydrated electrons in aqueous solutions) resulted in different ratios of guanine oxidation products. Future studies could potentially use this strategy to determine the likely active species responsible for plasma-induced guanine oxidation. The adenine + O adduct could also be one of a number of structures, including 2-oxoadenine, 8-hydroxyladenine, etc.

The loss of a carbon atom from thymine suggests oxidation at the carbon to which the methyl side group is bound. The addition of two oxygen atoms further suggests an ozone-mediated attack; this is consistent with our knowledge that ozone is the major oxidizing species produced by the surface microdischarge at low power [126]. Studies of ozonolysis of double-stranded and single-stranded DNA and of free thymine have demonstrated its susceptibility to ozone attack. [251], [252] A complex set of mechanisms leading to various decomposition products is discussed in [253].

We also were able to assess the efficacy of several types of plasma treatment – a surface microdischarge at high and low-power, and electrospray corona discharge – in modifying free DNA bases in solution. The surface microdischarge produced nucleic acid modifications consistent with the generation of ozone, as expected. Although such corona discharges are also known to produce ozone under low power conditions [254], [255], the low levels of oxidation observed suggests that the electrospray-corona discharge treatment applied in these experiments does not produce significant amounts of ozone, or that the solution-contact time is not sufficient. The low efficiency of the electrospray corona discharge helped us re-examine the reasons that we were investigating the electrospray. Specifically, the plasma-liquid contact improvement one might expect from the increase in surface area of tiny electrospray droplets is more than offset by the short residence time of the liquid in the plasma channel. Following these experiments, the corona-discharge device was modified to the setup discussed in Section 2.2.

In general, we were surprised by the complete absence of nitrated species formed. When run in high-power mode, the surface microdischarge has been shown to create large concentrations of  $\text{NO}_x$ . As this project has progressed, we still have not seen any evidence of nitration of organic compounds due to non-thermal plasma treatment.

A recent (2015) review describes roughly 50 studies in which the interactions between non-thermal plasmas and DNA and/or its constituents have been investigated. [250] The vast majority of these used an argon or helium plasma jet, although a handful of studies used some form of a dielectric barrier discharge (DBD) in air. There have been no reports of the effects of corona-like discharges on these systems, which is perhaps not surprising given the lack of approved medical devices based on this type of discharge. This review provides considerable detail on possible mechanisms of DNA and DNA base modification by numerous oxidizing species and plasma sources; the reader is pointed here for additional discussion of these topics.

#### **5.4 Effects of Non-Thermal Plasma on Amino Acids**

In this preliminary work, we examine the effects of corona-like discharges on selected amino acids. A group of the most reactive amino acids (cysteine, methionine, tryptophan, tyrosine, and histidine) were investigated, since protein modification is most likely to take place at these sites. [220] Valine was also included as an example of a species without reactive side chains. The chemical structures of these species are shown in Figure 5.6.

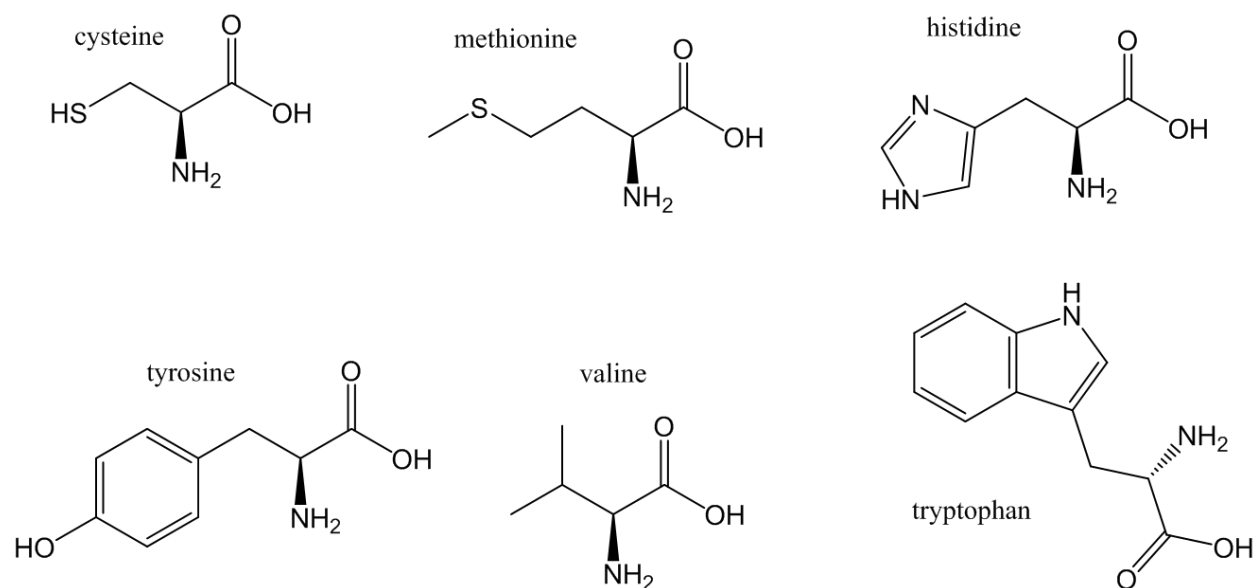


Figure 5.6. Chemical structures of amino acids used in non-thermal plasma experiments.

#### 5.4.1 Experimental Notes

Two sets of experiments involving free amino acids in water were carried out. In the first round, 1mM solutions of cysteine, histidine, tyrosine and valine were electrosprayed through a positive- or negative-polarity corona discharge, as in the nucleic acid experiments.

In the second round, 5mL of solution containing 1mM of methionine, tryptophan or histidine was placed in a reservoir with submerged electrode and exposed to a positive- or negative-polarity corona discharge for either 5 or 20 minutes. The applied voltage was 10kV, the ballast resistance was 20 M $\Omega$ , and the inter-electrode (pin-to-solution) distance was 5mm. For the negative-polarity corona discharge experiments, this resulted in a trichel pulse discharge with a frequency of 3-5 MHz and peak currents of 0.3-0.4 mA. For the positive-polarity corona discharge experiments, this resulted in a streamer discharge with a frequency of 25-30 kHz and peak currents of 20-30 mA. The electrode arrangement used in these experiments is shown in Figure 5.7.

All samples were analyzed on a ThermoFisher Orbitrap mass spectrometer unless otherwise noted.

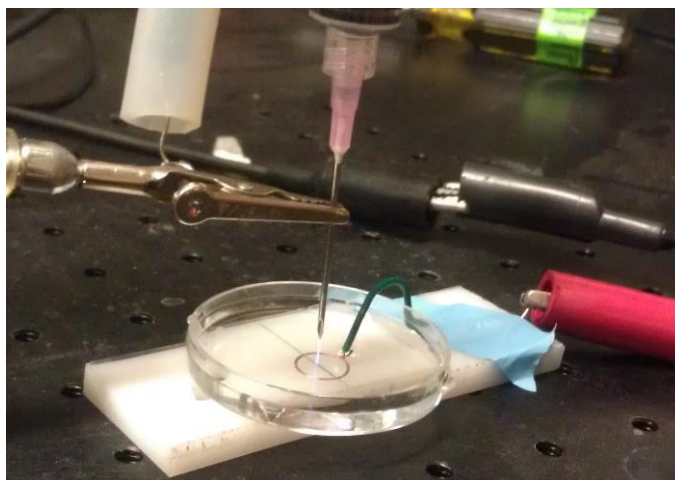


Figure 5.7. Electrode configuration for positive polarity corona discharge (streamer) treatment of 1mM methionine, histidine and tryptophan solutions. In the negative polarity experiments, the needle is grounded and the high-voltage probe (alligator clip attached to needle) is instead placed in the path from the copper “ring” electrode (loop of submerged copper wire) to ground.

#### 5.4.2 Results

The results of ESI-MS analyses of the plasma-treated solutions of each amino acid are described below. Cysteine, tyrosine and valine were electrosprayed through positive or negative polarity corona discharge. Mass spectra of these solutions are included at the end of this chapter (Figure 5.18 through Figure 5.24).

Methionine and tryptophan solutions were exposed to a streamer (positive polarity) or trichel pulse (negative polarity) plasma discharge in direct contact with the solution. Histidine solutions were both electrosprayed and treated with streamer and trichel pulse discharges directly. Tables of all adducts observed in the streamer and trichel pulse experiments, the intensity (relative abundance) of these species compared to the signal from the unmodified amino acid, and the assigned chemical formula based on exact mass are included at the end of this chapter (histidine: Table 5.3, methionine: Table 5.4, and tryptophan: Table 5.5).

*Cysteine.* The cysteine reference sample displays signals at an  $m/z$  of 122.03 (cysteine) and 241.03 (disulfide-bound cysteine dimer, cystine). The C(+) sample (positive-polarity electrospray) contains a strong adduct signal at  $m/z = 257.03$ , corresponding to cystine with added oxygen (cystine + O), and a weak signal at 138.02 (cysteine + O). Both C(+) and C(-) samples contain a very small signal at 154.02, corresponding to the two-oxygen adduct of cysteine, cysteine + 2O.

The negative polarity C(-) electrospray sample showed a smaller signal at  $m/z = 257.03$  (cysteine + O), and also resulted in a very small signal at 154.02 (cysteine + 2O). The signal from the disulfide dimer relative to reduced cysteine is stronger in the C(-) sample. This is somewhat surprising given that the negative polarity corona creates a flux of negative ions to the solution surface, which one would expect to result in a more strongly reducing environment. Selected  $m/z$  ranges for all three electrosprayed solutions (cysteine reference, cysteine treated with positive-polarity corona discharge C(+), and with negative-polarity corona discharge C(-)) are shown in Figure 5.18, Figure 5.19, and Figure 5.20.

*Tyrosine.* Tyrosine did not appear to be modified by corona discharge treatment to a significant extent. A small signal (< 10% relative abundance of unmodified tyrosine) corresponding to the single oxygen adduct, tyrosine + O was observed in both C(+) and C(-) samples (see Figure 5.23 and Figure 5.24).

*Valine.* Valine was modified to very small extent (< 5% relative abundance of unmodified valine). In both C(+) and C(-) experiments, the adduct at  $m/z = 150.08$  (valine + 2O) was the next most abundant compound, followed by valine - 2H + O ( $m/z = 132.07$ ) and valine + O ( $m/z = 134.08$ ). A very weak signal at  $m/z = 148.06$  (valine - 2H + 2O) was also observed. (See Figure 5.25 and Figure 5.26.)

*Histidine.* Histidine solutions were only weakly oxidized by corona discharge electrospray. Only very small signals (<5% relative abundance) at  $m/z = 172.07$  and  $188.07$  corresponding to histidine + O and histidine + 2O adducts, respectively, were observed in C(+) and C(-)-treated solutions, with the signal in the C(-) case perhaps slightly larger. (See Figure 5.21 and Figure 5.22).

Histidine solutions were not significantly modified by streamer or trichel pulse treatment. An adduct at  $188.07$  (histidine + 2O) was observed in the sample exposed to the streamer discharge (CD+) for 20 min.

*Methionine.* In methionine solutions treated for 20 minutes with the negative-polarity trichel pulse discharge (CD-), adducts were observed at  $m/z = 166.05$  (methionine + O, 92% relative abundance to methionine),  $148.04$  (methionine - H, 12% rel. abundance), and  $167.06$  (methionine + OH, 5% rel. abundance). The solution treated for 5 minutes contained only the methionine + O adduct (21% rel. abundance).

The solutions treated with the streamer discharge (CD+) showed larger methionine + O adducts compared to the CD(-)-treated solutions. The relative abundance of the met + O signal at 5 minutes was 29% that of the parent compound, and at 20 minutes was 183% (i.e. more methionine was present as the oxygen adduct than unmodified). The signal at  $167.06$  corresponding to methionine + OH was also observed in the solution treated for 20 minutes (5% rel. abundance).

*Tryptophan.* The most abundant adduct in trichel-pulse (CD-) treated tryptophan samples was a tryptophan + 2O signal at  $m/z = 237.09$  (15% rel. abundance at 5 minutes and 59% at 20 minutes). A number of very small signals possibly corresponding to other degradation products were also observed; because the intensity of these signals was increased in the 20 minute sample relative to the 5 minute sample, it is likely that they arose from plasma treatment (rather than unrelated degradation processes). Adducts observed in the 20 minute sample were at  $m/z = 221.09$  (Trp + O, 7.4%),  $192.07$  (Trp - C - N - 3H + O, 6.2%), and  $220.06$  (Trp - N - 3H + 2O, 5.3%). These adducts were also visible in the 5 minute sample at relative abundances of < 2%.

Exposure to the streamer corona discharge (CD+) resulted in greater modification of tryptophan in solution. The signal from tryptophan + 2O present ( $m/z = 237.09$ ) was 150% that of the unmodified amino acid in the sample treated for 20 min. Three other adducts had relative intensities of more than 50%:  $209.09$  (Trp - C + O, 74%),  $192.07$  (Trp - C - N - 3H + O, 64%) and  $221.09$  (Trp + O, 47%). These species were also observed in the 5 minute sample at lesser intensities.

### 5.4.3 Discussion

Of the solutions investigated (cysteine, histidine, tyrosine, and valine), only cysteine solutions were significantly modified by electrospray plasma treatment. Electrospray treatment is considered to be a relatively weak non-thermal plasma treatment due to the short contact time between the plasma and the

liquid (which is limited to the amount of time necessary for the liquid to traverse the inter-electrode gap). The pulsed nature of these discharges also means that there may not be active plasma present in the inter-electrode channel for the majority of the time, such that the liquid is exposed to a different set of species (slow-moving cations and neutrals) remaining in the space.

In solutions treated directly with a corona-like discharge (streamer or trichel pulse), significant modifications to methionine and tryptophan were observed. The streamer discharge (positive polarity) appears to be more effective than the trichel pulse (negative polarity) at oxidizing these amino acids at the same applied voltage. A greater variety of oxidation products was observed in tryptophan treated solutions, although the ratio of modified to unmodified compounds was significantly greater for methionine solutions. Because these solutions were unbuffered, the final pH of these solutions is expected to be slightly acidic (more so for the streamer-treated solutions).  $\text{H}_2\text{O}_2$  and  $\text{NO}_2^-$  were likely formed by the plasma in these solutions; thus, peroxyxynitrite chemistry may have contributed to the oxidation of these amino acids.

Peroxyxynitrous acid is known to react with methionine at the sulfhydryl site, yielding methionine sulfoxide and nitrite. [223] Cysteine and methionine are also attacked at the sulfhydryl group by  $\text{O}_3$ , at rate constants greater than  $10^6 \text{ M}^{-1} \text{ s}^{-1}$ , with cysteine being the most reactive followed by tryptophan and methionine, then histidine, then others. [256] Thus, it is likely that the oxygen adducts observed correspond to these species, rather than products with oxygen at other locations.

There is an enormous body of literature devoted to the effects of various oxidizing species on amino acids, both free and in proteins. Reviews on the reactivity of individual oxidizing species, e.g. hydroxyl radicals [257], ozone [256] and peroxyxynitrite [223], with amino acids and the associated mechanisms and decomposition products are available. More specifically, reviews on the effects of singlet oxygen [258] and Fenton chemistry [259] on tryptophan as determined by mass spectrometry can be found to help guide structural determination of the degradation products observed, if this work is continued. Indeed, the plasma community has begun to participate in this area; Takai et al. published a summary of modifications to 20 free amino acids resulting from exposure to a helium jet in 2014. [260]

## 5.5 Further Study of Targets Containing Sulfhydryl Moieties

In biological systems, the antioxidant glutathione (and other groups containing sulfhydryl (R-SH) moieties) play a critical role in maintaining the redox balance. The effect of non-thermal plasma on solutions of such molecules is thus of particular interest, particularly in determining the extent to which damaging irreversible oxidation of these species occurs.

As previously discussed, oxidizing species typically react with cysteine at the sulfhydryl (-SH) side chain. Mass spectrometry analyses indicated the formation of a cysteine + oxygen adduct. The addition of an oxygen atom to the (-SH) group to form (-SOH) is one possible interpretation of the mass spectrometry results, but other products may form as well. This is particularly true if the oxidizing species is the highly reactive hydroxyl radical  $\text{OH}^\bullet$  or hydrated electrons, which can react more indiscriminately. Here, we begin to investigate the NMR-active products generated by non-thermal plasma in solution to gain more information about the structure and identity of these compounds.

In this section, we look at the effect of the non-thermal plasma discharge studied in Chapter 4, the transient spark discharge, on two simple targets containing sulfhydryl groups: free cysteine and glutathione. In this preliminary work, NMR is used as a tool to compare the effects of transient spark treatment vs other oxidizing treatments (Fenton reagents or O=NOOH precursors) on cysteine (Section 5.5.1) and glutathione (Section 5.5.2).

### 5.5.1 Cysteine

Because NMR analyses requires relatively high concentrations (or more exactly, a high number of “spins”) to observe a population of nuclei at a particular site, attempts were made to increase the concentration of plasma-modified species. This was primarily done by decreasing the solution volume such that the ratio of modified to unmodified targets would be higher for a given plasma exposure, i.e. using the “thimble cell” (0.8 mL) or 0.2 mL of solution pipetted directly onto a copper electrode (“bare electrode”) rather than the 5 mL “standard cell”. These cathode geometries were shown in Figure 2.8.

The  $^1\text{H}$  NMR spectrum of buffered solution of cysteine, treated on the bare electrode with a transient spark for 3 min, is shown in Figure 5.8. Clearly this treatment is sufficiently harsh that decomposition products are observed. The peaks at locations A and D arise from unmodified cysteine, while the remaining peaks represent degradation products. The large peaks at sites B, D, and E were found to be correlated through COSY experiments, indicating that they arise from the same molecule (possibly serine, formed through the loss of the  $-\text{SH}$  group). Smaller quantities of other products are visible at F, G, H and between 3.2 and 3.4 ppm. This pattern of modification was also observed in thimble-cell transient spark experiments, with the ratio of the B-C-E signal intensity to the parent compound increasing with increasing treatment time.

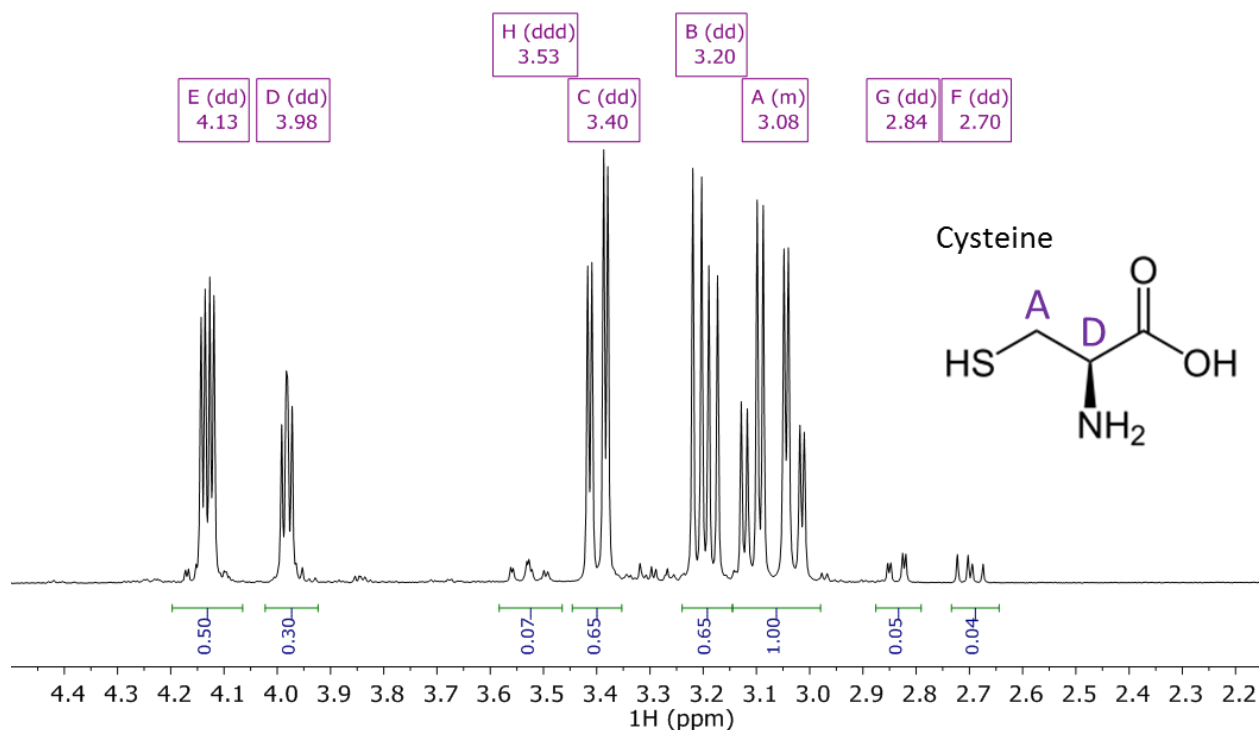
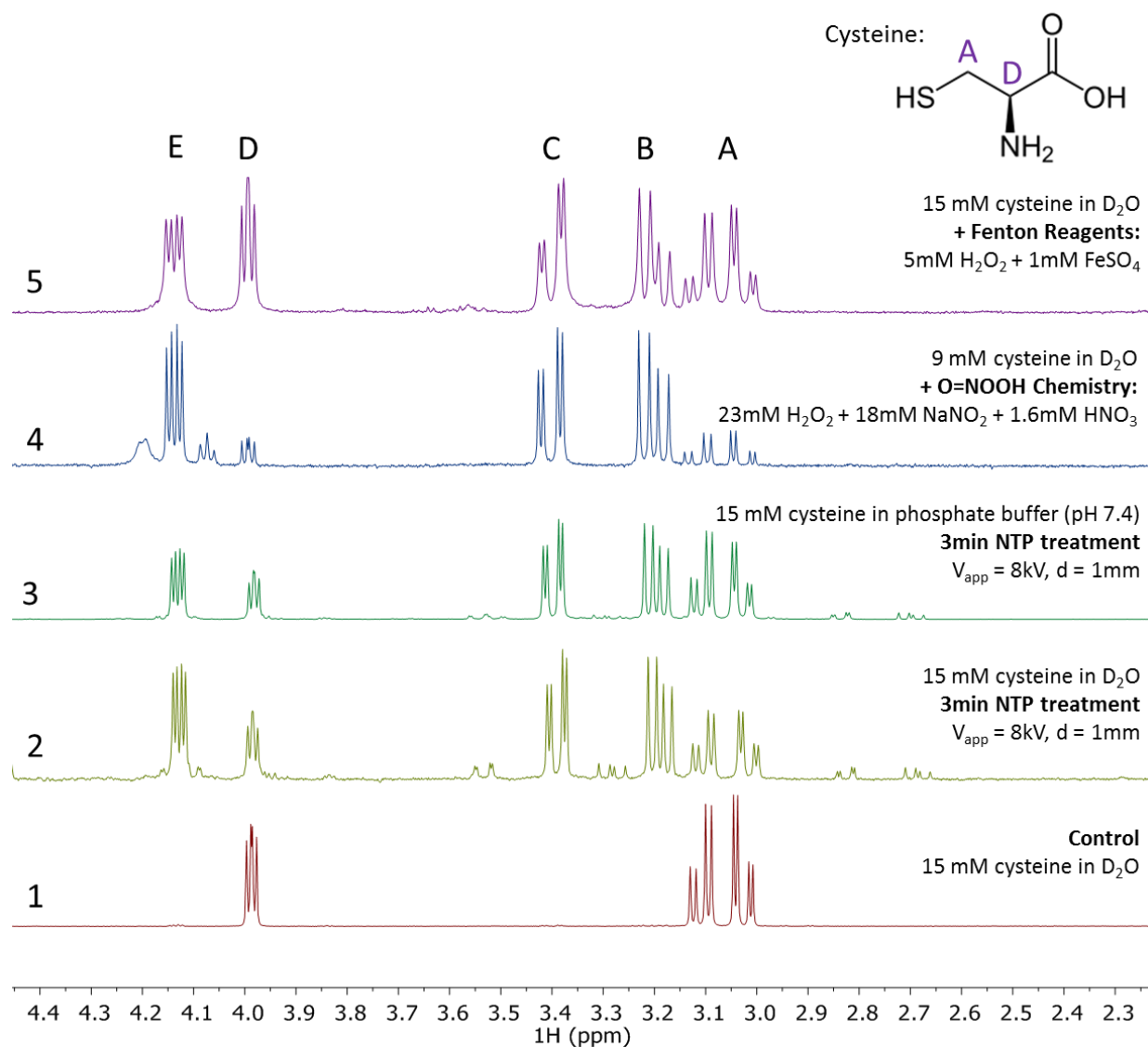


Figure 5.8.  $^1\text{H}$  spectra of 15mM cysteine in 10mM phosphate buffer (pH = 7.4) after 3min transient spark treatment. For transient spark treatment, the applied voltage was 8kV and 0.2 mL of solution was pipetted directly onto copper electrode. The distance between the anode and liquid surface was 1 mm. This spectra was acquired on an Avance Bruker 400MHz system using an excitation sculpting water suppression pulse sequence and represents 128 scans. Multiplet analysis of each significant peak is shown in purple; peaks A and D arise from protons on cysteine, as shown. The integrated peak areas are shown in blue (referenced to the two protons at site A).

The degradation products of cysteine exposed to the transient spark (observed with  $^1\text{H}$  NMR) are consistent with those arising from other oxidizing treatments, specifically exposure to Fenton reagents (the combination of  $\text{H}_2\text{O}_2$  and  $\text{Fe}^{2+}$ , which forms  $\text{OH}^\bullet$ ) and  $\text{O}=\text{NOOH}$  precursors. This indicates that the same end products are formed in each case. The  $^1\text{H}$  NMR spectra of solutions exposed to each treatment, including treatment of unbuffered solutions and solutions buffered to physiological pH (7.4) with non-thermal plasma (NTP), are shown in Figure 5.9. A single main decomposition product was observed with  $^1\text{H}$  signals at 3.19(dd), 3.39(dd), and 4.13(dd) ppm. Additional  $^1\text{H}$  peaks at 4.07 and 4.20 ppm were present in the solution exposed to  $\text{O}=\text{NOOH}$  precursors ( $\text{H}_2\text{O}_2$  and  $\text{NO}_2^-$ ).

This analyses does not capture the formation of cystine (RS-SR), which is less soluble and tends to settle out as a white precipitate. The formation of disulfide bonds in these simple solutions could be probed with Ellman's reagent [261], [262] or other techniques. The proton chemical shifts will likely not reflect oxidation of the  $-\text{SH}$  group to  $-\text{SOH}$ ,  $-\text{SO}_2\text{H}$ , etc., which can instead be identified through mass spectrometry as previous discussed. Mass spectrometry or  $^{13}\text{C}$  NMR would also be needed to identify products without C-H bonds, such as oxalic and oxamic acid, which have been identified as products of Fenton chemistry. [263]





*Figure 5.9. <sup>1</sup>H NMR spectra of cysteine solutions, following exposure to various oxidizing agents or non-thermal plasma, NTP, as indicated. See structure at top for proton peak assignments for unmodified cysteine. Spectra were referenced to 1mM TMS, which was added to the sample just before analysis (e.g. after oxidizing treatment). In the NTP treatments, 0.2 mL of solution was placed directly on the electrode surface, forming a droplet; the inter-electrode distance was set such that the anode was 1mm above the droplet surface. Slightly more degradation is observed in the unbuffered (acidic) NTP treatment (yellow) relative to the solution treated at pH 7.4 (green). Additional peaks at 4.20 and 4.07 ppm were observed in the sample exposed to O=NOOH chemistry.*

### 5.5.2 Glutathione

Modifications to glutathione in solution due to non-thermal plasma treatment (NTP) with a transient spark discharge were consistent across experiments performed in the thimble-cell (TC) and with the solution

sitting on the bare electrode (BE). The loss of  $^1\text{H}$  signal at 2.97 ppm (e) relatively to other peaks suggests that the region near the  $-\text{SH}$  functional group has been selectively modified. This pattern of modification (loss of signal at peak (e)) is consistent across the oxidizing treatments considered, which should all result in the production of  $\text{OH}^\bullet$ . The  $^1\text{H}$  spectra from unmodified glutathione and glutathione solutions after transient spark and other oxidizing treatments are shown in Figure 5.10. The extent to which each peak corresponding to unmodified glutathione is reduced, relative to the protons at site (b) (which did not appear to be significantly modified) is shown in Table 5.2. While the protons at site (e) underwent the greatest degree of oxidation in all cases, the signal arising from the protons at location (c) also decreased slightly (to 85-90% of that of its neighbors at (b)). The protons at (d) were at least partially saturated by the water suppression pulse sequence used in experiments with oxidizing agents, such that their signal could not be quantified. The signal from protons at site (f) was convoluted with other peaks in several instances, preventing quantitative integration.

The results of exposure to Fenton reagents are shown in two spectra in Figure 5.10, one taken immediately after treatment, and one 24 hours later. The small proton peaks between 3.0–3.4 ppm and 4.3–4.4 ppm observed in the sample immediately analyzed are absent in the later sample, suggesting that these products are transient and undergo further degradation reactions following oxidizing treatment. These types of effects may have important biological implications, and may be responsible for the efficacy of “plasma-activated media” in other studies. It would be interesting to follow the evolution of these products on an hourly (or greater) basis following plasma or oxidizing treatment to estimate the lifetimes of these species.

Additional 2D NMR analyses or other analytical techniques are required to assign the peaks appearing in Figure 5.10. A gCOSY spectrum of a glutathione solution exposed to “artificial PAW” ( $\text{H}_2\text{O}_2$  and  $\text{NO}_2^-$ , resulting in the formation of  $\text{O}=\text{NOOH}$ ) is shown in Figure 5.11. This spectrum indicates that the peaks at 3.0, 3.3 and 3.4 ppm arise from the same compound, and gives some information about their connectivity. Other couplings among smaller abundance products between 3.5 and 4.0 ppm, and near the water peak at 4.8 - 5.0 ppm, are also visible.

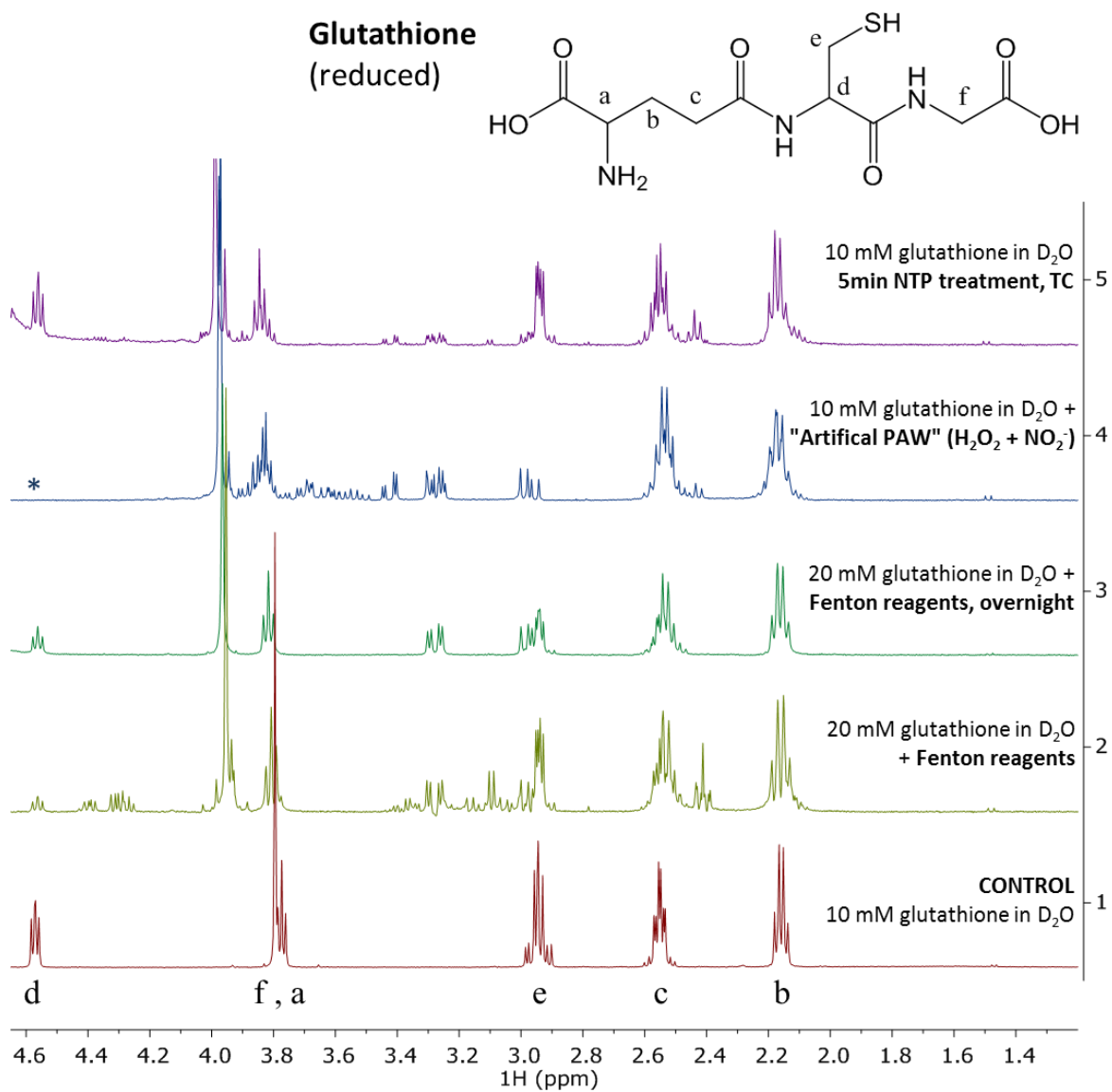


Figure 5.10.  $^1\text{H}$  NMR spectra of GSH solutions, following exposure to various oxidizing agents (2-4) or non-thermal plasma, NTP (5). See structure at top for proton peak assignments. (\*) indicates loss of signal due to water suppression.

Table 5.2. Extent to which signal from each peak is reduced by oxidizing agent, relative to peak **b** which is relatively unreactive. An asterisks (\*) indicates that the signal could not be integrated, either due to interference from water suppression (d) or due to convolution with peaks arising from degradation products (f).

Peak	#H/GSH	<sup>1</sup> H δ, ppm	<sup>1</sup> H signal, relative to <b>b</b>					Fenton + 24hr
			Control	NTP	H <sub>2</sub> O <sub>2</sub>	O=NOOH	Fenton	
a	1	3.77 (t)	100%	90%	100%	100%	90%	100%
b	2	2.17 (q)	-	-	-	-	-	-
c	2	2.54 (td)	100%	85%	100%	93%	90%	90%
d	1	4.56 (t)	100%	*	100%	*	*	25%
e	2	2.94 (m)	100%	50%	100%	0%	50%	35%
f	2	3.80 (s)	100%	*	100%	*	*	100%

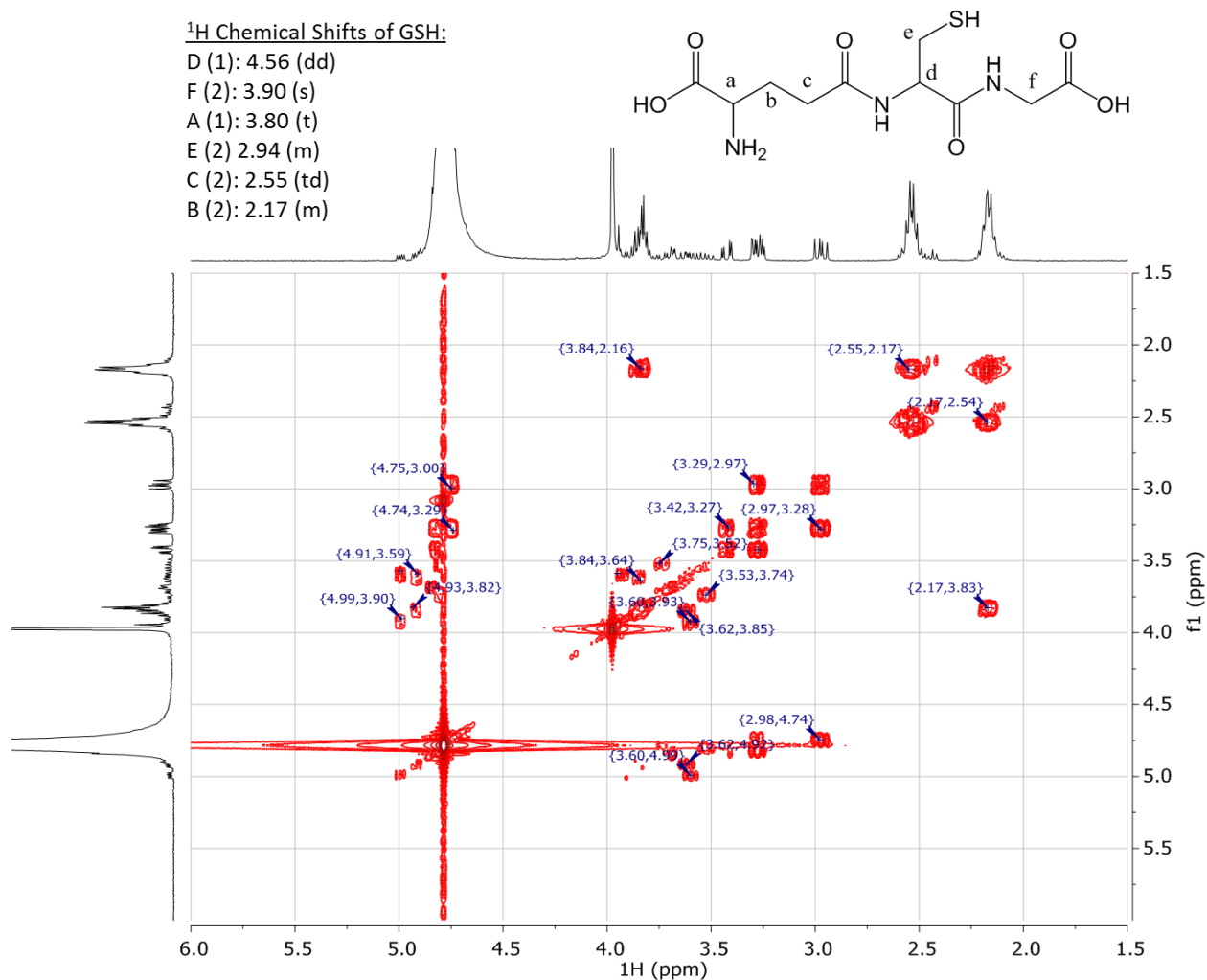


Figure 5.11. gCOSY spectrum of 10mM glutathione in D<sub>2</sub>O oxidized with “artificial PAW”: 25mM H<sub>2</sub>O<sub>2</sub>, 20mM NaNO<sub>2</sub>, and 1.8mM HNO<sub>3</sub>. Spectrum was acquired on an Avance Bruker 400 instrument with broadband probe. The structure and assignments for unmodified glutathione are shown at top. The protons at site ‘e’ are no longer visible, indicating that oxidation has occurred at the sulfhydryl group. The cluster of new peaks in the 4.7 – 5.0 ppm range correlated with signals between 3.0 and 3.9 suggest hydrated reaction products. The signals at 2.97, 3.29 and 3.42 ppm are clearly correlated, indicating that they arise from the same molecule / decomposition product.

## 5.6 Conclusions

Preliminary studies of the effects of non-thermal plasma on nucleic acid and selected amino acid solutions demonstrates the ability of non-thermal plasma to oxidize these species. Studies of the five nucleic acids (adenine, cytosine, guanine, thymine and uracil) showed that guanine was the most readily oxidized by non-thermal plasmas, forming one- and two-oxygen adducts, followed by thymine, which is hypothesized to react with plasma-generated ozone to yield a  $-C + 2O$  adduct (structure currently undetermined).

Preliminary work on species containing sulfhydryl (-SH) groups, specifically cysteine, methionine, and glutathione, showed that these species are oxidized by non-thermal plasma treatment to a greater extent than other free amino acids. Mass spectrometry analyses of cysteine and methionine solutions demonstrated that non-thermal plasma produces oxygen adducts of these compounds, as expected based on the oxidizing nature of plasma-generated species. Studies of similar solutions with NMR indicated that other decomposition products are formed as well, largely from oxidation at atoms near the sulfhydryl moiety. Although we have established that the NMR-active products produced by non-thermal plasma treatment are consistent with the reaction products of GSH and  $OH^\bullet$  produced from other sources ( $O=NOOH$  and Fenton chemistry), identification of these byproducts must await further experiments and a careful analysis of this substantial body of literature.

## 5.7 Supplementary Information: Mass spectra of nucleic and amino acids

The following pages contain the various mass spectra referenced in the preceding results sections.

# Adenine

## Entire Spectra

Chemical Formula:  $C_5H_5N_5$

Exact Mass: 135.0545

m/z: 135.0545 (100.0%), 136.0579 (5.4%), 136.0515 (1.8%)

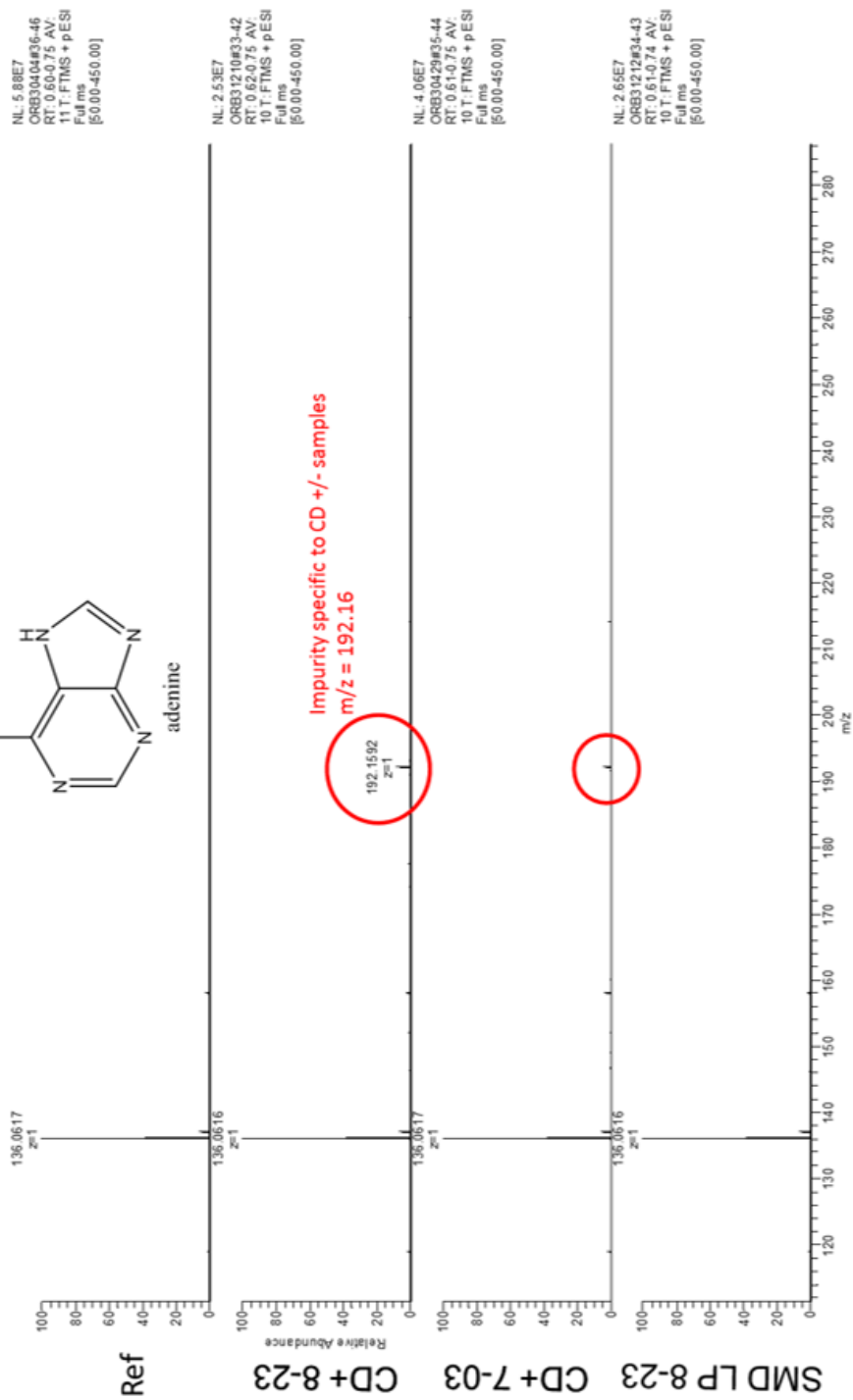
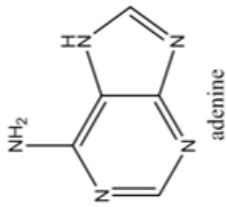
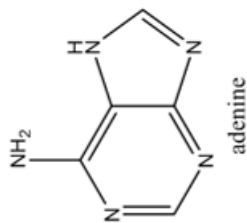


Figure 5.12. Comparison of adenine solutions treated with either a surface microdischarge (SMD) at low power (LP) or electrosprayed through a positive-polarity corona discharge (CD+). Two samples of CD+ solutions were analyzed (7-03 and 8-23).

# Adenine

Spectra outside of main Adenine peak (136),  $m/z = 140 - 250$



NL 1.50E6  
ORB30404#36-46  
RT: 0.60-0.75 AV.  
11 T: FTMS + p ESI  
Full ms  
[50.00-450.00]

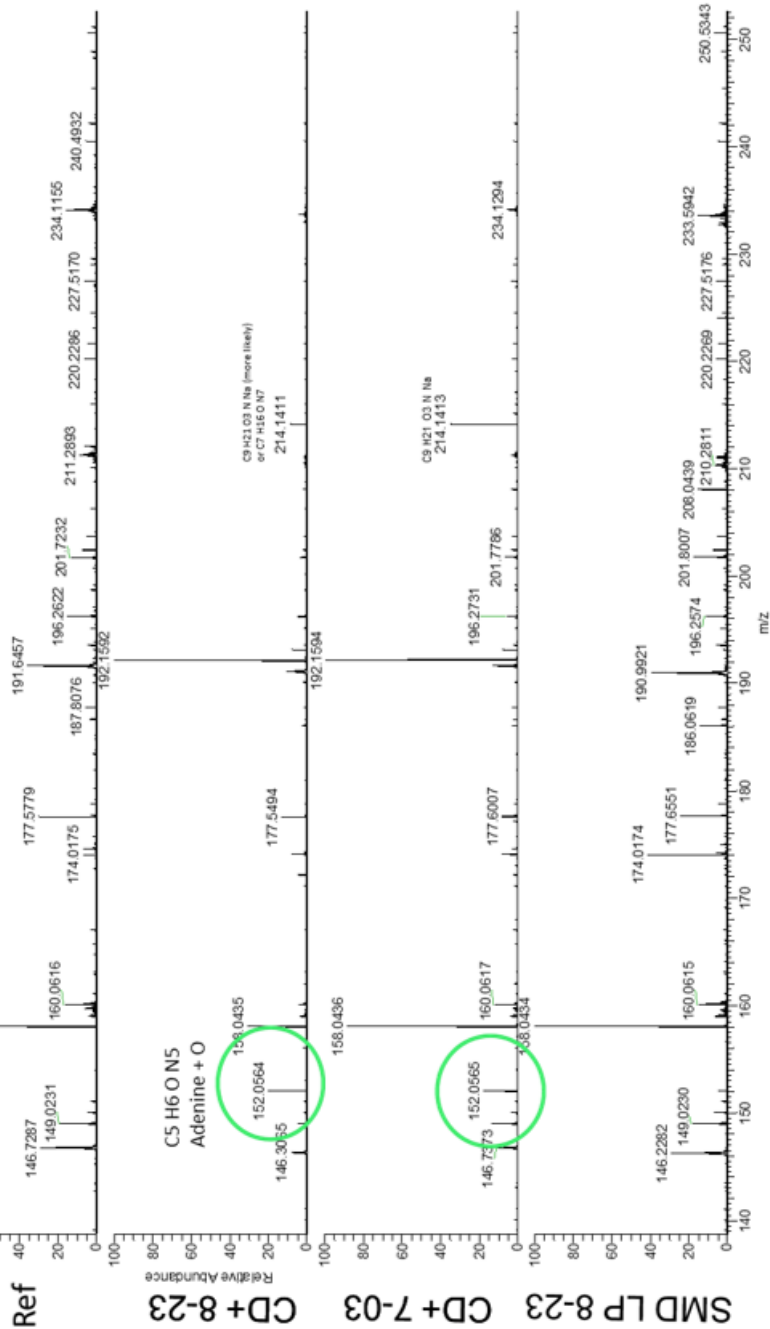


Figure 5.1.3. ESI-MS analysis of adenine solutions exposed to non-thermal plasma. Enlarged view of the region between  $m/z = 140$  and  $250$  for adenine solutions treated with a surface microdischarge (SMD) or positive-polarity corona discharge (CD+).



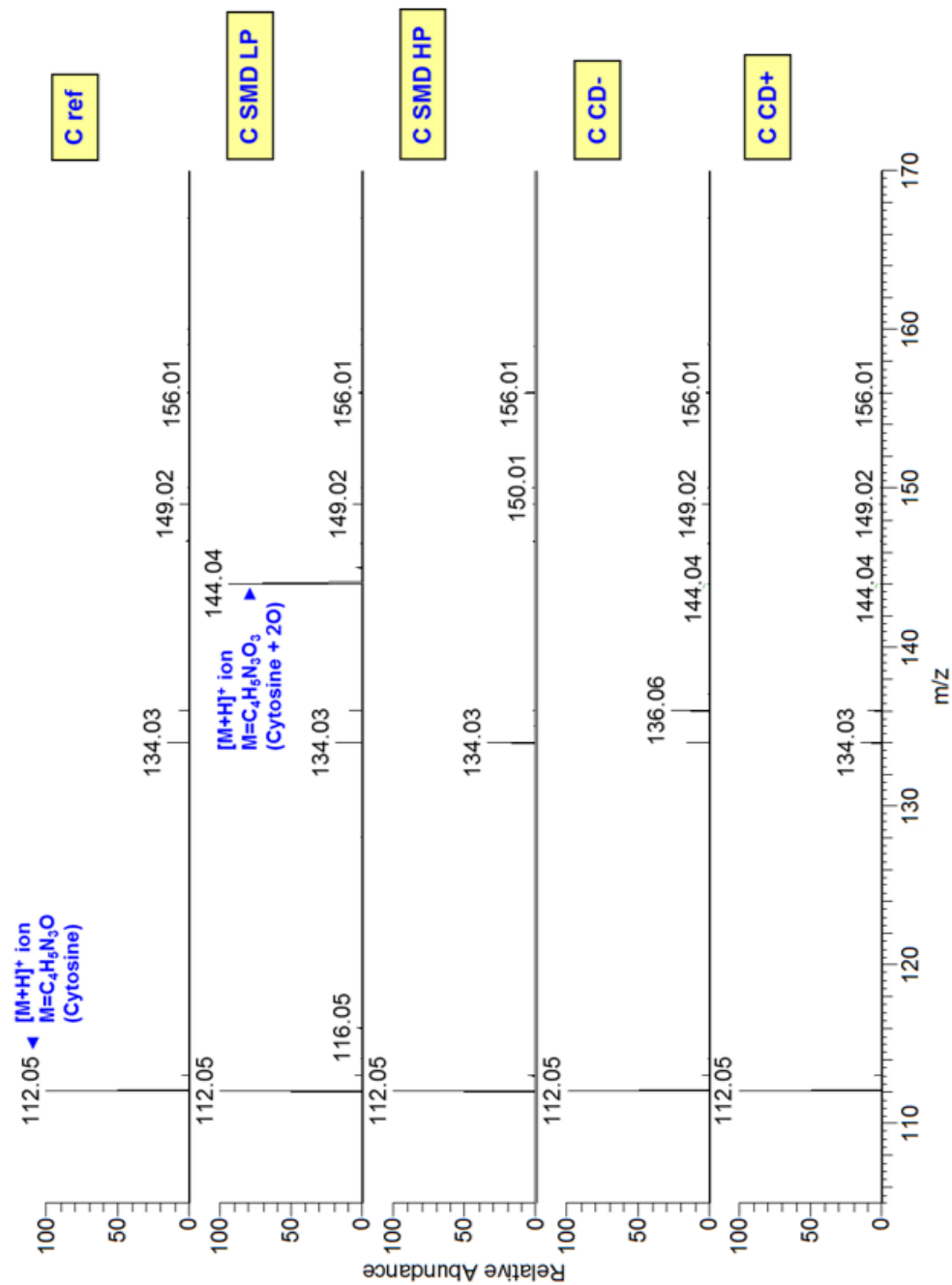
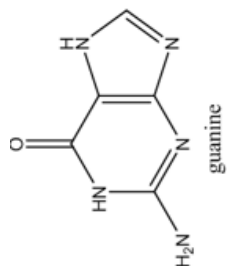


Figure 5.14. Comparison of cytosine (C) solutions treated with either a surface microdischarge (SMD) at low power (LP) or high power (HP), or electrosprayed through a positive-polarity corona discharge (CD+) or negative polarity corona discharge (CD-). The entire range of mass-to-charge ratios ( $m/z$ ) is shown.

# Guanine

## Entire spectra



NL: 1.32E6  
ORB30450463-43  
RT: 0.60-0.76 AV:  
11 T: FTMS + pESI  
Full ms  
[50.00-450.00]

NL: 4.15E5  
ORB31207463-42  
RT: 0.60-0.76 AV:  
10 T: FTMS + pESI  
Full ms  
[50.00-450.00]

NL: 4.31E5  
ORB3041964-44  
RT: 0.60-0.76 AV:  
11 T: FTMS + pESI  
Full ms  
[50.00-450.00]

NL: 2.49E6  
ORB30437464-44  
RT: 0.60-0.76 AV:  
11 T: FTMS + pESI  
Full ms  
[50.00-450.00]

NL: 2.10E6  
ORB31208462-42  
RT: 0.60-0.76 AV:  
11 T: FTMS + pESI  
Full ms  
[50.00-450.00]

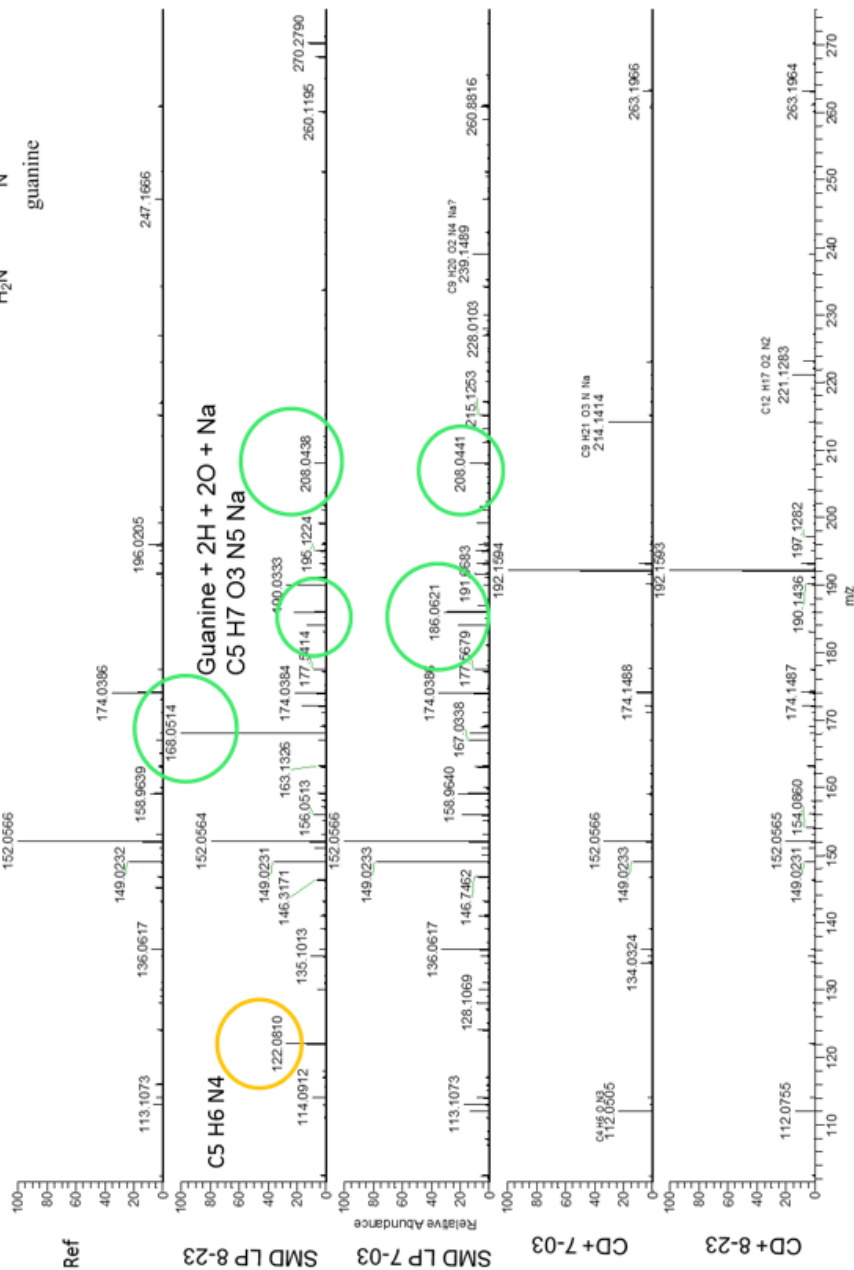


Figure 5.15. Comparison of guanine solutions treated with either a surface microdischarge (SMD) at low power (LP) or electrosprayed through a positive-polarity corona discharge (CD+). Two samples of CD+ solutions were analyzed (7-03 and 8-23).

# Thymine

Comparing SMD LP and CD+ results, entire spectra

Chemical Formula: C<sub>5</sub>H<sub>6</sub>N<sub>2</sub>O<sub>2</sub>  
Exact Mass: 126.0429  
m/z: 126.0429 (100.0%), 127.0463 (5.4%)

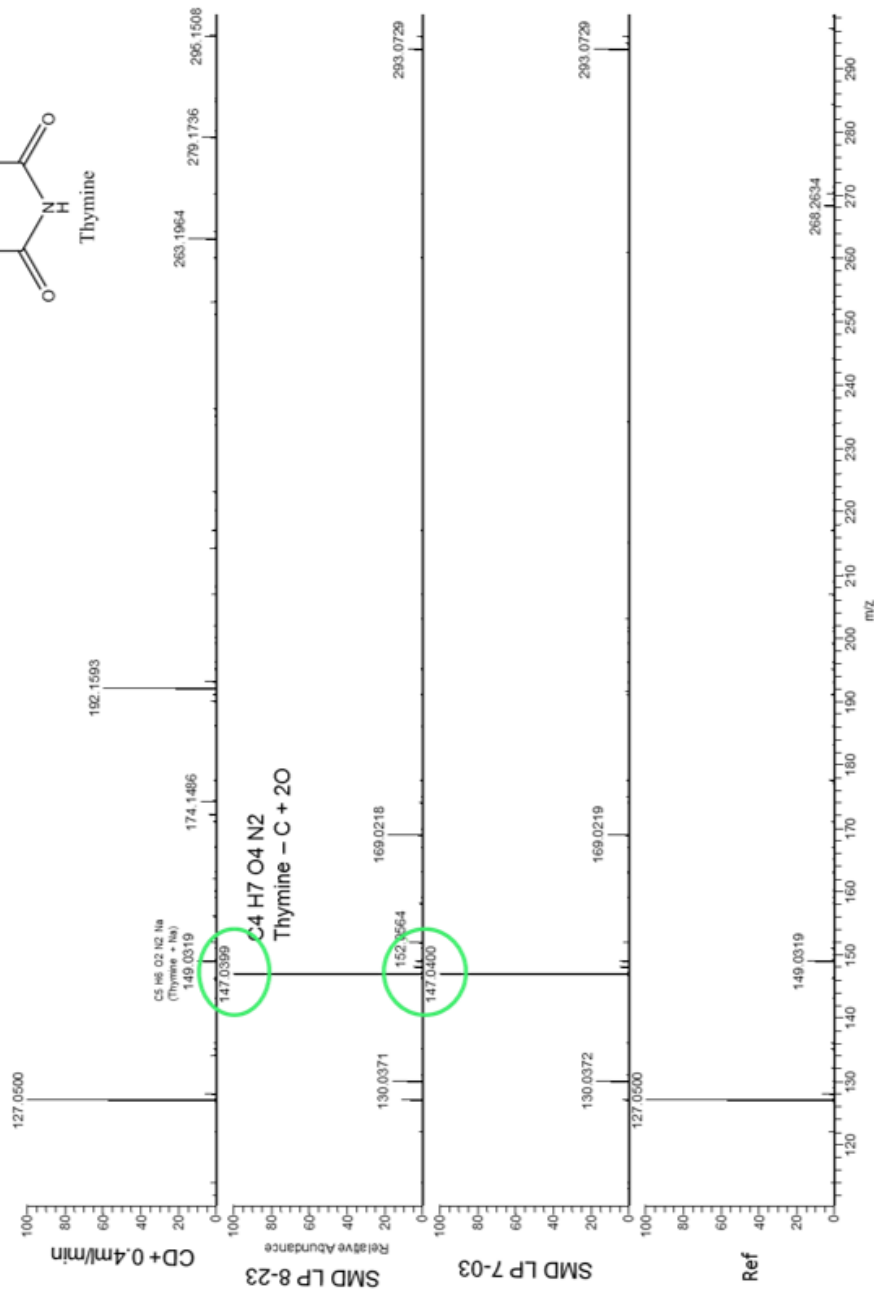
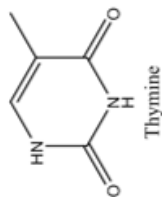


Figure 5.16. Comparison of thymine solutions treated with either a surface microdischarge (SMD) at low power (LP) or electrosprayed through a positive-polarity corona discharge (CD+) at high flow rate (0.4 mL/min). An untreated 1mM thymine solution is also shown as reference (Ref). Two samples of SMD LP-treated solutions were analyzed (7-03 and 8-23); significant oxidation to the -C + 2O adduct is observed in both.

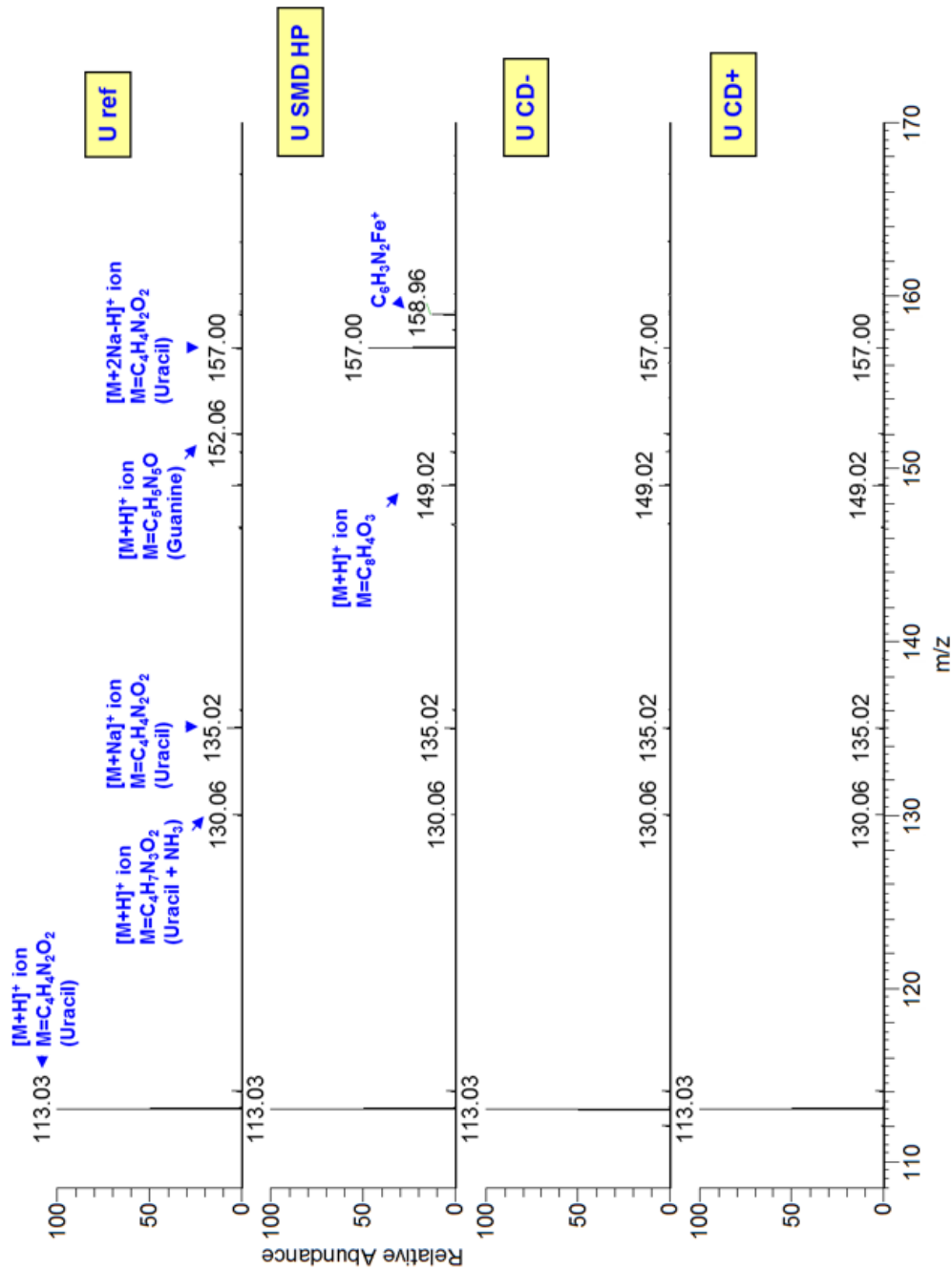


Figure 5.17. Comparison of uracil (U) solutions treated with either a surface microdischarge (SMD) at high power (HP), or electrospayed through a positive-polarity corona discharge (CD<sup>+</sup>) or negative polarity corona discharge (CD<sup>-</sup>). The entire range of mass-to-charge ratios (*m/z*) is shown.

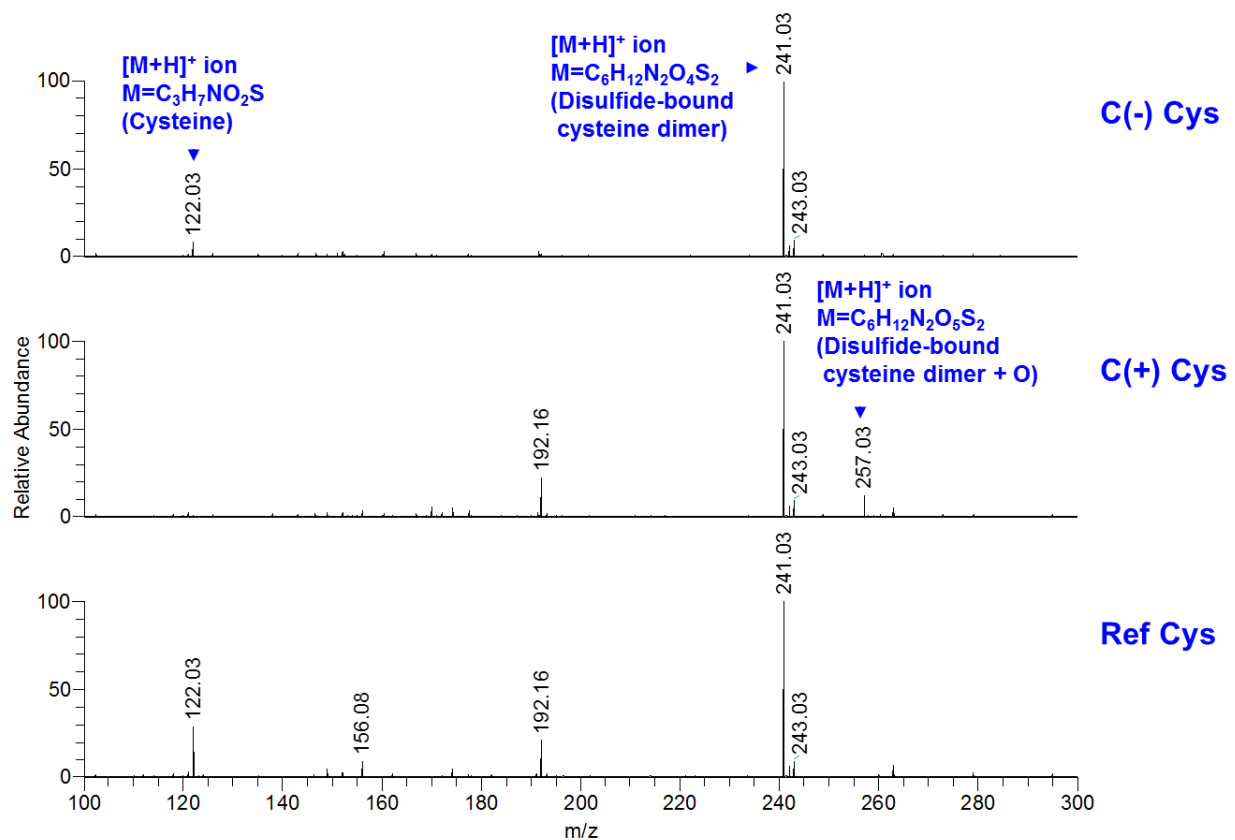


Figure 5.18. ESI-MS spectra of 1 mM cysteine solutions electrosprayed through either a negative polarity corona discharge (C-), a positive polarity corona discharge (C+), or not exposed to plasma (Ref) over the entire mass-to-charge (m/z) range of detection. .

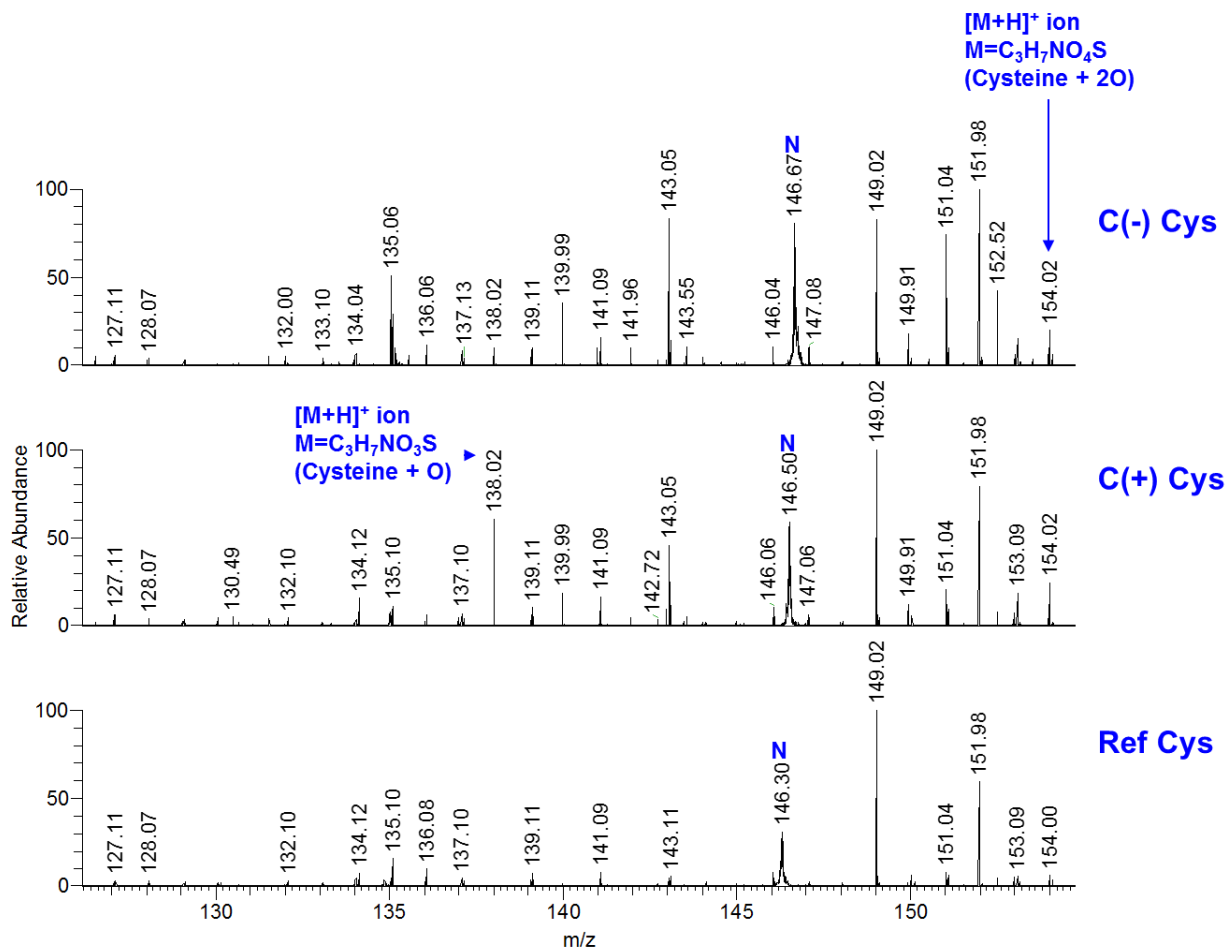


Figure 5.19. ESI-MS spectra of 1mM cysteine solutions electrosprayed through either a negative polarity corona discharge (C-), a positive polarity corona discharge (C+), or not exposed to plasma (Ref) over the mass-to-charge ( $m/z$ ) containing oxygen adducts, 125 – 155. The relative abundance (y-axis) is compared to the largest peak visible in the spectrum, not the parent compound cysteine.

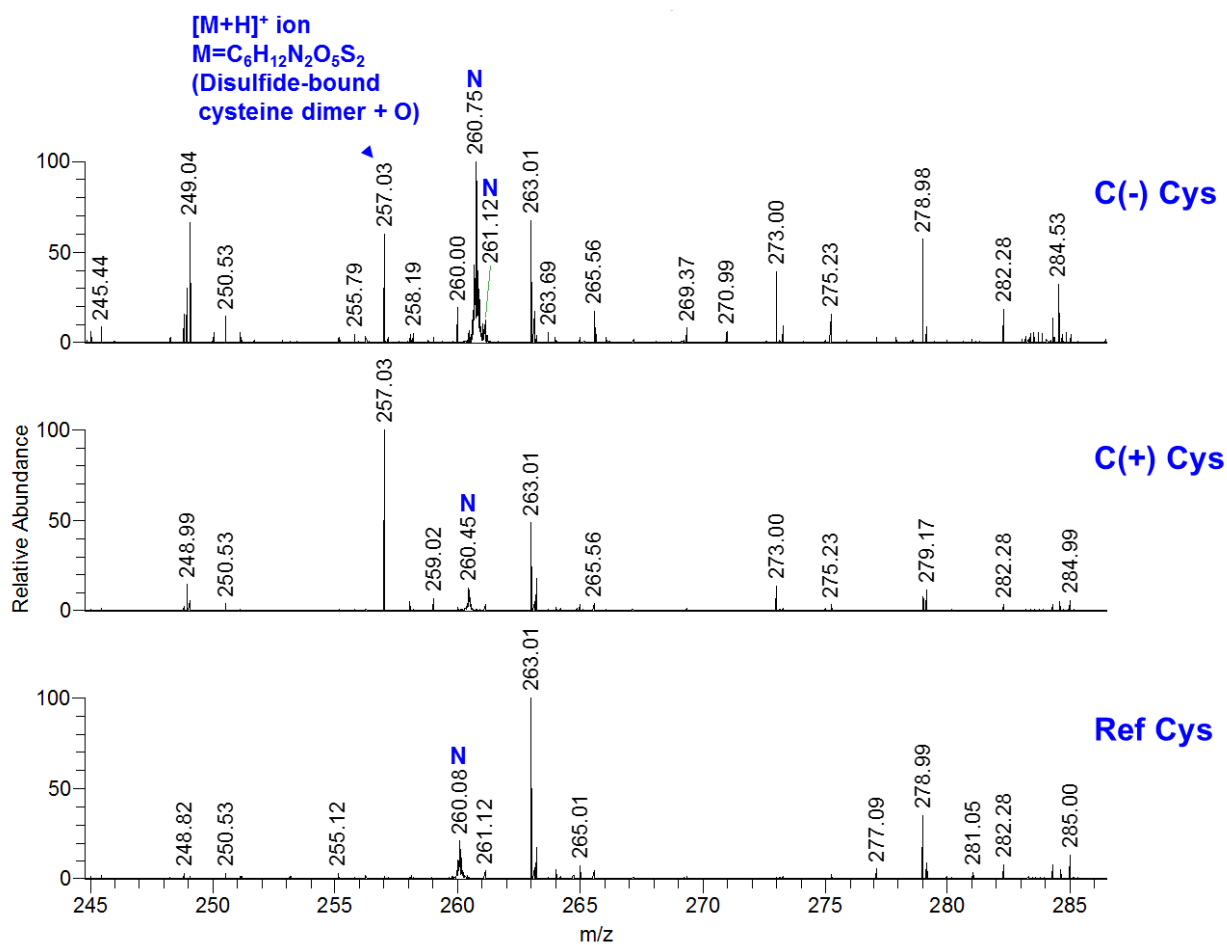


Figure 5.20. ESI-MS spectra of 1mM cysteine solutions electrosprayed through either a negative polarity corona discharge (C-), a positive polarity corona discharge (C+), or not exposed to plasma (Ref) over the mass-to-charge (m/z) range near the mass of the cysteine dimer, cystine, and oxidized products, 245 – 285. The relative abundance (y-axis) is compared to the largest peak visible in the spectrum, not the parent compound cysteine.

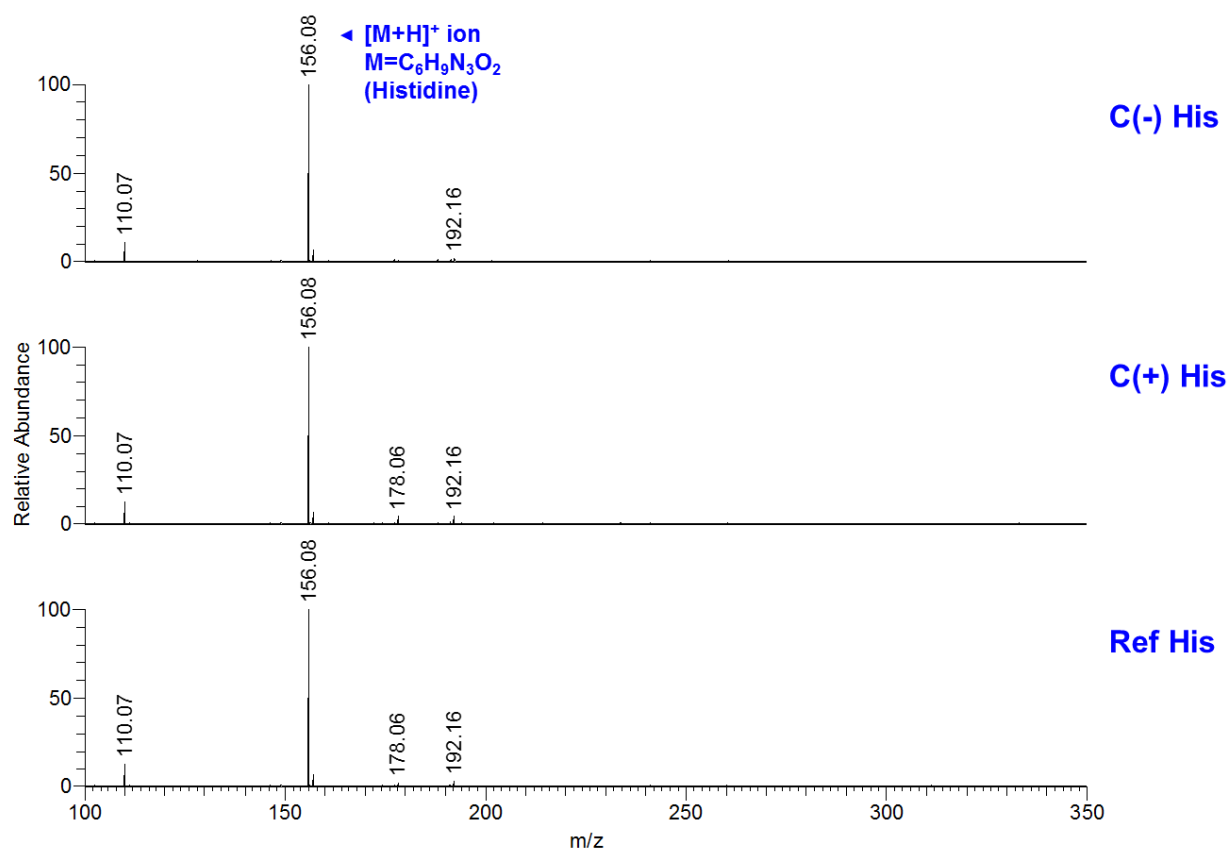


Figure 5.21. ESI-MS spectra of 1mM histidine solutions electrosprayed through either a negative polarity corona discharge (C-), a positive polarity corona discharge (C+), or not exposed to plasma (Ref) over the entire mass-to-charge ( $m/z$ ) range of interest.



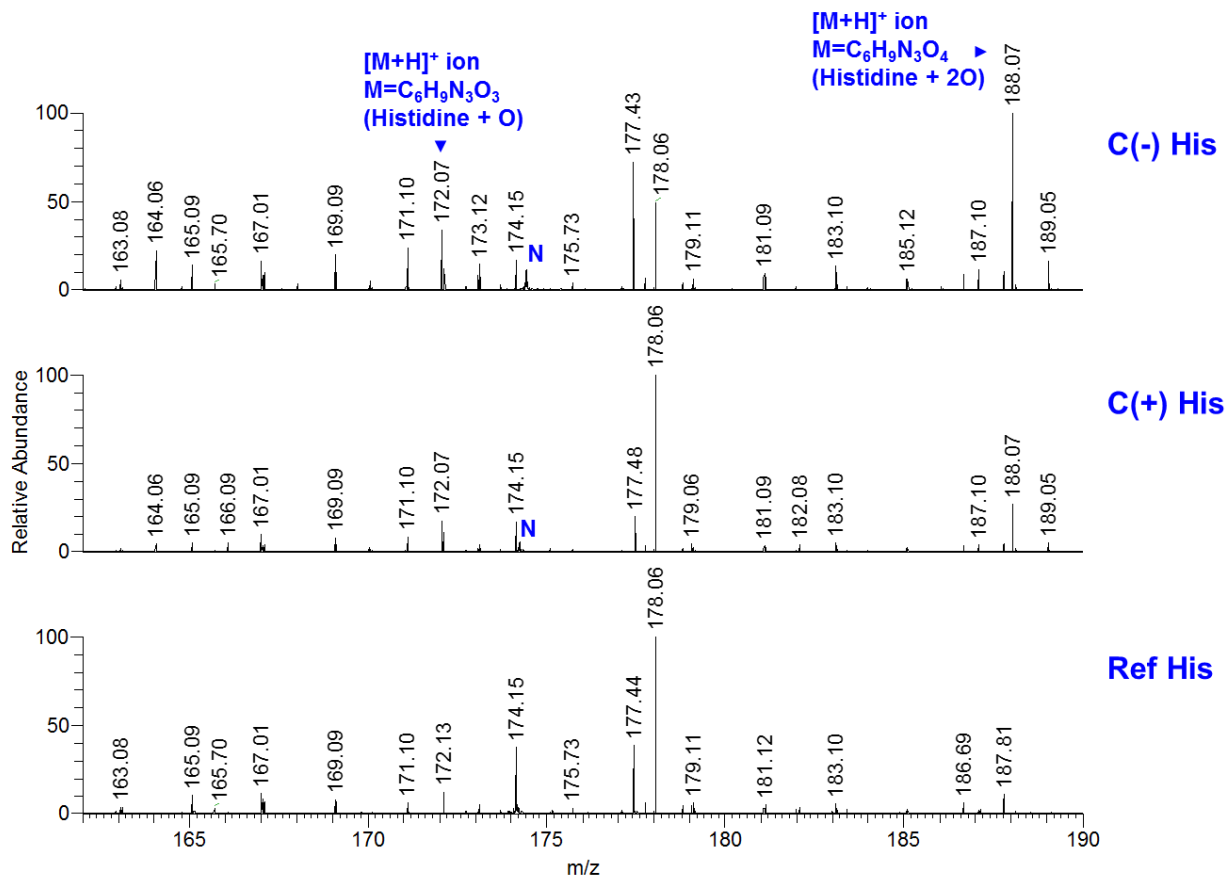


Figure 5.22. ESI-MS spectra of 1mM histidine solutions electrosprayed through either a negative polarity corona discharge (C-), a positive polarity corona discharge (C+), or not exposed to plasma (Ref) over the mass-to-charge (m/z) range around histidine adducts. The relative abundance (y-axis) is compared to the largest peak visible in the spectrum, not the parent compound histidine.

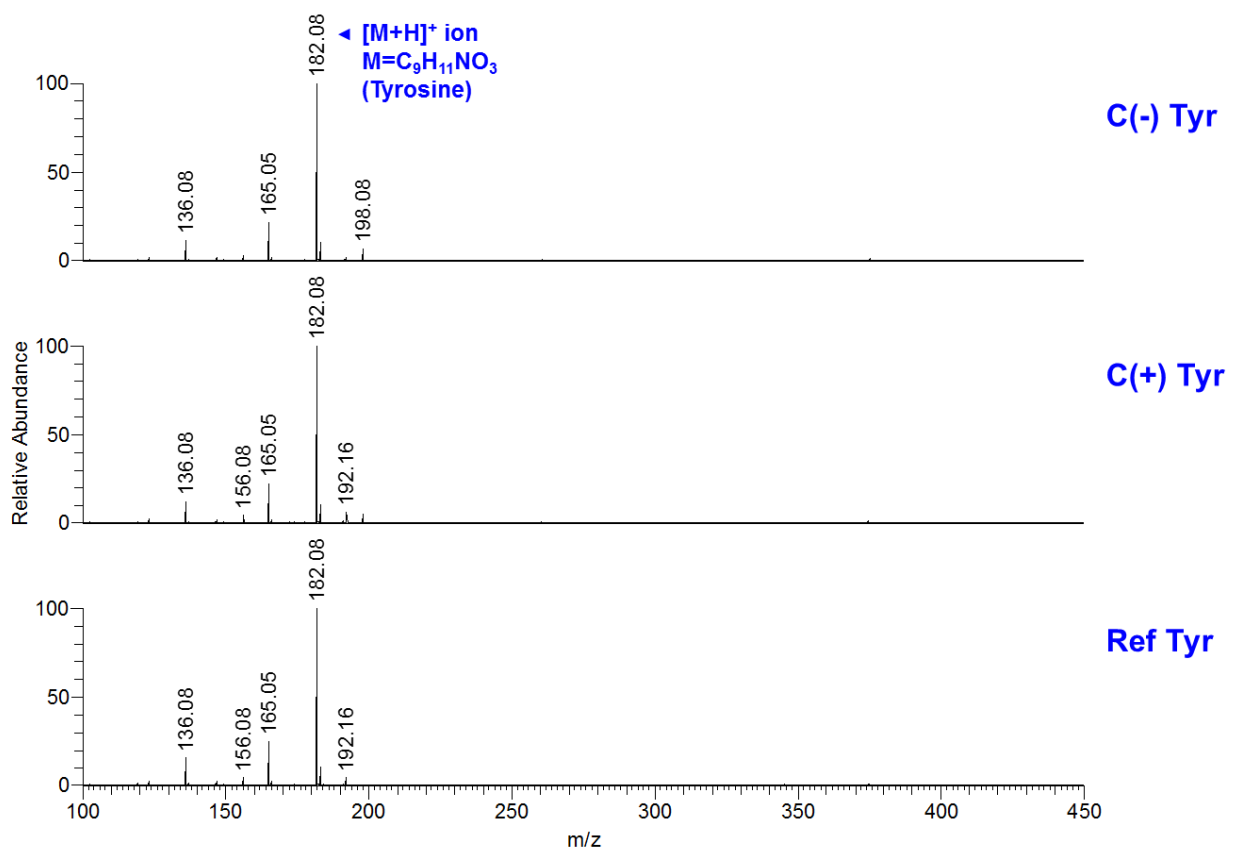


Figure 5.23. ESI-MS spectra of 1mM tyrosine solutions electrosprayed through either a negative polarity corona discharge (C-), a positive polarity corona discharge (C+), or not exposed to plasma (Ref) over the entire mass-to-charge (m/z) range of interest.

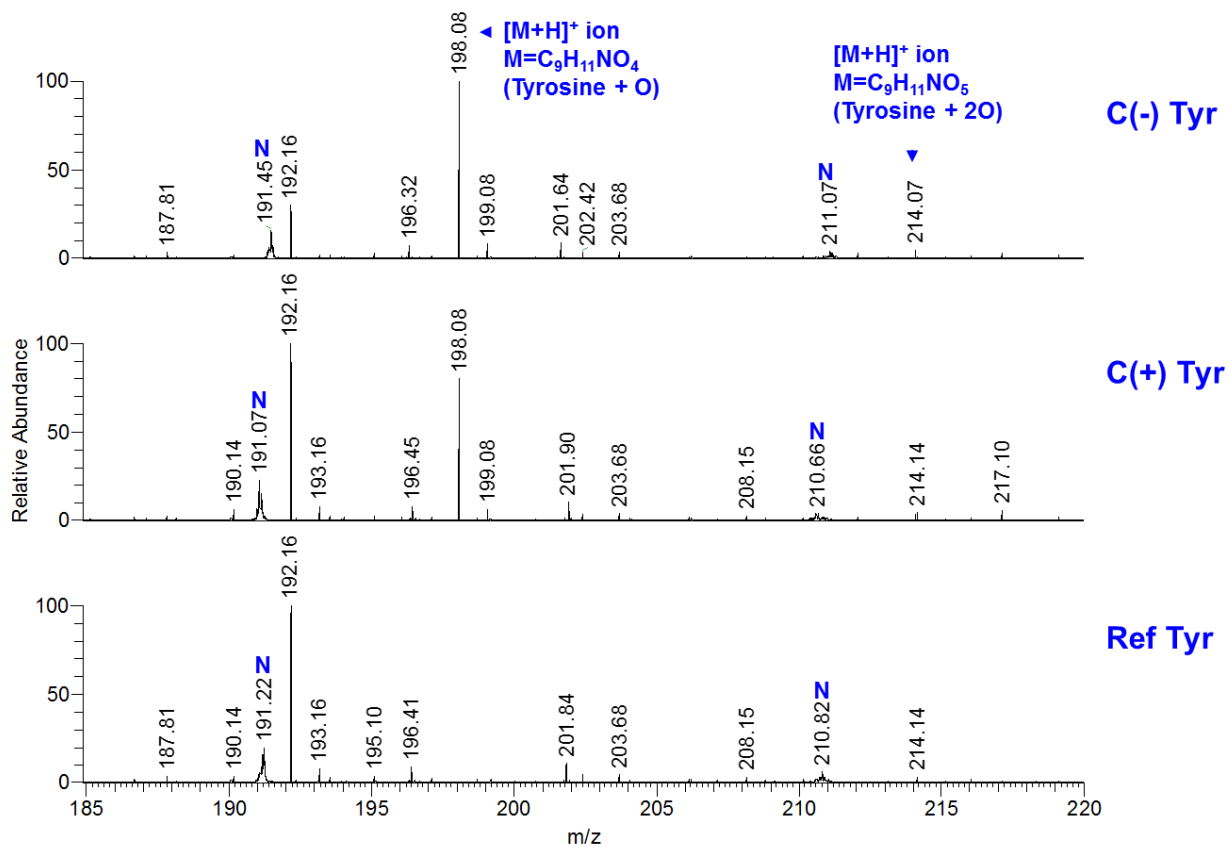


Figure 5.24. ESI-MS spectra of 1mM tyrosine solutions electrosprayed through either a negative polarity corona discharge (C-), a positive polarity corona discharge (C+), or not exposed to plasma (Ref) over the mass-to-charge ( $m/z$ ) range around the tyrosine + oxygen adducts. The relative abundance (y-axis) is scaled to the largest peak visible in the spectrum, not the parent compound tyrosine.

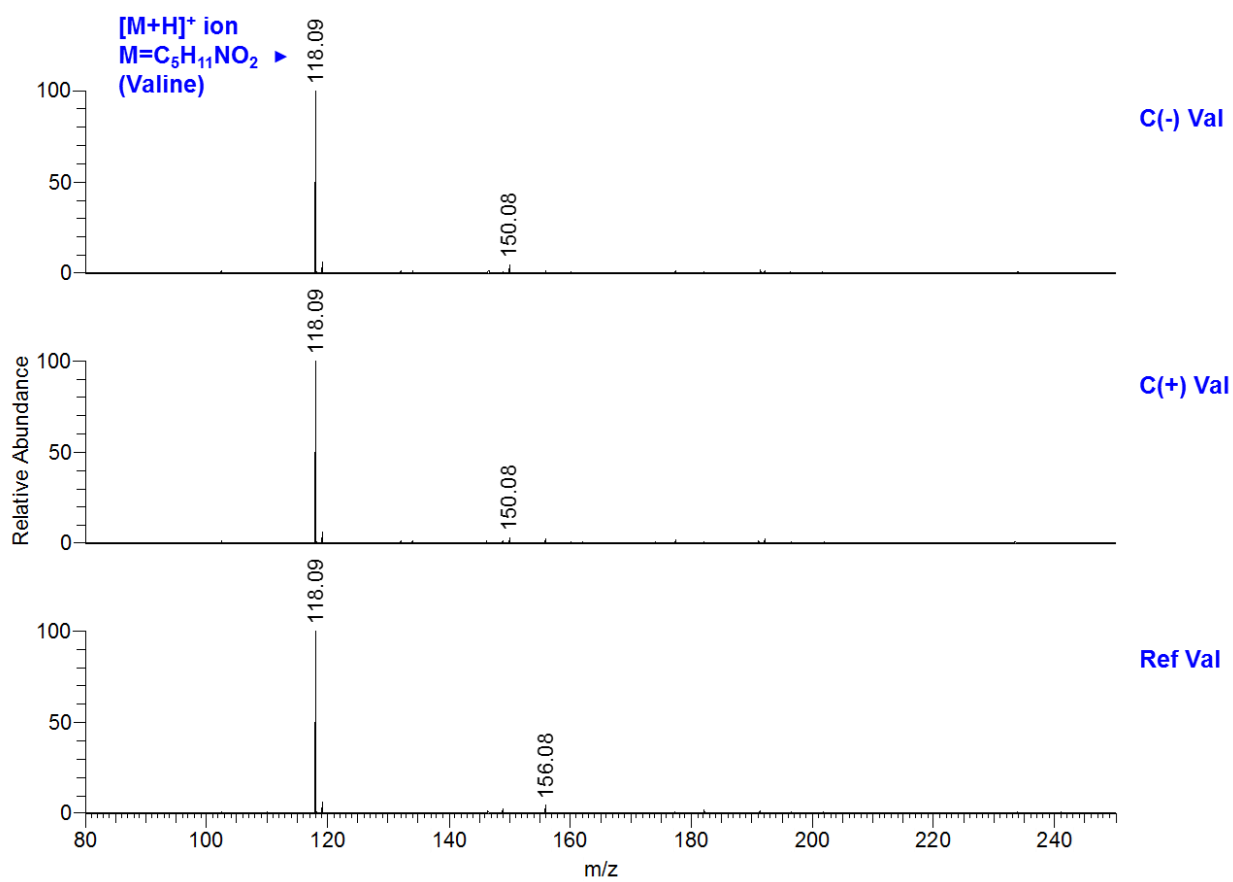


Figure 5.25. ESI-MS spectra of 1mM valine solutions electrosprayed through either a negative polarity corona discharge (C-), a positive polarity corona discharge (C+), or not exposed to plasma (Ref) over the entire mass-to-charge (m/z) range of interest.

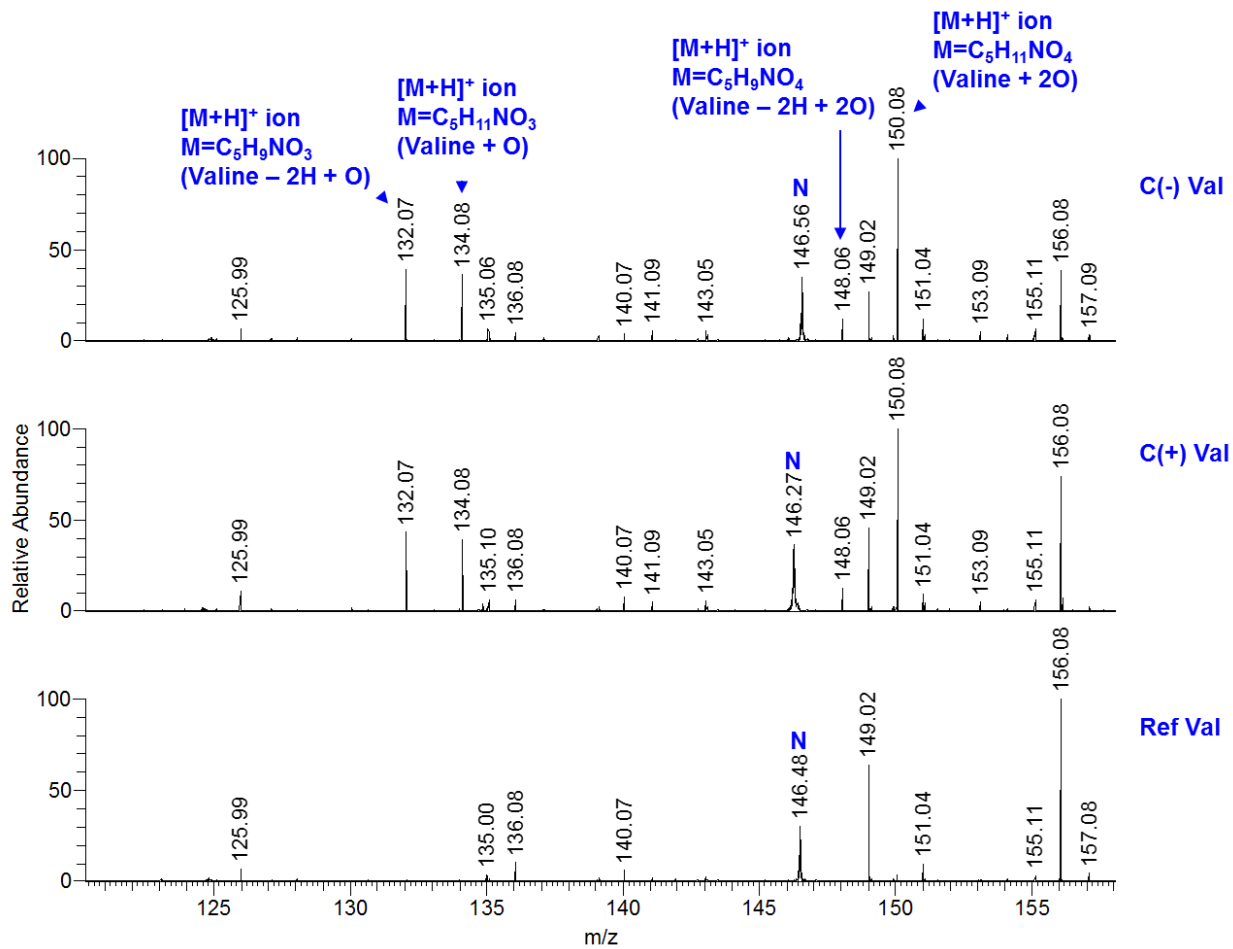


Figure 5.26. ESI-MS spectra of 1mM valine solutions electrosprayed through either a negative polarity corona discharge (C-), a positive polarity corona discharge (C+), or not exposed to plasma (Ref) over the mass-to-charge (m/z) range around the valine + oxygen adducts. The relative abundance (y-axis) is scaled to the largest peak visible in the spectrum, not the parent compound valine.

Table 5.3. Adducts of histidine observed with ESI-MS after solutions containing 1mM methionine were treated with either a trichel pulse plasma discharge (CD-) or a streamer plasma discharge (CD+) for the amount of time indicated.

Amino Acid	Chemical formula and mass of parent	Discharge Mode	Treatment Time	m/z	Chemical Formula	Intensity rel. to parent	Adduct
His	C6H9N3O2+H	CD-	5 min		NO SIGNIFICANT MODIFICATION		
His	156.0767	CD-	20 min		NO SIGNIFICANT MODIFICATION		
His	C6H9N3O2+H	CD+	5 min		NO SIGNIFICANT MODIFICATION		
His	C6H9N3O2+H	CD+	20 min	188.0665	C6H9N3O4+H	5.33	His+2O
	156.0767			161.0556	C5H8N2O4+H	5.3	His-C-N-H+2O

Table 5.4. Adducts of methionine observed with ESI-MS after solutions containing 1mM methionine were treated with either a trichel pulse plasma discharge (CD-) or a streamer plasma discharge (CD+) for the amount of time indicated.

Amino Acid	Chemical formula and mass of parent	Discharge Mode	Treatment Time	m/z	Chemical Formula	Intensity rel. to parent	Adduct
Met	C5H11NO2S+H	CD-	5 min	166.0532	C5H11NO3S+H	21.4	Met+O
	150.0582			188.0352	C5H11NO3S+Na	7.34	Met+O
				134.035	C5H9O2S+H?	1.48	Met-NH2
Met	C5H11NO2S+H	CD-	20 min	166.0532	C5H11NO3S+H	92.13	Met+O
	150.0582			188.0352	C5H11NO3S+Na	18.99	Met+O
				148.0427	C5H9NO2S+H	12.34	Met-H
				167.0565	C5H12NO3S+H	5.04	Met+OH
				134.035	C5H9O2S+H	1.36	Met-NH2
Met	C5H11NO2S+H	CD+	5 min	166.0532	C5H11NO3S+H	28.8	Met+O
	150.0582			188.0352	C5H11NO3S+Na	6.65	Met+O
				134.035	C5H9O2S+H?	1.67	Met-NH2
Met	C5H11NO2S+H	CD+	20 min	166.0532	C5H11NO3S+H	183.28	Met+O
	150.0582			188.0352	C5H11NO3S+Na	31.76	Met+O
				167.0564	C5H12NO3S+H	5.35	Met+OH
Met	C5H11NO2S+H	S+	5 min	166.0532	C5H11NO3S+H	57.35	Met+O
	150.0582			188.0352	C5H11NO3S+Na	23.97	Met+O
				167.0565	C5H12NO3S+H	2.93	Met+OH

Table 5.5. Adducts of tryptophan observed with ESI-MS after solutions containing 1mM methionine were treated with either a trichel pulse plasma discharge (CD-) or a streamer plasma discharge (CD+) for the amount of time indicated.

Amino Acid	Chemical formula and mass of parent	Discharge Mode	Treatment Time	m/z	Chemical Formula	Intensity rel. to parent	Adduct
Trp	C11H12N2O2+H	CD-	5 min	237.0869	C11H12O4N2+H	15.19	Trp+2O
	205.0971			221.0921	C11H12N2O3+H	1.80	Trp +O?
				238.0903	C11H13O4N2+H	1.72	Trp+2O+H
				192.0655	C10H9NO3+H	1.28	Trp-C-N-3H+O
				220.0604	C11H9NO4+H	1.19	Trp-N-3H+2O
Trp	C11H12N2O2+H	CD-	20 min	237.0869	C11H12N2O4+H	59.48	Trp+2O
	205.0971			221.0921	C11H12N2O3+H	7.41	Trp +O
				192.0655	C10H9NO3+H	6.21	Trp-C-N-3H+O
				220.0604	C11H9NO4+H	5.39	Trp-N-3H+2O
				174.055	C10H7NO2+H??	4.00	Trp-C-N-4H
				202.05	C11H7NO3+H	3.34	Trp-N-5H+O
				259.0689	C11H12N2O4+Na	2.67	Trp+2O
Trp	C11H12N2O2+H	CD+	5 min	237.0869	C11H13O4N2O4	29.19	Trp+2O
	205.0971			221.0921	C11H12N2O3+H	6.55	Trp+O
				209.0921	C10H12N2O3+H	5.64	Trp-C+O
				174.055	C10H7NO2+H??	3.08	Trp-C-N-4H
				220.0605	C11H9NO4+H	2.88	Trp-N-3H+2O
				175.0867	C10H10N2O+H	2.67	Trp-C
Trp	C11H12N2O2+H	CD+	20 min	237.0871	C11H13N2O4	146.67	Trp+2O
	205.0971			209.0921	C10H12N2O3+H	74.89	Trp-C+O
				192.0655	C10H9NO3+H	64.38	Trp-C-N-3H+O
				221.0921	C11H12N2O3+H	47.40	Trp +O
				136.0757	C8H9NO+H??	26.66	Trp-3C-3H-N-O
				220.0605	C11H9NO4+H	15.76	Trp-N-3H+2O
				202.05	C11H7NO3+H	12.12	Trp-N-5H+O
Trp	C11H12N2O2+H	S+	5 min	237.087	C11H13N2O4	11.41	Trp+2O
	205.0971			192.0654	C10H9NO3+H	3.43	Trp-C-N-3H+O
				209.092	C10H12N2O3+H	2.48	Trp-C+O

## 6 Conclusions and Future Work

### 6.1 Non-thermal Plasma Device Development

The first part of this dissertation described the development and characterization of non-thermal plasma devices in contact with liquids. Specifically, a device that produces a pin-to-plane corona-like plasma discharge in direct contact with the liquid surface was studied in detail: the dominant plasma discharge mode formed as a function of the applied voltage, inter-electrode distance, and ballast resistance was established for positive polarity operation of this device. It was also shown that  $\text{H}_2\text{O}_2$  and other reactive species produced in solution can be controlled by adjusting the electrical and circuit parameters and the properties of the target solution (pH, conductivity). The resulting device can be tuned for solution acidification, greater oxidative power, limited peak current flow or other attributes depending on the user's priorities.

Corona-like discharges have several advantages over other plasma devices. They can be operated in air (do not require noble gases), operated in direct contact with a liquid, and require less complex electrical equipment than other plasma devices. The properties of the discharge can be adjusted to a great extent using the previously stated parameters, allowing access to a range of discharge modes with a single device. The convective mixing induced in the liquid phase by the ionic wind improves the uptake of some reactive species from the gas phase. While the power can also be used to adjust the active species in surface-microdischarge (SMD) plasma devices, these devices cannot be operated with a liquid electrode. While it is possible to engineer dielectric barrier devices (DBDs) in direct contact with a liquid electrode (i.e. a floating-electrode DBD, or FE-DBD), such devices is considerably more complex. Specifically, maintaining a sufficiently small yet uniform inter-electrode gap becomes challenging.

The biggest limitation of the corona discharge device developed in this work is that the plasma-liquid contact area is very small ( $\sim 0.8 \text{ mm}^2$  or less). This could be increased by creating an array of points in series (similar the approach taken by Pei et al. [116]), or by changing the electrode geometry (e.g. to a wire-to-plane). Maintaining highly consistent experimental conditions – specifically the anode curvature – is also crucial to achieving reproducible results. Despite these limitations, the corona discharge provides an excellent model system to study the fundamental interactions between non-thermal plasmas and an aqueous phase.

### 6.2 Evolution of Reactive Species in the Bulk Solution

Unbuffered solutions exposed to a transient spark discharge (and other air plasmas) are quickly acidified due to the uptake and generation of  $\text{HNO}_3$  in solution, which is also responsible for the observed changes in solution conductivity. While the flux of  $\text{H}_2\text{O}_2$  and  $\text{NO}_2^-$  into the liquid is roughly constant in time (a zero-order process), acid-catalyzed reactions result in significant consumption of these species at low pH ( $< 3.4$ ). The accumulation of relatively stable species ( $\text{H}_2\text{O}_2$ ,  $\text{NO}_2^-$ , and  $\text{NO}_3^-$ ) proceeds linearly with time in neutral solutions (pH 7.4) exposed to a transient spark discharge. The rates of  $\text{H}_2\text{O}_2$  production and nitric acid production generally increase with increasing discharge power for the streamer and transient spark discharge modes. Under acidic conditions, the rates of  $\text{H}_2\text{O}_2$  and  $\text{NO}_2^-$  consumption by other reactions become significant; this happens above a concentration of  $\sim 0.5 \text{ mM}$  at pH 3.5.



Our studies of plasma-activated water (PAW) and “artificial” PAW (containing  $\text{H}_2\text{O}_2 + \text{NO}_2^-$ ) demonstrate that the reaction products of  $\text{H}_2\text{O}_2 / \text{NO}_2^-$  can explain the activity of acidic PAW through the generation of  $\text{OH}^\bullet$ . These experiments confirmed the published third-order rate constant for the formation of  $\text{O}=\text{NOOH}$ ,  $k = 1.1 \times 10^3 \text{ M}^{-2} \text{ s}^{-1}$ , and indicated that ~24% of  $\text{O}=\text{NOOH}$  generated resulted in oxidation of a target compound, presumably through reaction with  $\text{OH}^\bullet$ . These experiments also provided evidence that exposure to a transient spark discharge does not result in significant concentrations of other, long-lived reactive species such as  $\text{O}_3$  or  $^1\text{O}_2$  in solutions of pure water or simple buffers (4-100mM phosphate or citrate buffer). The model developed for artificial PAW can thus be applied to predict oxidative processes occurring in the bulk solution during transient spark exposure.

Questions that remain regarding evolution of reactive species in bulk solution include the extent to which peroxyntrous acid ( $\text{O}=\text{NOOH}$ ) and peroxyntrite participate in oxidizing reactions, as suggested by scavenger experiments with “artificial” PAW solutions. A more complete understanding of nitrite decomposition at low pH would also help to identify contributions from other reactive intermediates (e.g.  $\text{NO}^\bullet$  and  $\text{NO}_2^\bullet$  radicals).

### 6.3 Sources of Oxidative Species in Liquids from Direct Plasma Exposure

The activity of  $\text{OH}^\bullet$  (or other highly oxidizing species) near the plasma-liquid interface dominates the effects of NEAPP treatment. This result is striking given the small area of contact between the discharge and liquid ( $<1 \text{ mm}^2$ ), and highlights the importance of gas-liquid transport phenomena in these systems. The observed surface-induced oxidation of indigo carmine could be due to either direct reaction with plasma-generated species, most likely  $\text{OH}^\bullet$ , at the interface, or other plasma effects such as UV and/or ions directly on indigo carmine. Our initial results are consistent with  $\text{OH}^\bullet$  being the primary oxidizing agent produced by this system.

The increase in indigo carmine oxidation observed at low pH may result from a) locally elevated concentrations of  $\text{H}_2\text{O}_2$ ,  $\text{NO}_2^-$ , and  $\text{NO}_3^-$  at the surface, leading to acceleration of the  $\text{O}=\text{NOOH}$  pathway in this region; b) an increase in the rate of other pH-dependent reactions involving highly reactive species near the interface, e.g.  $\text{HO}_2$ ; or c) complicating effects of the citrate buffer in solution (e.g. leading to the production of carbon-centered radicals near the interface). While we have estimated that the oxidation of indigo carmine observed could reasonably be attributed to  $\text{OH}^\bullet$  produced in the gas phase (based on LIF measurements of the gas-phase  $\text{OH}^\bullet$  density reported in the literature), this result suggests that the situation is more complicated, and that conditions in the liquid phase may strongly affect near-surface reactions.

A simple estimate of diffusive and kinetic resistances for indigo carmine oxidation, combined with the presence of convective forces in the liquid phase, strongly suggest that the arrival of reactants limits the oxidation process. Comparison of rates of dye oxidation at varied initial concentrations of indigo carmine indicates that diffusion of indigo carmine to the surface is not limiting. This suggests that, for applications in which greater oxidizing power is desired (e.g. for the elimination / mineralization of water contaminants), the focus should be on increasing the plasma-mediated generation of oxidative species rather than on transport limitations in the bulk solution.

## 6.4 Effects of Non-Thermal Plasma on Biological Targets

Preliminary studies of the effects of non-thermal plasma on nucleic acid and selected amino acid solutions demonstrates the ability of non-thermal plasma to oxidize these species. Studies of the five nucleic acids (adenine, cytosine, guanine, thymine and uracil) were consistent with expectations that guanine was the most readily oxidized by non-thermal plasmas, forming one- and two-oxygen adducts, followed by thymine, which is hypothesized to react with plasma-generated ozone to yield a  $-C + 2O$  adduct (structure currently undetermined).

Preliminary work on species containing sulfhydryl (-SH) groups, specifically cysteine, methionine, and glutathione, showed that these species are oxidized by non-thermal plasma treatment to a greater extent than the other species considered. Mass spectrometry analyses of cysteine and methionine solutions demonstrated that non-thermal plasma produces oxygen adducts of these compounds, as expected based on the results of studies producing  $OH^\bullet$  and other oxidizing agents through other methods. Studies of similar solutions with NMR indicated that other decomposition products are formed as well, with atoms near the sulfhydryl moiety being particularly susceptible to modification. Although we have established that the NMR-active products produced by non-thermal plasma treatment are consistent with the reaction products of GSH and  $OH^\bullet$  produced from other sources ( $O=NOOH$  and Fenton chemistry), identification of these byproducts must await future work.

## 6.5 Suggestions for Future Work

As this is a new area of research in the field of low temperature plasma science, there are many scientific questions, large and small, that could be pursued. A few of these are discussed below.

As discussed in Section 4.5, the reason for the increased rate of dye oxidation in acidic solutions (with citrate buffer) remains unclear. The possible effect of carbon-centered radicals produced through reactions with citrate (present at millimolar concentrations as a buffer) could be ruled out by simple experiments with varied concentrations of citrate, or by repeating these studies with different buffers. EPR could be another tool to address this question, although it is possible that spin traps for carbon-centered radicals may also be degraded by the plasma or other reactive species produced (as DMPO was). Repeating these studies at additional pH values may also give insight into whether the protonation state of indigo carmine is important. It should be remembered that below a pH of 3.4, additional  $NO_2^-$  consumption reactions become significant. The rate of  $H_2O_2$  and  $NO_2^-$  generation could be varied by changing the discharge power and related to the rate of indigo oxidation to check for correlation.

The efficiency of plasma mineralization of various compounds could also be explored to help further develop our understanding of these technologies. For example, it has been proposed that the presence of species that act as surfactants are particularly amenable to degradation in these systems, as their hydrophobic regions extend above the solution interface and can be degraded by plasma electrons (or other species in the plasma-phase). The rate of decomposition of indigo, indigo carmine, and indigo trisulfonate (species with increasing numbers of hydrophilic sulfonate groups) could be compared, along with the loss of total organic carbon (TOC), to see if this hypothesis can be extended to aromatic compounds and similar industrial pollutants.

The work with radical scavengers and positive controls could also be completed and extended. The work with positive controls ( $\text{OH}^\bullet$  through Fenton chemistry and through the production of  $\text{O}=\text{NOOH}$ ) raises additional questions about how interactions of reactive species with other solution components, namely organics, influences or creates other degradation pathways. Additional studies using  $\text{KO}_2$  to generate superoxide, rose Bengal for  $^1\text{O}_2$ , and the commercial ozone generator in lab to establish oxidation “fingerprints” for particular molecules exposed to each species may help identify the active species produced by plasma in limited situations where different decomposition products are formed.

For follow-up studies on the interactions of non-thermal plasma with biological targets, model species should be selected that are biologically relevant, experimentally well-behaved, and readily available. Ideally, their response to individual RONS would already be known. To this end, molecules such as albumin and ubiquitin may make interesting early targets. Albumin is often used as a model protein and is thought to act as a nitric oxide “sink” in cells; the addition of ubiquitin to key proteins plays an important role in cell-cycle regulation and signal transduction. [264], [265] Phosphatidylcholines (PC) may also be of interest; PCs are a major component of biological membranes that are readily available and have been studied extensively by mass spectrometry, and the efficiency of lipid peroxidation by plasma is an important question in understanding plasma-cellular interactions. Other targets, including mixtures and complex proteins, may be added as the project advances. Collaborations must be established in order to effectively and accurately perform many of the complex analyses that would be needed for this work to be informative.

There is also great potential for understanding the set of complex electrochemical reactions occurring at the interfaces in this system, both plasma-liquid and liquid-electrode. The initial work using an H-cell to separate reactions occurring at the two interfaces could be expanded to look at the gas-phase species ( $\text{H}_2$ ,  $\text{CO}_2$ ,  $\text{O}_2$ ) and liquid-phase species ( $\text{H}_2\text{O}_2$ ,  $\text{O}_2^-$ , and potentially radicals if spin traps are used) generated in various gas and liquid-phase chemistries. For such studies, it may be more interesting to look at alternative types of plasma discharges, i.e. plasma jets in noble-gas environments, or negative polarity corona discharges in order to explore the chemistry created by solvated electrons.

The field of plasma-liquid interactions is rapidly expanding and offers many opportunities to study highly complex, interdisciplinary problems. It will be fascinating to watch progress advance in this area.

## 7 References

- [1] H. Cavendish, “Experiments on Air,” *Philos. Trans. R. Soc. London*, vol. 75, pp. 372–384, 1785.
- [2] J. Gubkin, “Electrolytische Metallabscheidung an der freien Oberfläche einer Salzlosung,” *Ann. Phys.*, vol. 268, no. 9, pp. 114–115, 1887.
- [3] J. Zeleny, “the Electrical Discharge From Liquid Points , and,” *Phys. Rev.*, vol. III, no. 2, pp. 69–91, 1914.
- [4] A. Makowetzky, “Über die bildung von wasserstoffsperoxyd, salpetersaure und ammoniak bei der glimmbogenentladung , unter verwendung von wasser als einer elektrode.,” *Zetischrift fur Elektrochemie*, vol. 185, no. 6, 1907.
- [5] E. G. Linder and A. P. Davis, “Reactions of Hydrocarbons in the Glow Discharge,” *J. Phys. Chem.*, vol. 35, no. 12, pp. 3649–3672, 1930.
- [6] A. R. Denaro and A. Hickling, “Glow-Discharge Electrolysis in Aqueous Solutions,” *J. Electrochem. Soc.*, vol. 105, no. 5, p. 265, 1958.
- [7] A. Hickling and M. D. Ingram, “Contact glow-discharge electrolysis,” *Trans. Faraday Soc.*, vol. 60, p. 783, 1964.
- [8] B. Jiang, J. Zheng, S. Qiu, M. Wu, Q. Zhang, Z. Yan, and Q. Xue, “Review on electrical discharge plasma technology for wastewater remediation,” *Chem. Eng. J.*, vol. 236, pp. 348–368, 2014.
- [9] A. Hickling and M. D. Ingram, “Contact glow-discharge electrolysis,” *Trans. Faraday Soc.*, vol. 60, p. 783, 1964.
- [10] K. Harada and T. Iwasaki, “Syntheses of amino acids from aliphatic carboxylic acid by glow discharge electrolysis,” *Nature*, vol. 250, no. 5465, pp. 426–428, Aug. 1974.
- [11] K. Harada and S. Suzuki, “Formation of amino acids from elemental carbon by contact glow discharge electrolysis,” *Nature*, vol. 266, no. 5599, pp. 275–276, Mar. 1977.
- [12] J. Gao, X. Wang, Z. Hu, H. Deng, J. Hou, X. Lu, and J. Kang, “Plasma degradation of dyes in water with contact glow discharge electrolysis,” *Water Res.*, vol. 37, no. 2, pp. 267–272, 2003.
- [13] P. J. Bruggeman, M. J. Kushner, B. R. Locke, J. G. E. Gardeniers, W. G. Graham, D. B. Graves, R. C. H. M. Hofman-Caris, D. Maric, J. P. Reid, E. Ceriani, D. Fernandez Rivas, J. E. Foster, S. C. Garrick, Y. Gorbanev, S. Hamaguchi, F. Iza, H. Jablonowski, E. Klimova, J. Kolb, F. Krcma, P. Lukes, Z. Machala, I. Marinov, D. Mariotti, S. Mededovic Thagard, D. Minakata, E. C. Neyts, J. Pawlat, Z. L. Petrovic, R. Pflieger, S. Reuter, D. C. Schram, S. Schröter, M. Shiraiwa, B. Tarabová, P. A. Tsai, J. R. R. Verlet, T. von Woedtke, K. R. Wilson, K. Yasui, and G. Zvereva, “Plasma–liquid interactions: a review and roadmap,” *Plasma Sources Sci. Technol.*, vol. 25, no. 5, p. 53002, 2016.
- [14] P. Bruggeman and C. Leys, “Non-thermal plasmas in and in contact with liquids,” *J. Phys. D. Appl. Phys.*, vol. 42, no. 5, p. 53001, Mar. 2009.
- [15] J.-L. Brisset, B. Benstaali, D. Moussa, J. Fanmoe, and E. Njoyim-Tamungang, “Acidity control of plasma-chemical oxidation: applications to dye removal, urban waste abatement and microbial inactivation,” *Plasma Sources Sci. Technol.*, vol. 20, no. 3, p. 34021, 2011.

- [16] M. G. Kong, G. Kroesen, G. Morfill, T. Nosenko, T. Shimizu, J. van Dijk, and J. L. Zimmermann, "Plasma medicine: an introductory review," *New J. Phys.*, vol. 11, no. 11, p. 115012, Nov. 2009.
- [17] P. Brun, M. Vono, P. Venier, E. Tarricone, V. Deligianni, E. Martines, M. Zuin, S. Spagnolo, R. Cavazzana, R. Cardin, I. Castagliuolo, A. L. G. Valerio, and A. Leonardi, "Disinfection of ocular cells and tissues by atmospheric-pressure cold plasma.," *PLoS One*, vol. 7, no. 3, p. e33245, Jan. 2012.
- [18] D. B. Graves, "Low temperature plasma biomedicine: A tutorial review," *Phys. Plasmas*, vol. 21, no. 2014, p. 80901, 2014.
- [19] D. B. Graves, "The emerging role of reactive oxygen and nitrogen species in redox biology and some implications for plasma applications to medicine and biology," *J. Phys. D. Appl. Phys.*, vol. 45, no. 26, p. 263001, Jul. 2012.
- [20] T. von Woedtke, H.-R. Metelmann, and K.-D. Weltmann, "Clinical Plasma Medicine: State and Perspectives of in Vivo Application of Cold Atmospheric Plasma," *Contrib. to Plasma Phys.*, vol. 54, no. 2, pp. 104–117, Feb. 2014.
- [21] X. Lu, M. Laroussi, and V. Puech, "On atmospheric-pressure non-equilibrium plasma jets and plasma bullets," *Plasma Sources Sci. Technol.*, vol. 21, no. 3, p. 34005, 2012.
- [22] M. Y. Alkawareek, Q. T. Algwari, G. Laverty, S. P. Gorman, W. G. Graham, D. O'Connell, and B. F. Gilmore, "Eradication of *Pseudomonas aeruginosa* Biofilms by Atmospheric Pressure Non-Thermal Plasma," *PLoS One*, vol. 7, no. 8, pp. 13–15, 2012.
- [23] J. Raiser and M. Zenker, "Argon plasma coagulation for open surgical and endoscopic applications: state of the art," *J. Phys. D. Appl. Phys.*, vol. 39, no. 16, pp. 3520–3523, Aug. 2006.
- [24] F. Brehmer, H. a. Haenssle, G. Daeschlein, R. Ahmed, S. Pfeiffer, a. Görlitz, D. Simon, M. P. Schön, D. Wandke, and S. Emmert, "Alleviation of chronic venous leg ulcers with a hand-held dielectric barrier discharge plasma generator (PlasmaDerm® VU-2010): Results of a monocentric, two-armed, open, prospective, randomized and controlled trial (NCT01415622)," *J. Eur. Acad. Dermatology Venereol.*, pp. 148–155, 2014.
- [25] S. Emmert, F. Brehmer, H. Hänßle, A. Helmke, N. Mertens, R. Ahmed, D. Simon, D. Wandke, W. Maus-Friedrichs, G. Däschlein, M. P. Schön, and W. Viöl, "Atmospheric pressure plasma in dermatology: Ulcus treatment and much more," *Clin. Plasma Med.*, vol. 1, no. 1, pp. 24–29, 2013.
- [26] A. S. Wu, S. Kalghatgi, D. Dobrynin, R. Sensenig, E. Cerchar, E. Podolsky, E. Dulaimi, M. Paff, K. Wasko, K. P. Arjunan, K. Garcia, G. Fridman, M. Balasubramanian, R. Ownbey, K. A. Barbee, A. Fridman, G. Friedman, S. G. Joshi, and A. D. Brooks, "Porcine intact and wounded skin responses to atmospheric nonthermal plasma," *J. Surg. Res.*, vol. 179, no. 1, pp. 1–12, 2013.
- [27] J. Schlegel, J. Köritzer, and V. Boxhammer, "Plasma in cancer treatment," *Clin. Plasma Med.*, vol. 1, pp. 2–7, Dec. 2013.
- [28] M. Vandamme, E. Robert, S. Lerondel, V. Sarron, D. Ries, S. Dozias, J. Sobilo, D. Gosset, C. Kieda, B. Legrain, J.-M. Pouvesle, and A. Le Pape, "ROS implication in a new antitumor strategy based on non-thermal plasma.," *Int. J. Cancer*, vol. 130, no. 9, pp. 2185–94, May 2012.
- [29] H. Tanaka, M. Mizuno, K. Ishikawa, K. Takeda, K. Nakamura, F. Utsumi, H. Kajiyama, H. Kano, Y. Okazaki, S. Toyokuni, S. Maruyama, F. Kikkawa, and M. Hori, "Plasma Medical Science for

- Cancer Therapy: Toward Cancer Therapy Using Nonthermal Atmospheric Pressure Plasma,” *IEEE Trans. Plasma Sci.*, vol. 42, no. 12, pp. 3760–3764, 2014.
- [30] J. Köritzner, V. Boxhammer, A. Schäfer, T. Shimizu, T. G. Klämpfl, Y.-F. Li, C. Welz, S. Schwenk-Zieger, G. E. Morfill, J. L. Zimmermann, and J. Schlegel, “Restoration of sensitivity in chemo-resistant glioma cells by cold atmospheric plasma,” *PLoS One*, vol. 8, no. 5, p. e64498, Jan. 2013.
- [31] R. E. J. Sladek, E. Stoffels, R. Walraven, P. J. a. Tielbeek, and R. a. Koolhoven, “Plasma Treatment of Dental Cavities: A Feasibility Study,” *IEEE Trans. Plasma Sci.*, vol. 32, no. 4, pp. 1540–1543, Aug. 2004.
- [32] B. Yang, J. Chen, Q. Yu, H. Li, M. Lin, A. Mustapha, L. Hong, and Y. Wang, “Oral bacterial deactivation using a low-temperature atmospheric argon plasma brush,” *J. Dent.*, vol. 39, no. 1, pp. 48–56, Jan. 2011.
- [33] Z. Xiong, J. Roe, T. C. Grammer, and D. B. Graves, “Plasma Treatment of Onychomycosis,” *Plasma Process. Polym.*, pp. 588–597, 2016.
- [34] J. Ehlbeck, U. Schnabel, M. Polak, J. Winter, T. von Woedtke, R. Brandenburg, T. von dem Hagen, and K.-D. Weltmann, “Low temperature atmospheric pressure plasma sources for microbial decontamination,” *J. Phys. D. Appl. Phys.*, vol. 44, no. 1, p. 13002, Jan. 2011.
- [35] M. Naïtali, J.-M. Herry, E. Hnatiuc, G. Kamgang, and J.-L. Brisset, “Kinetics and Bacterial Inactivation Induced by Peroxynitrite in Electric Discharges in Air,” *Plasma Chem. Plasma Process.*, vol. 32, no. 4, pp. 675–692, May 2012.
- [36] H. A. Aboubakr, P. Williams, U. Gangal, M. M. Youssef, S. A. A. El-Sohaimy, P. J. Bruggeman, and S. M. Goyal, “Virucidal Effect of Cold Atmospheric Gaseous Plasma on Feline Calicivirus, a Surrogate for Human Norovirus,” *Appl. Environ. Microbiol.*, vol. 81, no. 11, pp. 3612–3622, 2015.
- [37] J. Julak, V. Scholtz, S. Kotucova, and O. Janouskova, “The persistent microbicidal effect in water exposed to the corona discharge,” *Phys. Medica*, vol. 28, no. 3, pp. 230–239, 2012.
- [38] M. Laroussi and F. Leipold, “Evaluation of the roles of reactive species, heat, and UV radiation in the inactivation of bacterial cells by air plasmas at atmospheric pressure,” *Int. J. Mass Spectrom.*, vol. 233, no. 1–3, pp. 81–86, Apr. 2004.
- [39] A. Helmke, D. Hoffmeister, F. Berge, S. Emmert, P. Laspe, N. Mertens, W. Vioel, and K. D. Weltmann, “Physical and microbiological characterisation of staphylococcus epidermidis inactivation by dielectric barrier discharge plasma,” *Plasma Process. Polym.*, vol. 8, no. 4, pp. 278–286, 2011.
- [40] H. A. Aboubakr, U. Gangal, M. M. Youssef, S. M. Goyal, and P. J. Bruggeman, “Inactivation of virus in solution by cold atmospheric pressure plasma: identification of chemical inactivation pathways,” *J. Phys. D. Appl. Phys.*, vol. 49, no. 20, p. 204001, 2016.
- [41] M. J. Pavlovich, H.-W. Chang, Y. Sakiyama, D. S. Clark, and D. B. Graves, “Ozone correlates with antibacterial effects from indirect air dielectric barrier discharge treatment of water,” *J. Phys. D. Appl. Phys.*, vol. 46, no. 14, pp. 1–10, Apr. 2013.
- [42] M. A. Malik, “Water purification by plasmas: Which reactors are most energy efficient?,” *Plasma Chem. Plasma Process.*, vol. 30, no. 1, pp. 21–31, 2010.

- [43] J.-L. Brisset, B. Benstaali, D. Moussa, J. Fanmoe, and E. Njoyim-Tamungang, "Acidity control of plasma-chemical oxidation: applications to dye removal, urban waste abatement and microbial inactivation," *Plasma Sources Sci. Technol.*, vol. 20, no. 3, pp. 1–12, Jun. 2011.
- [44] B. R. Locke, M. Sato, P. Sunka, M. R. Hoffmann, and J.-S. Chang, "Electrohydraulic Discharge and Nonthermal Plasma for Water Treatment," *Ind. Eng. Chem. Res.*, vol. 45, no. 3, pp. 882–905, Feb. 2006.
- [45] B. R. Locke, "Environmental Applications of Electrical Discharge Plasma with Liquid Water -- A Mini Review --," *Int. J. Plasma Environ. Sci. Technol.*, vol. 6, pp. 194–203, 2012.
- [46] B. R. Locke and K.-Y. Shih, "Review of the methods to form hydrogen peroxide in electrical discharge plasma with liquid water," *Plasma Sources Sci. Technol.*, vol. 20, no. 3, p. 34006, Jun. 2011.
- [47] B. R. Locke and S. M. Thagard, "Analysis and Review of Chemical Reactions and Transport Processes in Pulsed Electrical Discharge Plasma Formed Directly in Liquid Water," *Plasma Chem. Plasma Process.*, vol. 32, no. 5, pp. 875–917, Aug. 2012.
- [48] S. M. Thagard, K. Takashima, and A. Mizuno, "Chemistry of the Positive and Negative Electrical Discharges Formed in Liquid Water and Above a Gas–Liquid Surface," *Plasma Chem. Plasma Process.*, vol. 29, no. 6, pp. 455–473, Oct. 2009.
- [49] M. R. Webb, F. J. Andrade, and G. M. Hieftje, "Use of electrolyte cathode glow discharge (ELCAD) for the analysis of complex mixtures," *J. Anal. At. Spectrom.*, vol. 22, no. 7, pp. 766–774, 2007.
- [50] M. R. Webb and G. M. Hieftje, "Spectrochemical analysis by using discharge devices with solution electrodes," *Anal. Chem.*, vol. 81, no. 3, pp. 862–867, 2009.
- [51] A. L. Rosen and G. M. Hieftje, "Inductively coupled plasma mass spectrometry and electrospray mass spectrometry for speciation analysis: Applications and instrumentation," *Spectrochim. Acta - Part B At. Spectrosc.*, vol. 59, no. 2, pp. 135–146, 2004.
- [52] M. Smoluch, P. Mielczarek, and J. Silberring, "Plasma-based ambient ionization mass spectrometry in bioanalytical sciences," *Mass Spectrom. Rev.*, vol. 35, no. 1, pp. 22–34, Jan. 2016.
- [53] L. V Ratcliffe, F. J. M. Rutten, D. a Barrett, T. Whitmore, D. Seymour, C. Greenwood, Y. Aranda-Gonzalvo, S. Robinson, and M. McCoustra, "Surface analysis under ambient conditions using plasma-assisted desorption/ionization mass spectrometry.," *Anal. Chem.*, vol. 79, no. 16, pp. 6094–101, Aug. 2007.
- [54] V. Hessel, A. Anastasopoulou, Q. Wang, G. Kolb, and J. Lang, "Energy, catalyst and reactor considerations for (near)-industrial plasma processing and learning for nitrogen-fixation reactions," *Catal. Today*, vol. 211, pp. 9–28, Aug. 2013.
- [55] W. Piavis and S. Turn, "An experimental investigation of reverse vortex flow plasma reforming of methane," *Int. J. Hydrogen Energy*, vol. 37, no. 22, pp. 17078–17092, Nov. 2012.
- [56] H. H. Nguyen and K.-S. Kim, "Combination of plasmas and catalytic reactions for CO<sub>2</sub> reforming of CH<sub>4</sub> by dielectric barrier discharge process," *Catal. Today*, vol. 256, pp. 88–95, 2015.
- [57] H. L. Chen, H. M. Lee, S. H. Chen, Y. Chao, and M. B. Chang, "Review of plasma catalysis on hydrocarbon reforming for hydrogen production-Interaction, integration, and prospects," *Appl.*

- Catal. B Environ.*, vol. 85, no. 1–2, pp. 1–9, 2008.
- [58] J. Van Durme, J. Dewulf, C. Leys, and H. Van Langenhove, “Combining non-thermal plasma with heterogeneous catalysis in waste gas treatment: A review,” *Appl. Catal. B Environ.*, vol. 78, no. 3–4, pp. 324–333, 2008.
- [59] C. Richmonds and R. M. Sankaran, “Plasma-liquid electrochemistry: Rapid synthesis of colloidal metal nanoparticles by microplasma reduction of aqueous cations,” *Appl. Phys. Lett.*, vol. 93, no. 13, p. 131501, 2008.
- [60] M. Bouchard, M. Létourneau, C. Sarra-Bournet, M. Laprise-Pelletier, S. Turgeon, P. Chevallier, J. Lagueux, G. Laroche, and M.-A. Fortin, “Rapid nucleation of iron oxide nanoclusters in aqueous solution by plasma electrochemistry,” *Langmuir*, p. 150618163551002, 2015.
- [61] D. Mariotti and R. M. Sankaran, “Microplasmas for nanomaterials synthesis,” *J. Phys. D. Appl. Phys.*, vol. 43, no. 32, p. 323001, Aug. 2010.
- [62] D. Mariotti, J. Patel, V. Švrček, and P. Maguire, “Plasma-liquid interactions at atmospheric pressure for nanomaterials synthesis and surface engineering,” *Plasma Process. Polym.*, vol. 9, no. 11–12, pp. 1074–1085, 2012.
- [63] W. Tian and M. J. Kushner, “Atmospheric pressure dielectric barrier discharges interacting with liquid covered tissue,” *J. Phys. D. Appl. Phys.*, vol. 47, no. 16, p. 165201, Apr. 2014.
- [64] S. a Norberg, W. Tian, E. Johnsen, and M. J. Kushner, “Atmospheric pressure plasma jets interacting with liquid covered tissue: touching and not-touching the liquid,” *J. Phys. D. Appl. Phys.*, vol. 47, p. 475203, 2014.
- [65] C. Chen, D. X. Liu, Z. C. Liu, a. J. Yang, H. L. Chen, G. Shama, and M. G. Kong, “A Model of Plasma-Biofilm and Plasma-Tissue Interactions at Ambient Pressure,” *Plasma Chem. Plasma Process.*, vol. 34, no. 3, pp. 403–441, Apr. 2014.
- [66] A. Lindsay, C. Anderson, E. Slikboer, S. Shannon, and D. Graves, “Momentum, heat, and neutral mass transport in convective atmospheric pressure plasma-liquid systems and implications for aqueous targets,” *J. Phys. D. Appl. Phys.*, vol. 48, no. 42, p. 424007, Oct. 2015.
- [67] I. S. Djakaou, R. M. Ghezzar, M. E. M. Zekri, F. Abdelmalek, S. Cavadias, and S. Ognier, “Removal of Model Pollutants in Aqueous Solution by Gliding Arc Discharge. Part II: Modeling and Simulation Study,” *Plasma Chem. Plasma Process.*, vol. 35, no. 1, pp. 143–157, 2015.
- [68] H. Tanaka, M. Mizuno, K. Ishikawa, K. Nakamura, H. Kajiyama, H. Kano, F. Kikkawa, and M. Hori, “Plasma-Activated Medium Selectively Kills Glioblastoma Brain Tumor Cells by Down-Regulating a Survival Signaling Molecule, AKT Kinase,” *Plasma Med.*, vol. 1, no. 3–4, pp. 265–277, 2011.
- [69] F. Utsumi, H. Kajiyama, K. Nakamura, H. Tanaka, M. Mizuno, K. Ishikawa, H. Kondo, H. Kano, M. Hori, and F. Kikkawa, “Effect of Indirect Nonequilibrium Atmospheric Pressure Plasma on Anti-Proliferative Activity against Chronic Chemo-Resistant Ovarian Cancer Cells In Vitro and In Vivo,” *PLoS One*, vol. 8, no. 12, p. e81576, Jan. 2013.
- [70] M. K. Ramseier, U. von Gunten, P. Freihofer, and F. Hammes, “Kinetics of membrane damage to high (HNA) and low (LNA) nucleic acid bacterial clusters in drinking water by ozone, chlorine, chlorine dioxide, monochloramine, ferrate(VI), and permanganate,” *Water Res.*, vol. 45, no. 3, pp.



1490–500, Jan. 2011.

- [71] L. Bundscherer, K. Wende, K. Ottmüller, A. Barton, A. Schmidt, S. Bekeschus, S. Hasse, K.-D. Weltmann, K. Masur, and U. Lindequist, “Impact of non-thermal plasma treatment on MAPK signaling pathways of human immune cell lines,” *Immunobiology*, vol. 218, no. 10, pp. 1248–55, Oct. 2013.
- [72] F. Vatansever, W. C. M. a de Melo, P. Avci, D. Vecchio, M. Sadasivam, A. Gupta, R. Chandran, M. Karimi, N. a Parizotto, R. Yin, G. P. Tegos, and M. R. Hamblin, “Antimicrobial strategies centered around reactive oxygen species--bactericidal antibiotics, photodynamic therapy, and beyond,” *FEMS Microbiol. Rev.*, vol. 37, no. 6, pp. 955–89, Nov. 2013.
- [73] K. H. Becker, U. Kogelschatz, K. H. Schoenbach, and R. J. Barker, *Non-Equilibrium Air Plasmas at Atmospheric Pressure*. London: Institute of Physics Publishing, 2005.
- [74] J. S. Townsend, “XVII. The Conductivity produced in gases by the motion of negatively charged ions,” *London, Edinburgh, Dublin Philos. Mag. J. Sci.*, vol. 1, no. 2, pp. 198–227, 1901.
- [75] F. B. Dunning and a C. H. Smith, “Secondary electron ejection from metal surfaces by metastable atoms. II. Measurements of secondary emission coefficients using a gas cell method,” *J. Phys. B At. Mol. Phys.*, vol. 4, no. 12, pp. 1696–1710, 2001.
- [76] V. Phelps and Z. L. Petrovic, “Cold-cathode discharges and breakdown in argon: surface and gas phase production of secondary electrons,” *Plasma Sources Sci. Technol.*, vol. 8, no. 3, pp. R21–R44, 1999.
- [77] Y. V. Yurgelenas and H. E. Wagner, “A computational model of a barrier discharge in air at atmospheric pressure: the role of residual surface charges in microdischarge formation,” *J. Phys. D (Applied Physics)*, vol. 39, no. 18, pp. 4031–4043, 2006.
- [78] M. P. Sarma and W. Janischewskyj, “D.C. corona on smooth conductors in air. Steady-state analysis of the ionisation layer,” *Electr. Eng. Proc. Inst.*, vol. 116, no. 1, pp. 161–166, 1969.
- [79] J. D. Pace and a B. Parker, “The breakdown of argon at low pressure,” *J. Phys. D. Appl. Phys.*, vol. 6, no. 12, pp. 1525–1536, 2002.
- [80] G. Auday, P. Guillot, and J. Galy, “Secondary emission of dielectrics used in plasma display panels,” *J. Appl. Phys.*, vol. 88, no. 8, pp. 4871–4874, 2000.
- [81] D. Mariotti, J. a McLaughlin, and P. Maguire, “Experimental study of breakdown voltage and effective secondary electron emission coefficient for a micro-plasma device,” *Plasma Sources Sci. Technol.*, vol. 13, pp. 207–212, 2004.
- [82] K. Baba, T. Kaneko, and R. Hatakeyama, “Ion irradiation effects on ionic liquids interfaced with rf discharge plasmas,” *Appl. Phys. Lett.*, vol. 90, no. 20, pp. 88–91, 2007.
- [83] E. Husain and R. Nema, “Analysis of Paschen Curves for air, N<sub>2</sub> and SF<sub>6</sub> Using the Townsend Breakdown Equation,” *IEEE Trans. Electr. Insul.*, vol. EI-17, no. 4, pp. 350–353, Aug. 1982.
- [84] E. T. Protasevich, *Cold non-equilibrium plasma*. Cambridge: Cambridge International Science Publishing, 2000.
- [85] M. J. and V. M. and K. H. and L. D. and Z. Machala, “Measurement of the electron density in Transient Spark discharge,” *Plasma Sources Sci. Technol.*, vol. 23, no. 6, p. 65016, 2014.

- [86] Z. Machala, L. Chládková, and M. Pelach, “Plasma agents in bio-decontamination by dc discharges in atmospheric air,” *J. Phys. D. Appl. Phys.*, vol. 43, no. 22, p. 222001, 2010.
- [87] M. Janda, Z. Machala, A. Niklová, and V. Martišoviš, “The streamer-to-spark transition in a transient spark: a dc-driven nanosecond-pulsed discharge in atmospheric air,” *Plasma Sources Sci. Technol.*, vol. 21, no. 4, p. 45006, 2012.
- [88] M. Janda, V. Martišoviš, and Z. Machala, “Transient spark: a dc-driven repetitively pulsed discharge and its control by electric circuit parameters,” *Plasma Sources Sci. Technol.*, vol. 20, no. 3, p. 35015, Jun. 2011.
- [89] Z. Machala, I. Jedlovský, and V. Martišoviš, “DC discharges in atmospheric air and their transitions,” *IEEE Trans. Plasma Sci.*, vol. 36, no. 4, pp. 918–919, 2008.
- [90] L. B. Loeb, *Electrical Coronas and Their Basic Physical Mechanisms*. Berkeley: University of California Press, 1965.
- [91] L. B. Loeb and J. M. Meek, “The mechanism of spark discharge in air at atmospheric pressure. I,” *J. Appl. Phys.*, vol. 11, no. 6, pp. 438–447, 1940.
- [92] L. B. Loeb and A. F. Kip, “Electrical discharges in air at atmospheric pressure: The nature of the positive and negative point-to-plane coronas and the mechanism of spark propagation,” *J. Appl. Phys.*, vol. 10, no. 3, pp. 142–160, 1939.
- [93] L. B. Loeb, “Statistical Factors in Spark Discharge Mechanisms,” *Rev. Mod. Phys.*, vol. 20, no. 1, pp. 151–160, Jan. 1948.
- [94] M. N. Hirsh and H. J. Oskam, Eds., *Gaseous Electronics, Volume 1: Electrical Discharges*. San Francisco: Academic Press, 1978.
- [95] M. J. and V. M. and K. H. and L. D. and Z. Machala, “Measurement of the electron density in Transient Spark discharge,” *Plasma Sources Sci. Technol.*, vol. 23, no. 6, p. 65016, 2014.
- [96] Z. Machala, M. Janda, K. Hensel, I. Jedlovský, L. Leštinská, V. Foltin, V. Martišoviš, and M. Morvová, “Emission spectroscopy of atmospheric pressure plasmas for bio-medical and environmental applications,” *J. Mol. Spectrosc.*, vol. 243, no. 2, pp. 194–201, Jun. 2007.
- [97] Z. (Comenius U. Machala, M. (Comenius U. Morvová, E. (Ecole S. d’électricité) Marode, and I. (Comenius U. Morva, “Removal of cyclohexanone in transition electric discharges at atmospheric pressure,” *J. Phys. D. Appl. Phys.*, vol. 33, pp. 3198–3213, 2000.
- [98] Z. Machala, B. Tarabova, K. Hensel, E. Spetlikova, L. Sikurova, and P. Lukes, “Formation of ROS and RNS in Water Electro-Sprayed through Transient Spark Discharge in Air and their Bactericidal Effects,” *Plasma Process. Polym.*, p. n/a-n/a, Apr. 2013.
- [99] R. Ono and T. Oda, “Measurement of gas temperature and OH density in the afterglow of pulsed positive corona discharge,” *J. Phys. D. Appl. Phys.*, vol. 41, no. 3, p. 35204, 2008.
- [100] R. Ono, Y. Nakagawa, and T. Oda, “Effect of pulse width on the production of radicals and excited species in a pulsed positive corona discharge,” *J. Phys. D. Appl. Phys.*, vol. 44, no. 48, p. 485201, 2011.
- [101] A. Komuro, R. Ono, and T. Oda, “Numerical simulation for production of O and N radicals in an atmospheric-pressure streamer discharge,” *J. Phys. D. Appl. Phys.*, vol. 45, no. 26, p. 265201,

- 2012.
- [102] R. Ono and T. Oda, “Dynamics and density estimation of hydroxyl radicals in a pulsed corona discharge,” *J. Phys. D. Appl. Phys.*, vol. 35, no. 17, pp. 2133–2138, 2002.
  - [103] R. Ono and T. Oda, “Dynamics of ozone and OH radicals generated by pulsed corona discharge in humid-air flow reactor measured by laser spectroscopy,” *J. Appl. Phys.*, vol. 93, no. 10, p. 5876, 2003.
  - [104] P. K. Chu, X. Lu, and F. Group, *Low Temperature Plasma Technology*. .
  - [105] A. Pedersen, “Calculation of Spark Breakdown or Corona Starting Voltages in Nonuniform Fields.,” *IEEE Trans. Power Appar. Syst.*, vol. PAS-86, no. 2, pp. 200–206, Feb. 1967.
  - [106] A. Fridman and L. A. Kennedy, “Nonequilibrium Cold Atmospheric Pressure Discharges,” in *Plasma Physics and Engineering*, Second., New York: CRC Press, 2011, pp. 561–611.
  - [107] J.-S. Chang, P. a. Lawless, and T. Yamamoto, “Corona discharge processes,” *IEEE Trans. Plasma Sci.*, vol. 19, no. 6, pp. 1152–1166, 1991.
  - [108] A. Luque, V. Ratushnaya, and U. Ebert, “Positive and negative streamers in ambient air: modeling evolution and velocities,” *J. Phys. D Appl. Phys.*, vol. 41, p. 18, 2008.
  - [109] M. Janda and Z. Machala, “Imaging of Transient Spark in Atmospheric Air by Fast iCCD Camera,” *IEEE Trans. Plasma Sci.*, vol. 39, no. 11, pp. 2246–2247, Nov. 2011.
  - [110] M. Janda, V. Martišovitš, K. Hensel, and Z. Machala, “Evolution of the streamer-to-spark transition influenced by memory effect,” *IEEE*, 2013.
  - [111] M. Robinson, “Movement of air in the electric wind of the corona discharge,” *Am. Inst. Electr. Eng. Part I Commun. Electron.*, vol. 80, no. 2, pp. 143–150, 1961.
  - [112] L. Zhao and K. Adamiak, “EHD flow in air produced by electric corona discharge in pin–plate configuration,” *J. Electrostat.*, vol. 63, pp. 337–350, Mar. 2005.
  - [113] S. Kanazawa, H. Kawano, S. Watanabe, T. Furuki, S. Akamine, R. Ichiki, T. Ohkubo, M. Kocik, and J. Mizeraczyk, “Observation of OH radicals produced by pulsed discharges on the surface of a liquid,” *Plasma Sources Sci. Technol.*, vol. 20, no. 3, p. 34010, Jun. 2011.
  - [114] T. M. P. Briels, J. Kos, G. J. J. Winands, E. M. van Veldhuizen, and U. Ebert, “Positive and negative streamers in ambient air: measuring diameter, velocity and dissipated energy,” *J. Phys. D. Appl. Phys.*, vol. 41, p. 20, 2008.
  - [115] P. Rumbach, D. M. Bartels, R. M. Sankaran, and D. B. Go, “The solvation of electrons by an atmospheric-pressure plasma,” *Nat. Commun.*, vol. 6, p. 7248, 2015.
  - [116] X. Pei, X. Lu, J. Liu, D. Liu, Y. Yang, K. Ostrikov, P. K. Chu, and Y. Pan, “Biofilm By a Room-Temperature, Battery-Operated, Handheld Air Plasma Jet,” *J. Phys. D. Appl. Phys.*, vol. 45, no. 16, p. 165205, 2012.
  - [117] M. R. Webb, F. J. Andrade, and G. M. Hieftje, “Use of electrolyte cathode glow discharge (ELCAD) for the analysis of complex mixtures,” *J. Anal. At. Spectrom.*, vol. 22, no. 7, pp. 766–774, 2007.

- [118] G. W. Trichel, "The mechanism of the negative point to plane corona near onset," *Phys. Rev.*, vol. 54, no. 12, pp. 1078–1084, 1938.
- [119] R. Gopalakrishnan, E. Kawamura, A. J. Lichtenberg, M. A. Lieberman, and D. B. Graves, "Solvated electrons at the atmospheric pressure plasma–water anodic interface," *J. Phys. D. Appl. Phys.*, vol. 49, no. 29, p. 295205, Jul. 2016.
- [120] Y. Akishev, O. Goossens, T. Callebaut, C. Leys, a Napartovich, and N. Trushkin, "The influence of electrode geometry and gas flow on corona-to-glow and glow-to-spark threshold currents in air," *J. Phys. D. Appl. Phys.*, vol. 34, no. 18, pp. 2875–2882, 2001.
- [121] U. Kogelschatz, "Dielectric-barrier Discharges : Their History , Discharge Physics , and Industrial Applications," vol. 23, no. 1, pp. 1–46, 2003.
- [122] R. Tiede, J. Hirschberg, W. Viöl, and S. Emmert, "A  $\mu$ s-Pulsed Dielectric Barrier Discharge Source: Physical Characterization and Biological Effects on Human Skin Fibroblasts," *Plasma Process. Polym.*, p. n/a-n/a, 2016.
- [123] S. G. Joshi, M. Cooper, A. Yost, M. Paff, U. K. Ercan, G. Fridman, G. Friedman, A. Fridman, and A. D. Brooks, "Nonthermal dielectric-barrier discharge plasma-induced inactivation involves oxidative DNA damage and membrane lipid peroxidation in Escherichia coli," *Antimicrob. Agents Chemother.*, vol. 55, no. 3, pp. 1053–1062, 2011.
- [124] S. R. Plimpton, M. Golkowski, D. G. Mitchell, C. Austin, S. S. Eaton, G. R. Eaton, C. Golkowski, and M. Voskuil, "Remote delivery of hydroxyl radicals via secondary chemistry of a nonthermal plasma effluent," *Biotechnol. Bioeng.*, vol. 110, no. 7, pp. 1936–1944, 2013.
- [125] M. J. Traylor, M. J. Pavlovich, S. Karim, P. Hait, Y. Sakiyama, D. S. Clark, and D. B. Graves, "Long-term antibacterial efficacy of air plasma-activated water," *J. Phys. D. Appl. Phys.*, vol. 44, no. 47, Nov. 2011.
- [126] M. J. Pavlovich, D. S. Clark, and D. B. Graves, "Quantification of air plasma chemistry for surface disinfection," *Plasma Sources Sci. Technol.*, vol. 23, no. 6, p. 65036, 2014.
- [127] E. A. J. Bartis, P. Luan, A. J. Knoll, D. B. Graves, J. Seog, and G. S. Oehrlein, "A comparative study of biomolecule and polymer surface modifications by a surface microdischarge," *Eur. Phys. J. D*, vol. 70, no. 2, p. 25, 2016.
- [128] E. a J. Bartis, D. B. Graves, J. Seog, and G. S. Oehrlein, "Atmospheric pressure plasma treatment of lipopolysaccharide in a controlled environment," *J. Phys. D. Appl. Phys.*, vol. 46, no. 31, p. 312002, Aug. 2013.
- [129] K. Oehmigen, J. Winter, M. Hähnel, C. Wilke, R. Brandenburg, K.-D. Weltmann, and T. von Woedtke, "Estimation of Possible Mechanisms of Escherichia coli Inactivation by Plasma Treated Sodium Chloride Solution," *Plasma Process. Polym.*, vol. 8, no. 10, pp. 904–913, Oct. 2011.
- [130] K. Oehmigen, M. Hähnel, R. Brandenburg, C. Wilke, K.-D. Weltmann, and T. von Woedtke, "The Role of Acidification for Antimicrobial Activity of Atmospheric Pressure Plasma in Liquids," *Plasma Process. Polym.*, vol. 7, no. 3–4, pp. 250–257, Mar. 2010.
- [131] K. Panngom, K. Y. Baik, M. K. Nam, J. H. Han, H. Rhim, and E. H. Choi, "Preferential killing of human lung cancer cell lines with mitochondrial dysfunction by nonthermal dielectric barrier discharge plasma.," *Cell Death Dis.*, vol. 4, no. 5, p. e642, Jan. 2013.

- [132] N. K. Kaushik, H. Uhm, and E. Ha Choi, "Micronucleus formation induced by dielectric barrier discharge plasma exposure in brain cancer cells," *Appl. Phys. Lett.*, vol. 100, no. 8, pp. 4–7, 2012.
- [133] N. K. Kaushik, N. Kaushik, D. Park, and E. H. Choi, "Altered antioxidant system stimulates dielectric barrier discharge plasma-induced cell death for solid tumor cell treatment," *PLoS One*, vol. 9, no. 7, pp. 1–11, 2014.
- [134] G. Fridman, A. Shereshevsky, M. M. Jost, A. D. Brooks, A. Fridman, A. Gutsol, V. Vasilets, and G. Friedman, "Floating electrode dielectric barrier discharge plasma in air promoting apoptotic behavior in Melanoma skin cancer cell lines," *Plasma Chem. Plasma Process.*, vol. 27, no. 2, pp. 163–176, 2007.
- [135] K. P. Arjunan, G. Friedman, A. Fridman, and A. M. Clyne, "Non-thermal dielectric barrier discharge plasma induces angiogenesis through reactive oxygen species.," *J. R. Soc. Interface*, vol. 9, no. 66, pp. 147–57, Jan. 2012.
- [136] R. Zhang, Y. Wu, G. Li, N. Wang, and J. Li, "Plasma induced degradation of Indigo Carmine by bipolar pulsed dielectric barrier discharge (DBD) in the water-air mixture," *J. Environ. Sci.*, vol. 16, no. 5, pp. 808–812, 2004.
- [137] S. Samukawa, M. Hori, S. Rauf, K. Tachibana, P. Bruggeman, G. Kroesen, J. C. Whitehead, A. B. Murphy, A. F. Gutsol, S. Starikovskaia, U. Kortshagen, J.-P. Boeuf, T. J. Sommerer, M. J. Kushner, U. Czarnetzki, and N. Mason, "The 2012 Plasma Roadmap," *J. Phys. D. Appl. Phys.*, vol. 45, no. 25, p. 253001, Jun. 2012.
- [138] C. E. Anderson, N. R. Cha, A. D. Lindsay, D. S. Clark, and D. B. Graves, "The Role of Interfacial Reactions in Determining Plasma-Liquid Chemistry," *Plasma Chem. Plasma Process.*, vol. 36, no. 6, pp. 1–23, 2016.
- [139] E. S. Bobkova, S. A. Smirnov, Y. V. Zalipaeva, and V. V. Rybkin, "Modeling chemical composition for an atmospheric pressure dc discharge in air with water cathode by 0-D model," *Plasma Chem. Plasma Process.*, vol. 34, no. 4, pp. 721–743, 2014.
- [140] S. Kanazawa, Y. Shuto, N. Sato, T. Ohkubo, Y. Nomoto, J. Mizeraczyk, and J. S. Chang, "Two-dimensional imaging of NO density profiles by LIF technique in a pipe with nozzles electrode during NO treatment," *IEEE Trans. Ind. Appl.*, vol. 39, no. 2, pp. 333–339, 2003.
- [141] K. Niemi, V. S. Der Gathen, and H. F. Döbele, "Absolute atomic oxygen density measurements by two-photon absorption laser-induced fluorescence spectroscopy in an RF-excited atmospheric pressure plasma jet," *Plasma Sources Sci. Technol.*, vol. 14, no. 2, pp. 375–386, 2005.
- [142] T. Verreycken, R. Mensink, R. Van Der Horst, N. Sadeghi, and P. J. Bruggeman, "Absolute OH density measurements in the effluent of a cold atmospheric-pressure Ar–H<sub>2</sub>O RF plasma jet in air," *Plasma Sources Sci. Technol.*, vol. 22, p. 1, 2013.
- [143] R. Ono and T. Oda, "Measurement of hydroxyl radicals in pulsed corona discharge," *J. Electrostat.*, vol. 55, no. 3–4, pp. 333–342, 2002.
- [144] Y. Nakagawa, R. Ono, and T. Oda, "Density and temperature measurement of OH radicals in atmospheric-pressure pulsed corona discharge in humid air," *J. Appl. Phys.*, vol. 110, no. 7, pp. 1–7, 2011.
- [145] W. Tian and M. J. Kushner, "Atmospheric pressure dielectric barrier discharges interacting with

- liquid covered tissue,” *J. Phys. D. Appl. Phys.*, vol. 47, no. 16, p. 165201, Apr. 2014.
- [146] Y. F. Yue, S. Mohades, M. Laroussi, X. Lu, and S. Member, “Measurements of Plasma-Generated Hydroxyl and Hydrogen Peroxide Concentrations for,” *IEEE Trans. Plasma Sci.*, vol. accepted, pp. 1–5, 2016.
- [147] J. Winter, H. Tresp, M. U. Hammer, S. Iseni, S. Kupsch, a Schmidt-Bleker, K. Wende, M. Dünnbier, K. Masur, K.-D. Weltmann, and S. Reuter, “Tracking plasma generated H<sub>2</sub>O<sub>2</sub> from gas into liquid phase and revealing its dominant impact on human skin cells,” *J. Phys. D. Appl. Phys.*, vol. 47, p. 285401, 2014.
- [148] Y. Gorbanev, D. O’Connell, and V. Chechik, “Non-Thermal Plasma in Contact with Water: The Origin of Species,” *Chem. - A Eur. J.*, vol. 22, no. 10, pp. 3496–3505, 2016.
- [149] R. J. Wandell and B. R. Locke, “Hydrogen peroxide generation in low power pulsed water spray plasma reactors,” *Ind. Eng. Chem. Res.*, vol. 53, pp. 609–618, 2014.
- [150] M. J. Pavlovich, H.-W. Chang, Y. Sakiyama, D. S. Clark, and D. B. Graves, “Ozone correlates with antibacterial effects from indirect air dielectric barrier discharge treatment of water,” *J. Phys. D. Appl. Phys.*, vol. 46, no. 14, pp. 1–10, Apr. 2013.
- [151] T. Takamatsu, K. Uehara, and Y. Sasaki, “Investigation of reactive species using various gas plasmas,” *RSC Adv.*, vol. 4, no. 75, p. 39901, Aug. 2014.
- [152] R. B. Bird, W. E. Stewart, and E. N. Lightfoot, *Transport Phenomena*, 2nd ed. New York: John Wiley & Sons, Inc., 2007.
- [153] L. F. Kosak-Channing and G. R. Helz, “Solubility of ozone in aqueous solutions of 0-0.6 M ionic strength at 5-30°C,” *Environ. Sci. Technol.*, vol. 17, no. 3, pp. 145–149, 1983.
- [154] J. Lelieveld and P. J. Crutzen, “The role of clouds in tropospheric photochemistry,” *J. Atmos. Chem.*, vol. 12, no. 3, pp. 229–267, 1991.
- [155] R. Andreozzi, V. Caprio, I. Ermellino, A. Insola, and V. Tufano, “Ozone Solubility in Phosphate-Buffered Aqueous Solutions: Effect of Temperature, tert -Butyl Alcohol, and pH,” *Ind. Eng. Chem. Res.*, vol. 35, no. 4, pp. 1467–1471, Jan. 1996.
- [156] Y. Sakiyama, D. B. Graves, H.-W. Chang, T. Shimizu, and G. E. Morfill, “Plasma chemistry model of surface microdischarge in humid air and dynamics of reactive neutral species,” *J. Phys. D. Appl. Phys.*, vol. 45, no. 42, p. 425201, Oct. 2012.
- [157] J. M. Khalack and A. P. Lyubartsev, “Solvation structure of hydroxyl radical by Car-Parrinello molecular dynamics,” *J. Phys. Chem. A*, vol. 109, no. 2, pp. 378–86, 2005.
- [158] R. L. McMurtrie and F. G. Keyes, “A Measurement of the Diffusion Coefficient of Hydrogen Peroxide Vapour into Air,” *J. Am. Chem. Soc.*, vol. 70, no. 11, pp. 3755–3758, 1948.
- [159] I. G. Zacharia and W. M. Deen, “Diffusivity and solubility of nitric oxide in water and saline,” *Ann. Biomed. Eng.*, vol. 33, no. 2, pp. 214–222, 2005.
- [160] B. T. Skinn and W. M. Deen, “A nitrogen dioxide delivery system for biological media,” *Free Radic. Biol. Med.*, vol. 56, no. 2, pp. 44–53, Mar. 2013.
- [161] G. B. Wills and H. Yeh, “Diffusion coefficient of aqueous nitric acid at 25.deg. as function of

- concentration from 0.1 to 1.0M,” *J. Chem. Eng. Data*, vol. 16, no. 1, pp. 76–77, Jan. 1971.
- [162] J. U. Kreft, C. Picioreanu, J. W. Wimpenny, and M. C. van Loosdrecht, “Individual-based modelling of biofilms,” *Microbiology*, vol. 147, no. Pt 11, pp. 2897–912, 2001.
- [163] N. Agmon, “The Grotthuss mechanism,” *Chem. Phys. Lett.*, vol. 244, no. 5–6, pp. 456–462, 1995.
- [164] H. Masahura, F. C. De Schryver, N. Kitamura, and N. Tamai, *Microchemistry: Spectroscopy and Chemistry in Small Domains*. Amsterdam: Elsevier Science B.V., 1994.
- [165] P. J. Bruggeman, M. J. Kushner, B. R. Locke, J. G. E. Gardeniers, W. G. Graham, D. B. Graves, R. C. H. M. Hofman-Caris, D. Maric, J. P. Reid, E. Ceriani, D. Rivas Fernandez, J. E. Foster, S. C. Garrick, Y. Gorbanev<sup>12</sup>, S. Hamaguchi, F. Iza, H. Jablonowski, E. Klimova, J. Kolb, F. Krcma, P. Lukes, Z. Machala, I. Marinov, D. Mariotti, S. M. Thagard<sup>21</sup>, D. Minakata<sup>22</sup>, E. Neyts<sup>23</sup>, J. Pawlat, Z. L. Petrovic, R. Pflieger, S. Reuter, D. C. Schram, S. Schröter, M. Shiraiwa, B. Tarabová, P. A. Tsai, J. R. R. Verlet, T. von Woedtke, K. R. Wilson, K. Yasui, and G. Zvereva, “Plasma - Liquid Interactions : A Review and Roadmap,” *Plasma sources Sci. Technol.*, vol. submitted, pp. 1–113, 2016.
- [166] A. Bachi, I. Dalle-Donne, and A. Scaloni, “Redox proteomics: chemical principles, methodological approaches and biological/biomedical promises,” *Chem. Rev.*, vol. 113, no. 1, pp. 596–698, Jan. 2013.
- [167] P. Bruggeman, E. Ribežl, A. Maslani, J. Degroote, A. Malesevic, R. Rego, J. Vierendeels, and C. Leys, “Characteristics of atmospheric pressure air discharges with a liquid cathode and a metal anode,” *Plasma Sources Sci. Technol.*, vol. 17, no. 2, p. 25012, May 2008.
- [168] M. Naïtali, G. Kamgang-Youbi, J.-M. Herry, M.-N. Bellon-Fontaine, and J.-L. Brisset, “Combined effects of long-living chemical species during microbial inactivation using atmospheric plasma-treated water,” *Appl. Environ. Microbiol.*, vol. 76, no. 22, pp. 7662–4, Nov. 2010.
- [169] J. Park and Y. Lee, “Solubility and Decomposition Kinetics of Nitrous Acid in Aqueous Solution,” *J. Phys. Chem.*, vol. 92, pp. 6294–6302, 1988.
- [170] P. Lukes and B. R. Locke, “Plasmachemical oxidation processes in a hybrid gas–liquid electrical discharge reactor,” *J. Phys. D. Appl. Phys.*, vol. 38, no. 22, pp. 4074–4081, Nov. 2005.
- [171] S. Goldstein, J. Lind, and G. Merényi, “Chemistry of peroxyxynitrites as compared to peroxyxynitrates,” *Chem. Rev.*, vol. 105, no. 6, pp. 2457–2470, 2005.
- [172] P. Lukes, E. Dolezalova, I. Sisrova, and M. Clupek, “Aqueous-phase chemistry and bactericidal effects from an air discharge plasma in contact with water: evidence for the formation of peroxyxynitrite through a pseudo-second-order post-discharge reaction of H<sub>2</sub>O<sub>2</sub> and HNO<sub>2</sub>,” *Plasma Sources Sci. Technol.*, vol. 23, no. 1, p. 15019, Feb. 2014.
- [173] A. H. Harvey, S. G. Kaplan, and J. H. Burnett, “Effect of dissolved air on the density and refractive index of water,” *Int. J. Thermophys.*, vol. 26, no. 5, pp. 1495–1514, 2005.
- [174] N. N. Greenwood and A. Earnshaw, *Chemistry of the Elements*, Second. Amsterdam: Elsevier Butterworth-Heinemann, 1997.
- [175] G. V Buxton, C. L. Greenstock, W. P. Helman, and A. B. Ross, “Critical-Review of Rate Constants for Reactions of Hydrated Electrons, Hydrogen-Atoms and Hydroxyl Radicals (.OH/.O-) in Aqueous-Solution,” *J. Phys. Chem. Ref. Data*, vol. 17, no. 2, pp. 513–886, 1988.

- [176] J. Newman and K. E. Thomas-Alyea, *Electrochemical Systems*, Third. Hoboken, NJ, USA: John Wiley & Sons, Inc., 2004.
- [177] G. Eisenberg, "Colorimetric Determination of Hydrogen Peroxide," *Ind. Eng. Chem. Anal. Ed.*, vol. 15, no. 5, pp. 327–328, May 1943.
- [178] Z. Machala, B. Tarabova, K. Hensel, E. Spetlikova, L. Sikurova, and P. Lukes, "Formation of ROS and RNS in Water Electro-Sprayed through Transient Spark Discharge in Air and their Bactericidal Effects," *Plasma Process. Polym.*, vol. 10, no. 7, pp. 649–659, Jul. 2013.
- [179] C. N. Satterfield and a. H. Bonnell, "Interferences in Titanium Sulfate Method for Hydrogen Peroxide," *Anal. Chem.*, vol. 27, no. 7, pp. 1174–1175, Jul. 1955.
- [180] K. Marouf-Khelifa, F. Abdelmalek, A. Khelifa, M. Belhadj, A. Addou, and J. L. Brisset, "Reduction of nitrite by sulfamic acid and sodium azide from aqueous solutions treated by gliding arc discharge," *Sep. Purif. Technol.*, vol. 50, no. 3, pp. 373–379, 2006.
- [181] C. A. Abeledo and I. M. Kolthoff, "THE REACTION BETWEEN NITRITE AND IODIDE AND ITS APPLICATION TO THE IODIMETRIC TITRATION OF THESE ANIONS," *J. Am. Chem. Soc.*, vol. 53, no. 8, pp. 2893–2897, Aug. 1931.
- [182] L. Dózsa, I. Szilassy, and M. T. Beck, "Mechanism of the nitrite-iodide reaction," *Inorganica Chim. Acta*, vol. 17, no. C, pp. 147–153, 1976.
- [183] M. J. Traylor, M. J. Pavlovich, S. Karim, P. Hait, Y. Sakiyama, D. S. Clark, and D. B. Graves, "Long-term antibacterial efficacy of air plasma-activated water," *J. Phys. D. Appl. Phys.*, vol. 44, no. 47, Nov. 2011.
- [184] J. Mack and J. R. Bolton, "Photochemistry of nitrite and nitrate in aqueous solution: a review," *J. Photochem. Photobiol. A Chem.*, vol. 128, no. January 2016, pp. 1–13, 1999.
- [185] M. M. Tarpey and I. Fridovich, "Methods of Detection of Vascular Reactive Species: Nitric Oxide, Superoxide, Hydrogen Peroxide, and Peroxynitrite," *Circ. Res.*, vol. 89, no. 3, pp. 224–236, Aug. 2001.
- [186] D. Tsikas, "Methods of quantitative analysis of the nitric oxide metabolites nitrite and nitrate in human biological fluids.," *Free Radic. Res.*, vol. 39, no. 8, pp. 797–815, Aug. 2005.
- [187] K. M. Miranda, M. G. Espey, and D. a Wink, "A rapid, simple spectrophotometric method for simultaneous detection of nitrate and nitrite.," *Nitric Oxide*, vol. 5, no. 1, pp. 62–71, Feb. 2001.
- [188] D. Tsikas, "Analysis of nitrite and nitrate in biological fluids by assays based on the Griess reaction: appraisal of the Griess reaction in the L-arginine/nitric oxide area of research.," *J. Chromatogr. B. Analyt. Technol. Biomed. Life Sci.*, vol. 851, no. 1–2, pp. 51–70, May 2007.
- [189] G. R. Buettner, "Spin Trapping: ESR parameters of spin adducts," *Free Radic. Biol. Med.*, vol. 3, no. 4, pp. 259–303, Jan. 1987.
- [190] S. Yue Qian, M. B. Kadiiska, Q. Guo, and R. P. Mason, "A novel protocol to identify and quantify all spin trapped free radicals from in vitro/in vivo interaction of HO . and DMSO: LC/ESR, LC/MS, and dual spin trapping combinations," *Free Radic. Biol. Med.*, vol. 38, no. 1, pp. 125–135, 2005.
- [191] N. Hogg, "Detection of Nitric Oxide by Electron Paramagnetic Resonance Spectroscopy," *Free*



- Radic. Biol. Med.*, vol. 49, no. 2, pp. 122–129, 2011.
- [192] H. Wu, P. Sun, H. Feng, H. Zhou, R. Wang, Y. Liang, J. Lu, W. Zhu, J. Zhang, and J. Fang, “Reactive Oxygen Species in a Non-thermal Plasma Microjet and Water System: Generation, Conversion, and Contributions to Bacteria Inactivation-An Analysis by Electron Spin Resonance Spectroscopy,” *Plasma Process. Polym.*, vol. 9, no. 4, pp. 417–424, Apr. 2012.
- [193] H. Tresp, M. U. Hammer, J. Winter, K.-D. Weltmann, and S. Reuter, “Quantitative detection of plasma-generated radicals in liquids by electron paramagnetic resonance spectroscopy,” *J. Phys. D. Appl. Phys.*, vol. 46, no. 43, p. 435401, Oct. 2013.
- [194] H. Uchiyama, Q.-L. Zhao, M. A. Hassan, G. Andocs, N. Nojima, K. Takeda, K. Ishikawa, M. Hori, and T. Kondo, “EPR-Spin Trapping and Flow Cytometric Studies of Free Radicals Generated Using Cold Atmospheric Argon Plasma and X-Ray Irradiation in Aqueous Solutions and Intracellular Milieu,” *PLoS One*, vol. 10, no. 8, p. e0136956, 2015.
- [195] X. Shi, Y. Mao, L. N. Daniel, N. Ahmed, U. Saffiotti, Y. Rojanasakul, P. Gannett, and K. Liu, “Generation of thiyl and ascorbyl radicals in the reaction of peroxynitrite with thiols and ascorbate at physiological pH,” *J. Inorg. Biochem.*, vol. 56, no. 2, pp. 77–86, 1994.
- [196] J. Vásquez-Vivar, a M. Santos, V. B. Junqueira, and O. Augusto, “Peroxynitrite-mediated formation of free radicals in human plasma: EPR detection of ascorbyl, albumin-thiyl and uric acid-derived free radicals.,” *Biochem. J.*, vol. 314, pp. 869–876, 1996.
- [197] O. Augusto, R. M. Gatti, and R. Radi, “Spin-Trapping Studies of Peroxynitrite Decomposition and of 3-Morpholinopyridone N-Ethylcarbamide Autooxidation: Direct Evidence for Metal-Independent Formation of Free-Radical Intermediates,” *Arch. Biochem. Biophys.*, vol. 310, no. 1, pp. 118–125, Apr. 1994.
- [198] H. Bader and J. Hoigne, “Determination of Ozone in Water by the Indigo Method,” *Water Res.*, vol. 15, pp. 449–456, 1981.
- [199] C. Galindo, P. Jacques, and A. Kalt, “Photochemical and photocatalytic degradation of an indigoid dye: a case study of acid blue 74 (AB74),” *J. Photochem. Photobiol. A Chem.*, vol. 141, no. 1, pp. 47–56, 2001.
- [200] A. Y. Sychev, V. G. Isak, and U. Pfanmeller, “Determination of rate constants of hydroxyl radicals with organic and inorganic substances under conditions for the catalytic decomposition of hydrogen peroxide,” *Russ. J. Phys. Chem.*, vol. 53, pp. 1595–1598, 1979.
- [201] “NDRL/NIST Solution Kinetics Database,” *NIST Standard Reference Database 40*, 2002. [Online]. Available: <http://kinetics.nist.gov/solution/>. [Accessed: 19-Jan-2016].
- [202] A. J. Kettle, B. M. Clark, and C. C. Winterbourn, “Superoxide converts indigo carmine to isatin sulfonic acid: implications for the hypothesis that neutrophils produce ozone.,” *J. Biol. Chem.*, vol. 279, no. 18, pp. 18521–5, Apr. 2004.
- [203] A. T. Sugiarto, S. Ito, T. Ohshima, M. Sato, and J. D. Skalny, “Oxidative decoloration of dyes by pulsed discharge plasma in water,” *J. Electrostat.*, vol. 58, pp. 135–145, 2003.
- [204] M. Magureanu, C. Bradu, D. Piroi, N. B. Mandache, and V. Parvulescu, “Pulsed corona discharge for degradation of methylene blue in water,” *Plasma Chem. Plasma Process.*, vol. 33, no. 1, pp. 51–64, 2013.

- [205] L. R. Grabowski, E. M. Van Veldhuizen, a J. M. Pemen, and W. R. Rutgers, "Breakdown of methylene blue and methyl orange by pulsed corona discharge," *Plasma Sources Sci. Technol.*, vol. 16, no. 2, pp. 226–232, 2007.
- [206] J.-L. Brisset, B. Benstaali, D. Moussa, J. Fanmoe, and E. Njoyim-Tamungang, "Acidity control of plasma-chemical oxidation: applications to dye removal, urban waste abatement and microbial inactivation," *Plasma Sources Sci. Technol.*, vol. 20, no. 3, p. 34021, Jun. 2011.
- [207] M. Vautier, "Photocatalytic Degradation of Dyes in Water: Case Study of Indigo and of Indigo Carmine," *J. Catal.*, vol. 201, no. 1, pp. 46–59, 2001.
- [208] B. R. Van Dyke, D. a. Clopton, and P. Saltman, "Buffer-induced anomalies in the Fenton chemistry of iron and copper," *Inorganica Chim. Acta*, vol. 242, no. 1–2, pp. 57–61, 1996.
- [209] N. Spear and S. D. Aust, "Effects of glutathione on Fenton reagent-dependent radical production and DNA oxidation," *Arch. Biochem. Biophys.*, vol. 324, no. 1, pp. 111–116, 1995.
- [210] P. Wardman and L. P. Candeias, "Fenton chemistry: an introduction.," *Radiat. Res.*, vol. 145, no. 5, pp. 523–531, 1996.
- [211] P. Bautista, A. F. Mohedano, J. A. Casas, J. A. Zazo, and J. J. Rodriguez, "An overview of the application of Fenton oxidation to industrial wastewaters treatment," *J. Chem. Technol. Biotechnol.*, vol. 83, no. 10, pp. 1323–1338, Oct. 2008.
- [212] C. Walling, "Fenton's reagent revisited," *Acc. Chem. Res.*, vol. 8, no. 4, pp. 125–131, 1975.
- [213] R. V Lloyd, P. M. Hanna, and R. P. Mason, "The origin of the hydroxyl radical oxygen in the Fenton reaction.," *Free Radic. Biol. Med.*, vol. 22, no. 5, pp. 885–888, 1997.
- [214] J. E. Grebel, J. A. Charbonnet, and D. L. Sedlak, "Oxidation of organic contaminants by manganese oxide geomedia for passive urban stormwater treatment systems," *Water Res.*, vol. 88, pp. 481–491, 2016.
- [215] A. Samuni, M. Chevion, and G. Czapski, "Unusual copper-induced sensitization of the biological damage due to superoxide radicals," *J. Biol. Chem.*, vol. 256, no. 24, pp. 12632–12635, 1981.
- [216] L. Zhou, S. Li, Y. Su, X. Yi, A. Zheng, and F. Deng, "Interaction between histidine and Zn(II) metal ions over a wide pH as revealed by solid-state NMR spectroscopy and DFT calculations," *J. Phys. Chem. B*, vol. 117, no. 30, pp. 8954–8965, 2013.
- [217] R. M. Evans, L. Currie, and a Campbell, "The distribution of ascorbic acid between various cellular components of blood, in normal individuals, and its relation to the plasma concentration.," *Br. J. Nutr.*, vol. 47, no. 3, pp. 473–82, 1982.
- [218] M. Z. Hoffman and E. Hayon, "Pulse radiolysis study of sulfhydryl compounds in aqueous solution," *J. Phys. Chem.*, vol. 77, no. 8, pp. 990–996, 1973.
- [219] R. Radi, J. S. Beckman, K. M. Bush, and B. A. Freeman, "Peroxynitrite Oxidation of Sulfhydryls. The cytotoxic potential of superoxide and nitric oxide.," *J. Biol. Chem.*, vol. 266, no. 7, pp. 4244–4250, 1991.
- [220] J. R. Kanofsky and P. Sima, "Singlet Oxygen Production from the Reactions of Ozone with Biological Molecules," *J. Biol. Chem.*, vol. 266, no. 14, pp. 9039–9042, 1991.

- [221] M. Rougee, R. V Bensasson, E. J. Land, and R. Pariente, "Deactivation of singlet molecular oxygen by thiols and related compounds, possible protectors against skin photosensitivity.," *Photochem. Photobiol.*, vol. 47, no. 4, pp. 485–489, 1988.
- [222] C. C. Winterbourn and M. B. Hampton, "Thiol chemistry and specificity in redox signaling.," *Free Radic. Biol. Med.*, vol. 45, no. 5, pp. 549–61, Sep. 2008.
- [223] B. Alvarez and R. Radi, "Peroxynitrite reactivity with amino acids and proteins," *Amino Acids*, vol. 25, no. 3–4, pp. 295–311, 2003.
- [224] A. Schrammel, A. C. F. Gorren, K. Schmidt, S. Pfeiffer, and B. Mayer, "S-nitrosation of glutathione by nitric oxide, peroxynitrite, and NO/O<sub>2</sub>-," *Free Radic. Biol. Med.*, vol. 34, no. 8, pp. 1078–1088, 2003.
- [225] Z. Abedinzadeh, M. Gardes-Albert, and C. Ferradini, "Reactions of OH and Br<sup>•</sup>- radicals with glutathione. A radiolysis study," *Int. J. Radiat. Appl. Instrumentation. Part*, vol. 40, no. 6, pp. 551–558, 1992.
- [226] S. Goldstein and G. Czapski, "Mannitol as an OH. scavenger in aqueous solutions and in biological systems.," *Int. J. Radiat. Biol. Relat. Stud. Phys. Chem. Med.*, vol. 46, no. 6, pp. 725–9, 1984.
- [227] P. T. Chou and A. U. Khan, "L-ascorbic acid quenching of singlet delta molecular oxygen in aqueous media: Generalized antioxidant property of vitamin C," *Biochem. Biophys. Res. Commun.*, vol. 115, no. 3, pp. 932–937, 1983.
- [228] R. S. Bodannes and P. C. Chan, "Ascorbic Acid as a Scavenger of Singlet Oxygen," *FEBS Lett.*, vol. 105, no. 2, pp. 195–196, 1979.
- [229] B. Alvarez, G. Ferrer-Sueta, and R. Radi, "Slowing of Peroxynitrite Decomposition in the Presence of Mannitol and Ethanol," *Free Radic. Biol. Med.*, vol. 24, no. 7–8, pp. 1331–1337, May 1998.
- [230] M. G. Salgo, E. Bermúdez, G. L. Squadrito, and W. A. Pryor, "Peroxynitrite causes DNA damage and oxidation of thiols in rat thymocytes.," *Archives of biochemistry and biophysics*, vol. 322, no. 2. pp. 500–5, 1995.
- [231] B. Alvarez, V. Demicheli, R. Durán, M. Trujillo, C. Cerveñansky, B. A. Freeman, and R. Radi, "Inactivation of human Cu,Zn superoxide dismutase by peroxynitrite and formation of histidinyl radical," *Free Radic. Biol. Med.*, vol. 37, no. 6, pp. 813–822, Sep. 2004.
- [232] S. Iseki, K. Nakamura, M. Hayashi, H. Tanaka, H. Kondo, H. Kajiyama, H. Kano, F. Kikkawa, and M. Hori, "Selective killing of ovarian cancer cells through induction of apoptosis by nonequilibrium atmospheric pressure plasma," *Appl. Phys. Lett.*, vol. 100, no. 11, p. 113702, 2012.
- [233] T. Adachi, H. Tanaka, S. Nonomura, H. Hara, S. I. Kondo, and M. Hori, "Plasma-activated medium induces A549 cell injury via a spiral apoptotic cascade involving the mitochondrial-nuclear network," *Free Radic. Biol. Med.*, vol. 79, pp. 28–44, 2015.
- [234] A. Saha, S. Goldstein, D. Cabelli, and G. Czapski, "Determination of optimal conditions for synthesis of peroxynitrite by mixing acidified hydrogen peroxide with nitrite," *Free Radic. Biol. Med.*, vol. 24, no. 4, pp. 653–659, 1998.
- [235] T. Shimizu, Y. Iwafuchi, G. E. Morfill, and T. Sato, "Formation of thermal flow fields and

- chemical transport in air and water by atmospheric plasma,” *New J. Phys.*, vol. 13, no. 5, p. 53025, May 2011.
- [236] P. Pacher, J. S. Beckman, and L. Liaudet, “Nitric Oxide and Peroxynitrite in Health and Disease,” *Am. Physiol. Soc. Physiol. Rev.*, vol. 87, pp. 315–424, 2007.
- [237] R. Roots and S. Okada, “Estimation of life times and diffusion distances of radicals involved in X-ray-induced DNA strand breaks or killing of mammalian cells,” *Radiat. Res.*, vol. 64, no. 2, p. 306–320, 2014.
- [238] H. Liao, D. Stenman, and M. Jonsson, “Study of Indigo carmine as radical probe in photocatalysis,” *J. Photochem. Photobiol. A Chem.*, vol. 202, no. 2–3, pp. 86–91, 2009.
- [239] Y. Q. Li, P. Davidovits, C. E. Kolb, and D. R. Worsnop, “Mass and Thermal Accommodation Coefficients of H<sub>2</sub>O(g) on Liquid Water as a Function of Temperature,” *J. Phys. Chem. A*, vol. 105, no. 47, pp. 10627–10634, Nov. 2001.
- [240] W. L. Chameides and D. D. Davis, “The Free Radical Chemistry of Cloud Droplets And Its Impact Upon the Composition of Rain,” *J. Geophys. Res.*, vol. 87, no. C7, pp. 4863–4877, 1982.
- [241] K. Takeuchi and T. Ibusuki, “Quantitative Determination of Aqueous-Phase Ozone by Chemiluminescence Using Indigo-5,5’-disulfonate,” *Anal. Chem.*, vol. 61, no. 6, pp. 619–623, 1989.
- [242] M. Tabrizchi, T. Khayamian, and N. Taj, “Design and optimization of a corona discharge ionization source for ion mobility spectrometry,” *Rev. Sci. Instrum.*, vol. 71, no. 2000, p. 2321, 2000.
- [243] P. Bruggeman, F. Iza, D. Lauwers, and Y. A. Gonzalvo, “Mass spectrometry study of positive and negative ions in a capacitively coupled atmospheric pressure RF excited glow discharge in He–water mixtures,” *J. Phys. D. Appl. Phys.*, vol. 43, no. 1, p. 12003, 2009.
- [244] J. D. Skalny, J. Orszagh, S. Matejcik, N. J. Mason, J. a. Rees, Y. Aranda-Gonzalvo, and T. D. Whitmore, “A mass spectrometric study of ions extracted from point to plane DC corona discharge fed by carbon dioxide at atmospheric pressure,” *Int. J. Mass Spectrom.*, vol. 277, no. 1–3, pp. 210–214, 2008.
- [245] J. S. S. De Melo, R. Rondão, H. D. Burrows, M. J. Melo, S. Navaratnam, R. Edge, and G. Voss, “Spectral and photophysical studies of substituted indigo derivatives in their keto forms,” *ChemPhysChem*, vol. 7, no. 11, pp. 2303–2311, 2006.
- [246] N. Gandra, A. T. Frank, O. Le Gendre, N. Sawwan, D. Aebisher, J. F. Liebman, K. N. Houk, A. Greer, and R. Gao, “Possible singlet oxygen generation from the photolysis of indigo dyes in methanol, DMSO, water, and ionic liquid, 1-butyl-3-methylimidazolium tetrafluoroborate,” *Tetrahedron*, vol. 62, no. 46, pp. 10771–10776, 2006.
- [247] I. Dalmázio, A. P. F. M. de Urzedo, T. M. A. Alves, R. R. Catharino, M. N. Eberlin, C. C. Nascentes, and R. Augusti, “Electrospray ionization mass spectrometry monitoring of indigo carmine degradation by advanced oxidative processes,” *J. Mass Spectrom.*, vol. 42, no. 10, pp. 1273–1278, Oct. 2007.
- [248] M. J. Pavlovich, H.-W. Chang, Y. Sakiyama, D. S. Clark, and D. B. Graves, “Ozone correlates with antibacterial effects from indirect air dielectric barrier discharge treatment of water,” *J. Phys.*

- D. Appl. Phys.*, vol. 46, no. 14, p. 145202, Apr. 2013.
- [249] L. Cui, W. Ye, E. G. Prestwich, J. S. Wishnok, K. Taghizadeh, P. C. Dedon, and S. R. Tannenbaum, "Comparative analysis of four oxidized guanine lesions from reactions of DNA with peroxynitrite, singlet oxygen, and gamma-radiation," *Chem. Res. Toxicol.*, vol. 26, no. 2, pp. 195–202, 2013.
- [250] K. Arjunan, V. Sharma, and S. Ptasinska, "Effects of Atmospheric Pressure Plasmas on Isolated and Cellular DNA—A Review," *Int. J. Mol. Sci.*, vol. 16, pp. 2971–3016, 2015.
- [251] J. a. Theruvathu, R. Flyunt, C. T. Aravindakumar, and C. von Sonntag, "Rate constants of ozone reactions with DNA, its constituents and related compounds," *J. Chem. Soc. Perkin Trans. 2*, no. 3, pp. 269–274, 2001.
- [252] K. Ito, S. Inoue, Y. Hiraku, and S. Kawanishi, "Mechanism of site-specific DNA damage induced by ozone.," *Mutat. Res.*, vol. 585, no. 1–2, pp. 60–70, Aug. 2005.
- [253] R. Flyunt, J. a. Theruvathu, A. Leitzke, and C. von Sonntag, "The reactions of thymine and thymidine with ozone," *J. Chem. Soc. Perkin Trans. 2*, vol. 2, no. 9, pp. 1572–1582, Aug. 2002.
- [254] J. Chen and J. H. Davidson, "Ozone Production in the Positive DC Corona Discharge: Model and Comparison to Experiments," *Plasma Chem. Plasma Process.*, vol. 22, no. 4, pp. 495–522, 2002.
- [255] J. Chen and J. H. Davidson, "Ozone Production in the Negative DC Corona: The Dependence of Discharge Polarity," *Plasma Chem. Plasma Process.*, vol. 23, no. 3, pp. 501–518, 2003.
- [256] V. K. (FIT) Sharma and N. J. D. (Imperial C. L. Graham, "Oxidation of Amino Acids, Peptides and Proteins by Ozone: A Review," *Ozone Sci. Eng.*, vol. 32, no. 2, pp. 81–90, Apr. 2010.
- [257] G. Xu and M. R. Chance, "Hydroxyl radical-mediated modification of proteins as probes for structural proteomics," *Chem. Rev.*, vol. 107, no. 8, pp. 3514–3543, 2007.
- [258] M. Gracanin, C. L. Hawkins, D. I. Pattison, and M. J. Davies, "Singlet-oxygen-mediated amino acid and protein oxidation: formation of tryptophan peroxides and decomposition products.," *Free Radic. Biol. Med.*, vol. 47, no. 1, pp. 92–102, Jul. 2009.
- [259] M. R. M. Domingues, P. Domingues, A. Reis, C. Fonseca, F. M. L. Amado, and A. J. V Ferrer-Correia, "Identification of oxidation products and free radicals of tryptophan by mass spectrometry.," *J. Am. Soc. Mass Spectrom.*, vol. 14, no. 4, pp. 406–16, Apr. 2003.
- [260] E. Takai, T. Kitamura, J. Kuwabara, S. Ikawa, S. Yoshizawa, K. Shiraki, H. Kawasaki, R. Arakawa, and K. Kitano, "Chemical modification of amino acids by atmospheric-pressure cold plasma in aqueous solution," *J. Phys. D. Appl. Phys.*, vol. 47, no. 28, p. 285403, Jul. 2014.
- [261] G. L. Ellman, "Tissue sulfhydryl groups," *Arch. Biochem. Biophys.*, vol. 82, no. 1, pp. 70–77, 1959.
- [262] P. W. Riddles, R. L. Blakeley, and B. Zerner, "Ellman's reagent: 5,5'-dithiobis(2-nitrobenzoic acid)—a reexamination," *Anal. Biochem.*, vol. 94, no. 1, pp. 75–81, Apr. 1979.
- [263] C. Flox, S. Ammar, C. Arias, E. Brillas, A. V. Vargas-Zavala, and R. Abdelhedi, "Electro-Fenton and photoelectro-Fenton degradation of indigo carmine in acidic aqueous medium," *Appl. Catal. B Environ.*, vol. 67, no. 1–2, pp. 93–104, 2006.

- [264] A. Ciechanover, "The ubiquitin-proteasome proteolytic pathway," *Cell*, vol. 79, no. 1, pp. 13–21, 1994.
- [265] E. G. Mimnaugh, P. Bonvini, and L. Neckers, "The measurement of ubiquitin and ubiquitinated proteins.," *Electrophoresis*, vol. 20, no. 2, pp. 418–28, 1999.
- [266] M. Witzke, P. Rumbach, D. B. Go, and R. M. Sankaran, "Evidence for the electrolysis of water by atmospheric-pressure plasmas formed at the surface of aqueous solutions," *J. Phys. D. Appl. Phys.*, vol. 45, no. 44, p. 442001, Nov. 2012.